Crystal formation during the vitrification of HLW in Ca/Zn base glass

Michal Miekina
MEng.

NATIONAL NUCLEAR LABORATORY

A thesis submitted to the Department of Materials Science and Engineering at the University of Sheffield in partial fulfilment of the requirement for the Degree of Doctor of Philosophy

July 2018

Abstract

This thesis investigates the incorporation and solubility of Post Operational Clean-Out (POCO) waste simulant into Ca/Zn borosilicate glass comprising mainly of MoO_3, ZrO_2 and BaO, where the first two oxides have a low solubility in borosilicate glass. Moving from MW borosilicate glass, used by the UK nuclear sector, into its modified version including extra Al_2O_3, CaO and ZnO (Ca/Zn glass) requires further research. Nevertheless, initial findings from NNL and this study shows that the formation of water-soluble yellow phase is avoided on tested waste loadings (25 and 38 wt%), which translated into a better chemical durability in aqueous environment. The poor solubility of Mo and Zr in the borosilicate glass is the main factor that controls the POCO waste loading during the vitrification of nuclear waste. To tackle the problem with formation of undesirable alkali molybdates, producing water-insoluble molybdates such as Ca and Ba molybdates was used as a feasible approach based on that already employed by the French nuclear industry to combat similar issues. Melting of POCO waste glasses has demonstrated a detrimental effect on Inconel 601 and Nicrofer 6025 HT utilised by the industry as the melter vessel materials. Thus, it was crucial to understand the corrosion mechanism to choose the best material for the melters.

Hence the overall aims of the project were to

- Understand the chemistry of the crystals likely to form throughout the vitrification of different types of POCO simulant in Ca/Zn base glass and to determine whether these crystal phases form in the melter or on cooling
- Investigate how the viscosity affects any crystal phases formed and the role of crystalline phases on properties such as the chemical durability of the final products
- Investigate the effect of molten waste glass compositions on the corrosion of Inconel 601 and Nicrofer 6025 HT coupons

The viscosity of the modified POCO containing glasses (25 % waste loading) was lower in all cases compared to the unmodified counterparts. Additionally, the modified samples were much more crystalline, than the unmodified ones. However, the chemical durability in both cases was similar after 28-day tests, but the results after 7 day tests clearly exhibited that the modified glasses were more durable (PCT). Corrosion tests performed on Inconel 601 and Nicrofer 6025 HT showed that corrosive nature of the molten waste

glasses strictly depended on their composition, with the modified glasses demonstrating lower corrosiveness towards the examined metallic coupons, than the unmodified POCO waste products.

Crystals identified by X-ray diffraction exhibited that samples with lower waste loading were almost amorphous while higher waste loadings resulted in intensive crystallisation, where for example $CaMoO_4$ and $ZrSiO_4$ phases were common. The mechanism responsible for phase separation in the glasses with excess molybdate was liquid-liquid separation and then crystallisation, which arises during cooling within glass melts containing elevated amounts of MoO_3. The molybdate crystals, which are typically Ca/Ba molybdates are grouped into spherical shapes that are submicron in size and randomly distributed.

Charge compensation mechanisms were examined by incorporation of Na_2MoO_4 into a Ca/Zn base glass with additions of CaO and Fe_2O_3 and showed that $CaMoO_4$ can be produced. Mössbauer spectroscopy proved that majority of iron exists as Fe^{3+}, giving its structural role as FeO_4^- that may interact with "free" Na^+ which in turn strongly decreased the amount of Na_2MoO_4 or $NaMo_4O_6$ recrystallised after dissolution into glass. This experiment also showed that formation of water-soluble sodium molybdates is not inevitable and can be suppressed.

The POCO based waste glasses consist of two groups called unmodified and modified ones. The modifications were aimed to improve meltability and uniformity of the final waste products. This was achieved by addition of CaO, CuO and Mn_2O_3 to the Ca/Zn base glass. Glass densities steadily increased with increasing incorporation of the POCO–based waste, but their values were similar. Glass transition temperatures T_g all decreased with increasing POCO loadings. PCT tests showed that durability results with both unmodified and modified POCO waste glasses after 28 day tests were comparable.

Finally, incorporating Mo into durable Ca/Ba molybdates appears to be an effective method to immobilise this problematic element and avoiding the formation of yellow phase, which is totally undesired during vitrification. This approach is also supported by numerous papers from the French industry, where production of glass composites rich in insoluble molybdates of Ca/Ba has been identified as a feasible option.

"Never give up. Today is hard, tomorrow will be worse, but the day after tomorrow will be sunshine."

Chinese businessman and philanthropist ***- Jack Ma***

"Basic research is what I am doing when I don't know what I am doing."

German rocket scientist - ***Wernher von Braun***

Acknowledgements

Firstly, I would like to express my genuine appreciations to those who helped me throughout my PhD life in the University of Sheffield. Primarily, I would like to thank to my supervisor Prof. Russell Hand whose constructive guidance was invaluable during this project and led me to the completion of this PhD. I would also like to thank to my second supervisor Prof. Neil Hyatt for his support on my experiments and comments to my work. Special thanks to my industrial supervisor from National Nuclear Laboratory (NNL), James Stevens, whose vital industrial guidance plus nuclear waste simulants enhanced this work technically.

My appreciations also go to Carl Steele (Sellafield Ltd) and Mike Harrison (NNL) for their help with the project and some guidance to further improve this work. I have to highlight an unforeseen and great support from Prof. Ian Pegg (VSL, Washington DC) for analysing my samples with respect to viscosity and Mössbauer spectroscopy which made my scientific argument more robust.

Great appreciation is towards staff and students in Immobilisation Science Laboratory (ISL) group for their valuable advice during my study especially Sean, Lawan, Shengheng and Clive. I am also indebted to the technical staff in the Department of Materials Science and Engineering, in particular to Mr Ian Watts and Dr Lisa Holland who have helped me with plenty of glasses. Thanks, are also given to the Nuclear FiRST doctoral training centre.

Finally, I would like to convey my deep gratitude to Naheed, who accompanies me through the whole duration of my study and gives me endless support and understanding. Deepest gratefulness is also to my parents whose dedication throughout my life has always been the most influencing in pushing me forward.

Contents

List of Figures

List of Tables

1. Introduction

In the UK, 15 nuclear reactors currently account for about 21 % of the total electricity production. Nevertheless, almost half of that nuclear capacity will be shut down till 2025, which requires new build stations. The rising cost of fossil fuels and plans to phase out around 9 GWe of coal electricity in the following years suggests that nuclear new built is a viable solution to the upcoming power shortage (World Nuclear Association, 2017). Unfortunately, nuclear electricity generation is associated with a production of spent nuclear fuel that is highly radioactive, dangerous to living species and heat generating. In the UK, spent nuclear fuel is reprocessed to recover ^{235}U and ^{239}Pu and the remaining solution is considered as nuclear waste. The liquid High Level Waste (HLW) is stored in Highly Active Storage Tanks (HAST) which are constantly under cooling due to the significant heat generated by the waste (Ojovan & Lee 2005, Ojovan & Lee 2014 and Edmondson et al. 2012). As fuel reprocessing comes to an end those tanks will undergo a Post Operational Clean Out (POCO) in which so called POCO waste will be produced (Edmondson et al. 2012). Vitrification of this POCO waste, rich in Mo, Zr and Ba species requires an improved glass composition (ideally borosilicate) that can incorporate effectively some problematic elements and produce durable wasteforms. (NNL 2014, Dunnett et al. 2012 a&b). Vitrification of POCO waste is difficult due to the high quantities of MoO_3 (~ 61 wt%) and ZrO_2 (~ 23 wt%) that possess very low solubility in MW borosilicate glass (approx. 1 wt%) in the waste (NNL 2014, Dunnett at al. 2012b). Specifically Mo can lead to the formation of so called “yellow phase” - mainly a mixture of alkali and alkaline earth molybdates with high aqueous solubility which is a particular problem that reduces POCO waste loading.

To improve MoO_3 solubility in borosilicate glass, MW glass was modified by addition of CaO, Al_2O_3 and ZnO to produce CZ glass frit was formed, which demonstrated an enhanced solubility of Mo (Short et al. 2008, Dunnett at al. 2012b). Tackling the uncontrolled crystallisation seems to be a solution to produce a durable wasteform. In France similar difficulties with Mo waste has been combated by formation of durable compounds of Mo such as $CaMoO_4$ and $BaMoO_4$ over water-soluble molybdates e.g. Na_2MoO_4 or Cs_2MoO_4 occurs (Taurines & Boizot, 2011, Caurant et al. 2007).

The production of unwanted phases such as Cs_2MoO_4 and Na_2MoO_4 could be reduced through a charge compensation mechanism involving 'free' Na^+ ions involved in compensation of BO_4^-, AlO_4^- and FeO_4^- units (Cochain et al. 2012). Thus, the production of $CaMoO_4$ is promoted as a durable phase, uniformly distributed throughout the glass as tiny globules. Crystallisation may also be promoted by the radiogenic heat from decaying radionuclides in the HLW glass resulting in a retarded cooling. Therefore, it is crucial to modify the waste glass compositions to produce only the crystalline phases with acceptable aqueous durability to be able to retain radionuclides in glassy matrix. The $CaMoO_4$ phase also retains an ability to incorporate other species such as actinides and possesses a high radiogenic stability (10^{12} Gy), which is above the dose expected in geological repository (Taurines et al. 2013).

This work concerns incorporation of a few types of nuclear waste into Ca/Zn lithia borosilicate frit (CZ glass) produced for NNL at Sellafield. Those waste simulants include POCO waste and POCO blended with Magnox and Oxide waste in different ratios (referred to as P type simulants).

The aims of this work are to:

- Understand the chemistry of the crystals likely to form throughout the vitrification of different types of POCO simulant in Ca/Zn base glass and to determine whether these crystal phases form in the melter or on cooling
- Investigate how the viscosity affects any crystal phases formed and the role of crystalline phases on properties such as the chemical durability of the final products
- Investigate the effect of molten waste glass compositions on the corrosion of Inconel 601 and Nicrofer 6025 HT coupons

In Chapter 2, the literature review considers the background and categories of nuclear waste, and then compares different immobilisation techniques. Vitrification is the primary option of High Level Waste immobilisation, but it confronts difficulties in incorporating some troublesome elements such as Zr and Mo. The structure of modified borosilicate glasses is then reviewed, regarding their application in nuclear waste vitrification.

Vitrification related issues are discussed based on previous studies. These include corrosion of Inconel 601 and Nicrofer 6026 HT melters with respect to molybdenum rich glass melts and associated phenomena such as volatility, yellow phase and spinels

formation. The main components of POCO waste (MoO_3, ZrO_2 and BaO) and its incorporation into borosilicate glass are covered with dissolution mechanisms into a borosilicate glass and its dependence on the compositional modifications. Furthermore, chemical durability of waste glasses and corrosion mechanisms are explained in conjunction with crystallisation and amorphous phase separation during waste vitrification.

Chapter 3 describes the procedures of glass production and a variety of characterisation techniques used to assess the properties of glasses produced in this work. These include density measurements, X-ray diffraction, Differential Thermal Analysis, Raman, Scanning Electron Microscopy combined with energy dispersive X-ray spectroscopy, Mossbauer spectroscopy and viscosity measurements.

Chapter 4 focuses on incorporation of MoO_3 and Na_2MoO_4 into the CZ base glass enriched in CaO and Fe_2O_3. The discussion covers issues related to molybdate solubility and the structural changes caused by Mo incorporation in glass network, along with the phase separation mechanisms occurring in the different compositions.

Chapter 5 presents the results gained for lab-made POCO waste simulant solubility in CZ and MZ borosilicate glasses. In the MZ type glass CaO was substituted on a molar basis by MgO to investigate how this change will affect the incorporation of POCO waste. The results and discussion in this chapter are divided into parts similar to **Chapter 4,** namely the effects of POCO simulant incorporation on glass structure and properties followed by the microstructure of phase separated glasses plus chemical durability test.

Chapter 6 is about the incorporation and solubility of P type waste simulants received from the NNL, with variable POCO simulant contents. Each of the waste glasses has a modified version which contains extra CuO, CaO and Mn_2O_3 to aid the incorporation of the waste simulants. Similar characterisation techniques were used compared to chapter 5 plus viscosity measurements and Kissinger method to obtain the activation energy of crystallisation of some samples. The results and discussion in this chapter are more expanded than in the previous two chapters.

Chapter 7 is about corrosion tests conducted on Inconel 601 and Nicrofer 6025 HT in the P type waste glasses at 25 and 38 wt% waste loading. This chapter uses SEM/EDX to characterise the damaged caused to the metal surface by a molten waste glass. Generally, the metallic coupons were investigated above the glass melt and the area submerged in the melt. The results showed that the submerged part of the coupon was less corroded than the part above the melt. It was also found that corrosiveness of the modified P type glasses were lower compared to unmodified glass melts.

Chapter 8 includes the conclusions of this project and some recommendations for the future work

2. Literature review

2.1 Radioactivity and nuclear power generation

Radioactivity is a process of spontaneous disintegration (decay) of unstable atomic nuclei associated with emission of particles (e.g. electrons, He^{2+}) and/or photons (electromagnetic radiation) (Ojovan and Lee 2005) (L'Annunziata 2007). Natural radioactivity was discovered by Henri Becquerel in 1896 because of experiments to establish a connection between X-rays produced by Conrad Röntgen's X-ray tube and natural phosphorescence. Becquerel noticed that U emitted radiation that could be deflected by electric or magnetic field (unlike X-rays) and caused gases to be ionised. Marie and Pierre Curie working on uranium ore in Paris discovered new active elements polonium and radium (Palmer 1995). It turned out that radioisotopes can be used in medicine so-called nuclear medicine when radium was used for the treatment of cancer. A few years later in 1919 Rutherford manage to produce a stable isotope of oxygen-17 by bombarding nitrogen-14 by alpha particles. Following Rutherford's experiment Frederic and Irene Joliet achieved the first artificial production of isotopes in 1934 by bombarding elements such as Mg, B and Be with alpha particles (He^{2+}) from polonium (L'Annunziata 2007). In 1938, Otto Frisch and Lise Meitner interpreted the experimental results of Fritz Strassman and Otto Hahn, concluding that neutron induced fission of the ^{235}U nuclei had happened. Enrico Fermi and his team encouraged by the possibility of the emission of secondary neutrons and related chain reaction built the first nuclear reactor in 1942 – Chicago Pile 1. In this reactor scientists as a part of a Manhattan Project controlled a nuclear chain reaction for the first time. The final goal of the Manhattan project was to produce atomic bombs for WW2. That aim was realised on the 16th July 1945 in the so called Trinity test. Following WW2 the first nuclear power programmes were developed (Greenwood & Earnshaw 1997).

Nuclear electricity generation in the world in 2015 accounted for about 11 % of world energy generation. In the UK about 15 % of the electricity is provided by the nuclear sector. Currently, in the world, there are approximately 440 commercial nuclear power reactors in 31 countries and another 65 are under construction. The most developed

nuclear program is currently in China which completed and commenced operation of 28 new reactors in 2002-2015 with 24 reactors under construction (World Nuclear Association 2016).

Electricity generation mainly (~ 65%) uses two types of reactors Pressurised Water Reactor (PWR) and Boiling Water Reactor (BWR). A nuclear reactor uses the principle of a controlled chain reaction (fission) between fissile elements (^{235}U and ^{239}Pu) and neutrons. Splitting of fissile nuclei is caused by neutron (n) absorption to create an unstable nucleus which in turn splits up (fission) into two isotopes (FP fission product) and generates large amounts of energy as a heat. The range of fission products have a broad Z number reaching the mid-lanthanides (**Figure 2.1**) and the majority of nuclear reactors use ^{235}U that undergoes nuclear reaction that has many possible ways to go e.g.:

$$^{235}U + n \rightarrow {}^{236}U \rightarrow 2FP + 2.4n + 200MeV \qquad (2.1)$$

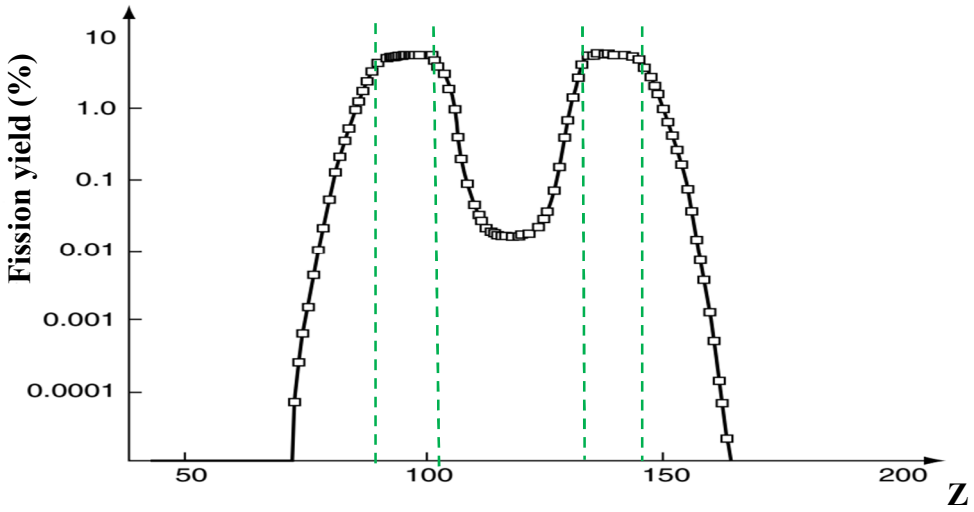

Figure 2.1 Mass distribution from fission fragments of 235U, where Z – mass number (Young 2014, Ojovan & Lee 2005)

The neutrons released during a fission reaction can induce fission in other suitable nuclei forming a self-propagating chain reaction. In order to control the intensity of chain reaction in nuclear reactors, neutron absorbers are used in a form of control rods. In practice "fast" neutrons are produced during fission (kinetic energy > 1MeV), which are ineffective at causing further fission of appropriate nuclei, therefore they need to be

slowed down (through elastic scattering with a material of low Z number – a moderator e.g. graphite) to become thermal neutrons (kinetic energies comparable to a molecule of gas at RT, approx. <1 eV).

Another type of reactor that utilises fast neutrons is the so-called Fast Breeder Reactor FBR) that does not require moderators, producing power from Pu decay while instantaneously transmuting U to Pu in the fuel (Pu breeder). India is looking at breeders as part of a Th cycle, interestingly, FBR is capable of producing more than 50 times more energy per kilogram of U than can be produced by reactors with moderators (e.g. PWR) and they are almost self-sufficient in fuel. Nevertheless, there has been limited acceptance of this type of technology because of a huge expense of construction and Pu proliferation.

The concentration of ^{235}U in natural U is sufficient (~ 0.72 %) to maintain the chain reaction, but very often fuel enrichment up to 3-5 % is beneficial because some neutrons are absorbed by fuel cladding and moderator. The heat produced after the fission comes from multiple collisions of fission products with neighbouring atoms, which is extracted by a cooling medium (very often water or CO_2) and then finally produces pressurised steam to drive a turbine connected to an electricity generator.

2.1.1 Reprocessing of Spent Nuclear Fuel (SNF)

Reprocessing is used to extract fissile isotopes (^{235}U and ^{239}Pu) which are added to the fuel fabrication process to be used again inside a reactor. Reprocessing of SNF in the UK is based on a plutonium and uranium extraction process (PUREX). Two reprocessing plants located at Sellafield are THORP (Thermal Oxide Reprocessing Plant, for spent UO_2 fuel) and B205 used for spent metallic U fuel. Reprocessing of SNF takes in removal of the fuel rods cladding and then dissolution of the remainder in 6 mol nitric acid before the Pu and U ions are extracted via the PUREX process. The residue solution is HLLW which contains dissolved fission products combined with impurities from the cladding material (e.g. Zr or Mg), transuranic elements formed during neutron capture (e.g. Np, Am), inactive process chemicals (kerosene, tributyl phosphate) plus traces of unseparated Pu (Ojovan and Lee 2014).

2.1.2 Nuclear waste categories and sources

Radioactive waste is a product of waste materials, which contain radioisotopes in concentrations greater than typical clearance levels, and they cannot be used as a feedstock. The categorisation of radioactive waste is critical and it is related to the viable processing methods and way of final disposal. Classifications of nuclear waste vary from one country to another. In the UK nuclear wastes are categorised as follows:

- Very Low Level Waste (**VLLW**),
- Low Level Waste (**LLW**),
- Intermediate-Level Waste (**ILW**)
- High Level Waste (**HLW**)

Class	Description
VLLW (Very Low Level Waste)	Waste, which can be disposed with an everyday refuse (dustbin disposal). Each of them ($0.1m^3$) contain less than 400kBq of gamma/beta activity or on its own hold less than 400 kBq
LLW (Low Level Waste)	Including radionuclides other than those appropriate for removal with casual waste, nevertheless, 4GBq/t of alpha or 12GBq/t of gamma/beta activity cannot be exceeded. This kind of waste is acceptable for authorised disposal sites such as Dounreay, Drigg and other landfill sites by secured burial e.g. shielding material
ILW (Intermediate-Level Waste)	These wastes exceed radioactivity boundaries for LLW, but heat generation is not considered in the design of removal and storage sites
HLW (High Level Waste)	Waste that produce significant amounts of radiogenic heat due to its high radioactivity and this has to be considered during planning disposal and storage facilities ($>2kW/m^3$)

Table 2.1. Categorisation of radioactive waste in the United Kingdom (Ojovan and Lee 2005; Ojovan and Lee 2014; Donald & Metcalfe 2004)

2.1.3 Sources

The first large scale industrial source of nuclear waste originated from The Manhattan Project (USA), which aimed to produce nuclear bombs, during World War 2. Because of the colossal potential of nuclear energy, some countries started their nuclear programs to produce both weapons and energy. Atomic reactors were also successfully employed to power ships, especially submarines. Generally, there are three main sources of radioactive waste:

1. Nuclear Fuel Cycle (NFC) – power generation and military tests

2. Non-NFC radioisotopes for medical and research institutions plus non-nuclear industries

3. Radioactive waste originating from accidents e.g. Three Mile Island, Chernobyl and Fukushima (Ojovan and Lee 2014; Ojovan and Lee 2005).

Unquestionably, the NFC produces nuclear waste. NFC waste can be separated into two categories: open cycle NFC and closed cycle NFC waste. In the former case, NFC spent fuel is removed from the reactor without reprocessing, but in the latter case, spent nuclear fuel is further processed to recover useable Pu and U and the resultant high-level liquid waste must be further treated before storage and disposal. Even though electricity from nuclear power plants is described as "the cheapest way for the UK to grow its low-carbon energy supply for at least a decade", waste production from typical power plant is significant (Black R. 2011; Ojovan and Lee 2005). Additionally, usually a 1 GW(e) nuclear reactor produces about 30 tons of SNF waste per annum. Typical SNF contains 95 % ^{238}U, fission products and transuranic elements gives about 3 % , but 1% ^{239}Pu and 1% ^{235}U (Ojovan and Lee 2005). Global production of SNF is about 10 000 tons per annum and comes from about 433 nuclear power plants. To further reduce SNF production waste minimisation programmes were introduced 1970s and 1980s. These programmes reduce the activity and amount of waste materials to as low as possible level by optimisation at all stages of nuclear processing from the power plant construction through operation to decommissioning. In terms of volume of radioactive waste LLW accounts for the biggest quantity. Waste minimisation programmes achieved a noteworthy 10–fold decrease of LLW over the previous 20 years, decreasing LLW volumes to around 100 m^3 each year per 1GW(e). Comparing the same amount of electricity from nuclear power generation with fossil fuel plants, the former generates much less waste. Finally, if all SNF was reprocessed the HLW from yearly worldwide production of electricity could be retained by vitrification in 10 m^3 (Ojovan and Lee 2005).

The Sellafield site stores numerous radioactive wastes produced in the UK since the beginning of nuclear era. In the past Magnox wastes were vitrified at Sellafield site, but currently Magnox and UO_2 HLW streams are blended in a 25:75 ratio (so called 'blend waste') before the vitrification. To deal with elevated levels of MoO_3 from POCO waste

another type of blended waste currently being considered including Magnox, POCO and Oxide waste **(Section 2.3**) (Dunnett et al. 2012; R. Short 2014).

2.1.4. Nuclear waste immobilisation technologies

The purpose of nuclear waste management is to dispose of radioactive waste in a manner that minimises and removes the possibility of environmental pollution. The most radiotoxic is HLW, which must be immobilised within a host material. Immobilisation is undertaken by its chemical incorporation at a molecular level in a suitable matrix (normally glass or ceramic) or by encapsulation of the waste within an inert matrix (e.g. cement or bitumen) (Donald et al. 1997; Ojovan and Lee 2005; Ojovan and Lee 2014).

The immobilisation of waste is required for up to 1 million years, after that time HLW will not be considered as dangerous for the environment. Numerous immobilisation methods have been evaluated: these include stacking between tectonic plates, dumping in the sealed containers in seas, monitoring storage either over or under ground and disposal in space. However, the most widely accepted is geological disposal of nuclear waste immobilised in durable materials e.g. cements, ceramics or glasses. This geological storage can be either above the water table (Yucca Mountain, USA) or under in a low water flow or dry environment (e.g. clay in Switzerland or salt mines in Germany). This geological 'vault' is assumed to be undisturbed and the only possible escape mechanism of radionuclides will be via ground water penetration. Moreover, the multi-barrier concept drastically reduces water penetration of the wasteforms ideally until the radionuclides are mostly decayed (Donald 2010; Donald et al. 1997).

The vitrification of nuclear waste in the In-Can-Melter was invented at Battelle Pacific Northwest National Laboratory (PNNL) in the USA. The calciner was sprayed into a disposal canister which function was also to be a glass-producing vessel. Subsequently the frit was added to the calcine as it drops into a container surrounded by a zoned furnace. That mixture was then heated to 1000-1100 °C producing a molten glass. The containers were typically filled up to 90 % level (Ojovan 2007).

The use of nuclear vitrification technology initially started in the 1950s in Canada using a natural silicate mineral, nepheline syenite as a base material. This was mixed with a lime and acidic solution of the waste and the whole batch was heated at 1250-1350 ^{o}C in

a clay crucible. The next step was to construct an active plant at Chalk River to prove the concept of vitrification process on a larger scale. Between 1957 and 1960 radioactive blocks of glass were produced. Nevertheless, the development of that programme was stopped in 1960 as no planned fuel reprocessing was planned in Canada then, a new programme was started in 1976 (Donald 2010; Donald 1997).

Some of them were more scandalous than others. For instance, in the UK at Sellafield some amounts of Tc-99 were discharged to the Irish Sea, resulting in an elevated level of Tc-99 in the seafood surrounding Great Britain, Ireland and Norway (McCubbin et al. 2006). Moreover, disposing LLW and ILW to sea was practised by many countries e.g. USA, Japan, France, Germany, USRR and Spain from 1949 to 1982. Fortunately, at present these approaches are considered environmentally unacceptable, and dispersion of radioactive waste in the oceans is internationally forbidden (Donald 2010).

2.1.4.1. Cementation

Conventional cements are widely employed for ILW/LLW immobilisation because of their low price and good availability. Ordinary Portland Cement (OPC) is mixed with pulverised fuel ash or blast furnace slag. The main advantages of cement matrix refers to the encapsulation of solid, liquid, and sludge and actinides as well have low solubility in water at pH >11. Unquestionably, low processing temperature reduces possible volatilisation of some waste components throughout the processing (Donald 2010; Ojovan and Lee 2005). It has been argued that hydroxides and oxyhydroxides are more secure thermodynamically than their oxide equivalents in water environment. As a result, hydrated forms of ordinary cement are thought to offer enhanced stability in geological regions (Donald 2010). Moreover, natural analogues such as Roman pozzolanic cements have survived for over 2000 years and they are still durable. Additionally, some cement-like forms, created in nature, date back about two million years. However, cements have hardly been considered as HLW hosts, due to the high likelihood of radiolysis and high concentration of isotopes (e.g. ^{137}Cs) resulting insignificant heat generation that make them unfeasible for immobilisation in the cementitious matrix (Ojovan and Lee 2005; Ojovan and Lee 2014; Donald 2010).

2.1.4.2. Ceramisation

Ceramisation is another alternative to deal with high level radioactive waste. Ceramic materials are utilised to lock dangerous radioisotopes into their crystalline structure, e.g. zirconolite ($CaATi_2O_7$, A= Gd, Zr, Sm or Hf) without the creation of exact actinide phases. The idea of utilising ceramics to immobilise nuclear waste was suggested by Hatch in 1953. First candidates were based on clay, while later ones contained sintered super-calcines made of natural minerals such as phosphates, pollucite, powellite and rare earth apatites (Donald 2010). However, the supercalcines needed very high operating temperatures and losses of volatile elements (e.g. Cs) were significant. Many ceramic materials possess very high corrosion resistance in contrast to borosilicate glasses under foreseen repository conditions, however, multiphase composition with some minor phases make them more problematic to foresee their long-time behaviour. Finally, the technology regarding crystalline ceramics is more complex, and require more expensive equipment, than that associated with vitrification (Donald 2010; Ojovan and Lee 2005).

2.1.4.3. Vitrification

Nuclear waste vitrification was only established in the 1950s in countries with nuclear technologies. The generic principle is based on producing suitable glass and dissolving maximum level of HLW possible while retaining a homogeneous and steady melt, which could produce a chemically durable glass (Donald 2010; Ojovan and Lee 2005). Glass as a material possesses a great flexibility for the accommodation of large changes in composition, this is due to a structure with variable degree of connectivity. In contrast to crystalline ceramics, stoichiometry in glass is not that important and glass can act like a solvent (Varshneya 1994).

The vitrification process used in the UK consists of three main stages (Donald 2010; Donald et. al 1997):

1. **Evaporation –** radioactive waste is dried at 100 ^oC
2. **Calcination –** thermal treatment in the calciner, where partial denitration to oxides occurs (up to 600 ^oC). The addition of sucrose (used to introduce reducing conditions to minimise volatility of Ru as RuO_4) and $LiNO_3$ to act as a flux in the glass melter

and to prevent the development of refractory crystals e.g. $MgAl_2O_4$ in the calciner. The reminder nitrites help waste calcine to be stickier and this reduces dust formation.

3. **Vitrification –** calcined waste is mixed with a glass frit and then melted in an inductively heated (Inconel 601 or Nicrofer 6025 HT for waste rich in Mo) melter (**Figure 2.2**). The frit is a sodium - lithium borosilicate glass mixed (~ 75 wt.%) with calcined waste. This batch is melted at 1060 ºC for up to 8 hours with air sparge to increase homogeneity. The glass melt is then poured into stainless steel canisters (400 kg of glass) in two stages, cooled and sent for storage.

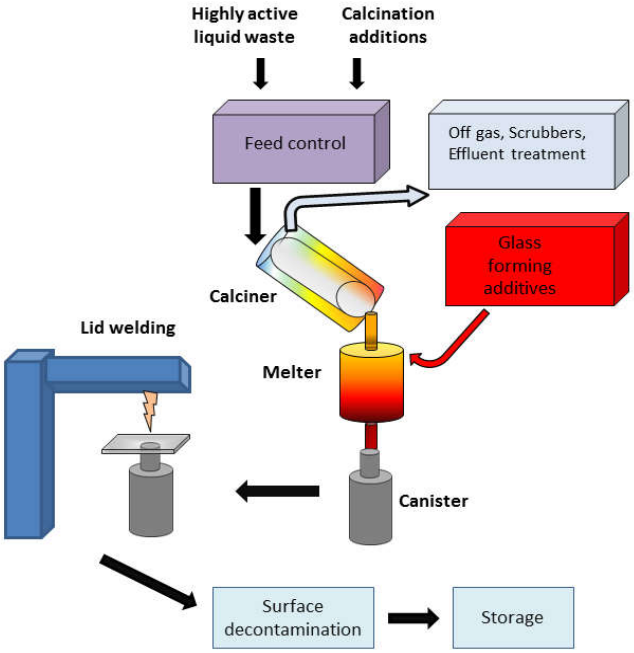

Figure 2.2 Schematic outline of the waste vitrification process (From Marples 1988)

2.2 HLW Vitrification issues

2.2.1 Glass melter issues (Inconel 601)

Glass melting is sometimes associated with unwanted processes such as precipitation of crystals. Incorporation of POCO waste into CZ glass results in significant formation of crystalline, so-called, yellow phase which is corrosive to the melter linings and thus has a detrimental effect on the longevity of melters. NNL showed that Inconel 601 is not durable enough to tackle Mo-rich waste; Inconel 601 coupons immersed in a CZ glass with 32 wt.% waste loading (12 wt.% Mo for 100 h at 1050 °C) were severely corroded - up to 60% of coupon thickness loss. On the other hand, when the same tests were conducted on Nicrofer 6025 HT samples they did not suffer macroscopic material losses, although there many similarities in the compositions of these metals (Table 2.2). These tests have led NNL to avoid Inconel 601 as a melter material for the future Mo containing wastes (Harrison et al. 2014a & Harrison et al. 2014b)

Additionally, other crystals which could be observed at high temperatures (> 1050° C) include spinel, platinoid phases (Izak et al. 2001; Hrma 2002), metallic phases and Zr-rich crystals (Hrma 2002). Although these phases are not as corrosive as the abovementioned yellow phase, platinoid phases (Galoisy et al. 1998; Marples 1988; Morgan 2005) and spinel (Marples 1988; Matyáš et al. 2012) tend to agglomerate and sediment at the bottom of the melter (Section 2.2.3.4). The bigger the agglomerates the faster they settle at the bottom (Sundaram & Perez Jr. 2000). Forming a 'sludge' layer at the bottom of the melter, causing problems with pouring (sometimes forming blockages) (Matyáš et al. 2012; Morgan 2005; Izak et al. 2001). To tackle the problem air sparging partially reduces the formation of sludge layer and improves glass uniformity (Short, 2004; Bickford et al. 1990). Additionally, Matyáš et al. (2012) and reported that introduction of RuO_2 to HLW borosilicate glass increases crystal density number, which resulted in decreasing the size of spinels and prevented their agglomeration at the bottom of the melter.

Modification of waste glass composition can decrease the corrosion of Inconel 601 crucibles. Hugon et al. (2009) reported that Fe_2O_3 (an oxidiser) incorporation into a glass reduces excessive corrosion of the melting pot by promoting the growth of a protective

Cr_2O_3 rich scale on the metallic substrate. It was observed that 4.7 wt.% of Fe_2O_3 is required to form a coherent Cr_2O_3 scale. However if the Fe_2O_3 content is lower than 3.8 wt.% the glass melt is reduced and the metal corrosion is stronger – breaking through the Cr_2O_3 scale (Hugon et al. 2009).

Alloy	Compositions (wt.%)									Others
	Cr	Ni	Fe	Al	Co	Si	C	Mn	W	
Inconel 601	23	60	14.5	1.3	<0.5	0.01	<0.1	<1.0	<1.0	Cu <1.0
Nicrofer 6025HT	25	Bal	10	2.1	-	<0.5	0.2	<0.1	-	Ti 0.1-0.2, Y 0.5-1.2, Zr 0.01-0.1

Table 2.2 Compositions of Inconel 601 and Nicrofer 6025 HT (Quayle 2003)

2.2.2 Glass melt/ Glass homogeneity/volatility

The initial signs of the limits of HLW incorporation in the borosilicate glass melt are explained as follows by (Larkin, 1986):

1. A lumpy glass pours showing too short reaction time/rate
2. Many bubbles in the glass samples
3. Remains build-up in the melter demonstrating the limit of digestion was achieved
4. Occurrence of phase separation (primarily 'yellow phase')
5. Incompletely reacted calcine with base glass in the products
6. Large–scale crystallisation of the products

Partly dissolved calcine in the glass samples was described as crystalline, Zr and lanthanide–rich and often accompanied with bubbles (Morgan 2005). The observed crystal phases within the dissolving calcine are lanthanide silicates and Ce-Zr oxides. Formation of these phases is caused by the local supersaturation of their components in the glass melt (inhomogeneity), followed by their precipitation on cooling (Bouchet et al. 2000). The laboratory scale glass samples of Morgan (2005) were melted at about 1050 °C for <1h. It has been reported that the remaining calcine in the borosilicate glasses reduces their chemical durability (Raman 2003). Furthermore, inhomogeneity of the HLW glass melts causes compositional layers of the glass samples (Abraitis 1999; Morgan 2005). Layers enriched in base glass components were interspersed with layers enriched in simulated HLW components that also demonstrated substantial crystallisation. The layers enriched in simulated HLW components showed lower

chemical durability than the layers rich in base glass components (Abraitis 1999, Rose 2007).

Volatility

Volatility is one of the factors that reduces HLW incorporation in the glass. Volatility decreases the efficiency of the vitrification process and increases the volume of radioactive waste after the decommissioning of scrubbers. Volatility exists in many forms (**Table 2.3**), where particulates can be trapped in the filtration system from the glass melt surface, whereas semi-volatiles could leave the melter in an aerosol form (Langowski et al. 1996; Rose 2007). Furthermore, volatility may also be very corrosive for the Inconel 601 crucible if the waste is enriched in Mo. However, the unsubmerged part of the coupon was corroded as well probably due to exposure to volatilised molybdate-containing compounds (Harrison et al. 2014).

Gasses	Semi-volatile	Particulate
H_2, H_2O, O2, Co, CO_2, NO, NO_2, SO_2, halogens (Cl_2)	Some compounds of Li, Na, K, Cs, Cd, Hg, Ru, Mo, Sb, Se, B, Te, Tc and halogens	Al, Fe, Sr, RE plus other feed components

Table 2.3 Volatile species noticed in off gas during HLW vitrification (Scott el al. 1985; Langowski et al.1996)

2.2.3 Crystallisation of borosilicate HLW glass

2.2.3.1 Crystallisation (Devitrification)

The two main processes in glass crystallisation are crystal nucleation and crystal growth. Nucleation falls into two categories homogeneous or heterogeneous. Homogeneous nucleation takes place when crystal nuclei form spontaneously in a homogeneous glass matrix. Heterogeneous nucleation is caused by foreign particles (e.g. platinoids) in the glassy matrix (Doremus 1994). Interestingly, platinoid concentrations as low as 0.001 to 0.1 % cause uniform nucleation. Finally, even small amounts of dust particles on the surface can provide preferred nucleation site (Shelby 2005; Doremus 1994).

2.2.3.2 Amorphous phase Separation (APS)

APS can come about in glass in two specific ways: the first is crystal nucleation and growth and the second is spinodal decomposition (Shelby 2005; Doremus 1994). Nucleation and growth resemble glass crystallisation in which nuclei of dissimilar composition from the base glass are created and then grow. In this type of APS the second phase forms spherical particles within the parent glass, with a limited connectivity to a second phase. Moreover, these two phases are sharply separated from each other. On the contrary, spinodal decomposition consists of progressive change in the composition of the two phases until they reach the immiscibility boundary (diffusion-controlled process) (McMillan 1979, Doremus 1994). The morphology of two separated phases is non-spherical and both phases have huge interconnectivity. At the end of spinodal decomposition, two phases present sharp phase boundaries between each other. In addition, phase boundaries created by APS can act as a nucleating site for following crystallisation. Finally, newly formed phases through APS mechanism could demonstrate greater tendencies to crystallise than the host glass (Shelby 2005; Doremus 1994).

2.2.3.3 Crystalline Phase Separation (CPS)

The CPS phenomenon takes place when two separating phases are amorphous at the melt temperature; these separate phases may start crystallizing on cooling. This process involves glasses that are immiscible at the glass melt temperature with the second liquid phase forming droplets. Typically, the matrix remains amorphous, but the droplets crystallise (Jantzen et al. 2000). According to Dietzel (Vogel 1994, Shelby 2005), CPS is directly related to the field strength difference (ΔF) of major glass formers and competition for the dominant structural role causes the cation with the highest field strength (e.g. P^{5+}) to govern the de-mixing process. If the ΔF between the main glass forming elements goes above 0.3, then the phase separation will have crystalline nature (CPS) e.g. the ΔF between B and Si is only 0.06 (APS), but between Si and P it is over 0.3 (0.53) which results in crystalline phase separation in phosphate systems. The borosilicate systems investigated by Jantzen et al. 2000 concluded that type of phase separation depended on the addition level of P_2O_5. Therefore, glasses with low P_2O_5 content (<2.6 wt%) underwent APS, but many glasses with higher content of P_2O_5 experienced CPS and were more chemically durable.

2.2.3.4 Platinoid phases

Immiscibility of Pt family metals is a well-known phenomenon in nuclear glasses, regardless of redox conditions; they form metallic (e.g. Pd or PdTe) or oxide phases (e.g. RuO_2) (Galoisy et al. 1998; Sundaram & Perez Jr. 2000; Morgan 2005). Most simulated HLW nuclear waste does not include noble metals such as Rh, Ru and Pd due to reasons such as high price and corrosion of Pt melting crucibles. In borosilicate glasses, such elements act as heterogeneous nucleating agents and might cause sedimentation of newly formed crystals at the melter bottom (Lutze & Ewing 1988). Izak et al. (2001) stated that minor additions of RuO_2 to borosilicate glass increased crystal density number (n_s – number of crystallites per volume unit) by two orders of magnitude and strongly reduced the spinel crystal size. Furthermore, Matyáš et al. (2012) noticed that noble metals plus Fe and Al significantly slowed down/stopped the accumulation of spinel crystals by reducing the size of average crystal by increasing the n_s. This in turn reduced the possibility of plugging the bottom of the discharge valve (riser), which is pushed upward to pour a glass melt. Additionally, incorporation of platinoids into borosilicate HLW glasses have variously been reported to have slightly positive (Pacaud et al. 1991) or practically unaffected (Bart et al. 2001) effect on their durability. Amongst all platinoids, RuO_2 is the most abundant one in the nuclear waste forms and it is mainly present as RuO_2 particles (Chouard et al. 2015). However, it is possible to reduce it to metallic Ru (globular morphology) under reducing melting conditions (Bickford & Jantzen 1986). The morphology of RuO_2 is mainly needle-like very often in clusters or swarms (Larkin 1986; Bart et al. 2001). Additionally, different morphologies such as granular (Larkin 1986) or cubic shapes (Bart et al. 2001) have also been witnessed. The addition of RuO_2 to R7T7 waste glass (the French sodium borosilicate waste glass) affects crystallisation in different ways. Chouard et al. (2014) reported that addition of RuO_2 did not change strongly the microstructure, the size and the density distribution of powellite and Na_2MoO_4 crystals, unlike its effect on spinels. In this study, molybdate crystals always grew from the Mo-rich globules. However, RuO_2 appears to have much larger impact on the crystallisation of apatite phase ($Ca_2Nd_8(SiO_4)_6O_2$); a higher nucleation rate of apatite phase with more uniform, smaller crystals distribution (higher n_s) was observed after an incorporation of RuO_2 (~1 mol.%) (Chouard et al. 2014).

2.2.3.5 Yellow phase/Molybdates

Yellow phase

Low Mo solubility in borosilicate glass (about 1 wt.%) and high fission yield make molybdenum a difficult element for vitrification route. Therefore, the vitrification of the Highly Active Storage Tank's (HAST) heel seems to be very limited by the devitrification processes. The crystalline phases enriched in Mo tend to separate from the melt and are given the generic name "yellow phase". That phase consists of mixed alkali molybdates, (chromates and/or sulphates if present), and is partially water soluble and corrosive to the Inconel melters used on Waste Vitrification Plant (WVP) (Short et al. 2004; Short et al. 2008; Dunnett et al. 2012). Chemical compositions of yellow phase could vary from one to another and it depends on a type of waste and frit. The complex nature of yellow phase is well reflected in its compositional ranges presented in tables below (**Table 2.4 and Table 2.5**). In addition, tests at NNL showed that about 80 % of the compounds that are present in yellow phase are water soluble, which make them unacceptable for a long term geological storage facility (Dunnet et al. 2012; Harrison et al. 2014). Maximising the incorporation of MoO_3 in vitrified products will determine the number of POCO waste canisters produced which is why higher waste loadings of MoO_3 are necessary.

Oxide composition	References
Mo, Cs, Li, Te, Sr, Cr, and La	Morgan 2005
Li, Na, Cs, Cr, S, and Sr	Pegg & Joseph 2001
Mo, Na, B, Zr, Ca, Zn, P, Al and Si	Henry 2004, Pinet 2006
Na, S, Ca, Cr, Fe, Al, Ba and U	Kaushik 2006

Table 2.4 Elements identified in yellow phases

Component	Wt.%
B_2O_3	2-3
CaO	0.5-3
Cs_2O	12-16
K_2O	0.6
MoO_3	63-65
Na_2O	9-14
SrO	0.3-0.8

Table 2.5 Compositional ranges of yellow phases (De et al. 1976)

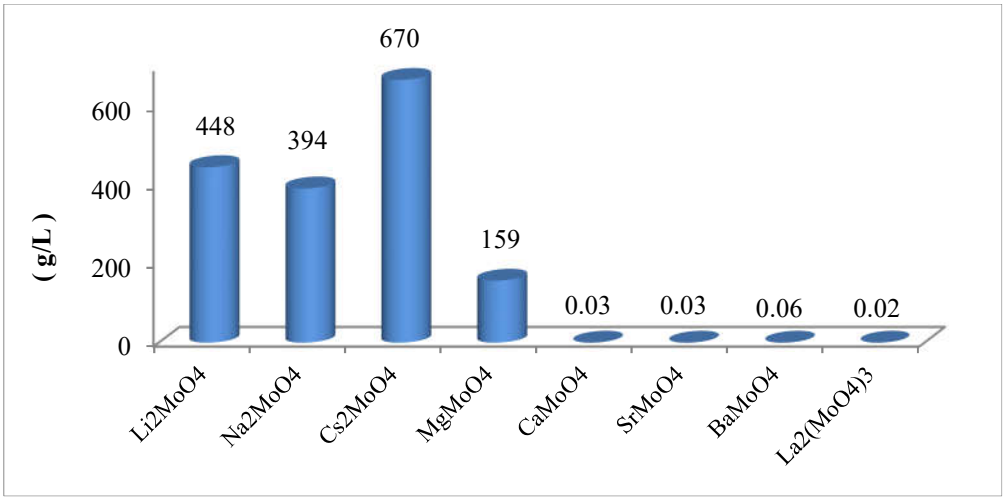

Figure 2.3 Solubility of molybdates in water at 18-25 °C (Perry D.L. 2011; Haynes 2011)

Since yellow phase in this project, mainly consists of molybdates it is necessary to know their solubility in an aqueous environment. **Figure 2.3** shows solubility of alkaline and alkaline earth molybdates. This graph clearly demonstrates that formation of alkaline molybdates and $MgMoO_4$ should be avoided in order to have a durable waste form. Formation of Na_2MoO_4 is especially unwanted because it easily incorporates Cs and is particularly water soluble (Donald 2010). However, alkaline earth molybdates are considered as acceptable phases. Powellite ($CaMoO_4$) is a tetragonal crystal that is isostructural with scheelite ($CaWO_4$). Powellite demonstrates high chemical flexibility can be described as $AMoO_4$, where A site could be substituted by +1,+2 and +3 cations and vacancies as long as charge neutrality is preserved (Short 2004). Studies have shown that powellite is highly resistant to external irradiation. Under a TEM beam, powellite amorphization begins between 10^{12} and 10^{13} Gy which is a dose much greater than the one absorbed in underground storage (< 10^9 Gy) (Crum et al. 2011; Taurines et al. 2013). The very common substitution is 2 Ca^{2+} <-> (RE^{3+}, R^+), where RE^{3+} is a trivalent rear earth and R^+ is a monovalent cation. Moreover, in powellite rich glass-ceramics, the crystal phase could act as a good host for actinide ions (Np^{3+}, Am^{3+} and Cm^{3+}) (Taurines and Boizot 2013).

During chemical durability test of borosilicate HLW glasses, the powellites (Nd, Pr, La, Ca, Na)MoO_4 (Abdelouas et al. 1997) and ($Ca_{0.88}Sr_{0.10}Ba_{0.02}$)$MoO_4$ (Gong et al. 1998) formed in/on the altered surface layers of glasses. Additionally, Bart et al. (2001) reported that powellite formation in HLW borosilicate glasses slightly improves chemical durability.

$CsLiMoO_4$

Magnox calcine waste demonstrated that early stages of vitrification produces $CsLiMoO_4$ (cubic crystal system) (Morgan 2005a; Short 2004), which has a low melting point (770-800 °C) plus it is water soluble (Morgan 2005). This layer separated out forming a fluid on the surface of the glass melt that in later stages of melting disappears due to convection currents, however, could be troublesome if mixing is unfinished (Donald 2010; Morgan 2005a)

Incorporation of higher amounts (~ 10 wt.%) of MoO_3 is possible by making Glass Composite Materials (GCM). GCM are not strictly glasses nor ceramics, although they are mainly amorphous (Dunnett et al. 2012; Rose et al. 2011).They also cannot be called glass-ceramics because crystallisation does not happen in a controllable manner to produce the desired crystal phases and microstructure, but the crystallisation is rather caused by a retarded cooling (Rose et al. 2011). This approach has been utilised in France to deal with their legacy solutions originating from Mo-Sn-Al fuels allowed immobilising of circa 12 wt.% of MoO_3 into Zr and Ca – enriched aluminoborosilicate matrix. The Mo was trapped as a $CaMoO_4$ in the amorphous medium. The glass consists of micro-beads incorporating Zn, Ca, P and Mo. This glass formulation requires cold crucible technology and melting temperature ~ 1250 - 1300 ºC. The technology on WVP uses a maximum melting temperature ~1060 ºC.

NNL have modified MW borosilicate glass to tackle the problem related to "yellow phase" by adding Ca, Zn and Al. In that way, calcium zinc base glass was produced (CZ glass). The addition of the first two oxides resulted in reduced viscosity and increased melt homogeneity, which helps with pouring the glass at a lower temperature. Short at al. (2008) suggested that Ca addition could increase Mo solubility and reduce the formation of yellow phase. It was also reported by Dunnett et al. (2012) that modified borosilicate glass containing up to 8.7 wt.% of MoO_3 could be successfully manufactured at 1050 ºC as a single phase. Incorporation of 10 wt.% of MoO_3 gave rise to $CaMoO_4$ and $BaMoO_4$ phases which were distributed throughout the sample producing a durable glass composite material.

Yellow phase was also problematic at the Rokkasho Reprocessing Plant in Japan. The formation of yellow phase interrupted the steady glass discharge from Joule heated ceramic melter's drain valve. The major crystalline phases identified in this case were

Na_2MoO_4, $CaMoO_4$ with minor quantities of Cs and Ba molybdates (Pegg et al. 2010). It was discovered that the phase was predominantly formed at the bottom of the melter after discharging the glass, even though the MoO_3 was present below its solubility limit. It was suggested that probably the viscous glass melt might have reduced mixing allowing alkali, alkaline earth and molybdenum oxide to combine form molybdenum salts, before the molybdates were fully incorporated into the glass. However, the modification of the feed blends based on redistribution of 6.9 wt.% of Al_2O_3 and B_2O_3 from the frit to waste simulant, led to about 50% lower melt viscosity. Additionally, it was observed that the following ions AlO_4^-, BO_4^-, SiO_4^{2-} and MoO_4^{2-} compete with each other for alkaline earth and alkalis from the waste, which probably explains why yellow phase was not observed from 700 to 1000 ^oC (Caurant et al. 2007; Pegg et al. 2010). The batch modification resulted in no Na_2MoO_4 being observed. Redistribution of Al_2O_3 and B_2O_3 to the waste simulant appears to increase their concentration in the melt. According to Caurant et al. (2007), higher concentration of B_2O_3 changes the way molybdate crystals are formed during slow cooling, which is related to local concentration of Na^+ preferentially situated closer BO_4^- units for charge compensation. What is more, Chouard et al. (2014) argues that unlike powellite, Na_2MoO_4 crystals are only produced on melt cooling, but never through glass heating in R7T7 glass. This suggests that amount of Na^+ ions available to form Na_2MoO_4 depends on the thermal treatment. This process involves the evolution of BO_4/BO_3 ratio on cooling, which increases the number of BO_4 units, therefore, less Na^+ ions are available at lower temperature (< 750 ^oC) to form Na_2MoO_4, (Na^+ preferentially charge compensates BO_4^-).

2.2.3.5 Spinels

The general spinel formula can be written as $A^{2+}B_2^{3+}O_4$, where the A is related to tetrahedral and B to octahedral sites in the crystal lattice. Looking at the $MgAl_2O_4$ spinel (cubic crystal system), the unit cell contents eight formula units, giving $Mg_8Al_{16}O_{32}$. In the formula, there are 24 cations sites per 32 oxygen atoms existing in the unit cell. The spinel formula shows that 8 tetrahedral and 16 octahedral sites could be filled in many ways, which depends on the type of spinel. Table 2.6 displays some of the examples of spinels, which were identified in borosilicate glasses. Generally, there are two types of spinel. The first type of spinel, called “normal” spinel, has the 8 tetrahedral sites (A) filled by divalent cations and the trivalent cations fill octahedral sites - $A^{[tet]}[B]_2^{[oct]}O_4$. In an

"inverse" spinel half the trivalent cations occupy the tetrahedral sites and the octahedral sites are occupied by half trivalent and half divalent cations - $B^{[tet]}[A,B]^{[oct]}O_4$ (Navrotsky & Kleppa 1968; Alton et al. 2002). Many types of spinel identified in borosilicate glasses possess better chemical durability than the parent glass (Hrma et al. 2005, Lutze & Ewing 1988). Additionally, spinels are present in the nitrate melt (Izak et al. 2001) and nucleate straight away after cooling of borosilicate HLW from the glass melt (Hrma 2002, Rose 2007). The presence of platinoid phases (**Section 2.2.3.4**) in borosilicate glass has a strong effect on spinel nucleation and increases crystal density number (Bickford & Jantzen 1986; Izak et al. 2001; Kim et al.1995; Matyáš et al. 2012). Spinel crystals might provide nucleation sites for other phases such as clinopyroxenes (monoclinic pyroxenes – silicates) (Kim et al. 1995; Bickford & Jantzen 1986; Rose 2007), also Ru and Rh were observed dissolving within the structure (Copobianco and Drake, 1990). Reported spinel morphologies in borosilicate nuclear glasses include cubic (Alton et al 2002; Matyáš et al. 2012), needle-like (Matyáš et al. 2012) and star-shaped (Alton et al. 2002; Hrma et al. 2000; Rose 2007). Finally, in real radioactive borosilicate glasses spinels have been demonstrated to be radiation tolerant crystals (Hrma et al. 2005, Sickafus et al. 2000).

Spinel	Formula	Reference
Nichromite	**$NiCr_2O_4$**	(Hrma et al. 2000)
Magnetite	**Fe_3O_4**	(Hrma et al. 2000; Kim et al. 1995)
Chromite	**$FeCr_2O_4$**	(Kim et al. 1995; Galoisy et al. 1998; Hrma et al. 2000)
Trevorite	**$NiFe_2O_4$**	(Kim et al. 1995; Hrma et al. 2000)
Cr-Fe-Mn-Ni-Zn spinel Fe-Ni-Cr-Zn spinel Fe-Cr-Mn-Ni spinel		(Bart et al. 2001) (Pacaud et al. 1991) (Sundaram & Perez 2000)
$(Ni_{0.95}Mn_{0.05})(Fe_{0.92}Cr_{0.08})_2O_4$ $(Ni_{0.85}Mn_{0.15})(Fe_{0.8}Cr_{0.2})_2O_4$ $(Fe,Ni,Mn)(Fe,Cr,Mn)_2O_4$ $(Mn_{0.3}Fe_{0.3}Zn_{0.4})Cr_2O_4$ $(Fe,Ni)(Fe,Cr)_2O_4$		(Bickford&Jantzen1986) (Bickford & Jantzen 1986) (Li et al. 2003) (Hrma et al. 2006) (Kim et al.1995; Izak et al. 2001)
	$(Mg,Zn)Cr_2O_4$ **$(Ni,Mn)Cr_2O_4$**	(Lutze & Ewing 1988) (Sundaram & Perez 2000)

Table 2.6 Some spinels observed in borosilicate glasses

2.3 POCO wastes and problematic elements

2.3.1 POCO wastes

Reprocessing of nuclear fuel at the Sellafield site led to storage of HLW streams in HASTs; HLW liquids that are a result of the dissolution of the SNF in HNO_3 and solvent extraction of U and Pu is stored in the tanks. The first eight HASTs were commissioned in 1955 and brought into active service sequentially until 1970. These so-called 'Old site' HAST tanks numbered 1-8 have no agitation (Turvey and Hone 2000, NNL 2014). This project focuses on the POCO waste from the so-called 'New site' HASTs. The 'New site' HASTs are vertical cylinders measuring 6x6 m with working volume of 145 m^3. In this case, the heat generation does not exceed 460 kW and the heat is constantly removed by the cooling system to prevent the liquid from boiling off. Finally, all the new HASTs are fitted with agitation systems to avoid plating on the surface and/or sedimentation (Turvey and Hone 2000). The real waste stream will be generated in the near future, when the HASTs will be subjected to Post Operational Clean Out (POCO) prior to decommissioning. This process will require removal of the HAST's heel (precipitated solids) that is considered to be rich in zirconium molybdate ($ZrMo_2O_7(OH)_2$. $2H_2O$, ZM), caesium phosphomolybdate ($Cs_3PMo_{12}O_{40}.14H_2O$, CPM) and zirconium phosphate (with variable composition, e.g. $Zr(HPO_4)(OH)_2.H_2O$) and variety of metal nitrates (Edmondson et al. 2012; Dunnett et al. 2012). Finally, initial estimates suggest that the volume of vitrified POCO waste could be approximately 200 m^3 (NDA 2011). Details of the POCO composition used in this work are given on page 51.

2.3.2 Waste simulant compositions - P series

P series waste simulants were formed by blending different types of waste available on the Sellafield site. In order to maintain high waste loading (to minimise waste canisters) it was necessary to mix different waste at certain ratios to achieve more balanced compositions, where certain compounds are strongly reduced (e.g. typical 'Blend' waste is a mixture of Magnox : Oxide, oxide ratio 75:25, e.g. Al_2O_3 was reduced from ~ 17 wt% (Magnox) to ~ 7 wt% (Blend)) (Short 2014). The same principle has been applied to produce P series simulants (**Table** 2.7), where Magnox (**Table** 2.8), Oxide and POCO waste streams were mixed in specific ratios to examine the most practical composition. The waste compositions also are affected by for example chemical reprocessing additives, soluble poisons (mainly Gd and B to prevent criticality), corrosion from fuel cladding and inside storage tanks. Thus, stored wastes undergo some changes over a time (Larkin, 1986). Due to a commercial sensitivity the Oxide waste composition cannot be presented without security clearance (NNL, 2014).

Definitions:

- P0 simulant, in all cases is made of 50 wt% : 50 wt% (Magnox : Oxide)
- POCO simulant containing zirconium molybdate hydrate crystals (ZMH), caesium phosphomolybdate hydrate crystals, barium and strontium nitrate

P48 simulant – calcine produced during setpoint finding for a 52 wt% P0 :48 wt% POCO simulant containing LiNO3 suitable for a 38 wt.% incorporation rate if the calcine was used for vitrification
P19 simulants – calcine produced during setpoint finding for 81 P0:19 POCO simulant again dosed with LiNO3 for a 38 wt.% incorporation rate as if the calcine was used for vitrification
P0 simulants – calcine produced from 50 Oxide:50 Magnox – this simulant used for diluting feed trials, $LiNO_3$ targeting a 28 wt.% incorporation rate

Table 2.7 Description of P-type simulants

Magnox waste			
Oxides	**Wt %**	**Oxides**	**Wt %**
MoO_3	14.4	Sm_2O_3	2.6
ZrO_2	13.9	Rh_2O_3	2.2
Nd_2O_3	13.1	Y_2O_3	1.7
Cs_2O	9.4	TeO_2	1.6
CeO_2	8.5	Rb_2O	1.1
RuO_2	7.8	Pm_2O_3	0.5
BaO	4.6	Eu_2O_3	0.3
La_2O_3	4.2	Sb_2O_5	0.2
Pr_6O_{11}	4.0	Ag_2O	0.1
Tc_2O_7	3.8	Gd_2O_3	0.1
PdO	3.3	In_2O_3	0.1
SrO	2.9	**Total**	**100.4**

Table 2.8 Chemical composition of the fission product of calcined Magnox waste (Marples, 1988). Total provided for information only.

2.3.3 Molybdenum oxide

MoO_3 solubility in glass

Molybdenum is a transition metal which has a low solubility in sodium borosilicate glass (~ 1 wt.%) making glass susceptible to phase separation and crystallisation. Glass preparation under neutral and oxidising conditions leads to Mo^{6+} which is the most stable form of Mo (Caurant et al. 2007; Donald 2010). In nuclear waste it originates from nuclear fission reactions (Magnin et al. 2011). Each hexavalent Mo is connected to four oxygens to create a molybdate unit $[MoO_4]^{2-}$ that is related to network modifiers and located within alkaline earth and alkaline rich domains (Hyatt et al. 2004; Short et al. 2005). Solubility of Mo in the glass is practically the solubility of molybdate units (MoO_4^{2-}) that is closely associated with modifying cations. Caurant et al. (2007) achieved the highest solubility of MoO_3 (2.5 mol.%) in a borosilicate glass by quenching the glass as a thin disc. Other workers have also tied to increase solubility of Mo in the glass (Chouard et al. 2011; Schuller et al. 2008; Magnin et al. 2011; Quang et al. 2003; Chouard et al. 2015; Caurant et al. 2007).

Simple compositions can use the fraction of NBOs in a glass as a tool to investigate glass. Farges et al. (2006) have examined the molybdate solubility dependence on the ratio of NBOs to silicon tetrahedra (NBO/T) in silicate glass, claiming that improved molybdate solubility is related to higher NBO/T ratios. Additionally, Mo remains highly soluble in the glass until NBOs attached to modifiers are present to stabilise molybdate anions. In glasses with a large excess of NBO atoms (in supercooled melts), to which Mo preferentially bonds, Mo^{6+} can follow its thermodynamic affinity for tetrahedral geometries. However, in highly polymerised glasses, a large excess of NBOs are not available which results in structural changes (formation of MoO_6^{6-} polyhedra too) and making the bonding for Mo more challenging. Therefore, Mo^{6+} decreases its bond valence with oxygens to be more 'connectable' with other types of oxygen atoms (BO atoms in the framework of tetrahedra). Formation of MoO_6^{6-} units decreases the bond valence from 1.5 to 1 (valence units) and allow those units to connect to network formers by consuming residual NBO atoms or by destabilising some bridging oxygens. The bond valence

explains why metallic Mo is insoluble in highly polymerised glasses. Therefore, the attempt to dissolve metallic traces of Mo in a pure silica melt at 2500 °C was unsuccessful (Farges et al. 2006).

The position of MoO_4^{2-} ions in the glass network indicates that the solubility is closely linked to the neighbouring cations. Molybdates demonstrate a strong tendency to separate from the glass melt and very often this governs the solubility limit of MoO_3 in the glass. According to Caurant et al. (2007), the addition of B_2O_3 to nuclear borosilicate glass polymerises the network, which in turn should reduce the incorporation capability of Mo. Addition of B_2O_3 changes the nature of crystallisation - formation of Na_2MoO_4 is reduced at the expense of $CaMoO_4$ which crystallises more readily. This can be explained through preferential charge compensation mechanism, where Na^+ ions are linked to BO_4^- and thus become less available rather than Ca^{2+} (see **Section 2.2.3.5**). In addition, precipitation of $CaMoO_4$ or powellite-like phases in the nuclear waste glasses could also be beneficial and is of interest for some authors due to good chemical durability (Taurines et al. 2013; Taurines & Boizot 2011; Schuller et al. 2008; Magnin et al. 2011; Dunnett et al. 2012; Short et al. 2008). Higher calcium level in nuclear glasses has been used in the UK and French glassy wasteforms to minimise the crystallisation of soluble alkaline molybdates (Short et al. 2008; Chouard et al. 2011). Finally, the charge compensation mechanism between MoO_4^{2-} anions and Ca^{2+} is more favoured than with Na^+ cations and this results in $CaMoO_4$ formation rather than soluble Na_2MoO_4 (Caurant et al. 2007).

Rare Earths and Mo solubility

Rare earth (RE) elements are often represented by Nd_2O_3 in nuclear glasses and together with Mo are abundant fission products, with limited solubility in borosilicate glasses. Chouard at al. (2011) showed that incorporation of Nd^{3+} increased the solubility of MoO_3 in the borosilicate glass, demonstrated by reduced crystallisation and phase separation of molybdate phases. The highest solubility of MoO_3 was observed at around 8 wt.% of Nd_2O_3. However, neodymium contents above 12 wt.% led to apatite formation ($Ca_2Nd_8(SiO_4)_6O_2$) on slow cooling and formation of $CaMoO_4$ and Na_2MoO_4 in the Nd glass depleted areas. The mechanisms causing this are not very clear, but relate to two hypotheses:

Hypothesis 1 – suggests that Nd^{3+} cations could have a preferential connection with $[MoO_4]^{2-}$ units in borosilicate glass. Therefore, Nd^{3+} should be directly placed straight in the vicinity of the molybdate tetrahedra in the first coordination sphere. According to that rule, Nd^{3+} would completely or partially replace charge compensating ions Ca and Na existing next to molybdate units. This hypothesis seems to elucidate the lack of crystallisation of alkali and alkaline earth molybdates with growing neodymium content. However, in Mo-free glasses, Nd^{3+} always satisfy their environment in depolymerised regions, and this indicates that $[MoO_4]^{2-}$ entities should have no significant effect on Nd surroundings. Moreover, the presumed special interaction between $[MoO_4]^{2-}$ entities and Nd ions, would suggest neodymium molybdate phases should be seen, which are absent after slow cooling (Chouard et al. 2011).

Hypothesis 2 – indicates that neodymium might possess a dispersing effect on $[MoO_4]^{2-}$ units. Nd_2O_3 in borosilicate glasses acts a network modifier by producing NBOs and by changing the distribution of alkali and alkaline-earth ions in the network of glass. In addition, Nd^{3+} and $[MoO_4]^{2-}$ are located in the depolymerised regions of the aluminoborosilicate glass. This theory explains the disappearance of crystallisation of molybdate phases at around 8 wt. % of neodymium oxide because increasing the amount of Nd_2O_3 prevents the formation of molybdate rich clusters. This results in the disappearance of crystallisation and separation of molybdate phases. What is more, this hypothesis could be reinforced by the "principle of confusion" utilised by Lucas for fluoride glasses (Lucas 1989; Chouard et al. 2011). This principle says that competition between cations in depolymerised areas to become connected to molybdates is so high (large number of possible crystalline phases), that none of them is successful and the glass remains homogenous. Nevertheless, the idea that Nd^{3+} ions are involved partially in charge compensation with molybdate units cannot be absolutely rejected, but requires further study (Chouard et al. 2011).

Improved solubility of MoO_3 in borosilicate glass owing to Gd_2O_3 incorporation, which originates from addition to the nuclear fuel as a neutron poison has been reported in many papers (Taurines & Boizot 2011; Taurines & Boizot 2012; Taurines et al. 2013). They state that addition of Gd_2O_3 significantly reduces the formation of Na and Ca molybdates and therefore increases Mo solubility. The formation of $CaMoO_4$ (powellite) is desirable because this phase is about three orders of magnitude more durable in an aqueous

environment than Na_2MoO_4, in which Na could be partially substituted e.g. by ^{137}Cs and leach radionuclides to the environment (Taurines & Boizot 2011; Taurines & Boizot 2012; Taurines et al. 2013). The crystallisation of powellite was affected by many parameters, e.g. cooling rate and parent glass composition. It appears that a slow cooling rate favours Na_2MoO_4 formation, but only higher cooling rates favoured $CaMoO_4$ crystallisation such as casting on the steel plate. It was shown that Gd_2O_3 possesses a strong effect on crystallisation and morphology of powellite. It was proposed that Gd^{3+} located in depolymerised regions already abundant in MoO_4^{2-} species leads to higher Mo solubility. It appears that Mo stabilisation in the glass structure by Gd^{3+} and crystallisation of $CaMoO_4$ are two competing processes (Taurines & Boizot 2012).

Molybdenum incorporation in glass

The strong crystallising tendencies of MoO_3 in BS glass are related to its high field strength (F) values. The average Mo^{6+}- O distance range is between 1.76-1.78 Å (Calas et al. 2003; Hyatt et al. 2004; Caurant et al. 2007) which results in F between 1.89-1.94 $Å^{-2}$. Additionally, Dietzel (Vogel 1994) argues that when the ΔF between glass forming elements (SiO_2^- 1.57 $Å^{-2}$ and BO_3^- 1.63 $Å^{-2}$) exceeds 0.3, so phase separation occurs readily. Due to a high F value, the Mo^{6+} ion exerts a strong ordering effect on the neighbouring O^{2-} ions, thus MoO_4^{2-} units are easily separated from a silicate network (Caurant et al. 2007; Szumera 2015; Tan et al. 2015). Hyatt el al. (2004) and Calas et al. (2003) agree that MoO_4^{2-} ions are preferentially associated with network modifying cations and are placed in the alkali and alkaline earth rich areas, giving the nuclei of the molybdate crystals that lead to molybdate crystallisation. Additionally, strong evidence does not exist for specific modifiers to charge compensate MoO_4^{2-} units in the glassy matrix. However, because of the greater bond-valence, bonding to alkaline earths would require about half the quantity of network modifiers to charge compensate molybdate anions as would alkali ions (Farges et al. 2006). This agrees with results obtained by Komarneni & White (1981), where Mo from Cs_2MoO_4 reacted directly with Ca ions from clays and shales to form powellite a water-insoluble mineral.

An incorporation of MoO_3 into BS glass usually leads to increased glass density (Tan 2015; Henry et al. 2004). On the contrary, T_g decreases after Mo addition, but the full explanation why this occurs is not provided by the authors (Caurant et al. 2009a; Caurant

et al. 2007). MoO_4^{2-} incorporation is expected to polymerise the glass network, that increases T_g with rising MoO_3 content. Caurant (2009) suggests that an increased size of depolymerised domains, rich in MoO_4^{2-}, overrides the higher connectivity of glass network and lead to a reduction of T_g, but this hypothesis is not proven yet and further investigation is required.

2.3.4 Zirconium oxide

Zirconium metal as a key constituent of fuel cladding is incorporated into waste during dissolution of spent UO_2 fuel into nitric acid. ZrO_2 is a common constituent in HLW present e.g. in Blended waste at 12.3 mol% and in POCO waste at 26.30 mol.% (Connelly et al. 2011; Stevens & Short 2014). Zirconium is a transition metal which properties resemble Hf, with which it creates solid solutions of oxides that are difficult to separate. Typically, zirconia properties in glasses are comparable to Be, Al and Sn oxides, which are isomorphous, especially regarding chemical durability. Zirconia is an amphoteric oxide, which can be combined with bases and acids. Additionally, its high melting point of 2700 ^oC is attributed to its high strength oxygen bond and difficult reducibility at elevated temperatures. Together with HfO_2 and ZrO_2 represent the highest refractoriness among the transition metal oxides. Comparable to all high field strength elements, ZrO_2 is an intermediate oxide, which together with glass forming compounds (e.g. SiO_2) is involved in the glass network. Therefore, when introduced into silicate glass it is responsible for increasing the density, T_g, viscosity (even 1 wt.%), chemical durability and strength. Typically, up to 20 wt% zirconia can be incorporated into the binary Na_2O-SiO_2 system, but 8 wt.% can be combined with Na_2O-CaO-SiO_2 (Volf 1984; Vogel 1994). In comparison, in borosilicate glass ZrO_2 is considered to cause phase separation and in enamels it produces opalescence. Increased solubility of zirconia in glass can be induced using polarizable elements (Pb) and by elements with low ionic potential (K, Na). In contrast, elements strongly bonded to oxygen anions (e.g. Mg) and with high ionic potential (Zn, Ti, Al) reduce its solubility in glass (Volf 1984).

Improving immobilisation of this refractory oxide in borosilicate glasses requires a better understanding of its structural role in the UK glasses. Technological constraints such as temperature < 1060 ^oC, low solubility in borosilicate glass and refractory character reduce high waste loading up to ~ 10 wt.%. It was presented by (Connelly et al. 2011) that ZrO_2 solubility is linked to four main sets of observations:

- The ratio of boron oxide to silica has only a small effect on the solubility of zirconia
- SrO, BaO and CaO increase the solubility of zirconia, circa 1 part for every 5 parts of alkaline earth

- The quantity of zirconia that can be incorporated into borosilicate glass is roughly proportional to the alkali content in the following order Li<Na<K
- Al_2O_3, MgO and ZnO reduce the amount of ZrO_2 that can be dissolved.

Alkali ions appear to play a significant role in Zr solubility. It was reported that solubility of ZrO_2 is based on fixed stoichiometry with the number of alkali ions, which are present in the glassy system in excess of that required to charge compensate AlO_4^- ions (Connelly et al. 2011; Volf 1984). Zirconia solubility is increased by alkali oxides (by K than Na - low ionic potential) and by alkaline earth plus by polarizable elements (Pb) (Volf 1984). In theory the preferential charge compensation of Al_2O_3, MgO and ZnO by alkali ions over ZrO_2 (oxyanion), might hypothetically be used. However, this phenomenon was observed with Al_2O_3 only. Finally, the exact role of these elements in the glass structure needs further investigation (Connelly et al. 2011).

2.4 Glass immobilisation matrices and chemical durability

In this project, modified borosilicate glasses are investigated for the incorporation of High Heel Waste (HHW) rich in Mo and Zr oxides. The incorporation of new elements to borosilicate glass such as Al, Zn and Ca oxides aims to improve chemical properties and solubility of HHW waste. Additionally, the main glass former in the aforementioned glasses is silica hence, it is necessary to first look into the structure of silicate glasses.

2.4.1 Silicate glasses

The term glass is utilised to define amorphous solids, which are characterised by a short-range order. The periodic long-range order, characteristic for crystals does not exist in the glassy state, therefore, the amorphous structure can be described on the short-range order, up to 3 closest atoms distance. The structural glass model proposed by Zachariasen-Warren in 1932 (Continuous Random Network model, CRN). It says that amorphous solids consist of non-periodic random network, which means that the neighbouring silicate tetrahedra are irregularly orientated unlike in crystals (Vogel 1994).

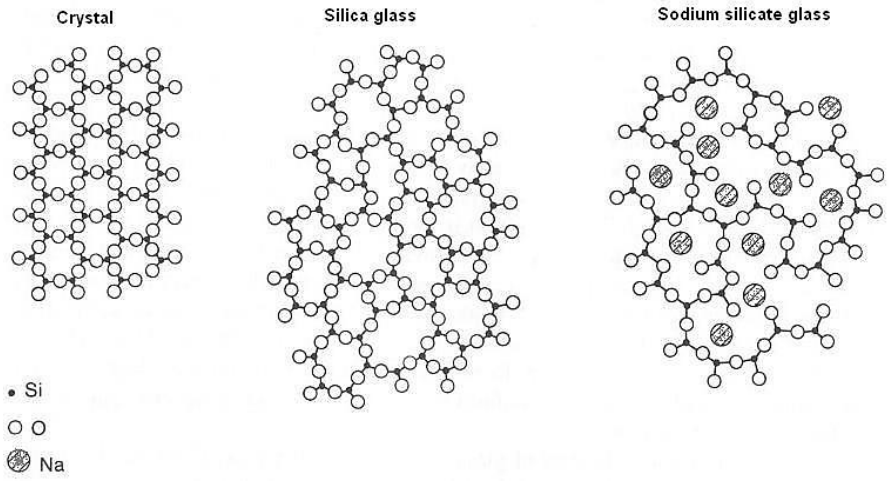

Figure 2.4 The 2D represenattion of the crystalline silica, silica glass and sodium silicate glass – Zachariasen model, from (Donald 2010)

Although there are some classic "glass formers" such as SiO_2, B_2O_3, P_2O_5 and GeO_2 practically any material could be turned into glass by cooling it down quickly enough from the liquid to below transformation temperature (T_g) to avoid crystallisation (Paul 1990; Vogel 1994; Donald 2010). Generally, T_g is described as the temperature at which viscosity achieves the values of 10^{12} Pa•s. When the temperature is above T_g, but lower than melting temperature T_m, the substance is called as supercooled liquid, but then when the temperature is below T_g the substance becomes a glass. However, on cooling another phenomenon might take place if the cooling rate is below the critical cooling rate, the glass melt may crystallise to form crystalline material. In addition, a sufficiently fast cooling rate can even transform metals into a glass e.g. splat quenching ($>10^6$ K s^{-1}) (Vogel 1994) .

Silicate glasses are normally made of network formers (SiO_2), network modifiers (e.g. CaO, MgO and Na_2O) and some intermediate oxides (e.g. Al_2O_3 - could be former or modifier depending on composition). A silicate glass network consists of SiO_4 tetrahedra that are connected via bridging oxygens (BOs, connected Si-O-Si). Meanwhile, network modifiers enter the silicate structure by occupying the interstitial space between the SiO_4 units and are poorly associated with the adjacent oxygen from the silicate network (**Figure 2.5**). Incorporation of network modifiers involves the formation of non-bridging oxygens (NBOs) through the breaking the bonds between SiO_4 tetrahedra. The alkali cations (e.g. Li^+, Na^+) act to balance the charge the NBOs in the network (**Figure. 2.7**)

1 mol of modifier oxide normally produces 2 moles of NBOs (Varshneya 1994). However, the deviation from this principle might happen when large ions e.g. Ba^{2+} are involved (Zhao et al. 2000).

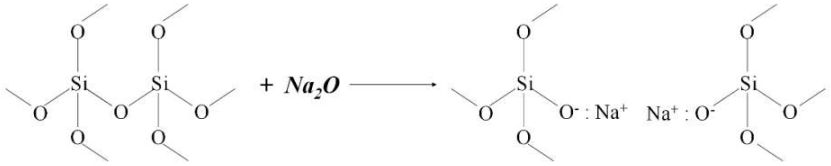

Figure 2.5 Depolymerisation of silicate network by Na_2O adding (network modifier)

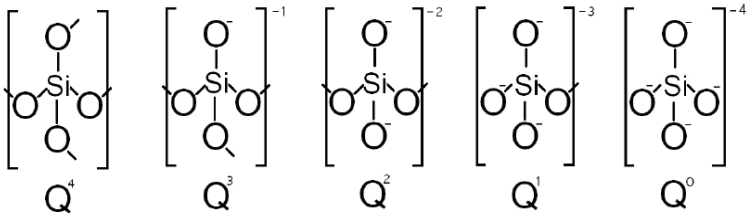

Figure 2.6 Possible structural units in a silicate glass Q_n (n- bridging oxygen) (Ojovan and Lee 2005)

The connectivity of a silicate network can be presented as Q_n, where n refers to the number of bridging oxygen per SiO_4 tetrahedron. As presented in **Figure 2.6**, silicate glass can be partially depolymerised (Q_1 units) or entirely polymerised (Q_4 units). Overall, silicate glass networks with higher n values possess higher connectivity than the glass network with lower n values. The Zachariasen-Warren model was suggested to be modified recently by Greaves et al. (1981). Based on XAFS (X-Ray Absorption Fine Structure) data from Na and Si K-edges they considered a system of bonded alkali clustering into channels linking the silicate network (**Figure 2.7**)

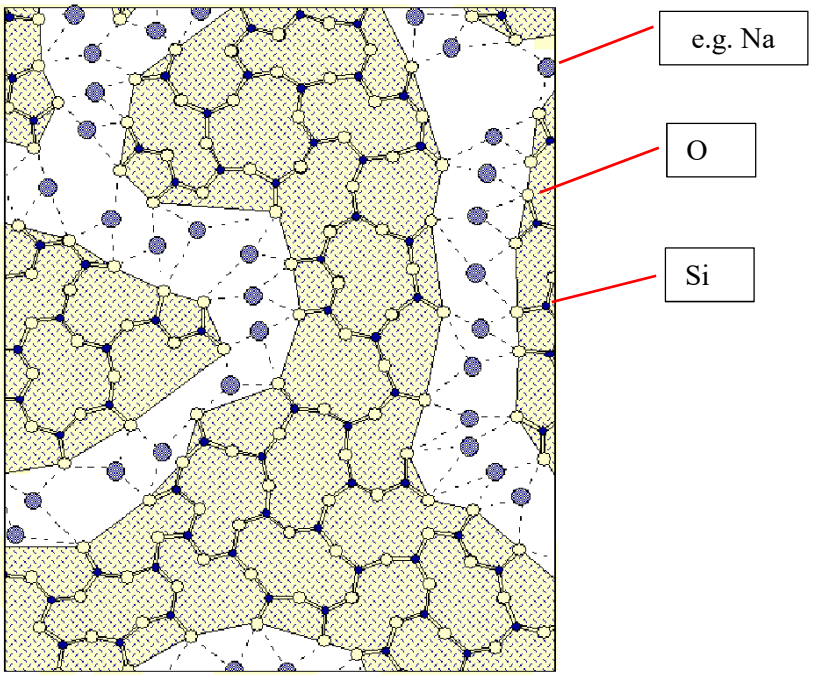

Figure 2.7 Schematic representation of the modified random network (MRN). The structure illustrates percolation channels formed by alkaline cations (e.g. Na^+) loosely bonded to oxygen atoms of the adjacent silicate groups (Hand & Seddon 1997).

2.4.2 Borosilicate glasses

Borosilicate glasses are a group of glasses where major network formers are SiO_2 and B_2O_3.Their structure is more complex than that of pure silicate glass. This is partly related to the difference in boron co-ordination with composition and to the likelihood of phase separation into Si rich and B rich areas. Either this might happen during the formation of these phases in the melt (spinodal decomposition) and these phases remain separated on cooling or the separation may be induced via heat treatment of a primarily homogeneous glass. The zone rich in B has reduced chemical durability, an outcome that is successfully utilised in Vycor glass production, but it is troublesome for nuclear waste production due to the potentially higher solubility of the glassy waste form (Varshneya 1994; Vogel 1994).

2.4.2.1 Structure of borosilicate glasses

Boron oxide exists in two transformable structural forms in borosilicate glasses: BO_4 tetrahedra and BO_3 triangles where the ratio between them is determined by network modifiers. Network modifying cations could be either connected to SiO_4 tetrahedral (forming NBOs) or associated with BO_3 converting to BO_4 units (forming no NBOs) (Varshneya 1994). In the second case, modifiers such as Na^+ work as charge compensators with respect to negatively charged $[BO_4]^-$ units. In terms of quantity, normally 1 mole of Na_2O compensates 1 mole of B_2O_3, however, other species might be involved such as Ca^{2+} or Nd^{3+} (Chouard et al. 2011; Manara et al. 2009).

Glass properties (density or thermal expansion coefficient) do not change in a monotonic manner following the compositional changes, but demonstrate maxima and minima values at a certain composition the so-called boron oxide anomaly. Moreover, the NBO are not created until the conversion ($[BO_3]\rightarrow[BO_4]$) achieves saturation. However, the point at which the maxima or minima take place is not consistent every time with the point where NBO creation starts. Borosilicate glasses thanks to that conversion are more chemically flexible, that allow them to incorporate more components (Varshneya 1994). Glass properties strongly depend on the molar ratio of glass formers to glass modifiers. A high content of glass (network) formers provides a greater connectivity whereas higher network modifiers cause depolymerisation reducing melting temperature and chemical

durability. What is more, when the ratio of network formers to network modifiers is about 2 this maximises the glass forming ability of the mixture. However, in nuclear borosilicate glasses, the silica ratio to other network formers (Al_2O_3, B_2O_3) should be higher than 1.5 to sustain low leaching rate of radionuclides even if this increases the melting temperature (Ojovan and Lee 2005).

2.4.2.2 Borosilicate glass in nuclear industry

Borosilicate glasses have been the material of choice for immobilisation of nuclear waste since tests conducted in the 1950s and 1960s. Since the waste compositions vary between reactors, these glasses had to be modified to incorporate variable waste streams **(Table 2.9)**. Basic borosilicate compositions involve Na and Li oxides as network modifiers. Glass melting temperature as well as crystallisation tendency are reduced by high alkali contents (Polyakova 2000). Moreover, when a fraction of Na^+ ions is replaced by another mobile ion such as Li^+ the *mixed alkali effect* occurs. This effect in silicate glasses depends on non-linear variation in properties regarding ionic transport (i.e. ion exchange). It was observed that when a Li/Na oxide molar ratio is close to unity when the glass reaches maximum durability compared to glasses containing single alkali ion only (e.g. Na). Furthermore, the thermal behaviour of borosilicate glasses could be further improved by utilising the boron anomaly.

Additional modification comes about by the addition of Ca, Al, Zn, and Mg oxides into borosilicate glass. Incorporation of Al_2O_3 at the expense of SiO_2 from 3 to 10 wt% is considered to considerably improve mechanical, chemical resistance and reduce tendencies for de-mixing. Al is an intermediate element and behaves as a network former at low concentration and exists as AlO_4 tetrahedra in the glassy structure. Moreover, alkalis located close to AlO_4 tetrahedra work as a charge compensator and they are no longer modifiers in the silicate network. These alkaline earth cations are not easily leached in comparison to alkalis more weakly bonded to NBO (true if the molar ratio follows $\gamma_{Na2O}/\gamma_{Al2O3} > 1$) (Ojovan and Lee 2005; Vogel 1994).
Components such as CaO, ZnO and MgO increase the viscosity of alkaline silicate glasses at lower temperatures (400-600 ^oC) and make the glass melt more fluid at high temperatures (1000-1300 ^oC) (Manaktala H. 1992; Ojovan and Lee 2005). The generic effect on viscosity is that a shorter glass is produced which means that its viscosity

decreases much faster within the operating temperature. Ca, Zn and Mg added to the glass improve durability by stabilising the glass structure because of the formation of coordination polyhedral around Ca, Zn and Mg by oxygen atoms attached to Si. Nonetheless, the addition of Na_2O, B_2O_3 and CaO increases volatility which requires some technological compromise (Ojovan and Lee 2005). Incorporation of Ca and Zn into borosilicate glass in the laboratory tests at NNL showed that waste glasses due to lower viscosity were poured at a lower temperature (1050 ºC) and possessed better homogeneity. In the nuclear industry, borosilicate glasses are the main matrix for the immobilisation of HLW. This is due to these compositions meeting criteria for an operational radioactive waste form (Donald I.W. 1997; Donald 2010; Ojovan and Lee 2005; Ojovan and Lee 2014).

These include:

- High tolerance for compositional changes
- Good chemical durability
- Low thermal expansion coefficient
- Mechanical integrity
- Good thermal and radiation stability, as well as resistance to crystallisation
- Low melting temperature (~ 1050 ºC)
- Usually, high waste loading > 25 wt% subject to waste composition

Name	Country	Waste loading	SiO_2	B_2O_3	Na_2O	Li_2O	CaO	Al_2O_3	Others
Magnox	UK	**25-31**	61.63	21.93	11.09	5.35	-	-	-
Ca/Zn*	UK	**25-38**	48.65	23.91	8.74	2.15	6.13	4.29	6.13 (ZnO)
R7T7	France	**16.5**	54.04	16.67	12.05	2.35	4.80	5.89	-
SM58	Belgium	**11.1**	63.93	13.82	5.17	4.16	4.27	1.35	7.31
Hanford 76-88	USA	**25**	59.7	14.18	11.19	-	2.99	-	11.94
K-26	Russia	**?**	48.2	7.5	17.8	-	15.5	2.5	8.5
Tokai	Japan	**18.29**	56.97	17.38	8.54	3.66	3.66	6.13	3.66

Table 2.9 Compositions of selected base borosilicate glasses (wt %).
*The glass frit currently under tests in the UK (Jantzen 2011; Ojovan and Lee 2005)

Magnox Waste (MW) glass has been successfully used in the UK to vitrify British nuclear waste. Another waste glass containing a high amount of Ca was borosilicate glass K-26 glass developed in Russia to cope with ILW rich in radioactive caesium and strontium. Several tonnes of K-26 based glass using radioactive waste from Kursk NPP were produced in the 1980s and some of the blocks (weighing circa 30 kg) then placed in a near surface environment for corrosion test. These field tests were performed since 1987 in order to evaluate the glass behaviour near the surface disposal (Ojovan et al. 2005). Moreover, the leaching experiments were run by treating the glass blocks by flowing non-saturated water at 1.7 m below the ground and covered by loamy soil (Ojovan et al. 2005; Ojovan et al. 2006). After 16 years, the leaching rate of Cs is 2.2×10^{-7} g cm^{-2} d^{-1} where the hydrolysis rate of the samples was evaluated as 0.1 μm $year^{-1}$, indicating that the ion exchange diffusion will dominate the corrosion process in geological disposal. Interestingly, the non-active version of K-26 in the laboratory condition demonstrated comparable leaching results. After 12 years the K-26 active glass demonstrated lower radioactivity and the only γ-emitter was ^{137}Cs (Ojovan et al. 2005). Higher calcium level in nuclear glasses has also been found in the UK glassy wasteforms (Ca/Zn base frit) to increase the solubility of MoO_3 in borosilicate glass and to minimise the crystallisation of soluble alkaline molybdates (Short et al. 2008) .

Barium oxide is another major component of POCO waste, where it is present in 12.88 wt. % (NNL 2014). The Ba^{2+} ion is one of the biggest with its effective radius similar to K^{+}, O^{2-} and Pb^{2+}. The high polarizability of Ba^{2+} ions relates to their size where the outer electrons are less bound to the atom nucleus. In addition, BaO field strength is one of the lowest between alkaline-earth cations and it is classified as a glass modifier (Volf 1984; Vogel 1994). Glass density and meltability increase with rising proton number in the order Ca<Ba<Pb. During decomposition of carbonates, $BaCO_3$ requires much higher temperature to decompose than calcium and strontium carbonate. The partial pressure of carbon dioxide reaches atmospheric pressure directly above 1400 ^{o}C and the strength of CO_2 and BaO bond is maintained in the glass. The high BaO glasses liberate fine bubble of CO_2 only at high temperatures that are difficult to be remove, therefore, especially in electric melting barium carbonate needs to be replaced by barium nitrate.

In binary and ternary systems of borate and silicate glasses BaO has greater miscibility than other elements from group 2 of the periodic table. Therefore, BaO is utilised instead of CaO in borosilicate glass with low alkali contents, where Ca cations could cause phase separation due to its stronger bond with oxygen (Volf 1984). That conversion to 4 coordinated boron increase interconnectivity of borate polyhedron in the glass network from 3 to 4 and results in higher glass strength. Further increase of alkalis leads to another conversion from BO_4^- to BO_3^- (planar BO_3 with one NBO) which leads to a lower stability of the glass (Lim et al. 2007).

In India ThO_2 based reactors are of special interest due to significant deposits of this element. Moreover, ThO_2 could be also used as simulant of more dangerous actinides e.g. ^{239}Pu and ^{241}Am. It was reported by Mishra (Mishra et al. 2007) that BaO in sodium borosilicate glass considerably increases the solubility of ThO_2. Moreover, it has been determined by ^{29}Si and ^{11}B MAS NMR analysis that Th incorporation did not affect the concentration of Q^n structural units of Si and BO_4 and BO_3 in the glass. Higher solubility of ThO_2 in the glass might be attributed to a huge number of NBOs that facilitates thoria incorporation at the network modifying positions in the glass structure. Additionally, MAS NMR studies indicated that there is no direct interaction between BaO and boron network because the relative concentration of BO_3 and BO_4 units remained unchanged. What is more, IR studies showed that borosilicate glass network was unaffected by BaO addition, because of the identical stretching and bending wave numbers related to Si-O-

B and Si-O-Si. Furthermore, the same T_g values also lead to comparable conclusion that the network was not strongly affected. The changes in glass transition temperature are caused by varied relaxation in the glass network and in this case the different BaO content did not considerably affect the glass network, so the nature of structural relaxations remain similar with the modified composition, and provide analogous glass transition temperature for varied BaO content (Mishra et al. 2008).

Iron oxide present in nuclear waste comes from activated corrosion products and process chemicals. Some waste streams stored in tanks at Savanah River Site can hold close to 30 wt. % of Fe_2O_3 (Stefanovsky et al. 2013). Iron content in UK nuclear waste is also significant and might be present from 11.67 wt.% for Magnox waste to 24.36 wt.% in some tanks (Connelly 2008). As so-called intermediate oxide, Fe ions may exist in the form of Fe^{2+} or Fe^{3+} and act as a network former in four-fold coordination or as a network modifier in six-fold coordination with oxygen, however, the final form depends on the glass composition. It was reported that in SB6 borosilicate glasses from Savannah River Site, Fe mainly is present as Fe^{3+} ions and behave similarly to Al^{3+} ions impeding conversion of 3-coordinated boron to 4-coordinated boron, but to a lesser extent than Al ions (Stefanovsky et al. 2013). Additionally, it was observed by (Musić et al. 1989) that the final ratio of Fe^{3+} / Fe^{2+} in Zn – borosilicate glasses was affected by a chemical form of iron introduced into the melt. Another finding indicates that both iron ions found in borosilicate glasses were tetrahedrally coordinated. On the other hand, the structural role of iron in silicate and aluminosilicate glasses seems to be different, because it was found that Fe^{2+} ions had an octahedral coordination.

The coordination chemistry of Mn ions in solids and liquids have even more complicated nature than that of Fe ions due to their polyvalent nature. Mn oxidation states might be from Mn^{2+} to Mn^{7+}. However, in glasses, Mn exists mainly as Mn^{2+} and Mn^{3+} ions, but the presence of Mn^{4+} cannot be totally excluded. The coordination number (CN) varies from 4 to 8. Electron spin resonance (ESR) indicated that Mn^{2+} is six-fold coordinated. This shows that Mn (II) ions can play a similar role to Fe in the glass i.e. to be either a network-modifier forming spinel phases at higher contents or network former at lower content. The ESR results state that Mn ions exist mainly in the vitreous state as Mn^{2+}, plus its CN was observed to be between 5 and 6. Some smaller values of CN could be

attributed to the existence of $Mn^{(2+, 3+)}$ in the spinel form. On the contrary, the iron in the SB6 borosilicate glasses existed mainly as a trivalent $Fe^{3+}O_4$ tetrahedra. The total iron CN just goes beyond 4 due to the influence of six-coordinated Fe^{3+} and Fe^{2+} from spinel (Stefanovsky et al. 2013). Additionally, this result remains in a good agreement with Schreiber that describes the mutual interaction between Mn and Fe ions as stoichiometric with a strong reducing potential $\Delta E^{'}=2.5$ which is one of the highest values between presented redox couples (Schreiber et al. 1987).

$$Mn^{3+} + Fe^{2+} \rightarrow Mn^{2+} + Fe^{3+} \quad (2.2)$$

The addition of Fe_2O_3 to a UK High Level Waste (HLW) borosilicate glass seems to have very positive effect on chemical durability. It was found by Cassingham et al. (2008) that the addition of iron oxide up to 15 wt. % has no noticeable effect on T_g and T_{c1} (first crystallisation peak) of the investigated glasses (25 wt.% HLW loading). Therefore, the thermal stability of that glassy waste form at this level of Fe_2O_3 was not decreased. Moreover, chemical durability measured by Product Consistency Test type B (PCT-B) during 7, 14 and 28 days period showed that leaching rate drastically reduced with a small addition of Fe_2O_3 (5-10 wt.%). It was noted that the release rate of all components was reduced after incorporation of Fe_2O_3 (5-10 wt.%). Nevertheless, the further increase of Fe_2O_3 results in small decrease in Si leaching, but increases the release of Cs, Li, Na, B and Mo. Even though, initial leaching rates (7 days) become decreased with increasing Fe_2O_3 amounts, longer tests (14 and 28 days) designate deterioration in long term durability at 15-20 wt% of Fe_2O_3 (Cassingham et al. 2008). It was noted by Cunnane (Cunnane et al. 1994) that addition of alumina to borosilicate glass might reduce the initial corrosion rate as a structurally active component 'by causing Na+ ions to be located adjacent to Al^{3+} ions to balance charge', but the latter increases its effect on solution chemistry. That is why, structural similarity between Al^{3+} and Fe^{3+} ions in silicate glasses appears feasible that the similar effect on corrosion behaviour could be attributed to addition of Fe_2O_3, where the amount of 5-10 wt.% delivers the most beneficial corrosion resistance. Moreover, higher leaching rate of Li, B, Na, Cs and Mo at the higher amount of Fe_2O_3 (15-20 wt.%) might indicate that tetrahedrally coordinated Fe^{3+} as a glass former should strengthen the glass structure, could be located in the SiO_2 enriched domains (Cassingham et al. 2008)(Stefanovsky et al. 2013).

2.4.3 Chemical durability of alkaline borosilicate glasses

Glass chemical durability is a direct measure of the wasteforms capability to immobilise its radionuclide content. The durability depends on numerous factors such as composition, waste loading, leachate composition, pH and flow rate; redox potential, diffusion coefficients, the formation of surface layers; crystallisation of the waste glass; phase separation and radiolysis (Lutze & Ewing 1988). The simplified mechanism of aqueous corrosion of alkali borosilicate glass is described below (**Figure 2.8 & Figure 2.9**) (Greenwood & Earnshaw 1997; Lutze & Ewing 1988; Donald et. al 1997; Ojovan et al. 2006).

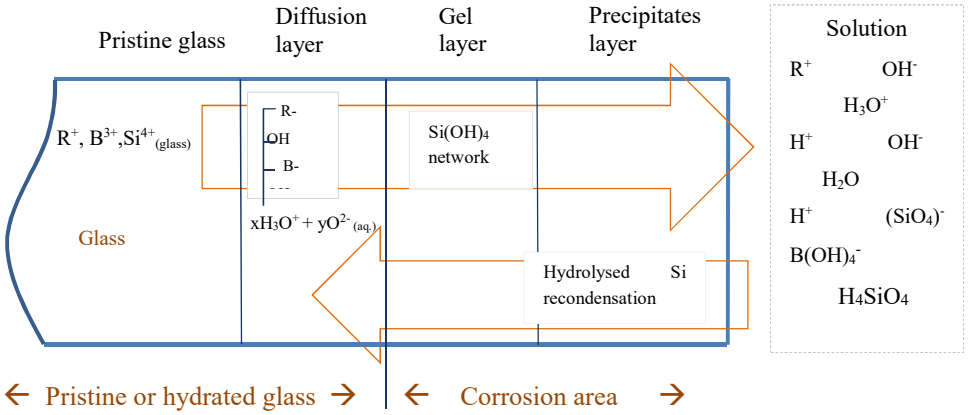

Figure 2.8 Schematic of corrosion mechanisms in alkaline borosilicate glasses.

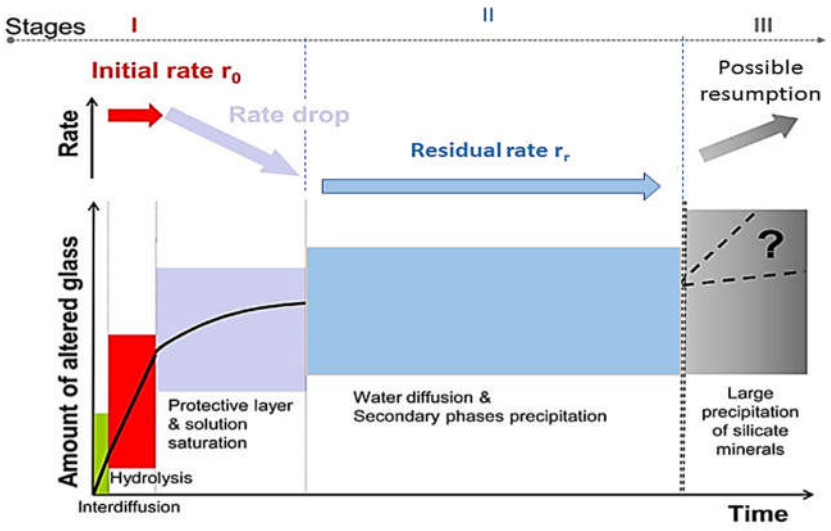

Figure 2.9 General schematic of HLW glass corrosion mechanisms in a static aqueous solution (Harrison 2014; Gin et al. 2013)

Interdiffusion (Hydration and Ion Exchange)

In a static leaching scenario, it is mainly considered that the early reactions include ion exchange of soluble alkaline ions with H_3O^+ and OH^-. This process is controlled by diffusion which rate is proportional to $t^{1/2}$. It is thought that diffusion occurs along the alkali channels mentioned in **Section 2.2.3.**

$$2\ H_2O \leftrightarrow H_3O^+ + OH^-$$
$$Si - O^- + H_3O^+ \rightarrow \equiv Si - O^-H^+ + M^+_{(aq)} + H_2O \qquad (2.3)$$

Moreover, the alkaline leaching rate becomes linear with time as an alkaline free hydrated surface layer is developed. As expected pH increases as more alkali leaves the glass, but that release is slowed down by increased concentration of alkali and hydroxide in solution (higher pH reduces ions release).

Hydrolysis and Dissolution

The silica gel layer forms due to congruent partial hydrolysis, dissolution and recondensation of the glass network. This process is enhanced by the high pH related to highly alkaline solution, which in turn slows the alkali release but speeds up the hydrolysis process.

$$\equiv Si - O - Si \equiv + H_{2+}O \rightarrow 2(Si - O^-H^+)$$
$$\equiv Si - O - Si \equiv + OH^- \rightarrow \equiv Si - O^-H^+ + \equiv Si - O \qquad (2.4)$$

The hydration of silica rich gel could release silicic acid (H_4SiO_4) into solution (water). Similar reactions occur for the other network formers (e.g. B producing boric acid). This acid production decreases the pH so the opposite happens after the release of alkaline ions. These two possible mechanisms are presented below:

$$\equiv Si - O - Si(OH)_3 + H_2O \rightleftharpoons \equiv Si - O^-H^+ + Si(OH)_4$$
$$\equiv Si - O - B(OH)_2 + H_2O \rightleftharpoons \equiv Si - O^-H^+ + B(OH)_3 \qquad (2.5)$$

The above equations show depolymerisation of the glass network and produce silanol groups (Si-OH). The dissolution rate is mainly controlled by the concentration of $H_4(SiO_4)$ in the solution, with higher $H_4(SiO_4)$ concentration resulting in reduced network dissolution rate. The hydrolysis of the glass network manages the total rate of dissolution following the primary period of ion exchange and surface gel layer formation.

$$\begin{aligned} 2(\equiv Si-O^{-}H^{+}) &\rightleftharpoons \equiv Si-O-Si\equiv + H_2O \\ (\equiv Si-O^{-}H^{+}) + H_4SiO_4 &\rightleftharpoons \equiv Si-O-Si(OH)_3 + H_2O \end{aligned} \quad (2.6)$$

Precipitation from the solution of crystalline and amorphous phases could also take place at the glass-liquid interface. This can have major consequences on the glass dissolution because the precipitation removes ions from the solution so giving a concentration gradient (driving force) for extra dissolution.

Borosilicate glasses are generally resistant to mildly acidic solutions (excluding phosphoric and hydrofluoric acids), however, are attacked more readily by alkaline solutions (Volf 1984). The durability of glasses such as borosilicate glass heavily depends on their compositions. Leaching rates of BS glasses are the smallest while alkaline oxides to boron content are equal on a molar basis (relating mainly to ^{IV}B), indicating the stability of 4 coordinated B (Marples 1988). Chemical durability can be further enhanced (lower leaching rate) by introducing equimolar quantities of different alkali oxides (mixed alkali effect). Additionally, higher a SiO_2 content tends to increase glass durability (lower NBO contents) as well as Al, Zn and Ca in a borosilicate glass have been associated with improving chemical durability (Lutze & Ewing 1988; Marples 1988; Harrison 2014).

The role of Mg is more complex. On one hand, it was reported that Mg incorporation had a positive effect on borosilicate glass durability (Lutze & Ewing 1988; Ojovan and Lee 2005). On the other hand, Curti et al. (2006) noticed that higher Mg content resulted in greater B and Li releases from UK HLW glass likened to SON68 glass (>12 years duration PCT) indicating that the role of Mg was to catalyse the degradation of the glassy sample by promoting the nucleation of stable Mg-clay alternation products. What is more, Thien et al. (2012) observed that Mg in French AVM glass had actually a dual role on long-term alteration. The first is about precipitation of aluminous hectorites (soft white clay mineral) which consume silicon and results in partial or complete dissolution of the protective gel layer. The second role is the incorporation of Mg ions into the gel layer,

which increases its passivation in a similar way to Ca in the French R7T7 glass. Finally, those two antagonistic mechanisms depend on the glass composition and potentially through its effect on the pH of the solution; however, this relationship is still poorly understood.

The redox potential (Eh) of aqueous solutions is noticed to have a strong effect on the solubility of multivalent cations. Anoxic (reducing) contacting solutions are considered to reduce the solubility of multivalent cations, therefore improving the durability of borosilicate glasses. Underground basaltic and granitic repositories possess anoxic groundwaters, and salt repositories have mildly anoxic groundwaters (Lutze & Ewing 1988; Rose 2007).

2.5 Glass phase transformations - chemical durability

2.5.1 Crystallisation (Devitrification)

Crystallisation of borosilicate glasses could have a varied effect on the chemical durability of the final glassy wasteform. Historically, crystallisation of glassy waste form has always been considered as unwanted due to a potentially harmful effect on durability and mechanical integrity (Ojovan & Batyukhnova 2007). A negative effect on durability by crystallisation has been observed by some researchers (Spilman et al. 1986; Lutze & Ewing 1988) as well as a positive one (Larkin 1986; Rose et al. 2011) or negligible (Shanggeng et al. 1990). The final aqueous durability of the glassy wasteform is related to a cumulative effect of all the formed crystals.

The crystallisation of borosilicate glass is detrimental when:

- the crystal phases deplete the glassy matrix of network formers and intermediates (Kim et al.,1995; Sproull 1994), producing a residual glass of lower durability that the parent glass
- the formed crystals have high water solubility, particularly if the radionuclides are incorporated into crystals
- preferential corrosion exists at the glass-crystal interface that could be due to thermal expansion coefficient mismatch and/or compositional gradient resulting in stresses and micro cracking (Hrma 2010; Kim et al.1995; Sproull 1994).

A perfect partially crystallised glassy wasteform would contain crystals with very low aqueous solubility with partly incorporated radionuclides, uniformly distributed within a residual glass matrix with a chemical durability that is higher than its original glass (caused by crystal). Moreover, crystal phases need to be radiation resistant and residual glass matrix and crystals should have a similar thermal expansion coefficient α. Finally, crystal phases should not undergo phase transitions during cooling which are usually associated with volumetric changes that may cause cracking of the wasteform.

2.5.2 Amorphous Phase Separation (APS)

Amorphous phase separation affects the borosilicate glass durability in varied ways. However, APS usually has a negative effect on the glass durability (**Table 2.10**).

Separation Type	APS microstructure	APS mechanism	Effect on durability of glass
A	Both phases are interconnected and continuous. The durability of the glass is ruled by the least robust phase	Spinodal decomposition	Negative
B	A SiO_2 rich droplets are distributed in a non-durable matrix of alkali-borate phase	Nucleation and growth	Negative
C	Alkaline borate droplets are dispersed in very durable SiO_2 matrix	Nucleation and growth	Positive

Table 2.10 shows the effect of APS on the chemical durability of HLW borosilicate glasses, based on their microstructure (Jantzen et al. 2001).

2.6 Summary

Nuclear waste immobilisation is closely linked to vitrification process that is a primary choice for the immobilisation of HLW and some ILW. Borosilicate glass combines many features such as low melting point, good thermal stability, both high chemical flexibility and durability plus proven technology, which make it internationally a suitable material of choice for vitrification of nuclear waste.

However, some problematic type of waste such as POCO waste that contains high levels of challenging elements with a low solubility in the glass, such as Zr, and Mo are considered in this project. In order to increase the effectiveness of vitrification process with respect to POCO simulant, CZ glass was created by the addition of Ca, Al and Zn. In nuclear glasses, Mo exists as a negative oxyanion (MoO_4^{2-}) located in the depolymerised cavities, where a charge compensation mechanism mainly with alkali and alkaline earth ions occur. This mechanism appears to control the way the crystallisation undergoes and that is related to a durability of the final wasteform. Formation of 'yellow phase' is another problematic issue, which strongly affect the durability of a waste glass. Moreover, the amount of that water-soluble phase is influenced by many factors including for instance: redox conditions, cooling regime, the absolute quantity of MoO_3 in the glass melt and alkali MoO_3 ratio.

Molybdate solubility is linked to NBO fractions and network modifiers in the glass. Increased NBO ratios lead to the higher capacity of the glass network to incorporate Mo, but its solubility could also be governed by the separation tendency of molybdate from the silicate network altogether. Additionally, an incorporation of MoO_4^{2-} in the glass, its solubility is both associated with network modifiers and molybdate located in the interstices of the glass network. The incorporation of MoO_4^{2-} results in increased glass densities and decreased T_g.

3. Experimental Procedures

3.1 Glass and waste compositions

3.1.1 Base glasses and POCO simulant

The CZ type glass frit was provided by NNL for vitrifying MoO_3 rich wastes. MZ glass was formed in the lab to investigate how the replacement of CaO by MgO (molar basis) affects the solubility of POCO waste simulant (**Table** 3.1). According to Tan et al. (2015) magnesia aluminosilicate glass demonstrated the greatest ability to incorporate MoO_3 amongst other alkaline earth aluminosilicate glasses. **Table** 3.2 shows a simplified composition of POCO waste, which will be formed during Post Operational Clean Out (POCO) before the decommissioning of HAST's (see p. 24) (Edmondson et al. 2014).

Glass type	SiO_2	B_2O_3	Li_2O	Na_2O	CaO	MgO	ZnO	Al_2O_3	Total
CZ	50.83	21.56	4.52	8.85	6.86	-	7.73	2.64	100
MZ	50.78	21.54	4.51	8.84	-	6.97	4.72	2.64	100

Table 3.1 Compositions of CZ and MZ type glasses (mol%)

Oxides	Wt.%
P_2O_5	0.28
SrO	1.19
BaO	12.88
ZrO	23.13
MoO_3	60.85
Cs_2O	1.66
Total	100

Table 3.2 Simplified POCO waste composition

3.1.2 Batch Compositions

3.1.2.1 Incorporation of POCO simulant with MoO_3

Table 3.3 shows the loading of CZ and MZ glasses with varying amounts of added wastes. The first group of samples commencing from CZ2Mo containing variable amount of MoO_3. The second group starting from CZ5N containing extra CaO and Na_2MoO_4. The last two types of samples starting from CZ and MZ are based on CZ frit and MZ frit with 15, 20 and 25wt% of POCO waste simulant. The addition of Fe_2O_3 and Mn_2O_3 was designed to improve melt fluidity and chemical durability (Cassingham et al. 2008) of the waste glasses as well (see Appendix 2).

Sample	CZ frit	MZ frit	Fe_2O_3	Mn_2O_3	POCO	MoO_3	CaO	Na_2MoO_4	Total
CZ2Mo	98	-	-	-	-	2	-	-	100
CZ6Mo	94	-	-	-	-	6	-	-	100
CZ8Mo	92	-	-	-	-	8	-	-	100
CZ5N	90	-	-	-	-	-	5	5	100
CZ15N	80	-	-	-	-	-	5	15	100
CZ15NF	75	-	5	-	-	-	5	15	100
CZMF-15P	69	-	8	8	15	-	-	-	100
CZMF-20P	64	-	8	8	20	-	-	-	100
CZMF-25P	59	-	8	8	25	-	-	-	100
MZMF-15P	-	69	8	8	15	-	-	-	100
MZMF-20P	-	64	8	8	20	-	-	-	100
MZMF-25P	-	59	8	8	25	-	-	-	100

Table 3.3 Loading of CZ and MZ type glasses with POCO simulant (wt%)

3.1.2.2 Incorporation of P-type waste simulant

Table 3.4 presents the waste compositions of the P-type waste simulants received from the NNL. The table also contains loss of ignition (LOI) which occurs due to a partial nitride presence during melting of the waste glasses. The detailed description how the given waste compositions were formed is available in chapter 2 (see page 25). The main components of POCO waste such as MoO_3 is gradually decreasing from around 30 wt % (P48) to 19 wt% (P19). The amount of ZrO_2 in P48 and P19 wastes is not changed that strongly such as MoO_3, however, BaO content decreases from approximately 7.5 wt% (P48) to 3.5 wt% (P19). The small addition of RuO_2 should simulate the presence of platinoids in the wastes which is responsible for nucleation and crystallisation of spinels (see page 22) (Matyáš et al. 2012; Izak et al. 2001).

LOI	1.44	1.34	1.51
Wt.%	**P48**	**P19**	**P0**
Al_2O_3	5.69	8.02	9.63
BaO	7.47	3.47	2.84
CeO_2	3.34	4.78	5.78
Cr_2O_3	1.42	2.06	2.61
Cs_2O	4.63	5.55	6.22
Fe_2O_3	6.38	9.20	11.29
Gd_2O_3	4.13	5.94	7.05
La_2O_3	1.71	2.49	2.99
Li_2O	3.76	3.35	4.93
MgO	5.96	8.44	10.14
MoO_3	30.28	19.09	8.60
Nd_2O_3	4.98	7.34	8.77
NiO	0.89	1.26	1.57
Pr_2O_3	1.52	2.22	2.61
<0.1 RuO_2	-	-	-
Sm_2O_3	1.13	1.72	2.06
SrO	1.61	1.68	1.66
TeO_2	0.54	0.76	0.96
Y_2O_3	0.67	0.99	1.16
ZrO_2	13.89	11.65	9.12
Total	**100.00**	**100.00**	**100.00**

Table 3.4 Waste simulant compositions used in this project ± 10 wt% (from NNL)

Table 3.5 presents glass compositions with P-type simulants mixed with CZ frit. Extra additions of CaO, Mn_2O_3 and CuO were introduced to help the incorporation of P-type simulants. CaO was used to promote the crystallisation of powellite, a durable phase that is acceptable in nuclear glasses (Brinkman et al. 2013; Taurines & Boizot 2012), additionally, K-26 borosilicate glass (see page 40) contains about 21.6 mol% of CaO and demonstrated good chemical durability (Ojovan & Lee 2005). The introduction of Mn_2O_3 and CuO increase fluidity of the melt (Volf 1984) and Mn works also a redox couple with Fe oxide (Schreiber et al. 1987). In this redox coupling, Fe is oxidised to Fe^{3+}, and this mostly should lead to its tetrahedral form, where Fe works as a glass former (FeO_4^-) which has a positive effect on chemical durability (see page 40) (Cassingham et al. 2008). Additionally, FeO_4^- tetrahedra have an unbalanced charge which requires electrostatic compensation usually by monovalent cations such as Na^+ (Cochain et al. 2013; Ciecińska et al. 2015). This, in turn changes the role of 'free' Na from network modifier into a charge compensator and this conversion increases stability and binding energy of structural units in glasses (Ciecińska et al. 2015) (see Appendix 1).

Sample	CZ frit	P19	P48	P0	CaO	Mn_2O_3	CuO	Total
P19-25	75	25	-	-	-	-	-	100
P19-38	62	38	-	-	-	-	-	100
P19-25C	59	25	-	-	8	4	4	100
P19-38C	46	38	-	-	8	4	4	100
P48-25	**75**	**-**	**25**	**-**	**-**	**-**	**-**	100
P48-38	**62**	**-**	**38**	**-**	**-**	**-**	**-**	100
P48-25C	**59**	**-**	**25**	**-**	**8**	**4**	**4**	100
P48-38C	**46**	**-**	**38**	**-**	**8**	**4**	**4**	100
P0-25	75	-	-	25	-	-	-	100
P0-38	62	-	-	38	-	-	-	100
P0-25C	59	-	-	25	8	4	4	100
P0-38C	46	-	-	38	8	4	4	100

Table 3.5 CZ glasses loaded with P type simulants (wt%)

3.1.3 Glass and POCO simulant batching

Raw materials used for glass batching and the POCO simulant are given in the **Table 3.6**. It is expected that all carbonates and hydroxides in batches decompose to oxides in the glass melt during heating. Mn and Fe were added as oxides to aid the incorporation of the wastes. In order to make circa 60 g of glass batches were weighed using an electronic scale (0.01 g accuracy). Subsequently, batches were mixed in sealed plastic bags and kept in a dry box prior to melt. During mixing, some batch loss occurred because of the adherence to the plastic bag, but it was less than 0.5 wt% of the total batch.

Oxide	Raw materials	Purity (%)	Supplier
SiO_2	Silica sand, SiO_2	99.8	Loch Aline, Tilcon UK
B_2O_3	Boric acid, H_3BO_3	99	Alfa Aesar
Al_2O_3	Aluminium hydroxide, $Al(OH)_3$	99.9	Sigma Aldrich
Na_2O	Sodium carbonate, Na_2CO_3	99	Fisher Scientific
Li_2O	Lithium carbonate, Li_2CO_3	99	Sigma Aldrich
CaO	Calcium carbonate, $CaCO_3$	99	Sigma Aldrich
MgO	Magnesium carbonate, $MgCO_3$	99	Alfa Assar
BaO	Barium carbonate, $BaCO_3$	99	Sigma Aldrich
SrO	Strontium carbonate, $SrCO_3$	99	Fisher Chemical, UK
ZnO	Zinc oxide, ZnO	99.9	Sigma Aldrich
MoO_3	Molybdenum oxide, MoO_3	99.5	Alfa Aesar
Fe_2O_3	Iron oxide, Fe_2O_3	99.9	Alfa Aesar
Mn_2O_3	Manganese oxide, Mn_2O_3	99.9	Sigma Aldrich
P_2O_5	Ammonia dihydrogen phosphate $NH_4H_2PO_4$	99.5	Fisher Chemical, UK

Table 3.6 Raw materials used for MZ glass and POCO simulant batching

3.1.4 Glass making

The prepared batch was transferred to a mullite crucible that was put into an electric furnace with a maximum temperature of 1200 °C. MZ and CZ glass batches were heated from RT to 1060 °C for 4 hours with stirring and then the melt was cast into a stainless steel mould to form a block. The batches with P-type simulants were melted at the same temperature, but with stirring. After casting all glasses were immediately transferred to an annealing furnace, where they were held for 1 h at 520 °C and subsequently cooled down to RT at 1°C/min. Afterwards, glasses were put into clean plastic sample bags.

Corrosion tests on Inconel 601 and Nicrofer 6025HT

Rectangular coupons of Inconel 601 and Nicrofer 6026 HT were machined to the following size prior to testing ~ 15mm×1.0mm×50.0 mm, and a 2 mm diameter hole drilled in one end. The coupons were polished with P1200 SiC paper and cleaned with isopropanol before the corrosion tests. The metal coupon was suspended by Pt wire and fixed by alumina rods into a mullite crucible filled with a 70 g of batch (CZ glass + waste simulant). The isothermal corrosion tests were conducted at 1060 ^{o}C for 1, 6 and 12h, and one coupon was used for each time condition.

3.2 Characterisation techniques

3.2.1 Density

Glass density was determined with a Mettler Toledo densimeter based on Archimedes' principle using deionised water as the immersion medium. The measurement can be explained as follows: The weight of a glass sample in air and in deionised water were measured as m_1 and m_2, respectively. Therefore, the volume of glass V_a that equals the volume change of deionised water ΔV_W when glassy sample is fully immersed, can be expressed as:

$$\boldsymbol{V_a = \Delta V_w = \Delta m_w/\rho_w = (m1 - m2)/\rho_w} \qquad (3.1)$$

where d_w, the density of deionised water at a given temperature. Hence, the density of glass ρ is given by:

$$\boldsymbol{\rho = m1/V_a = \rho_w\, m1/(m1 - m2)} \qquad (3.2)$$

The precision of the balance is 0.001 g cm^{-3}. Each glass sample was measured for three times; error bars record the reproducibility errors.

3.2.2 X-ray Diffraction (XRD)

XRD evaluates the amorphous nature of prepared glasses and to identify the crystalline phases in glass samples. The principle of X-ray diffraction in crystals is illustrated in **Figure 3.2**. The specific beam of X-rays hitting on a crystal is scattered in all directions by the atoms of the crystals (powdered sample). Nonetheless, in some directions an amplified intensity is observed, because of constructive interference (diffraction) of the dispersed X-rays. Therefore, diffraction takes place, when a beam of incident X-rays (wavelength (λ)) strikes a sample at some characteristic angle (θ) which follows Bragg's Law**:**

$$\boldsymbol{2dsin\theta = n\lambda} \qquad (3.3)$$

where n is considered as an integer representing the order of diffraction and d is the spacing amid two parallel atomic planes. For that reason for a fixed λ of X-rays, the interplanar spacing (d) in crystalline lattice gives rise to specific diffraction angles (θ). The diffraction angle series, which are reflected as XRD patterns - unique for particular

type of crystals. This results in characteristic XRD patterns which provides information about present crystals (crystalline structures).

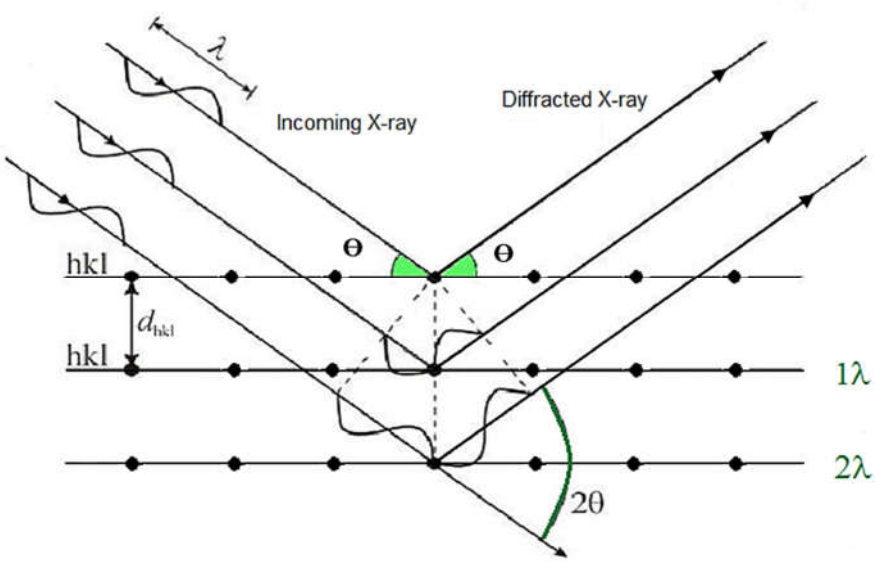

Figure 3.2 Schematic diagram of X-ray diffraction in crystals (from KU Leuven 2016)

XRD patterns for crystals typically are composed of a number of sharp peaks at specific diffraction angles, but XRD patterns for glassy samples are the opposite - formed of a wide peak (glass hump). The glass hump is produced by disordered structure of atomic arrangement in amorphous materials (glass), which results in broadly scattered diffraction angles. Moreover, XRD patterns for glass composites are typically made of some crystalline sharp peaks placed over on the glassy humps. Crushed glass samples were ground to fine powders in an agate mortar and sieved to < 75 μm and collected in clean bags for XRD analysis. Room temperature powder XRD tests were conducted using a Brucker D2 Phaser X-Ray Diffractometer, using Cu-*K*α (λ=1.54056 Å) as the radiation source operating at 30 kV and 40 mA. The examined glassy samples were scanned over the range of 10-70 °2θ with a step size of 0.05° and 2.9 s dwell time. The obtained XRD patterns were investigated by PDF4+ software for phase identification using the International Centre for Diffraction Data (ICDD).

3.2.3 Differential Thermal Analysis (DTA)

DTA examines the thermal behaviours of the made glass samples over a temperature range. A DTA curve records thermal reactions of samples on heating or cooling by comparison with an inert reference (alumina) undergoing an identical thermal treatment. A DTA curve can show temperatures of glass transition, crystallisation and melting. One of the most relevant was the glass transition temperature (T_g) which was estimated from the onset of the first endothermic peak in the DTA curve (**Figure 3.3)**. In the studied borosilicate glasses, T_g peaks appear at ~ 530 ºC. The exothermic crystallisation peak appears at a higher temperature than T_g, and the middle of the crystallisation peak was used as the glass crystallisation temperature (T_p). The powdered samples for DTA were prepared via an identical approach for XRD analysis. DTA curves were recorded in a Perkin Elmer STA8000 using platinum crucible in static airflow. Approximately 38 mg (balance sensitivity 0.2 μg) powders with an corresponding weight of Al_2O_3 as the inert reference were measured from RT to 1100°C at 10 °C min^{-1}.

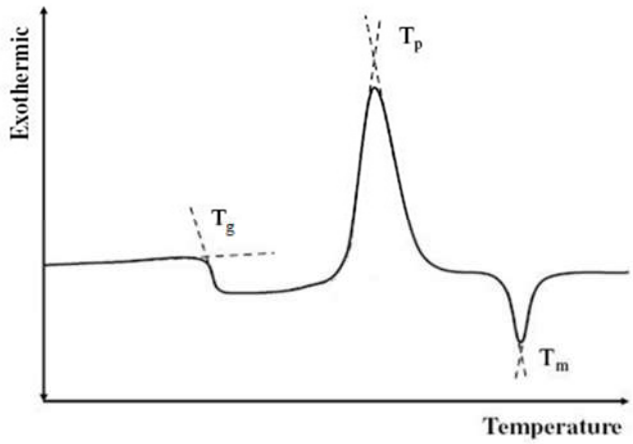

Figure 3.3 Typical DTA curve of glassy sample with T_g approximation (Paul 1990)

Kissinger method

In order to evaluate activation energy of crystallisation (E_a) the Kissinger Method was utilised. The chosen samples were scanned four times at different heating rates (β =10, 20, 25 and 30 °C/min). The next step involved plotting $1000/T_p$ versus $\ln(T_p^2/\beta)$ (T_p – crystallisation temperature). The data was fitted with a straight line and the slope was multiplied by a gas constant (R) which gave values of E_a (kJ/mol). Finally, the E_a values were plotted against waste loading (P type simulants) to identify crystallisation tendencies of the produced waste glasses.

3.2.4 Raman spectroscopy

Raman spectroscopy investigates the chemical bonds and structural changes in glass samples instigated by simulant waste incorporation. The principle of Raman spectroscopy relies on the inelastic scattering of light on measured samples and delivers the information of rotational, vibrational and other low-frequency modes. **Figure 3.4** presents how the scattered light (radiation) is produced when monochromatic beam of light (green laser) (ω_i) hits a sample. It can be divided into two basic categories:

- Rayleigh scattering (elastic scattering) is when the frequency of the scattered light remains at ω_i – electron cloud distortion is involved in scattering process, where the photons are dispersed with minute energy changes (no nuclear motion).
- Raman scattering (inelastic scattering) comes about when the frequency of scattered radiation shifts to ω_f – nuclear motion is caused in the course of the scattering process, which means that energy is transferred from incident photons to a molecule (vice versa).

The Raman shift $\Delta\omega = |\omega_i - \omega_f|$ is particular to the vibrational and rotational states of the investigated samples regardless of the energy (frequency) of incident radiation. For that reason, the collected Raman shifts is utilised to identify chemical and structural information of the examined samples.

This association of molybdate anions (MoO_4^{2-}) with metallic alkaline ions (e.g. K^+, Na^+, Ca^{2+}) is largely similar in crystalline or amorphous materials. Nevertheless, it is noticeable that Raman bands for molybdate anions in glassy samples are wider and to some extent shifted in comparison to those in crystals. Incorporation of molybdate species into the glassy structures can be assigned to a group of peaks in Raman spectra related to four vibrational modes of MoO_4^{2-} oxyanions (**Table 3.7**) (Saraiva et al. *2008;* Mahadevan Pillai et al. 1997; Pope & West 1995):

- υ_1 mode is related to symmetric stretching – 880-951 cm^{-1}
- υ_2 mode is associated with symmetric bending – 280-340 cm^{-1}
- υ_3 mode is related to asymmetric bending – 790-851 cm-1
- υ_4 mode is associated with asymmetric stretching – 35-400 cm^{-1}

The υ1 mode is related to the strongest peak for crystalline molybdates. An observable shift in frequencies account for the interaction of different cations with MoO_4^{2-} in the glassy network and makes available an additional evidence about these interactions. For instance, it was observed by Caurant et al. (2007) that the crystalline Na_2MoO_4 peak is at ~ 894 cm^{-1}, but in the borosilicate glass, that peak is shifted to 921 cm^{-1}.

Molybdates	υ1 frequency	Reference
Na_2MoO_4	894-899	(Saraiva et al. 2008)
$MgMoO_4$	930	(Ozeki et al.1987)
$CaMoO_4$	879	(Brinkman et al. 2013)
$SrMoO_4$	888	(Zverev et al. 2003)
$BaMoO_4$	890-892	(Ozeki et al.1987)
Cs_2MoO_4	881	(Wallez et al. 2014)

Table 3.7 Raman frequency of symmetric stretching modes (υ1) MoO_4^{2-} in some molybdate crystals

Glass bars were sliced to ~ 7 mm thick using a Buehler slow saw with a diamond blade at speed of 6 rev/s, using oil as a lubricant. The top surface of these slices was then ground to 1200 SiC grit, cleaned by isopropanol. Raman measurements were performed upon the polished plane of the samples in a Renishaw Invia Raman spectrometer, using the green line laser (514.5 nm) at about 20 mW power. The energy range 0-1800 cm^{-1} was scanned with a resolution of 1 cm^{-1} and exposure time of 11 s, where 7 spectra were accumulated for each sample. A quick calibration with silicon standard was done each time during a new session. In order to remove the interference of cosmic rays the sample was run by two scans prior to recording a spectrum to avoid these peaks in the final spectrum.

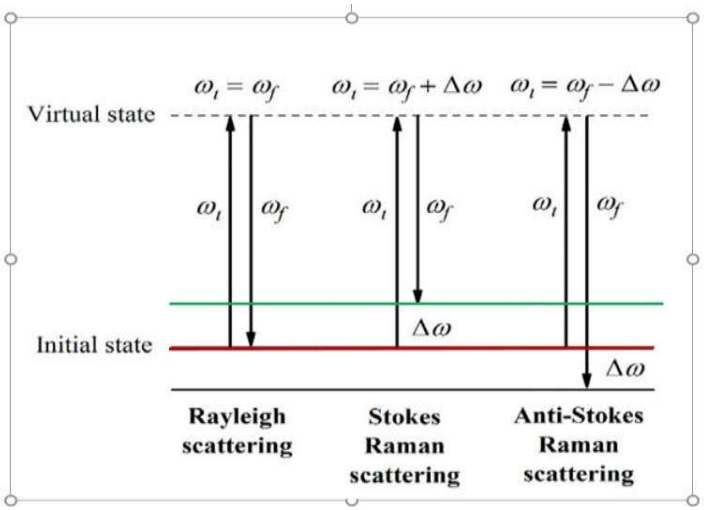

Figure 3.4 Frequency difference between incident and scattered radiation beam in Rayleigh and Raman scattering. Stokes and anti- Stokes scattering relates to a lower and higher scattered frequency, respectively

Raman shifts are dispersed in Raman scattering of glassy materials, which is responsible for broad bands in the Raman spectrum for tested samples. On the other hand, vibrational modes in crystals are completely different, the Raman shifts are very focused and the resulting Raman spectrum is made up of sharp peaks. There is an analogy between broad and sharp peaks in XRD with amorphous and crystalline samples.

3.2.5 Scanning Electron Microscopy (SEM)/ Energy Dispersive Spectroscopy (EDS)

SEM was used to examine the micro features and to observe the homogeneity of the prepared samples. As shown in **Figure 3.5**, a beam of accelerated electrons from the filament is focused by electromagnetic lenses to produce an electron probe on the specimen. That probe with the support of scanning coils then scans the specimen surface. The interaction of electrons with the sample surface generates numerous emissions, which are collected by detectors. The most suitable emitted radiations are normally secondary electrons (SE) and backscattered electrons (BE) for surface observations and X-rays for elemental analysis (EDX). The interaction volume of SEM is also shown in **Figure 3.5**.

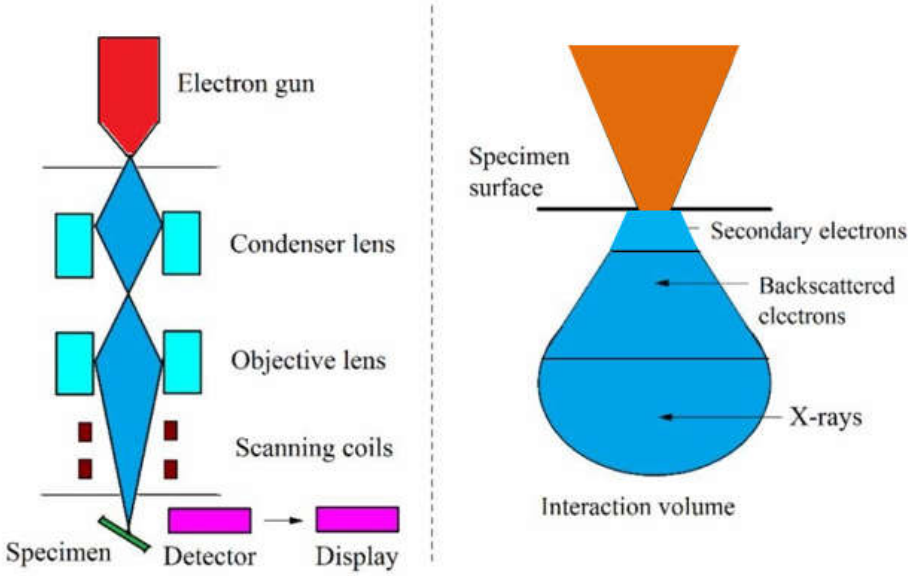

Figure 3.5 Schematic of typical SEM showing the interaction volume of incident beam

Both SE and BE can be used to observe the microstructural features of samples. Secondary electrons originate from the inelastic collisions between incident electrons and the *k*-orbital electrons of atoms of the specimen. The subsequent secondary electron images (SEI) reflect the topological features of the specimen surface. On the other hand, backscattered electrons are produced by the elastic collisions with the sample's atoms - the intensity of which depends on the atomic number (Z) of atoms. Higher Z elements contribute more to backscattered electrons, resulting in contrast between the signals of backscattered electrons from points of different compositions (brighter images). Henceforth, backscattered electron images (BEI) are used to observe dissimilar phases to evaluate the inhomogeneity of samples (e.g. crystals in a glass). Furthermore, characteristic X-rays are emitted from the excited atoms hit by incident electrons. The frequencies of emitted X-rays are distinctive to each element and in consequence by analysing the proportions of X-rays collected by the EDX detector, compositional analysis of individual points can be achieved. However, detection of light elements is problematic, so elements lighter than carbon (e.g. Li or Be) are not readily detected and differentiated by EDX.

Glass bars were sectioned into slices using a Buehler slow saw with a diamond blade lubricated by oil. The glass slices were then mounted into epoxy resin (or Bakelite), ground from 120 to 2500 grade SiC papers with running water and polished using 6 to 1 μm diamond pastes. The prepared samples were thoroughly rinsed with isopropanol. Subsequently, after drying the samples were painted with silver paint to increase conductivity and coated with carbon. SEM measurements were performed with a Toshiba TM 3030 SEM at magnifications of 100x to 18000x. Semi-quantitative EDX analysis was carried out with an energy dispersive X-ray spectrometer (Bruker- XFlash MIN SVE) attached to the TM 3030 SEM. The analysed glass compositions were expressed in atomic or weight percentages. An observation of elemental distribution mainly in the formed crystals, was performed by X-ray mapping during EDX analysis.

3.2.6 PCT- ICP-OES

Evaluation of chemical durability of the glasses was based on the American Society for Testing and Materials (ASTM) Product Consistency Test – B (**PCT-B**). Prior to testing glasses were prepared in the following way. Small pieces of glasses (~10 g) were powdered using a pestle and mortar made of stainless steel. The crushed glass was sieved numerous times and the retained fraction on the 75 μm sieve was utilised for further steps. Ensuring that the powder has the correct grain size on the 75 μm sieve, sieving was performed over white paper for about 10 min. Subsequently, all the powdered samples were transferred to plastic containers (~50 ml) and rinsed with distilled water (about 5 times) and isopropanol (98 % pure, about 5 times) until the liquid over the glass was clear. The sample was placed in an ultrasonic bath for 3 min and then the distilled water or isopropanol was drained and the process repeated up to 4 times, until the liquid over the sample became clear. Isopropanol was always used as the last cleaning agent. Afterwards, the samples were dried overnight in an oven at 90 °C. The dried samples were removed from the oven and approximately 0.6 ± 0.01g weighed out and placed into 50 ml high density polyethylene (HDPE) plastic bottles (Fisher Scientific), where 10 ± 0.1 ml of ultra-high purity distilled water (18 $M\Omega cm^{-1}$ conductivity) was added to give volume / surface area ratio of 1200 m^{-1}. After that, the bottles were sealed, shaken, weighed and put into an oven at 90 °C ± 2 °C for 7 and 28 days. These samples were prepared in duplicates. Additionally, the two blank samples, containing only distilled water, were made in the same manner. After 7 and 28 days, the samples were taken out from the oven and cooled down for 1 h. Subsequently, they were weighed, ensuring that the weight loss was below 10 % (above that value the experiment had to be repeated) and filtered (Whatman ashless, 20μm filter) attached to a syringe, into tubes (HDPE, Fisher Scientific, 10 ml). 50 μl of concentrated (69%) HNO_3 was added to each tube (~8 ml) to prevent any precipitation. All samples containing leachant were analysed using Inductively Coupled Plasma - Optical Emission Spectroscopy (ICP-OES) to check their chemical composition. After ICP-OES analysis the concentration of ions expressed in ppm were obtained the weight fraction of each element of interest in the waste glasses was calculated using:

$$f_i = \frac{wt_{ox(i)} \times (m_{i(ox)/M_{ox(i)}})}{100} \quad (3.4)$$

f_i – mass fraction of element i in the wasteform (unitless)
$wt_{ox(i)}$ - weight present of the oxide of element i in the wasteform
$m_{i(ox)}$ – mass of element i in the oxide of element (g mol^{-1})
$M_{ox(i)}$ – molar mass of the oxide of element i (g mol^{-1})
100 – conversion percentage into fraction

NL_i for each element of interest was subsequently calculated for investigated glasses utilising a modified equation from ASTM (2002):

$$NL_i = \frac{c_{i(n)}}{f_i \times SA/V} \quad (3.5)$$

NL_i – normalised mass loss of element i from the wasteform (g m^{-2})
$C_{i(n)}$ – concentration of element i in the leachate at n^{th} sampling after blank correction (mg L^{-1})
f_i – mass fraction of element i in the unleached wasteform (unitless)
SA/V – wasteform surface area divided by leachant volume (m^2 L^{-1})

Considering the errors from the glass preparation, testing and analysis of samples, each *NLi* data point was multiplied by R_i (Relative standard deviation) assigned as 0.15 calculated as follows:

a- Error in ppm - (5%)
b- Error in element f_i – (10%, verified by XRF)
c- Error SA/V – (10 %)

$$R_i = \sqrt{a^2 + b^2 + c^2} \quad (3.6)$$

3.2.7 Mossbauer Spectroscopy

In 1961, R.L. Mössbauer was awarded the Nobel Prize in Physics for discovering the phenomenon of recoilless nuclear gamma emission and resonant absorption by an irradiating atom embedded in a solid matrix. This phenomenon stimulated investigations into the interaction of gamma rays with materials nuclei e.g. ^{57}Fe, ^{151}Eu and ^{119}Sn. Mössbauer spectroscopy uses monochromatic gamma radiation to investigate the local environment of the target nucleus (Johnson *et al*. 2005, Dyar 1985). ^{57}Fe is the most typically investigated Mössbauer active element. In this case, ^{57}Co is the source which decays to ^{57}Fe in an excited state (5/2) (**Figure 3.6**). Further ^{57}Fe decay leads mainly to its 3/2 excited state (91%) at an energy level of 14.4 keV. Fe in the sample will resonantly absorb this γ radiation and characteristic γ radiation is emitted when it falls back to its ground state. To be able to scan the range of frequencies the source of γ radiation is in constant vibration normal to the sample.

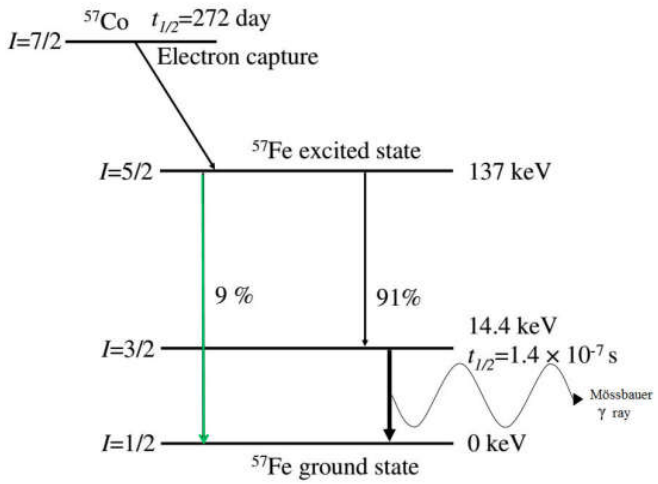

Figure 3.6 Diagram of decay of ^{57}Co to ^{57}Fe, I- spin state of the nucleus (Dickson and Berry 1986)

During the process of absorption or emission of a γ ray by an atom the nucleus will recoil according to:

$$R = \frac{E_\gamma^2}{2Mc^2} \qquad (3.3)$$

R- recoil energy of a free nucleus,
E_γ- the energy of the gamma ray emitted,
M- mass of the nucleus
c – the speed of light.

In order to identify the vicinity of targeted nucleus, recoilless emission or absorption of gamma radiation is necessary. When a recoil is weaker than a phonon (one lattice vibration of an atom) the atom is effectively fixed in the solid matrix. Hence, M is considered to be large and resonant absorption takes place, giving the opportunity to observe the local vicinity of the nucleus.

Considering the case in which the gamma source decays from ^{57}Fe (excited state) to the ground state emitting a γ ray absorbed in the sample by ^{57}Fe in a dissimilar environment this process will produce a difference between the source excited state and the sample excited state. Hence, this will result in a peak shift that is called the isomer shift (**Figure 3.7**)

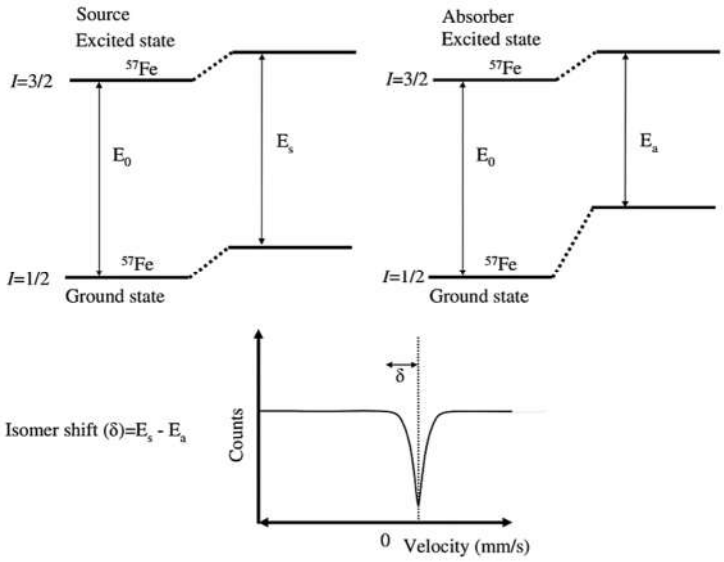

Figure 3.7 Mössbauer spectrum produced from emitter and absorber in varied conditions

Quadrupole splitting occurs in nuclei, which are spherically asymmetric e.g. ^{57}Fe while in its spin 3/2 excited state can show quadrupole splitting (**Figure 3.8**).

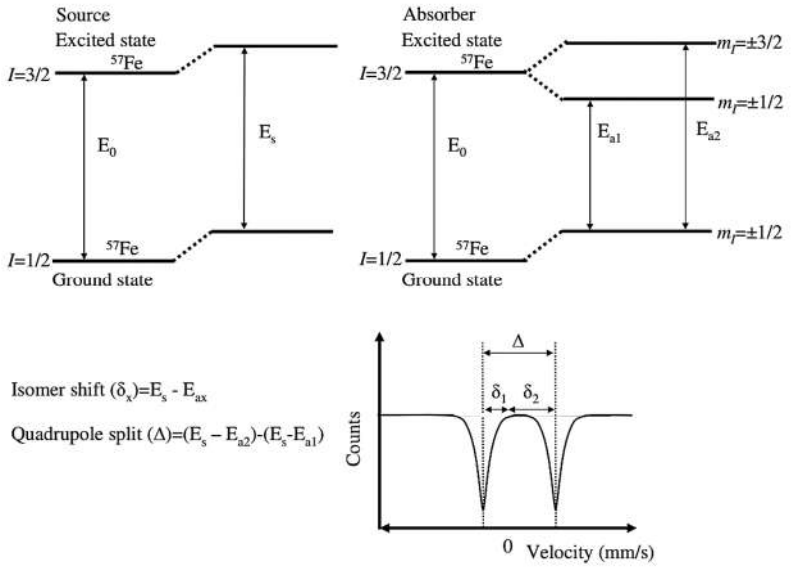

Figure 3.8 Mossbauer spectrum produced from source and absorber in dissimilar conditions with quadrupole splitting in the absorber (Dickson and Berry 1986)

Both quadrupole splitting and isomer shift can be utilised to recognise the local environment of the sample ^{57}Fe nucleus providing information on valence state and coordination (Table 3.8).

$^{57}Fe\delta$ (mm s^{-1})	Fe^{2+}	Fe^{3+}
Tetrahedral	0.9-0.95	0.2-0.32
Octahedral	1.05- 1.10	0.35-0.55

Table 3.8 Isomer shift values and their environments (Dyar 1985)

Spectra were measured using a Wissel ^{57}Fe Mössbauer spectrometer working at RT using a 25 mCi ^{57}Co source embedded in a Rh solid matrix. Powdered samples (< 75 μm sieve) were loaded into a copper holder with a perspex window and loaded into the spectrometer so that it vibrates normal to the γ source vibration direction. The gamma radiation passing through the sample to the counter is amplified and sent to the channel analyser. The next step involves combining the counts with values for the γ rays energy of the source at the moment of measurement. Finally, the obtained data was analysed with extended Voigt-based fitting (xVBF) analysis using the Recoil software package. All results were fitted by considering centre shift and quadrupole splitting values of investigated glasses from

the literature. Finally, crystalline phases identified by XRD (ICDD database) were also included in the analysis.

3.2.8 Viscosity measurements

Viscosity measurements were conducted on the P48, P19 and P0 type glasses with 25 wt% waste loading. Higher waste loadings (38 wt%) resulted in strong crystallisation and therefore risk of non-Newtonian behaviour of the glass melts. Six samples of glass frit (~ 85 g) were sent to Vitreous State Laboratory (Catholic University of America, Washington DC, USA) for measurements. The device used for examination was a Brookfield DV-III ultra-programmable rheometer. Crushed glass was put into a cylindrical alumina crucible, which then was placed into a furnace. During the controlled heating the glass frit was melted. Once the desired temperature was reached the rotating alumina spindle was lowered into a crucible and the viscosity (η) was evaluated by measuring the torque at the surface of the spindle (Q), necessary to maintain a fixed angular velocity (ω) as per:

$$\text{Shear stress} \quad \sigma = \eta \frac{V_{Spindle} - V_{Crucible}}{r_{Spindle} - r_{Crucible}} \equiv \eta \frac{\omega r_S}{r_S - r_C} \tag{3.4}$$

$$\text{Torque} \quad Q = \sigma * r_s * 2\pi r_s = \left(\eta \frac{\omega r_s}{r_S - r_C}\right) 2\pi {r_S}^2 \tag{3.5}$$

where: $V_{Spindle}$ – velocity of spindle, $V_{Crucible}$ – velocity of crucible, r_S – radius of spindle, r_C – radius of crucible

Torque measurements were taken at regular intervals as the glass melt stiffened throughout the controlled cooling cycle. When the viscosity rises, more torque is required to keep a given ω. The maximum torque the device can apply is circa 173 Nm. Whenever the torque reaches 90% of its maximum (Q_M) the spindle velocity is reduced by ω_I which changes between $\frac{\pi}{30}$ or $\frac{\pi}{60}$ rad^{-1}. A changeable angular speed increases the possibility of bringing non-Newtonian confounding variables into an experiment, but the viscometer cannot sample high η values otherwise. More precise details regarding methodology are given in **Table 3.9.** The error in the measurement is a function of torque and spindle diameter and is significantly larger at low η. Under the conditions used the random error does not exceed 2% of any recorded viscosity. The cooling rate to ambient temperature

was controlled to avoid probable damage of a crucible due to thermal stresses in the sample.

Property			**Values**
Starting T (K)			1488
Range (K)			1488-1173
Starting spindle velocity ω ($rads^{-1}$)			π
Spindle velocity increment ω_I ($rads^{-1}$)			$\pi/30$ or $\pi/60$
Max torque Q_M (Nm)			156
Crucible diameter r_C (m)			0.03
Spindle diameter r_S (m)			0.01
Measurement interval (s)			12
Total time (stages 2-7)			48520
Temperature profile			
Stage	**Process (K)**	**Heating rate (Ks^{-1})**	**Time (s)**
1	Anneal at 298	N/A	31200
2	Heat to 923	0.083	7500
3	Heat to 1373	0.050	11400
4	Anneal at 1373	N/A	600
5	Cool to 1173	-0.033	9450
6	Heat to 1273	0.083	1230
7	Cool to 298	-0.083	19600

Table 3.9 Parameters for viscosity measurements (operating software DilaSoft ver. 2.7)

4. CZ glass with MoO_3 and Na_2MoO_4

This chapter studies the incorporation behaviour of Mo into CZ base glass, where Mo was added as MoO_3 or Na_2MoO_4. Noting that alkali ions (Na) are preferentially charge compensated by MoO_4^{2-} compared to alkaline earth ions, this usually resulted in creation of soluble Na_2MoO_4 (Caurant et al. 2007). However, Komarneni & White (1981) showed that addition of Cs_2MoO_4 to Ca containing clays produced insoluble $CaMoO_4$. Thus, incorporation of Na_2MoO_4 (similar to Cs_2MoO_4) with extra CaO was studied to evaluate that mechanism. Furthermore Fe_2O_3 additions were made to test interaction between Na^+ and FeO_4^- ions and reduction of "free" Na, which in turn might decrease the formation of Na_2MoO_4 (Ciecińska et al. 2015, Cochain et al. 2012).

4.1 Results

4.1.1 Density

Figure 4.1 shows the dependence of density on waste loading for CZ4Mo, CZ6Mo and CZ8Mo type glasses. The density is lowest for CZ4Mo (2.476 g/cm^3) and it reaches the highest value for 8 wt% incorporation of MoO_3 for CZ8Mo (2.611 g/cm^3). For the second group containing Na_2MoO_4 (not shown in the Fig.4.1) - CZN type glass density increased with waste loading and reached maximum (2.765 g/cm^3) for CZ15NF where an additional 5 wt% of Fe_2O_3 was added.

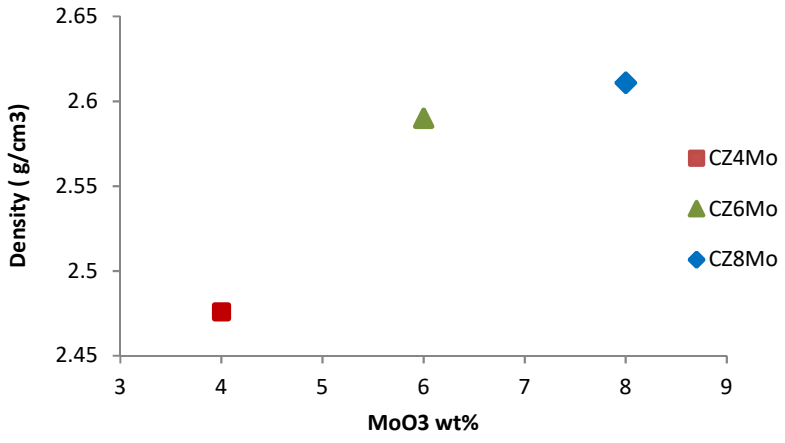

Figure 4.1 Density of CZ glass with MoO_3 incorporation

4.1.2 X-ray Diffraction

Figure 4.2 presents diffraction patterns for CZ and CZMo type glasses. Base CZ glass looks X-ray amorphous, but 4 wt% addition of MoO_3 produces peaks assigned to powellite (PDF 2015: 00-007-0212). The intensity of this crystalline phase increases with increasing incorporation of MoO_3. The physical appearance of CZ6Mo and CZ8Mo is completely white, unlike CZ4Mo which is transparent with whitish spots inside.

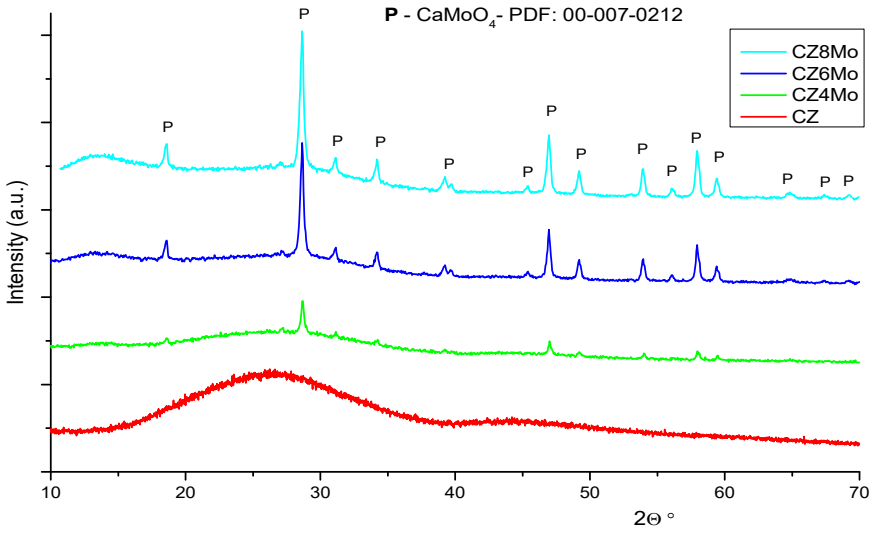

Figure 4.2 XRD patterns of CZ and CZMo type glasses

Figure 4.3 presents the XRD traces of CZN glasses. The CZ5N glass, with the lowest addition of Na_2MoO_4, remained crystal free. However, CZ15N glass shows strong peaks identified mainly as $CaMoO_4$ as a dominant phase (PDF 2015: 00-007-0212) plus Na_2MoO_4 and $NaMo_4O_6$. Interestingly, CZ15NF shows that addition of Fe_2O_3 reduces very strongly the formation of Na_2MoO_4 and to a lesser extent the formation of $CaMoO_4$. This crystalline transformation suggests that Fe oxide could be involved in a charge compensation mechanism that combines with 'free' Na^+ and makes it unavailable for Na_2MoO_4 production. It could also be observed that the intensity of the peaks for CZ15NF is much lower those of CZ15N, which suggests that charge compensation also involved Ca^{2+} ions.

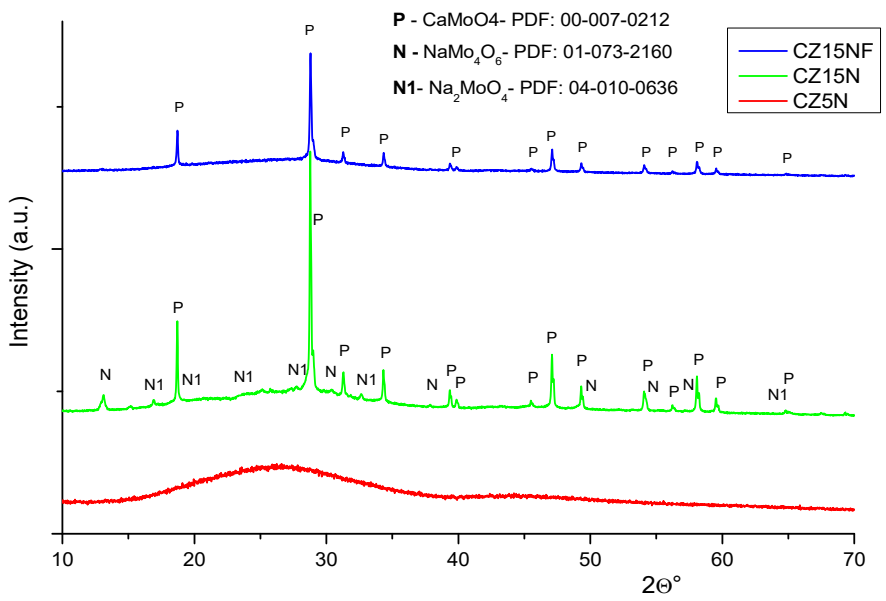

Figure 4.3 XRD patterns of CZN type glasses

4.1.3 DTA

Figure 4.4 presents DTA curves of CZN type glasses. The highest T_g and T_p values are observed for CZ5N being 505 and 598 ºC respectively. The base glass CZ shows comparable values of T_g and T_p at a level of 498 and 594 ºC although T_p peaks are difficult to observe. Interestingly CZ15N and CZ15NF glasses present lower values of T_g and T_p, where the lowest ones are for CZ15NF 488 and 584 °C respectively. Moreover, DTA curves from **Figure 4.4** show that T_g for CZMo type glasses decreased with increasing MoO_3 incorporation, but T_p slightly increased from 588 to 592 °C. Glass Forming Ability (GFA) in Table 4.1 can be defined as the temperature difference between T_p and T_g. The highest values of GFA was found for CZ and CZ5N (92 and 93 °C respectively). The CZ4Mo glass has a GFA value of 99 °C.

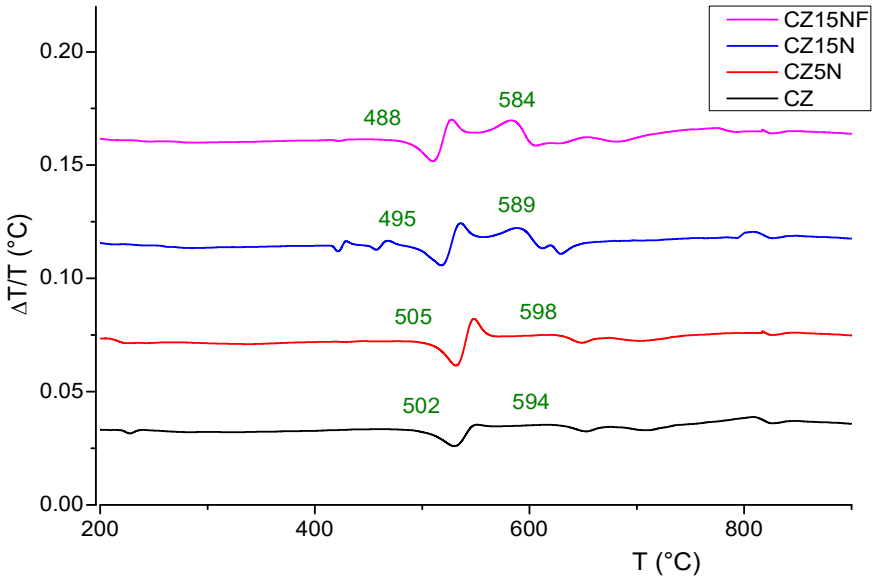

Figure 4.4 DTA curves of CZN glass series

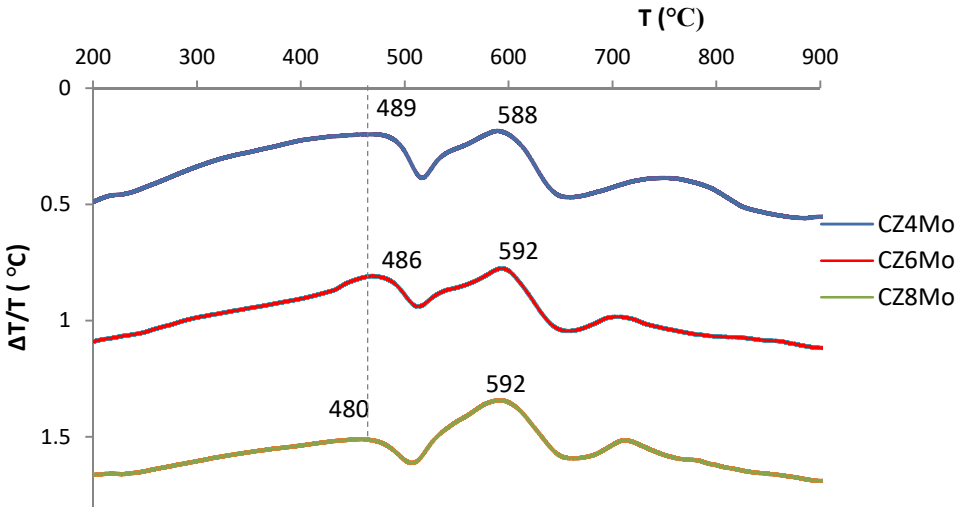

Figure 4.5 DTA curves of CZMo glass series

Glass	**ΔT= Tp - Tg**
CZ	92
CZ5N	93
CZ4Mo	**99**

Table 4.1 GFA of CZN and CZ4Mo type glasses

4.1.4 Raman spectroscopy

Figure 4.6 shows the Raman spectra obtained from CZN glasses. However, both glasses CZ15N and CZ15NF with 15 wt% incorporation of Na_2MoO_4 demonstrate sharp peaks related to Mo-O bonds associated with $CaMoO_4$ found by XRD (**Figure** 4.3). It is noticeable that greater peak intensities are observed for CZ15N than for CZ15NF, a similar observation was made for the XRD patterns. This lower peak intensity difference was suggested to be related to 5 wt% of Fe_2O_3 and charge compensation between Na^+ and FeO_4^- (Ciecińska et al. 2015, Cochain et al. 2012).

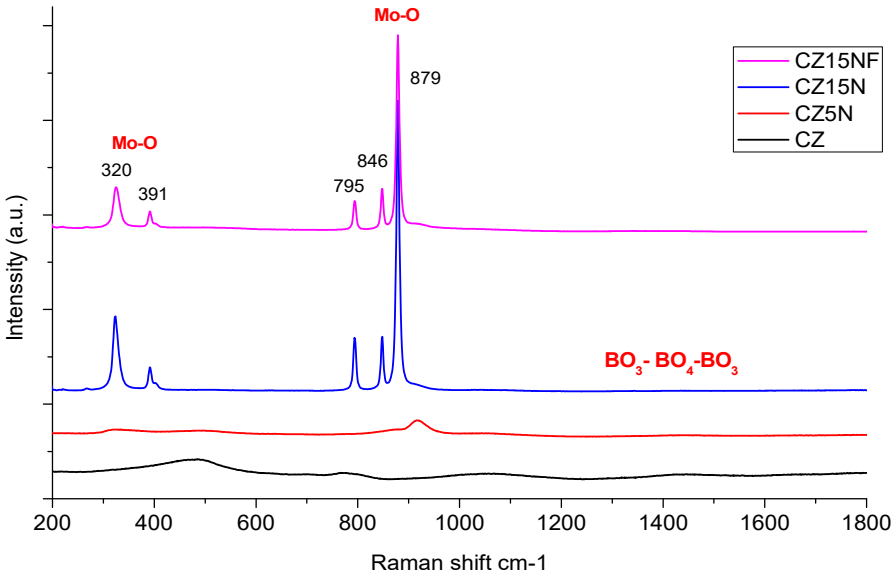

Figure 4.6 Raman spectra of CZN series

Raman spectra of CZMo glasses are shown in **Figure** 4.7. The incorporation of MoO_3 waste produced new peaks in the Raman spectra at 320, 390 cm^{-1}, and in the region from 793 to 879 cm^{-1}. The 320 and 390 cm^{-1} bands are a convolution of the symmetric and asymmetric bending vibration modes (υ_2 and υ_4) in MoO_4^{2-} tetrahedra while the bands from 793 to 879 cm^{-1} are the convolution of the symmetric and asymmetric stretching vibration modes (υ_1 and υ_3) in MoO_4^{2-} tetrahedra. The vibration modes of MoO_4^{2-} units are described in Saraiva et al. 2008 and Ozeki et al. 1987 for the crystals of alkaline and alkali earth molybdates. The sharp peak in **Figure** 4.7 shows crystalline nature of the final product, which corresponds well with the XRD results (**Figure** 4.2). The intensity of the peaks is the highest for 8 wt% waste loading. Therefore, vibration modes are likely to come from MoO_4^{2-} tetrahedra associated with Ca ($CaMoO_4$), which

also remains in a good agreement with powellite spectrum presented by Brinkman et al. (2013).

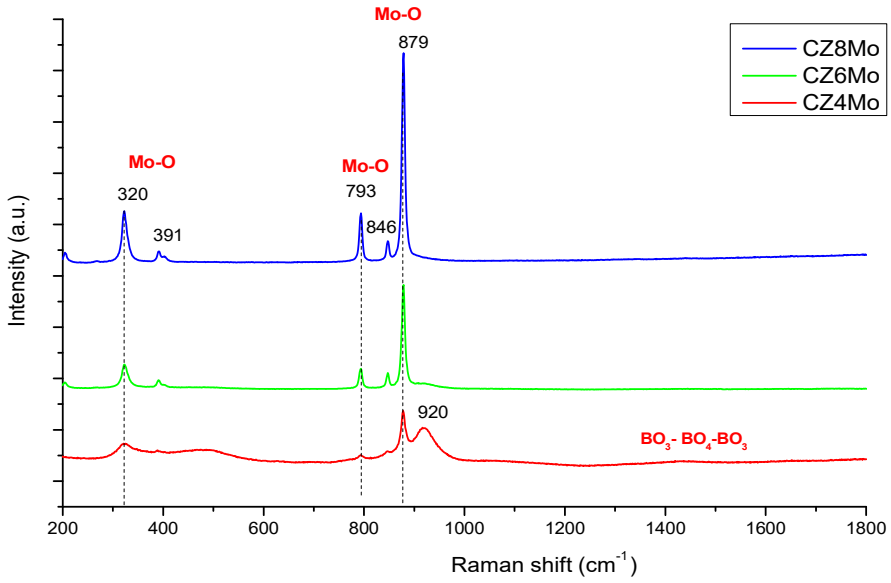

Figure 4.7 Raman spectra of CZMo series

4.1.5 SEM/EDX

Figure 4.8 illustrate BSE images of CZN glasses. The first image related to CZ5N glasses shows no crystals at a magnification of 1000, which corresponds well with XRD results (**Figure** 4.3). X-ray mapping of CZ15N (**Figure** 4.9) clearly establishes that spherical spots (crystals) are rich in Mo and Ca which agrees well with the XRD and Raman results. Thus, the white spots seen across the samples are considered to be $CaMoO_4$ for CZ15N and CZ15NF.

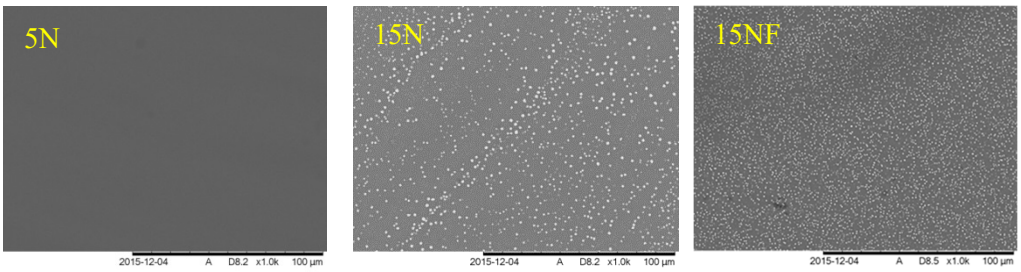

Figure 4.8 BSE images of CZN type glasses: a) CZ5N, b) CZ15N and c) CZ15NF

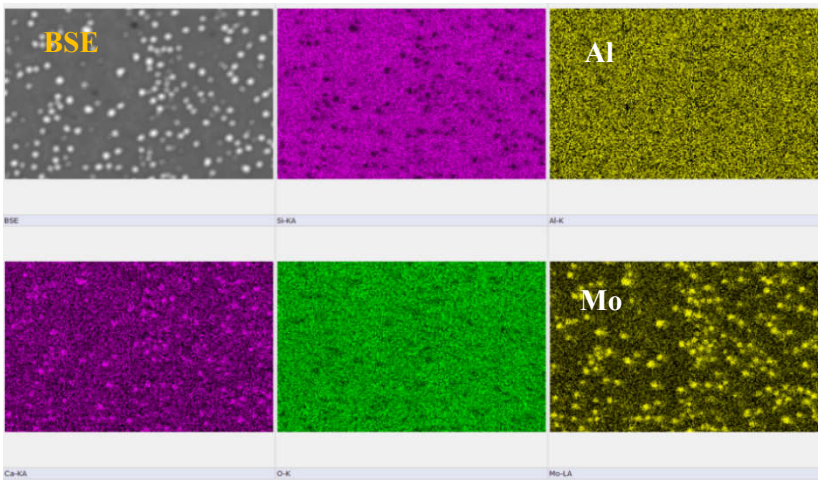

Figure 4.9 X-ray mapping of CZ15N (Mag. 2k)

The second group of glasses is CZMo shown in **Figure** 4.10. It can be seen even at low magnification (x100) CZ4Mo is phase separated. That phase separation is due to Mo incorporation that is visible in the **Figure** 4.12. Interestingly, the image of CZ6Mo glass does not confirm any crystals although XRD clearly indicates the partially crystalline nature of that sample (**Figure** 4.2). It appears that crystals are much smaller and cannot be seen at a magnification of 1000. Tiny spherical white spots distributed across the sample demonstrate crystalline morphology of CZ8Mo. Finally, X-ray mapping confirms the presence of Ca and Mo inside the crystals (**Figure** 4.11).

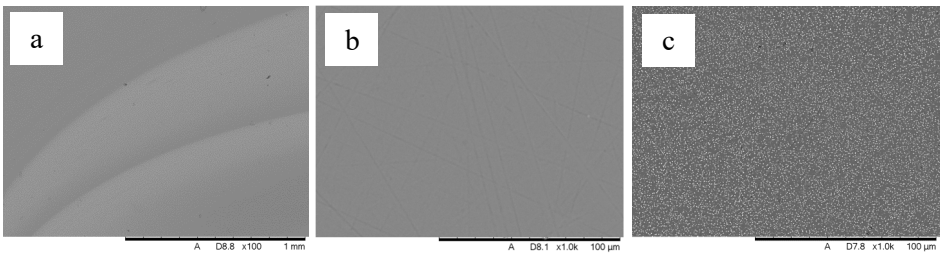

Figure 4.10 BSE images of CZMo type glasses: a) CZ4Mo, b) CZ6Mo and c) CZ8Mo

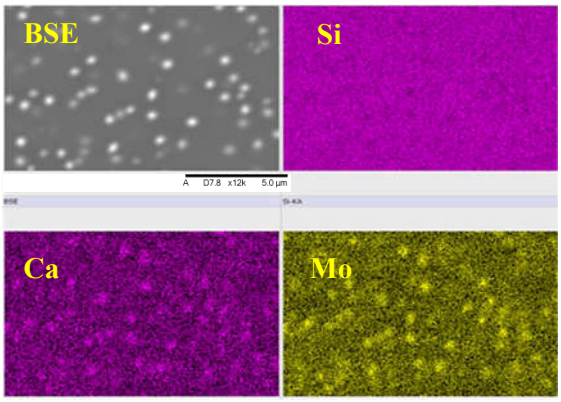

Figure 4.11 X-ray mapping of CZ8Mo (Mag. 12k)

Figure 4.12 X-ray mapping of CZ4Mo

4.2 Discussion

4.2.1 Effects of Na_2MoO_4 and MoO_3 incorporation on CZ glass structure and properties

Density

Incorporation of MoO_3 and Na_2MoO_4 into CZ glass has influenced the density of the newly formed glasses. The density of CZN type glasses increases with greater incorporation of Na_2MoO_4 and reaches its maximum for CZ15NF which also includes 5 wt% of Fe_2O_3. The higher density of CZMo type glasses arises from higher mass of incorporated oxides. **Figure** 4.1 demonstrates that increasing MoO_3 content resulted in higher values of density where CZ8Mo is the most dense (2.611 g/cm^3).

T_g and T_p

As presented in **Figure** 4.4 T_g in CZ base glass is 498 °C. However, in CZN type glasses which were modified by CaO, Na_2MoO_4 and Fe_2O_3 (CZ15NF) is reduced from 505 to 488 °C. Changes in T_g are affected by many factors such as samples are usually crystallised which means that incorporation of Na, Ca and Fe oxides as glass modifiers results in NBOs production, which in turn decrease T_g values (Volf 1984). Secondly, CZMo glasses are modified by MoO_3 only (**Figure** 4.5). It can be seen that Tg values are decreasing with increasing amount of MoO_3 where the lowest value is for CZ8Mo (480 °C). The effect of MoO_3 on T_g has been studied in nuclear waste borosilicate glasses by Courant et al. (2007), who observed that its incorporation resulted in T_g reduction in examined samples, claiming that increased size of depolymerised domains (rich in network-modifying cations) caused by the position of MoO_4^{2-} ions, which counteracts the higher connectivity of the glassy network. Another possibility is that network-modifying cations are related to both NBOs and MoO_4^{2-} ions at the same time. Nevertheless, the created large molybdate clusters are in the network, where the neighbouring oxygens remain as NBOs with some association with modifying cations. In that case, connectivity related to silicate network is similar and therefore the energy necessary to relax the structure on heating is reduced due to easily disassociation of NBOs with modifiers. These two explanations rely on varied connectivity results, nevertheless, strong overlapping of molybdate bands with silicate bands in Raman spectroscopy means that the deconvolution of the Raman spectra is not feasible. Therefore, identification of Q_n units is not possible; in order to explain fully the reduction of T_g further examination is necessary e.g. ^{29}Si NMR.

Figure 4.4 shows that T_p is not affected strongly by the addition of Na_2MoO_4 to the CZ base glass (598 °C). The lowest T_p value was obtained for CZ15NF (584 °C), with the extra addition of Fe_2O_3. Based on XRD (**Figure** 4.3) this exothermic peak can be related to $CaMoO_4$. Furthermore, **Figure** 4.5 demonstrates that crystallisation peak for all CZMo type glasses has a similar value from 588 to 592 °C with a measurement error ±5°C. The GFA values (**Table** 4.1) indicate that CZ5N and CZ base glasses have practically the same glass forming ability (~ 93 °C), but in the second family of glasses, CZ4Mo (the most glassy) has $T_p - T_g$ value of 99 °C. It appears that incorporation of Na_2MoO_4 and MoO_3 did not affect T_g and T_p values to a great extent in the examined samples.

Raman spectroscopy

The introduction of Na_2MoO_4 into CZ glass resulted in prominent changes in the Raman spectra (**Figure** 4.6). In the case of CZ5N a small band is formed with centre at 920 cm^{-1} compared to CZ base glass, which did not have that band. However, the most significant changes occurred for CZ15N and CZ15NF glasses where $CaMoO_4$ peaks were identified. The intensity of CZ15NF is observable lower than CZ15N which correspond well with XRD data (Figure 4.3) which showed that the incorporation of Fe_2O_3 strongly suppressed crystallisation especially with respect to sodium molybdate and (lesser extent to powellite). Assuming that Al^{3+} is structurally comparable to Fe^{3+} in silicate glasses (Cassingham et al. 2008), it is possible that FeO_4^- units have a similar effect on charge compensation behaviour to AlO_4^- units. Although as stated by Quintas et al. (2008) AlO_4^- ions are favourably compensated by alkali ions but alkaline earth ions such as Ca^{2+} are also present. Cochain et al. (2012) states that FeO_4^- units are preferentially charge compensated by Na ions instead of BO_4^- units.

In the case of CZMo glasses (**Figure** 4.7) 4 wt% incorporation results in peaks assigned to $CaMoO_4$ plus one extra peak around 920 cm^{-1} which can be associated with Q_1 units (Gaussian band centred around 910 cm^{-1}, see p. 35, Manara et al. 2009). This agrees with the suggestion of Caurant et al. (2007) that Mo is involved in producing depolymerised clusters with Na_2O being a network modifier.

SEM/EDX

SEM analysis of CZ5N glasses shows they are homogeneous; they are also X-ray amorphous. CZ15N and CZ15NF clearly contain droplet-like tiny crystals well distributed across the sample. EDX confirms that the crystals contain Mo and Ca, which corresponds well with XRD and Raman outcomes. The size of those crystals is well below 1μm. On the other hand, the SEM of CZ4Mo shows phase separation (layers) enriched in Mo (**Figure** 4.10). Interestingly, CZ6Mo although it produced crystalline XRD peaks indicative of powellite appears to be homogeneous at 1k magnification indicating that the crystals are very tiny. The image of CZ8Mo is full of tiny white spots indicating the presence of well-distributed powellite crystals.

4.3 Conclusions

The incorporation of water-soluble Na_2MoO_4 into borosilicate glass showed that it can be converted into $CaMoO_4$. This conversion is further enhanced with extra addition of Fe_2O_3 and CaO. Industrially, it is important to modify the waste glass compositions to avoid or minimise the formation of unwanted phases such as Na_2MoO_4.

Based on the results and discussion related to the incorporation of molybdates into CZ glass the following conclusions can be made:

- Addition of Mo compounds into CZ glass increases the density of the newly formed waste glass due to the higher density of Mo containing compounds than the base glass
- A general decrease in T_g is observable for CZMo and CZN type glasses, but the latter ones are modified by extra CaO and/or Fe_2O_3. However, a decreasing trend in T_p is noticeable for CZN glasses, but in case of CZMo T_p values remain at a similar level.
- XRD results show $CaMoO_4$ is present and increases with increasing MoO_3 loading. CZN glasses produce Na_2MoO_4 with $CaMoO_4$, but after incorporation of Fe_2O_3, only calcium molybdate is present, which is believed to be due to a charge compensation mechanism (Na^+ and FeO_4^-).
- Peaks in the Raman spectra are assigned to $CaMoO_4$ only for both types of glass.

5. CZ and MZ type glasses with POCO simulant

This chapter investigates incorporation of lab made POCO simulant into CZMF and MZMF glasses. The simulant was incorporated at a level of 15, 20 and 25 wt%. Additionally, some glasses have been enriched in Fe_2O_3 and Mn_2O_3 to increase the fluidity of the melt and to improve chemical durability of the waste glasses (Volf 1984, Cassingham et al. 2008). As before addition of Fe was intended to reduce the amount of so called "free" Na to reduce the formation of soluble sodium molybdate (Ciecińska et al. 2015). Table 3.2 shows compositional similarities between CZ and MZ type glasses where CaO was replaced by MgO on molar basis.

5.1 Results

5.1.1 Density

Incorporation of POCO waste simulant into base glasses increases the density of CZMF and MZMF glasses in a monotonic manner (**Figure** 5.1). It can be seen that CZMF glasses possess a slightly higher density than the MZMF glasses. This can be attributed to the fact that CaO has higher molar mass (~ 56 g/mol) than MgO (~ 40 g/mol). Both density curves look similar and are otherwise parallel to each other due to compositional similarities (See page 52, Table 3.2).

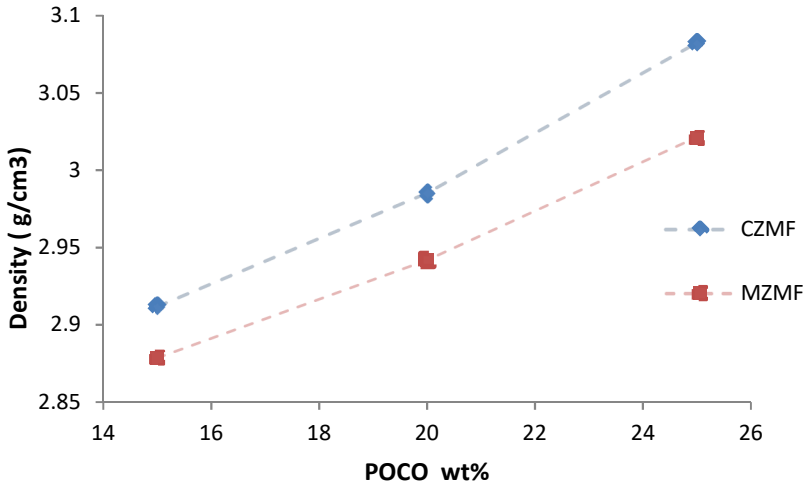

Figure 5.1 Density of CZMF and MZMF glasses with POCO waste; error bars ±0.03 g/cm^3

5.1.2 XRD

Figure 5.2 shows XRD patterns of CZMF type glasses. It can be seen that incorporation of POCO waste into CZ glasses results in crystal formation. The lowest POCO incorporation (15 wt%) looks almost X-ray amorphous with a broad peak centred around 28 2Θ°. However, clear diffraction patterns are characteristic for 20 and 25 wt% POCO loading. Identified phases are $CaMoO_4$, $BaMoO_4$, $ZrSiO_4$ and ZrO_2. The presence of molybdate crystals is due to a reaction between of Ca (glass) and Ba (waste) with MoO_3 rich POCO simulant. ZrO_2 is the third most abundant component in POCO waste, so $ZrSiO_4$ is a product of the reaction between silica from the CZ frit with ZrO_2. Finally, zirconia crystals appear to be precipitated from the glass melt; BSE images (Fig. 5.8) show Zr rich crystals with sharp edges suggesting that they were newly formed, rather than partly dissolved by the melt.

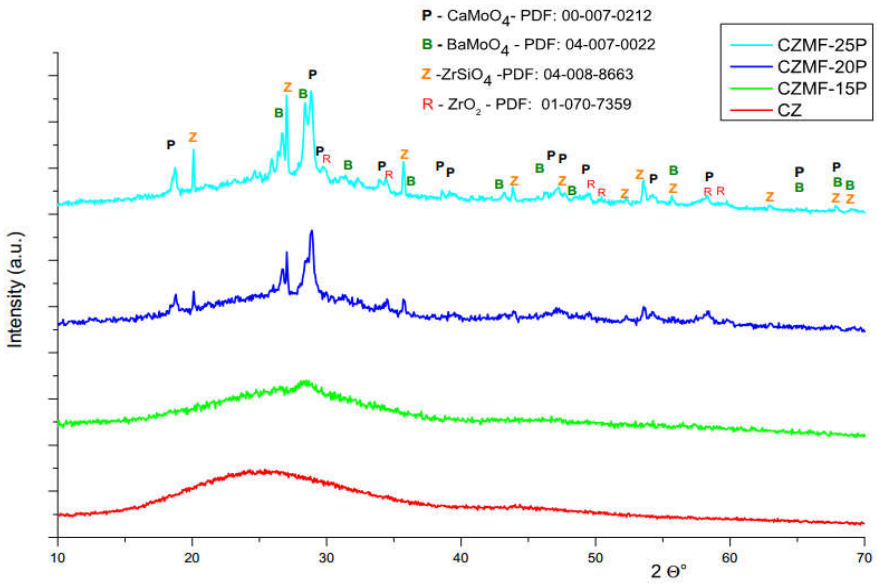

Figure 5.2 XRD of CZMF type glasses

Figure 5.3 shows XRD patterns of MZMF type glasses. It can be noticed that MZ and MZMF-15P look X-ray amorphous. The latter one contains one broad and short peak centred around 26.85 2Θ°. Nevertheless, clear diffraction patterns can be ascribed for 20 and 25 wt% of POCO waste similar to CZMF glasses. However, crystallisation that had occurred in MZ glass system formed different crystals. Identified crystal phases are $BaMoO_4$, $ZrSiO_4$, ZrO_2 and SiO_2 (low quartz). The formation of aforementioned phases is mainly a consequence of reaction between the MZ glass and POCO waste.

The presence of SiO_2 crystals might be associated with reaching solubility limits of silica in phase separated glass. Finally, the peak around 22 ° was unidentified.

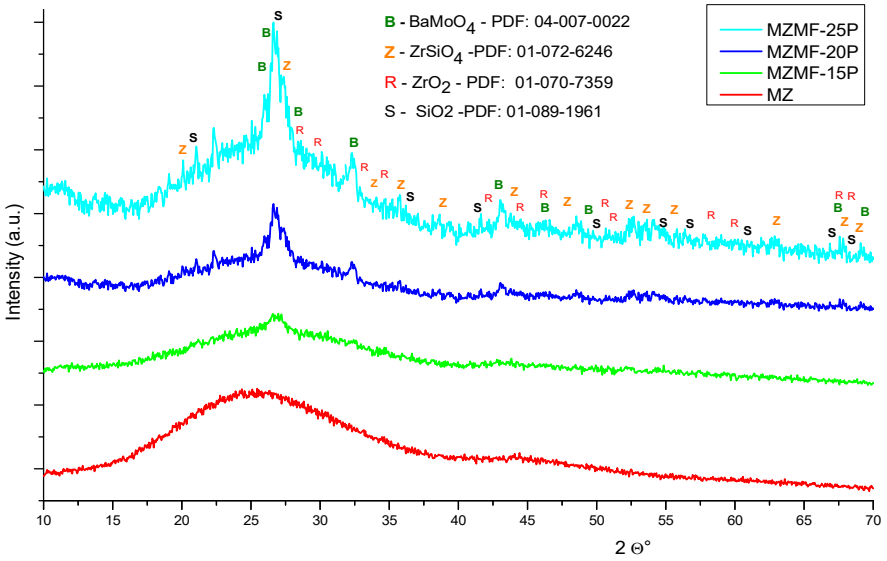

Figure 5.3 XRD of MZMF type glasses

5.1.3 DTA

Figure 5.4 shows the DTA traces of CZMF glasses. Incorporation of POCO waste generally resulted in a decrease of T_g and T_p values as compared CZ base glass. The lowest values of T_g and T_p are for CZMF-25P 473 and 554 °C respectively. On the other hand, **Figure** 5.5 shows a less clear pattern of T_g and T_p values. Actually, T_g and T_p values are greater for MZMF-15P and MZMF-20P than in MZ glass, however, MZMF-25P glass shows the lowest values of all the glasses examined, suggesting that this glass will crystallise most readily. The T_p value for MZMF-20P is totally different than expected (685 °C) and the area between 560 - 610 °C (expected peak) is a featureless plateau. Table 5.1 shows GFA values given as T_p - T_g values for the given glasses. Little change in values is observed.

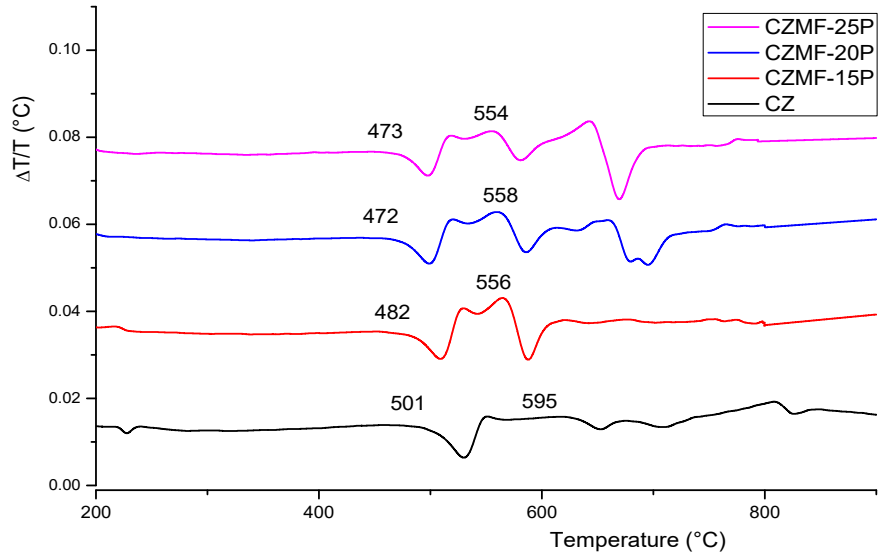

Figure 5.4 DTA of CZMF type glasses

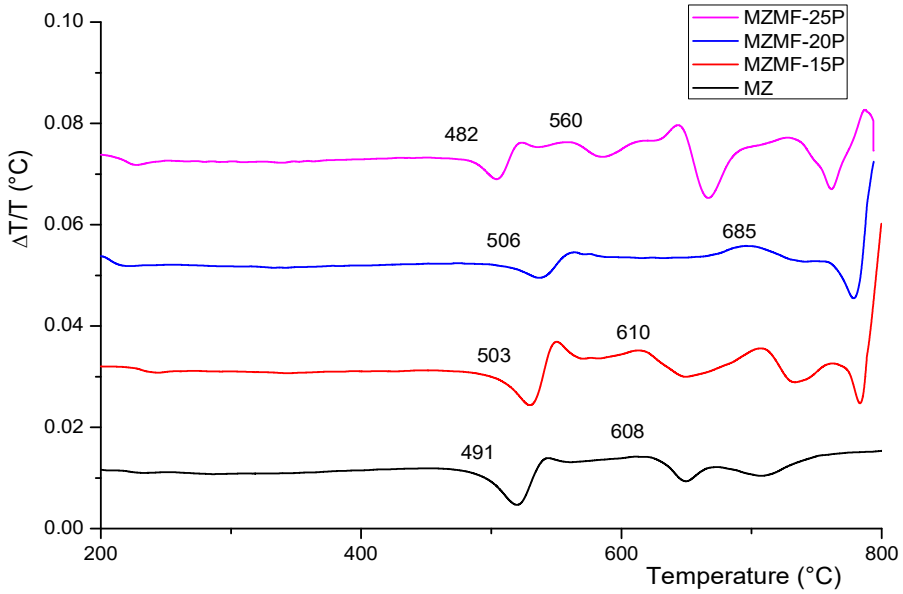

Figure 5.5 DTA of MZMF type glasses

Glass	ΔT= Tp - Tg
CZ	37
CZMF-15P	37
MZ	43
MZMF-15P	36

Table 5.1 GFA obtained from DTA traces for CZMF and MZMF glasses

5.1.4 Raman Spectroscopy

Figure 5.6 illustrates Raman spectra of CZMF glasses. The incorporation of POCO changed the structure of CZ base glass which is demonstrated in Raman spectra by the formation of new bands at 320, 390 cm^{-1}, and in the region from 793 to 920 cm^{-1}. Those 320 and 390 cm^{-1} bands are a convolution of the symmetric and asymmetric bending vibration modes (υ_2 and υ_4) in MoO_4^{2-} tetrahedra while the bands from 793 to 920 cm^{-1} are the convolution of the symmetric and asymmetric stretching vibration modes (υ_1 and υ_3) in MoO_4^{2-} tetrahedra. The vibration modes of MoO_4^{2-} units are described in Saraiva et al. 2008 and Ozeki et al. 1987 for the crystals of alkaline and alkali earth molybdates. In amorphous materials with variable local environments many bonds overlap each other and make it difficult to obtain separate bands for specific molybdate crystals. Multiple peaks present from 793 to 920 cm^{-1} make the description of these peaks difficult due to the variety of molybdates that may have vibrational frequencies in that area plus a complex glass composition. The intensity of the peaks is the highest for 25 wt% of waste loading which is the richest in MoO_3. XRD (**Figure** 5.2) and Raman both point to the presence of Ca and Ba molybdates.

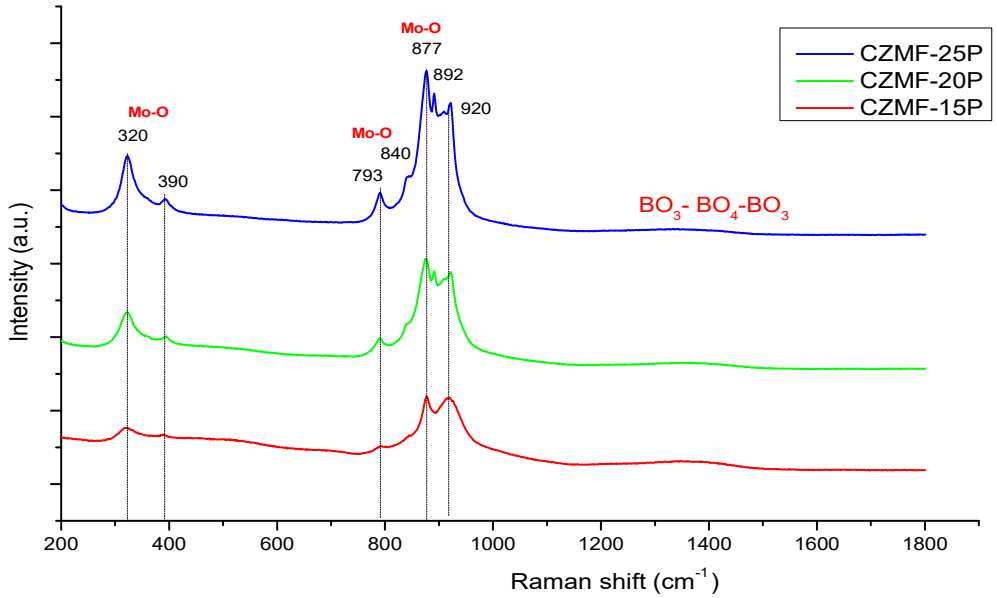

Figure 5.6 Raman spectra of CZMF type glasses

Figure 5.7 shows Raman spectra of MZMF glasses. The incorporation of POCO changed the structure of MZ base glass which is demonstrated in Raman spectra by the formation of new bands at 320 cm^{-1}, and in the region from about 789 to 925 cm^{-1}. The band at 390 cm^{-1} is not detected which is due to a lack of Ca (Brinkman et al. 2013). Chouard et al. (2011) observed that stretching vibration band typical for Mo-O bonds with a calcium is shifted from around 880 cm^{-1} (crystalline $CaMoO_4$) to around 919 cm^{-1} (in aluminoborosilicate glass). It appears that a strong interaction between Ca^{2+} and silicate glass is caused by the strong field strength of Ca ions. Therefore, the interaction of the Ca^{2+} ions with MoO_4^{2-} units might be noticeably weakened compared to that in crystalline $CaMoO_4$ and thus the MoO_4^{2-} stretching frequency is higher (Mo-O bond is strengthened) and shifts from 880 (powellite) to ~ 919 cm^{-1} for the glass. It is believed that that similar shift in stretching frequency occurred for $BaMoO_4$ identified in Figure 5.7, from 892 cm^{-1} to ~ 925 cm^{-1} (in glasses) (Brinkman et al. 2013). It seems logical to assume that Ba present in these compositions works mainly as a charge compensator of MoO_4^{2-} units, which resulted in a formation of 925 cm^{-1} peak, but a role for Mg as a charge compensation cannot be totally excluded.

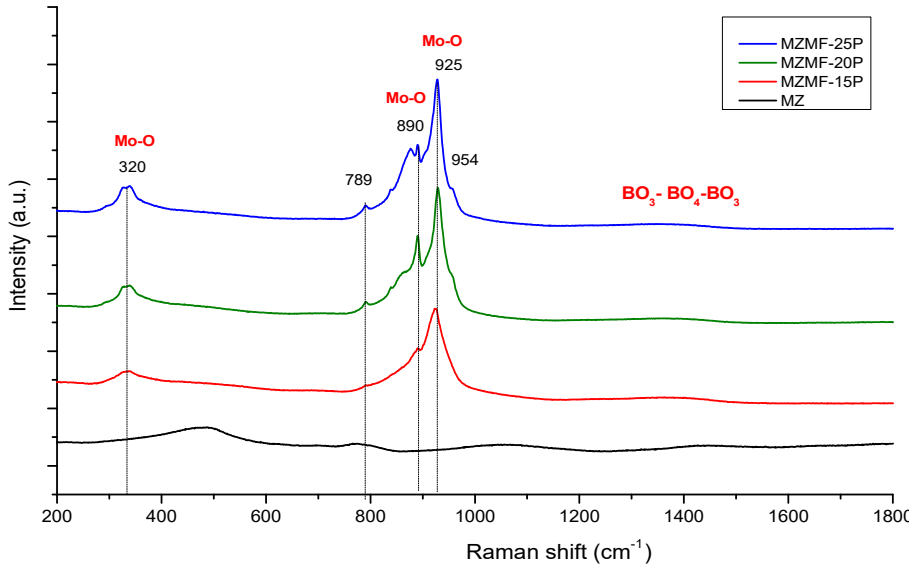

Figure 5.7 Raman spectra of MZMF type glasses

5.1.5 SEM

Figure 5.8 presents BSE images of CZMF glasses. The incorporation of 15 wt% of POCO waste did not produce any visible crystals, but 20 and 25 wt% of POCO waste resulted in crystal formation. **Figure** 5.9 with high magnification (15k) shows that these crystals are rich in Zr and Si (bigger grains) and Mo, Ca and Ba (small spherical spots). These X-ray maps agree with the XRD results presented above (**Figure** 5.2).

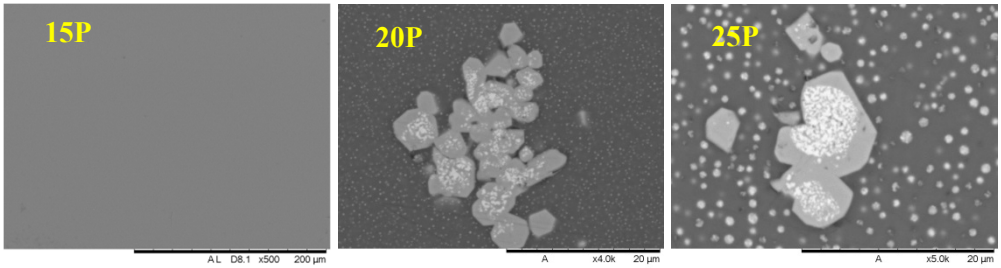

Figure 5.8 BSE imaging of CZMF type glasses

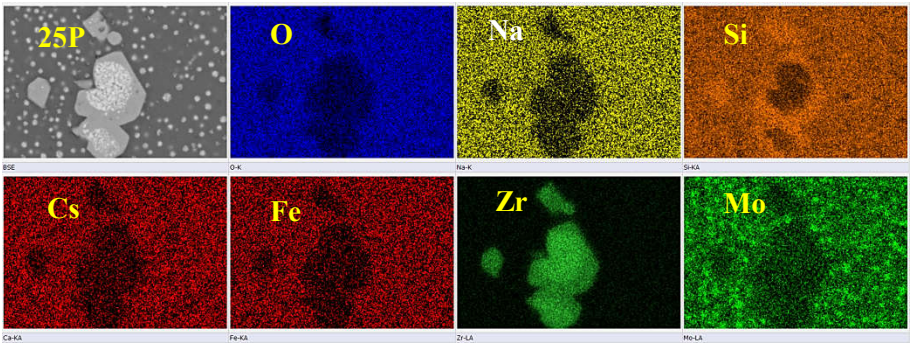

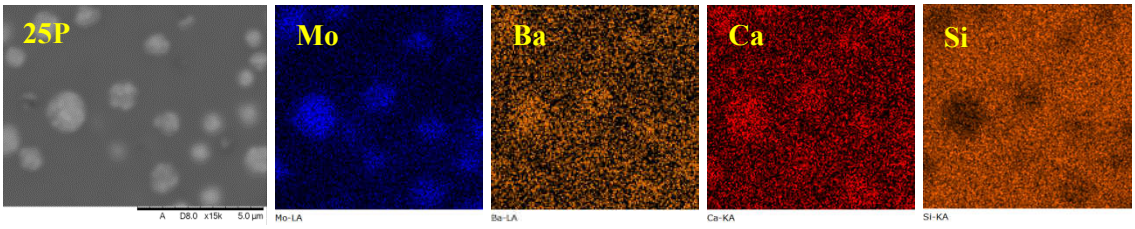

Figure 5.9 X-ray mapping of CZMF type glasses

Figure 5.10 shows BSE images of MZMF glasses. MZMF-15P contains some crystals rich in Zr, but the rest of the glassy matrix seems to be homogeneous. Further incorporation of POCO waste at 20 and 25 wt% produces samples with much greater crystallinity. **Figure** 5.11 demonstrate that MZMF-20P contains crystals containing Zr and Si plus tiny spots that cannot be identified in this sample. Higher magnification with respect to greater POCO incorporation (MZMF-25P) makes it feasible to identify the composition of small spherical crystals. They are rich in Mo, Ba and some Mn.

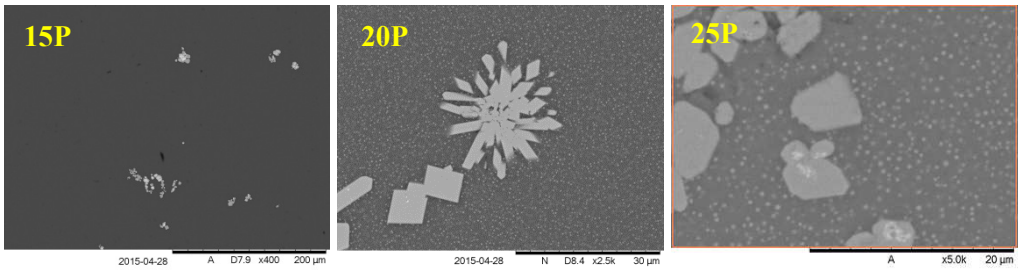

Figure 5.10 BSE imaging of MZMF type glasses

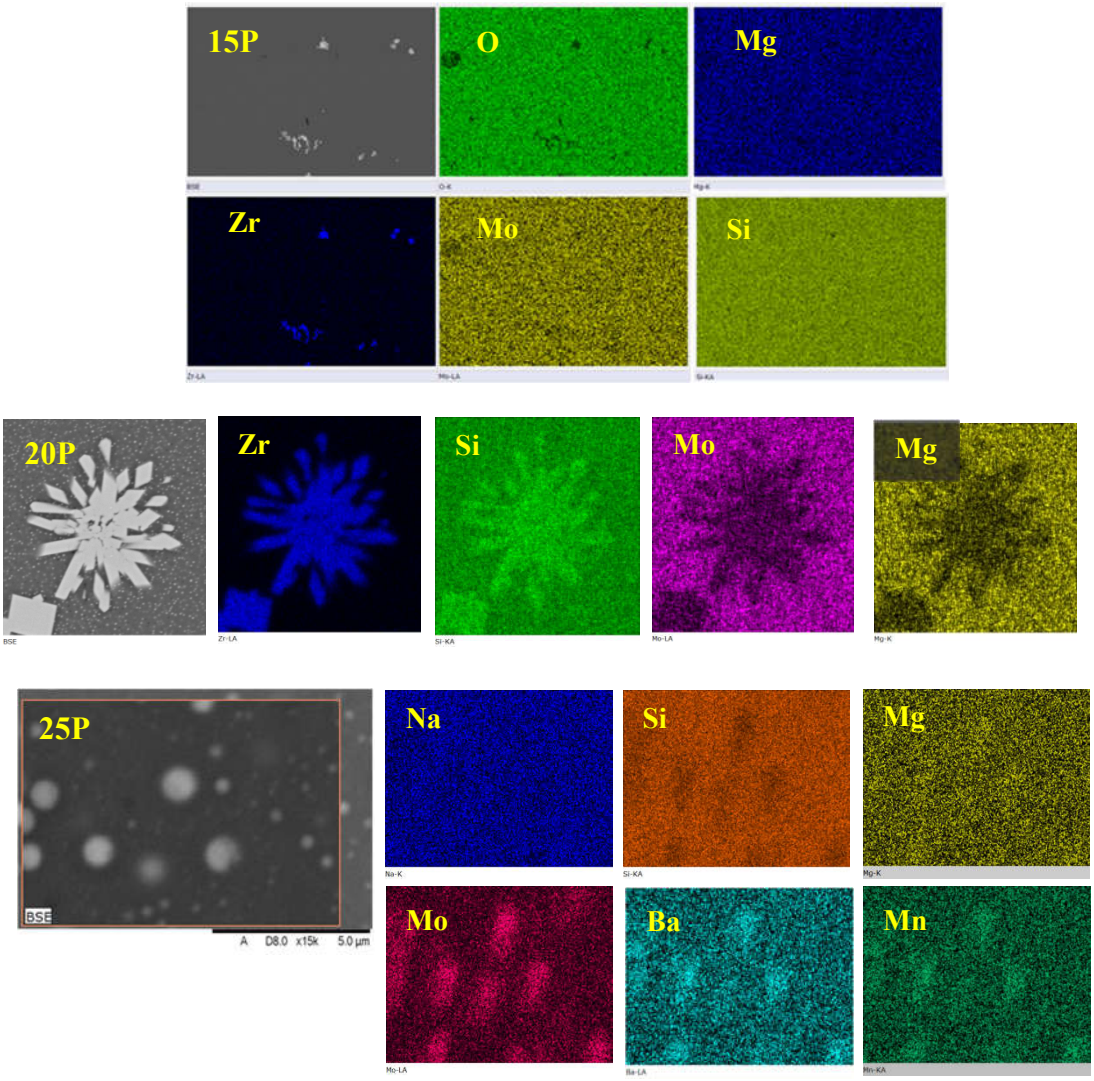

Figure 5.11 X-ray mapping of MZMF type glasses

5.1.6 Durability testing

Figure 5.12 shows normalised mass loss of CZMF-25P and MZMF-25P samples after 7 and 28 days PCT. Samples with 25 wt% of POCO have been chosen as the most representative of those with the higher waste incorporation. The NL values of MZMF-25P (7 and 28 days) are much higher than those of CZMF-25P. This means that durability of the latter glass is greater. Focusing on elements with the highest NL values it can be said that Al leaching is greater for MZMF type glass after 7 and 28 days than for CZMF type glass and reaches 1.2 and 1.9 g/m^2 respectively. Conversely, NL values for Al for CZMF type glass are around 0.2 g/m^2. The leaching of B is also much higher for MZMF type glass (4.3 g/m^2) than for CZMF (1.9 g/m^2) glass after 7 days. Leaching of B after 28 days is about 2.7 higher for MZMF glass too. Leaching of Li after 7 days is almost three times greater (2.9) for MZMF type glass and 2.4 times greater after 28 days. Even more dramatic is the difference observed for Mo leaching after 7 days, being about 7 times more for MZMF glass and about 6.2 times more after 28 days. Na is another element that leached in substantial quantities. In this case, MZMF is also less durable than CZMF glass and Na release was 3.6 and 4.8 greater after 7 and 28 days, respectively. Other elements investigated here present much lower NL values, significantly below 1 g/m^2 after 7 and 28 day tests.

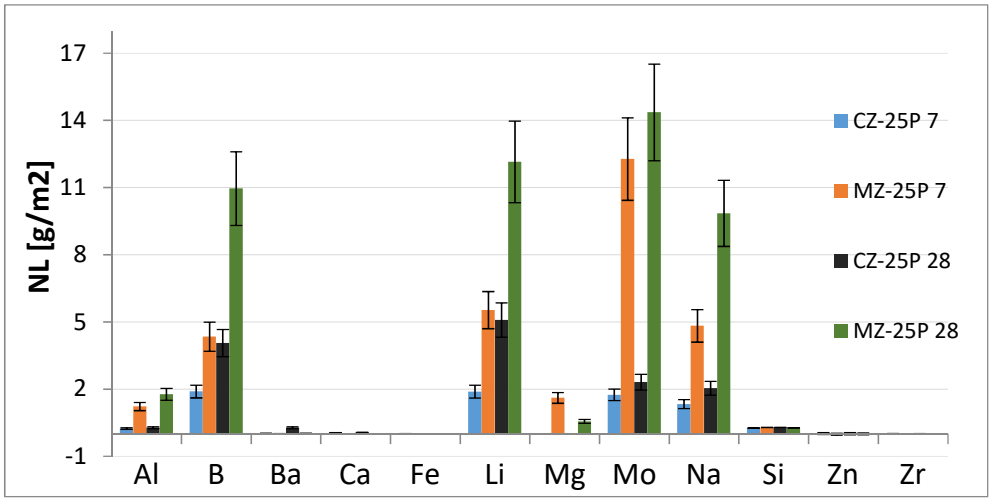

Figure 5.12 Normalised mass loss (NL) of CZMF and MZMF glasses after 7 and 28 days

Figure 5.13 shows elemental composition of powdered CZMF-20P glass after 28 day test. It can be observed that the glass grains mainly contain Ba, Mo and O, which are not the major components of the glass. This result suggests that possible precipitation

of $BaMoO_4$ occurred from the solution and this would explain the elemental composition of the formed coating. The XRD results also (Fig. 5.2) confirm the presence of $BaMoO_4$ in the examined glass.

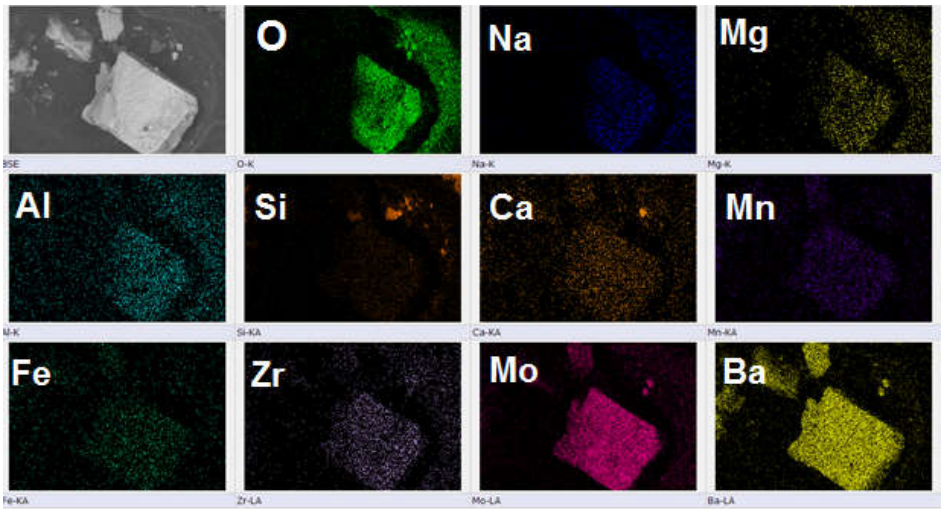

Figure 5.13 X-ray map of CZMF-20P 28 after PCT

5.2 Discussion

5.2.1 Effect of POCO incorporation into CZMF and MZMF glasses

Density

Incorporation of POCO simulant into CZMF and MZMF glasses resulted in a density increase (**Figure** 5.1). The three main components of POCO simulant (BaO – 5.72 g/cm^3, ZrO_2 – 5.68 g/cm^3 and MoO_3 – 4.69 g/cm^3), are denser than the main components in both glasses such as SiO_2 or B_2O_3, 2.65 and 2.46 g/cm^3 (Perry 2011). In both cases, the largest densities are for glasses with 25 wt% POCO loading which is 3.082 g/cm^3 (CZMF-25P) and 3.021 g/cm^3 (MZMF-25).

T_g and T_p

As presented in **Figure** 5.4 T_g and T_p values have changed after incorporation of POCO simulant with Fe and Mn oxides when compared to CZ base glass. The general tendency is that T_g decreases with higher POCO loading whereas T_p is little changed being 556 °C for CZMF-15P and 554 °C for CZMF-25P, but is still lower than that for CZ glass (595 °C). **Figure** 5.5 shows DTA curves of MZMF glasses. Incorporation of POCO with Fe and Mn oxides initially increases T_g from 491 (MZ) to 503 and 506 °C (MZMF-15P and MZMF-20P). T_g of MZMF-25P is reduced to 482 °C which indicates that this glass was most strongly affected by crystal formation. Crystal phases found in this glass (Figure 5.3) are $ZrSiO_4$ and SiO_2, which remove ZrO_2 and SiO_2 from the glassy matrix, resulting in lower T_g (Volf 1984).

Moreover, T_p values slightly increase for MZMF-15 and 20P (610 and 685 °C) compared to those for the MZ glass (608 °C), but T_p of MZMF-25P decreased to 560 °C. The XRD and EDX results show that CZMF-20 and 25P plus MZMF-20 and 25P glasses are rich in ZrO_2 and $ZrSiO_4$ which means that these elements were removed from the glass melt throughout crystallisation. It seems to be logical that decreasing content of Si and Zr resulted in lower T_g values in the remaining glass (Volf 1984 and Vogel 1994).

Raman spectroscopy

Figure 5.6 shows Raman spectra of MZMF glasses. Incorporation of POCO produced main bands at 320, 390 and 793 to 920 cm^{-1}. These bands are formed by MoO_4^{2-} units associated with Ca and Ba, which means that molybdate tetrahedra are charge compensated by these elements. Based on Brinkman et al. (2013) the peak positions of Ca and Ba are very similar in the glass and could not be distinguished. In a crystalline form $CaMoO_4$ peaks should be around 879 cm^{-1} however in the aluminoborosilicate glass it was spotted around 919 cm^{-1} due to a strong ionic interaction of Ca^{2+} (high field strength) with the silicate network. Moreover, Ca^{2+} ions are expected to bond to at least two NBOs and likely more by sharing NBOs. That is why the interaction between Ca^{2+} and MoO_4^{2-} units may be much weaker in the silicate glass compared to crystalline powellite and MoO_4^{2-} stretching frequency is higher in glass (Chouard et al. 2011). Furthermore, Caurant et al. (2010) state that the frequency of the symmetric stretching vibration for Mo-O in molybdate tetrahedra related to Ca could be shifted even to 922 cm^{-1} in borosilicate glass. In the case of crystalline $BaMoO_4$ the highest internal MoO_4 vibrations are assigned to 892 cm^{-1} (Brinkman et al. 2013). These considerations suggest that a similar phenomenon might happen regarding $BaMoO_4$. That is why the broad peak from 877 to 920 cm^{-1} might be due to a Ba contribution to charge compensation of molybdate units as well. Finally, XRD analysis (**Figure** 5.2) identified both Ca and Ba molybdates. **Figure** 5.7 describes Raman spectra related to MZMF glasses. In comparison to the previous section, Ca is not available here. Although, there is great similarity towards the previous Raman spectra the 390 cm^{-1} band is missing. The bands from 790 to 925 cm^{-1} possess one dominant peak at 925 cm^{-1}. The intensity of this peak increases with POCO waste loading due to a greater amount of BaO and MoO_3. However, the fact that MgO was introduced into a system (the highest field strength between alkaline earth) needs considering, even though XRD analysis did not detect any $MgMoO_4$ (Vogel 1984). Nevertheless, **Figure** 5.11 with X-ray maps shows that $BaMoO_4$ crystals contain some Mn and Mg. Molybdates are well-known for chemical flexibility and they can accommodate other elements including also trivalent cations (Caurant et al. 2007; Brinkman et al. 2013).

PCT

Figure 5.12 present normalised mass loss of two type of glasses examined for 7 and 28 days. It can be said that durability of CZMF-25P is much better than MZMF-25P due to the lower values of NL. The highest mass loss is related to MZMF-25P after 7 and 28 days for main elements in the following order Mo>Li>B>Na. High values of Mo in the solution (~ 14 g/m^2) plus mobile alkalis suggest that soluble molybdates could have formed on cooling, although they were not identified by XRD. On the other hand, Mo mass loss of CZMF-25P glass is around 6 times smaller after 28 days compared to MZMF-25P, suggesting that Mo was incorporated into an insoluble form such as $CaMoO_4$ or $BaMoO_4$. Furthermore, low NL values for Ca and Ba plus XRD results clearly indicate that those ions are well-contained in the samples, as insoluble molybdates. **Figure** 5.13 shows X-ray maps of glass grains after PCT test (CZMF20P); the strongest signals come from Ba, Mo and O, which indicate that $BaMoO_4$ precipitated from the solution and covered sporadically some grains from powdered sample. This agrees with low solubility values of $BaMoO_4$ in an aqueous environment (< 0.05 g/L). Low release values of Fe could be associated with iron's role as charge compensator (FeO_4^- units, Ciecińska et al. 2015) and its positive effect on chemical durability that was reported by some authors (Cassingham et al. 2008; Volf 1984). Additionally, Fe ions in small amounts might work as a glass former in borosilicate glasses and thus is not easily removable from the glass into solution (Volf 1984).

Finally, the only difference between these glasses was the use MgO instead of CaO. Soleimanzade et al. (2014) reported that MgO addition to zinc borosilicate glass, which is a well-known opacifier, enhanced the devitrification affinity of glass and lead to partial crystallisation of willemite (Zn_2SiO_4) and spinel. However, Tan et al. (2015) observed that the solubility of MoO_3 in aluminoborosilicate glasses was the highest for samples with MgO as the alkaline earth oxide. Therefore, this promising result provided an encouragement to investigate the role of MgO in this glassy system.

The role of MgO in nuclear glasses is complex. Harrison (2014) stated that generally addition of MgO into nuclear glasses has negative effect on chemical durability. However, Thien et al. (2012) determined that MgO had a dual role on the long-term durability of the French AVM borosilicate nuclear glass. Firstly, it is associated with

the precipitation of aluminous hectorites, which consumes Si and this leads to the partial (or total) dissolution of the protective gel layer. Secondly, the incorporation of Mg ions into the gel layer, improves its passivation capabilities in a similar way to Ca in the R7T7 borosilicate glass. The dominance of these antagonistic processes relies mainly on the glass chemical compositions and solution pH, however that mechanism is yet poorly understood.

5.3 Conclusions

Replacing CaO by MgO resulted in different waste products from the perspective of chemical durability being poor for MgO containing glass (MZMF-25P) compared to CZMF-25P. MgO is a well-known opacifier, enhancing the tendency of glass to devitrify when used alone. Although $MgMoO_4$ was not identified by XRD for MZ type samples the presence of this water soluble phase cannot be totally ruled out. Conversely, CZ type samples produced water-insoluble $CaMoO_4$ present in XRD patterns. This chapter shows that borosilicate glass containing MgO without CaO is not a good candidate as a host for POCO waste immobilisation. Based on the results and discussion in this chapter related to CZMF and MZMF waste glasses the following conclusions can be drawn:

- Density of resulting glasses increases linearly in both cases and reaching maximum for glasses with 25 wt% incorporation of POCO waste. The largest densities were observed for 25 wt% waste loading for both waste glasses with CZMF-25P being slightly denser
- XRD patterns show the formation of Ca and Ba molybdates with zircon and zirconia (CZMF glasses). However, MZMF glasses undergo different crystallisation resulting in Ba molybdate with zircon, zirconia plus low quartz.
- T_g and T_p values after incorporation of POCO simulant decrease slightly (CZMF glasses), but MZMF-15P and MZMF-20P have similar T_g with a distinct drop for MZMF-25P. The T_p is increasing between 15 and 20 wt% and finally decreases strongly for MZMF-25P.
- Thermal stability represented by ΔT is almost constant for CZMF glasses and demonstrates 11°C change within MZMF glasses
- Main peaks in Raman spectroscopy are related to molybdate species
- SEM/EDX confirm the presence of crystals identifies by XRD: Ca, Ba molybdates with zircon and zirconia. Moreover, the $BaMoO_4$ crystals identified for MZMF samples contain small amounts of Mg and Mn.
- PCT test clearly specifies much higher durability of CZMF-25P compared to MZMF-25P glasses after 7 and 28 days.

6. Glasses with P-type simulants

This chapter investigates incorporation of the P-type (POCO) simulants into a CZ base glass. The incorporation level of P-type simulants was 25 and 38 wt% labelled PX-25 and PX-38 respectively (Table 3.4). The modified glasses with P48 simulant (P48-25C and P48-38C) involved CZ glass modified by the addition of CaO, CuO and Mn_2O_3 to improve waste incorporation and fluidity at melting temperature (1060 °C) (Volf 1984, Ojovan & Lee 2005). From industrial perspective this chapter is the most relevant due to incorporation of POCO industrial grade simulants provided by NNL.

6.1 Results – P48, P19 and P0 type glasses

6.1.1 Density

Figure 6.1 shows the density of the four glasses incorporating P48 simulant with waste incorporation levels of 25 and 38 wt%. It can be seen that higher waste loading increases density from 2.815 (P48-25) to 2.986 g/cm^3 (P48-38). Similarly, for the P48-25C and P48-38C glasses the density increases from P48-25C (3.090 g/cm^3) and P48-38C (3.189 g/cm^3). It is observable that 38 wt% waste loading (P19 simulant) for the modified glass results in greater density values for instance 3.237 g/cm^3 (P19-38C) compared to 2.965 g/cm^3 (P19-38). A comparable situation is seen with P19-25C and P19-25, where densities are 3.062 and 2.796 g/cm^3 respectively. **Figure** 6.1 also shows the density of P0-25, P0-25C and P0-38, P0-38C glasses. It is observed that P0-25C and P0-38C (3.089 and 3.258 g/cm^3) are denser, than their unmodified counterparts P0-25 and P0-38 which have densities of 2.742 and 2.942 g/cm^3 respectively. Overall, modified glasses (e.g. P19-25C) present higher densities than their unmodified counterparts (e.g. P19-25) which is associated with the additions of Cu, Ca and Mn oxides. It also can be said that densities of modified and non-modified waste glasses at a given waste loading (25 or 38 wt%) are similar regardless of waste type.

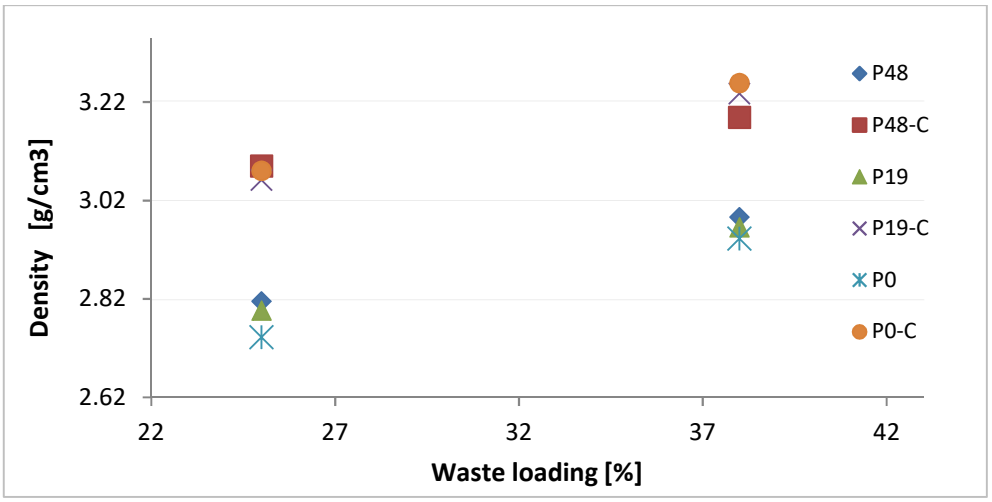

Figure 6.1 Density of all P type waste glasses (P48, P19 and P0) unmodifird and modified (C) with waste loading at 25 and 38 wt% e.g. P48-25, P48-25C, with error bars ± 0.003 g/cm^3

6.1.7 Viscosity

Figure 6.2 shows viscosity measurements of all investigated samples at 25 wt% waste loading. The general trend that can be drawn from the graph below is that, the three couples of glasses (P48-25 and P48-25C, P19-25 and P19-25C and P0-25 and P0-25C show a pattern, where viscosity values for unmodified samples between 950 and 1250 ºC are over three times larger than their modified counterparts (e.g. P19-25C and P19-25 at 1050 ºC are 1.47 and 5.12 dPa·s respectively, which is 3.47 times less). Moreover, the differences in viscosity values for 850 and 950 °C for the used compositions are over three times higher for unmodified glasses e.g. P0-25C and P0-25 at 850 ºC are 57.84 and 205.36 dPa·s respectively, which is 3.55 less). Even much higher difference in viscosity was observed for P19-25C and P19-25 at 850 ºC with values of 45.78 and 300.77 dPa·s which is 6.56 times less. It can be concluded that the addition of Cu, Mn and Ca oxides for investigated samples drastically reduced viscosities of this glass within the investigated range. This is in line with the literature; Volf (1984) reports that addition of Cu and Mn oxides had a strong effect on decreasing viscosity of borosilicate glass. It has also been reported that increasing the amount of CuO in a sodium silicate system resulted in an increasing NBO/BO ratio, suggesting that Cu plays a network modifying role (Sułowska et al. 2013; Mekki et al. 1997). Moreover, Szuszynska et al. (2010) confirmed that copper ions act as a modifier in soda-lime-silica glasses with a tendency to increase the compactness of the glassy framework (Cu-O interactions shorten the Si-O bonds), because of the smaller size of Cu^{2+} compared to Na^{+} or Ba^{2+} ions. Furthermore, the addition of CaO into alkaline silicate glasses

tends to decrease viscosity at high temperatures (1000-1300 °C) (Ojovan and Lee 2005). Additionally, strong differences in viscosities suggest that the diffusion coefficients for the supercooled melts were different for those two glasses for a short amount of time on cooling. This implies that for example P48-25C glass (more fluid) had a slightly longer time to form nuclei than P48-25 to enable the growth of crystals (Caurant et al. 2007). This would imply that crystallisation could be different in terms of formed crystal and/or their intensity. Indeed, P48-25C shows some XRD peaks that are not seen with P48-25. Assuming that the same viscosity trend is seen in the glasses with 38 wt% waste loading (not measured here) that are crystallised, it could explain why modified glass P48-38C underwent much stronger crystallisation (more peaks with higher intensity) than P48-38 (**Figure** 6.3). Surprisingly, the XRD pattern for P19-25C (more fluid) seems to be amorphous, which is the opposite to the earlier results regarding P48-25C which show small peaks. However, SEM image (**Figure** 6.21) shows some spinel crystals in the samples, which are undetected by XRD. If viscosity trend is applicable to glasses with 38 wt% waste loading it means that P19-38C is more fluid that P19-38 glass. This, in turn, can explain why P19-38C is more crystalline than P19-38 and why the SEM image of that glass contains white tiny globular crystals ($CaMoO_4$) across the sample in contrast to P19-38 glass (**Figure** 6.21).

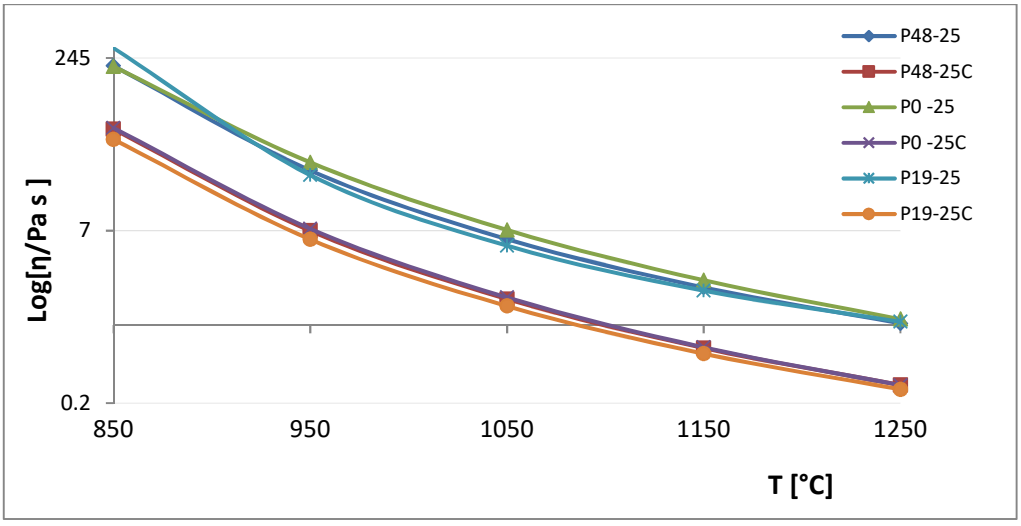

Figure 6.2 Viscosity of P19-25(C), P48-25(C) and P0-25(C) glasses

6.1.2 XRD

Figure 6.3 shows diffraction patterns for the P48 glasses with 25 and 38 wt% waste loading. P48-25 appears to be almost X-ray amorphous, but P48-38 presents clear peaks. The peaks are identified as $CaMoO_4$ and $FeCr_2O_4$ crystals. **Figure** 6.3b shows that crystallisation is more complex in the P48-C glasses. P48-25C contains some peaks but their intensity is not always clear with respect to signal noise. There are three peaks at ~ 18, 27 and 36 2°Θ, which can be explained by examining the diffraction pattern of P48-38C. This sample possesses very clear peaks, which belong to the crystalline phases identified in **Figure** 6.3a. Finally, the intensity and quantity of peaks clearly indicate that P48-38C is more crystalline than P48-38.

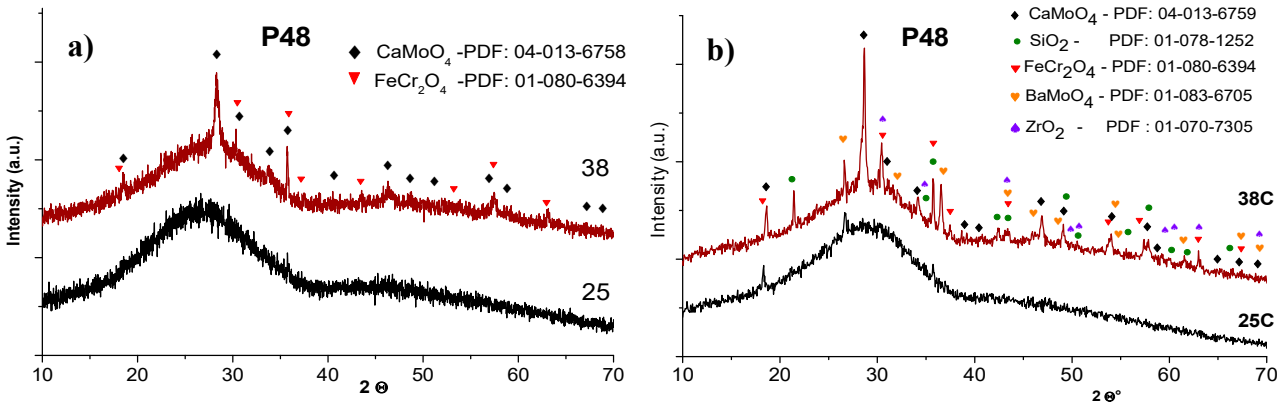

Figure 6.3 XRD of P48-25, P48-38 and P48-25C, P48-38C type glasses

Figure 6.4a illustrates the diffraction pattern of P19-25 and P19-38 glasses. P19-25 is not totally X-ray amorphous and shows some peaks. Comparing P19-25 to the P48-25 glass from the earlier paragraph, it is clear that the former is much crystalline. The largest peak of P19-25 sample around 28.35 2Θ° seems to be a powellite and it is shifted to 28.52 2Θ° for P19-38. Powellite is known for substituting other elements for Ca (chemical flexibility, Caurant et al. 2007), which in this case resulted in a delicate shift of peaks towards higher angles. The XRD peaks can be assigned to $CaMoO_4$ and $FeCr_2O_4$. The next glass P19-38 clearly has more peaks, which corresponds to the aforementioned phases plus α quartz. Moreover, **Figure** 6.4b shows the diffraction patterns of P19-25C and P19-38C samples. The former appears to be crystal free (opposite to P19-25), but the second pattern is crystalline. Identified phases are $CaMoO_4$, $FeCr_2O_4$, ZrO_2 and SiO_2.

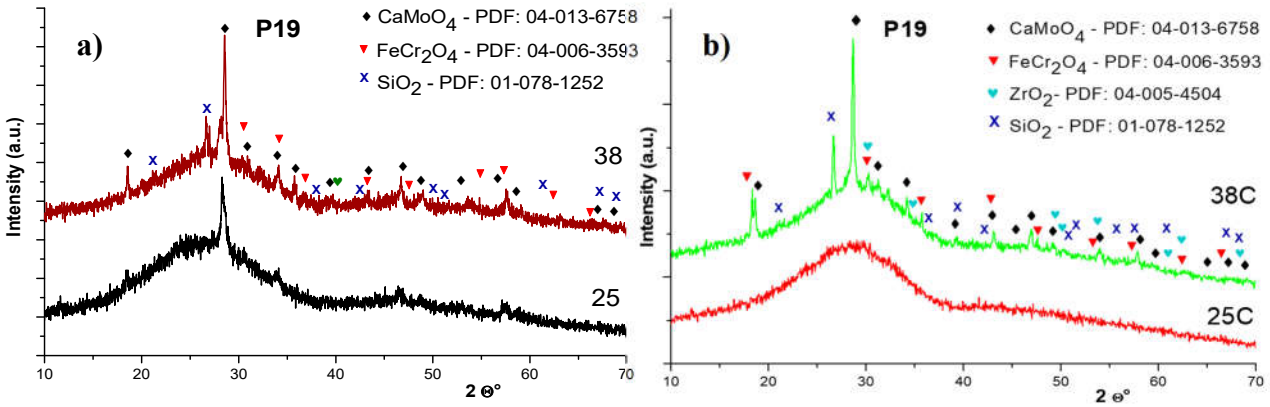

Figure 6.4 XRD of P19-25, P19-38 and P19-25C, P19-38C glasses

Figure 6.5a shows diffraction patterns of P0-25 and P0-38 glasses. Both samples have a strongly amorphous nature with small peaks. The peaks are slightly stronger for the latter sample and contain the following phases $CaMoO_4$, $FeCr_2O_4$ and $FeCr_{0.62}Zr_{0.38}O_2$. However, it was found that the former sample contains $CaMoO_4$ and $FeCr_2O_4$ only. Moreover, **Figure** 6.5b illustrates diffraction patterns of P0-25 and P0-38C glasses. P0-25C shows its amorphous nature with a small peak at ~ 36 2Θº, but the diffraction pattern of P0-38C has aforementioned crystals. Finally, the intensity and quantity of peaks indicate that P0-38C is more crystalline than P0-38 glass. It is believed that the strong crystallisation was affected by the lower viscosity of P0-38C.

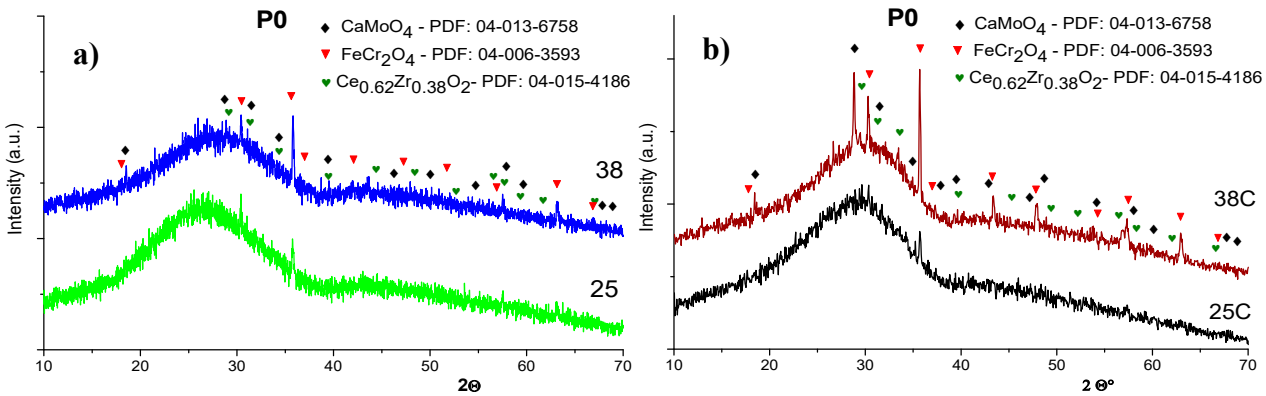

Figure 6.5 XRD of P0-25, P0-38 and P0 -25C, P0 -38C glasses

6.1.3 DTA

Figure 6.6 shows the DTA curves for P48 and P48-C type glasses loaded with 25 and 38 wt% waste. P48-25 and P48-38 glasses exhibit very similar values of T_g and different T_p values. The T_p values are 638 and 614 °C for P48-25 and P48-38. Nevertheless, P48-25C possess a slightly higher T_g (by 5 °C) than P48-38C (**Figure** 6.3) in addition T_p are 618 and 628 °C respectively.

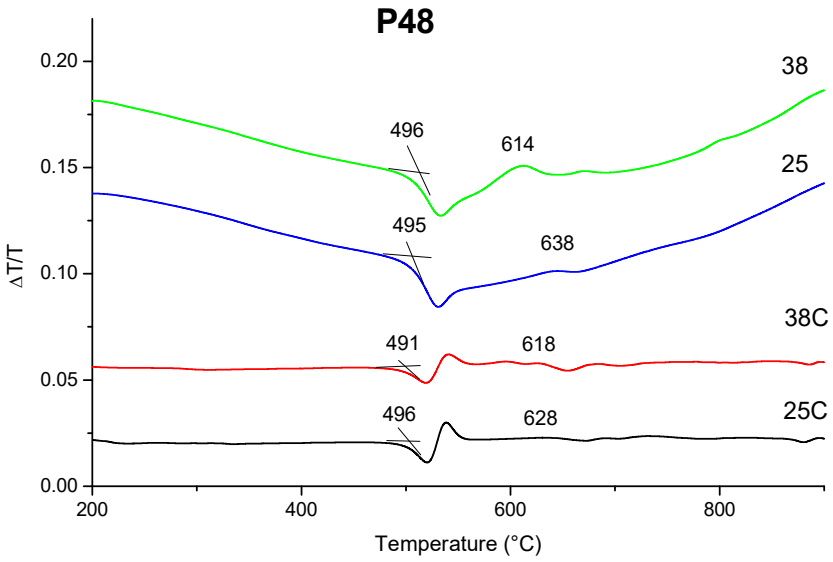

Figure 6.6 DTA of P48 and P48-C type glasses

Figure 6.7 shows the DTA series of P19 type glasses at 25 and 38 wt% waste loading. P19-25 and P19-38 glasses have almost identical T_g values (~ 492 °C), but very similar T_p values are 610 and 615 °C respectively. The second group consists of P19-25C and P19-38C presents comparable T_g and dissimilar T_p values to the previous samples. T_g values are almost the same which are 489 (P19-25C) and 486 °C (P19-38C), but T_p values are 577 and 640 °C respectively.

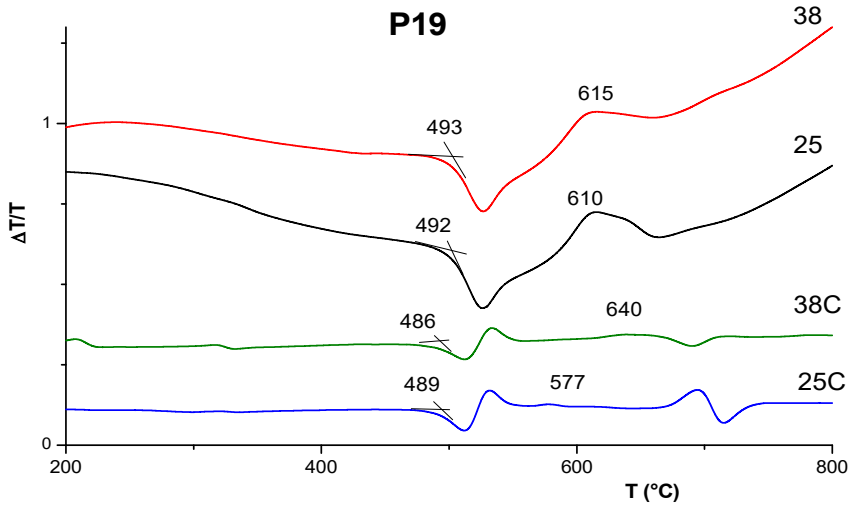

Figure 6.7 DTA of P19- 25, P19-38 and P19- 25C, P19-38C glasses

Figure 6.8 illustrates DTA curves of the scanned four glasses with waste loading at 25 and 38 wt%. Incorporation of P0 waste simulant resulted in T_g decrease from 503 to 497 °C and T_p from 631 to 626 °C for P0-25 and P0-38 glasses. Moreover, the modified samples (25C and 38C) also exhibit a drop in T_g values from 495 to 487 °C. However, T_p values increased from 605 to 646 °C for P0-38C.

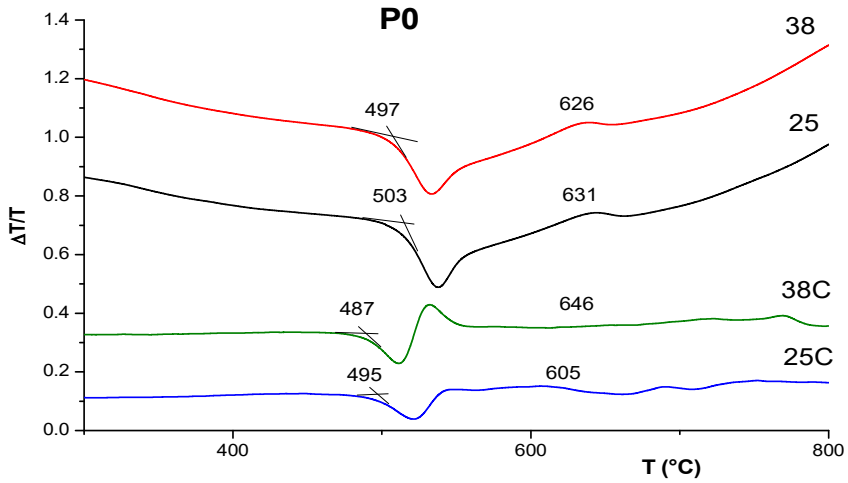

Figure 6.8 DTA of P0-25, P0-38 and P0-25C, P0-38C glasses

Kissinger method

Figure 6.9 is an example, which shows four DTA scans of the same P48-25 sample at different heating rate β: 10, 20, 25 and 30 °C/min. It is clear that T_g and T_p values are not constant for the particular glass and they depend on the heating rate, which also affects the rate of crystallisation.

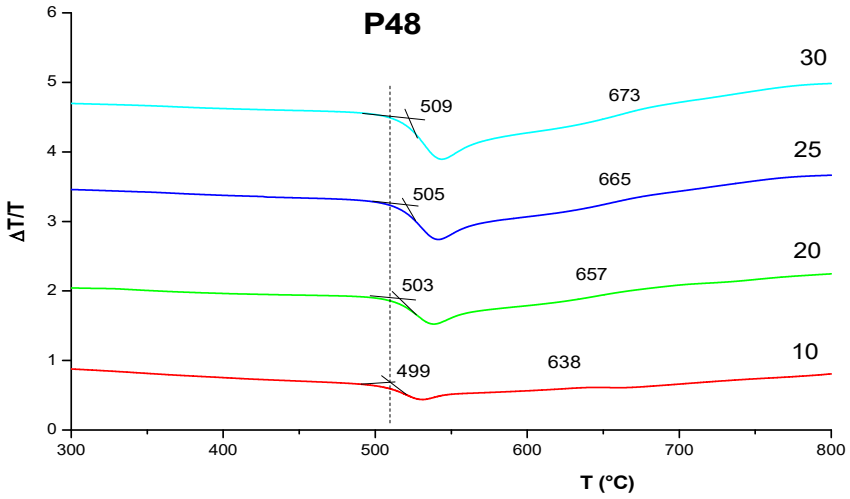

Figure 6.9 DTA of P48-25 glass scanned at variable heating rate four times

Figure 6.10 shows a Kissinger plot ($\ln(T_p^2/\beta)$ versus $1000/T_p$) for P48-15, P48-25 and E-38 glasses. The slopes of the graph can be used to calculate activation energy of crystallisation (E_a, kJ/mol). E_a can simply be obtained by multiplying the slope by the gas constant, R. Thus a linear regression function was used to obtain a standard error that further was multiplied by R to give E_a error values. **Figure** 6.11 gives correlation between E_a and waste loading for given waste simulant. It is clear that E_a for 15 wt% waste loading seems to be comparable for all types of simulants. However, E_a values for 38 wt% simulant incorporation are clearly dissimilar and reaches the highest value for P19-38 glass (372 kJ/mol). On the other hand, the lowest E_a values at 38 wt% waste loading are found with the P0-38 sample (223 kJ/mol) and P48-38 glass is located in-between with its E_a value at 345 kJ/mol. At 25 wt% waste incorporation shows two things that P0-25 and P48-25 have similar E_a values (192 and 226 kJ/mol) and P19-25 requires much higher activation energy to crystallise namely 293 kJ/mol.

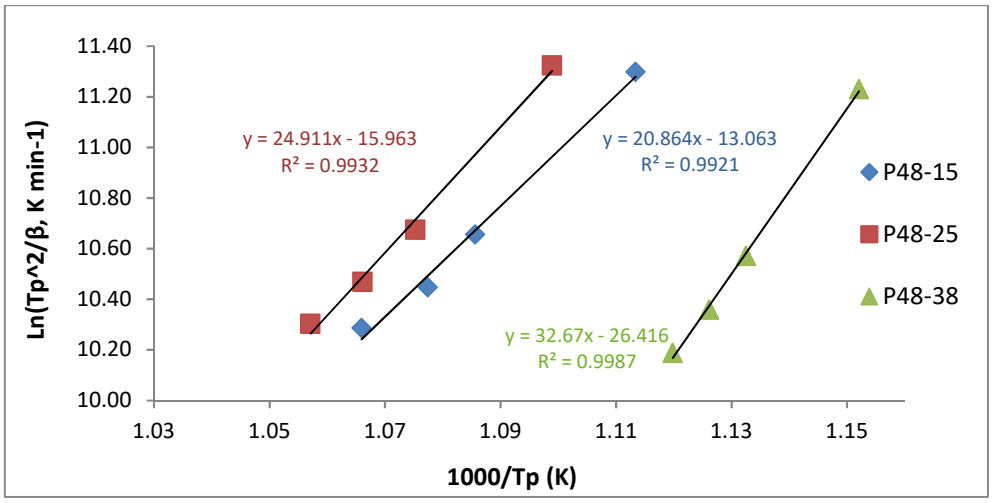

Figure 6.10 Kissinger plot for P48-15, P48-25 and P48-38 glasses

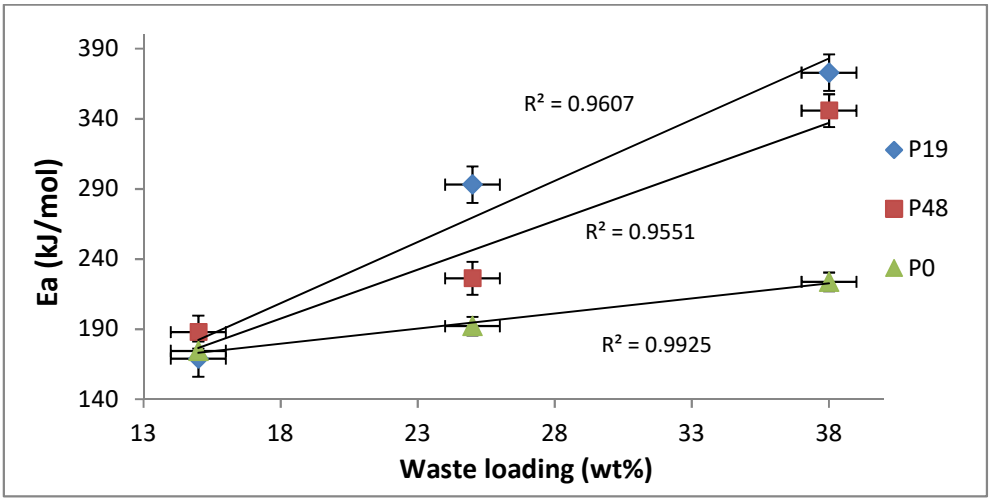

Figure 6.11 E_a in the function of P48, P19 and P0 waste loading

Figure 6.12 shows the Kissinger plot for all type modified glasses at 38 wt% waste loading. Due to the high cost of the DTA scans only samples with 38 wt% waste loading of modified glasses were analysed as being the most representative from an industrial perspective. **Figure** 6.13 clearly shows that the highest E_a values are for P19-38C (~ 500 kJ/mol), which corresponds well with a P19-38 sample which also has the highest E_a between unmodified glasses. Moreover, P48-38C has the second highest E_a value (~ 357 kJ/mol), whereas P0-38C possesses the lowest activation energy namely ~ 280 kJ/mol. All in all, E_a values of modified glasses versus their basic counterparts show that their activation energy of crystallisation is always greater. The E_a difference between modified and unmodified samples at 38 wt% waste loading is greater for modified waste glasses as follows: P19-38C (~ 21 %), P48-38C (~ 31 %) and P0-38C (~ 25%).

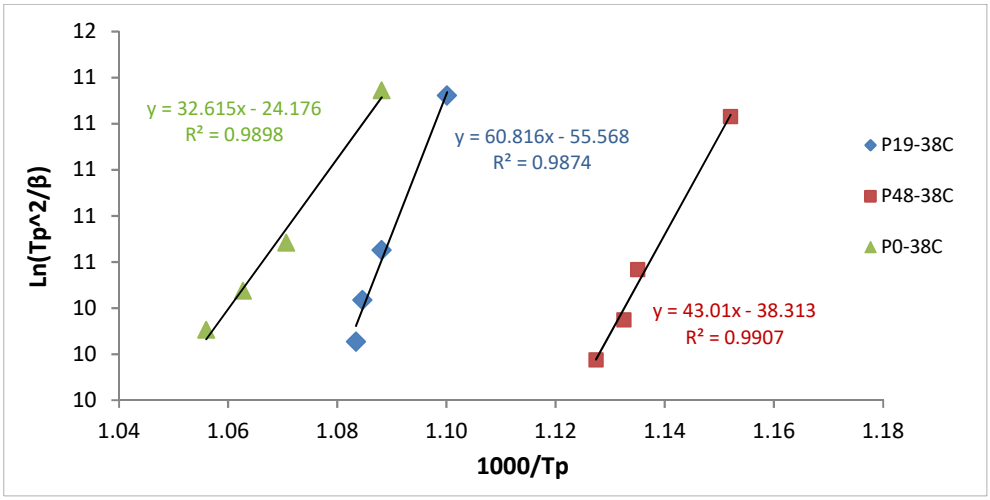

Figure 6.12 Kissinger plot for P19-38C, P48-38C and P0-38C glasses

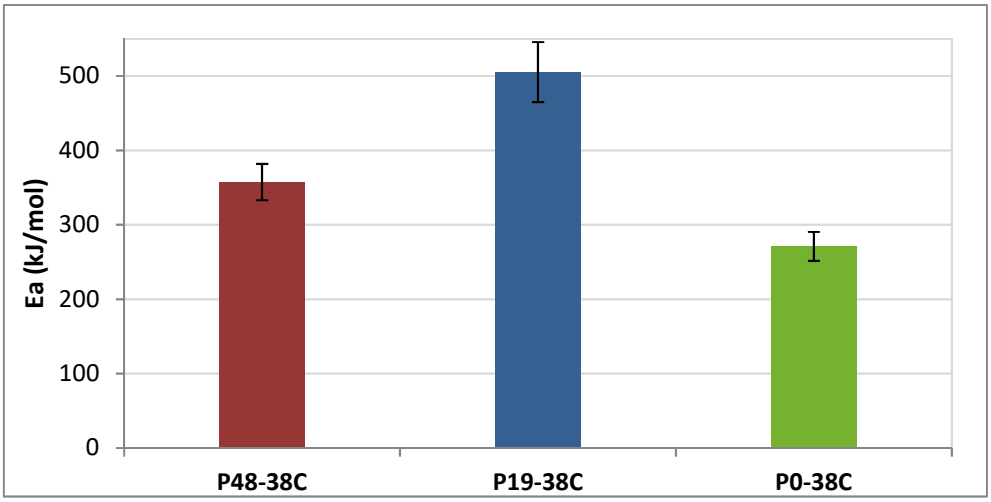

Figure 6.13 E_a of P48-38C, P19-38C and P0-38C

6.1.4 Raman Spectroscopy

Figure 6.14 shows Raman spectra of P48 and P48-C glass series. P48-25 contains two main bands at 320 and 921 cm^{-1} with a shoulder at ~ 878 cm^{-1}; this shoulder becomes a peak in the P48-38 glass. Moreover, the peak at 389 cm^{-1} becomes visible for P48-38 glass with a broad peak at circa 700 cm^{-1}. P48-25C shows two broad peaks in similar positions to the previous two glasses at 320 and circa 912 cm^{-1}. The 912 peak shifts from around the 921 initial position after addition of Ca, Cu and Mn oxides (P48-25C and P48-38C glasses) which suggest that MoO_4^{2-} tetrahedra are charge compensated by additional cations. Chouard et al. (2011) reported that molybdate tetrahedra compensated by Ca ions give a peak position at around 919 cm^{-1} in borosilicate glasses. Moreover, Caurant et al. (2010) argues that the peak shift from 922 to 913 cm^{-1} (Mo-O symmetric stretching band) is an intermediate position between that of its two basic reference borosilicate glasses (with Na or Ca) - proposing that MoO_4^{2-} units are compensated at the same time by Na^+ and Ca^{2+} cations. However, glasses investigated here have more complex compositions, so charge compensation mechanisms could be even more complicated including other cations. Interestingly, in the XRD section peaks associated with Na_2MoO_4 were not identified by XRD, but the presence of this phase cannot be completely excluded. Furthermore, P48 waste incorporation at 38 wt% resulted in the formation of new peaks, which were either present as shoulders or not visible before at all for P48-25 & P48-25C, these are at 794, 844 (P48-38C only) and 878 cm^{-1}. These peaks are mainly associated with $CaMoO_4$ based on XRD results (Fig. 6.3) (Brinkman et al. 2013).

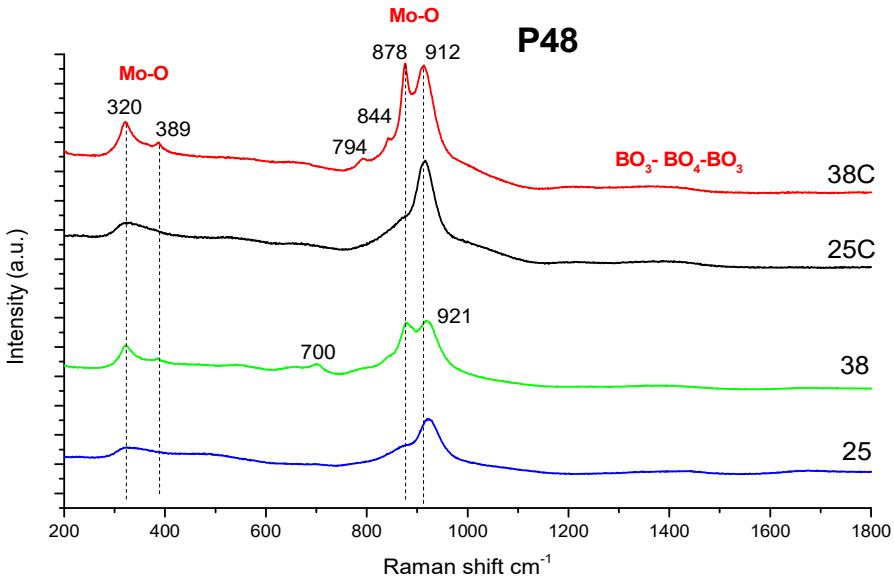

Figure 6.14 Raman spectra of P48-25(38) and P48-25(38)C glasses

Figure 6.15 shows the Raman spectra of P19-(25, 38) and P19-(25, 38)C glasses. Peaks at around 320, 389 and from 794 to 921 cm^{-1} were described in the previous section (P48 simulant). However, the shape and intensity of those peaks slightly vary in comparison to **Figure** 6.14. P19-25 and P19-38 at 912 cm^{-1} have more of a shoulder than a peak (mainly P19-38). The main peak around 878 cm^{-1} is assigned to Mo-O stretching vibrations bonds in $CaMoO_4$. Furthermore, P19-25C and P19-38C exhibit slightly different spectra. For example, P19-25C possesses a peak at 912 cm^{-1} and shoulder at 878 cm^{-1}, which transforms into a peak for P19-38C glass. A peak shift from 921 to 913 cm^{-1} is not observed. There are some new peaks at 655 cm^{-1} (P19-38) associated probably with high polymer pentaborate ($B_5O_8^-$) (Yadav & Singh 2015) units and at 1596 cm^{-1} which is associated with the bending mode of water molucules (Ikeda 2014). Moreover, a new band is also observed at 690 cm^{-1} (P19-38C), which corresponds with stretching vibrations of $B–O^-$ bonds with nonbridging oxygen (Yadav & Singh 2015).

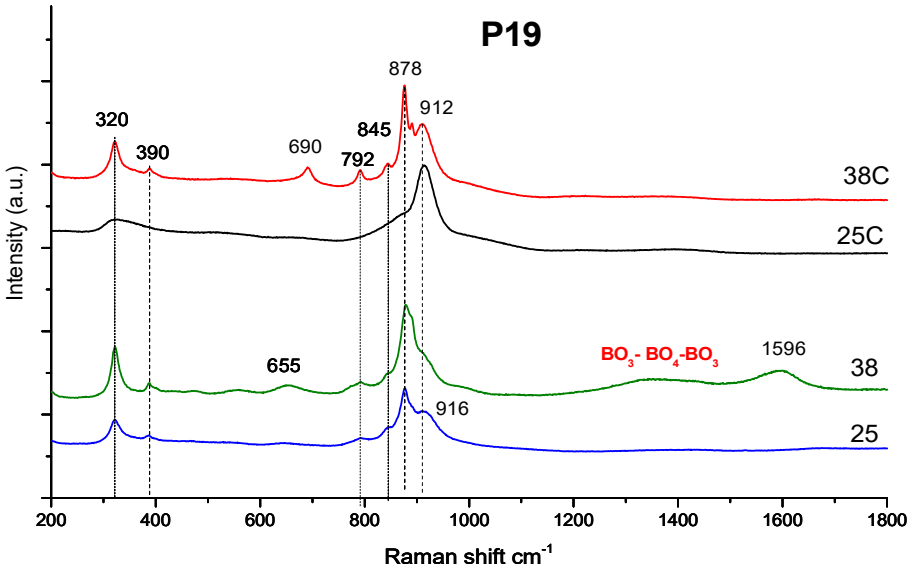

Figure 6.15 Raman spectra P19- 25, P19-38 and P19- 25C, P19-38C glasses

Figure 6.16 shows Raman spectra of P0-25, P0-38 and P0-25C, P0-38C investigated glasses. P0-25 sample exhibits two main bands at 320 and 792-921 cm^{-1}. As mentioned earlier the band centred at 921 cm^{-1} seems to show different charge compensation of MoO_4^{2-}, after adding extra oxides of Ca, Cu and Mn. P0-38 possesses band in very similar positions, but their intensity is much larger plus a new shoulder at 877 cm^{-1} is formed. The modified glasses have peaks in the same positions, but with a greater intensity, which suggests that there is a

higher content of crystalline molybdates compared to unmodified counterparts. As mentioned before molybdate tetrahedra can be charge compensated by both Na^+ and Ca^{2+} ions (P48 simulant). Peaks described above are associated with $CaMoO_4$, which agrees with XRD results where powellite was identified.

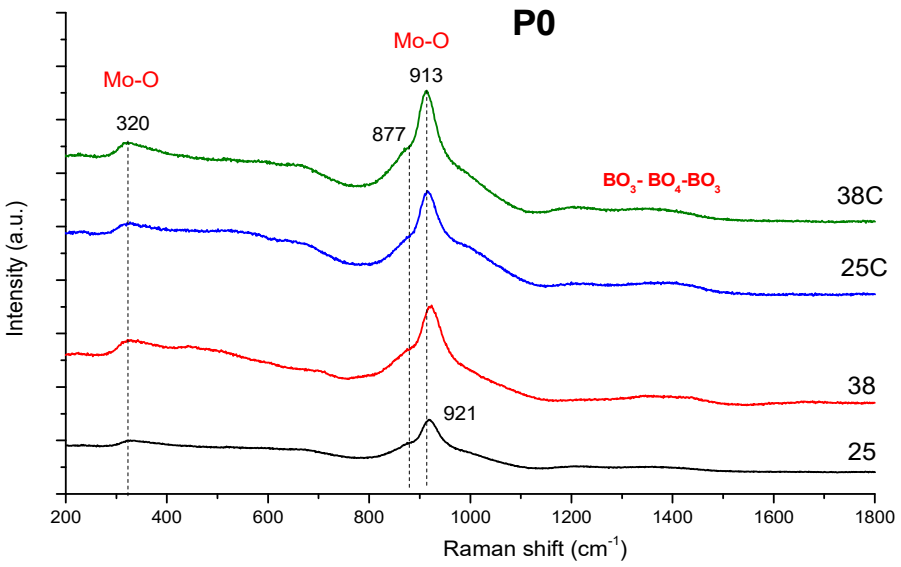

Figure 6.16 Raman spectra of P0-25, P0-38 and P0-25C, P0-38C glasses

6.4.8 Mossbauer spectroscopy

Figure 6.17 shows Mossbauer spectra of P19-25 and P19-25C glasses. The measurements were made at VSL in Washington DC. Those glass samples were chosen for analysis due to the fact that are reasonably crystal free, unlike P19-38 and P19-38C samples. It is clear that most of the Fe is oxidised and is present as Fe^{3+} for P19-25 and P19-25C samples ~ 98 and 93.2 % respectively. Hannant et al. 2009 reported that Fe^{3+} ions exist in at least two coordinations, namely tetrahedral [tet] and octahedral [oct]. It was noticed that Fe^{2+} is dominantly octahedral, but that Fe^{3+} exists in both coordinations. Moreover, while it was found that $^{[oct]}Fe^{3+}$ is not sensitive to any redox change, $^{[tet]}Fe^{3+}$ ions illustrate a clear preference for the redox reaction ($^{[tet]}Fe^{3+} \leftrightarrow Fe^{2+}$). Furthermore, Ca^{2+} can charge balance Fe^{3+} in tetrahedral sites (Dyar 1985). This fact sheds some light why charge compensators (e.g. Ca^{2+}, Na^+) are important to maintain more $^{[tet]}Fe^{3+}$ which is a glass former (FeO_4^-). It is especially important in nuclear glasses where for instance Na^+ ions adjust their role from glass modifier to charge compensator (Ciecińska et al. 2015, Weigel et al. 2008). This also implies that less Na^+ or Li^+ is available to form soluble molybdate phases such as Na_2MoO_4

that in turn positively affect glass waste durability. Finally, based on the literature it can be assumed that majority of Fe^{3+} would be 4 coordinated (~ 60 %) (Hannant et al. 2009 and Weigel et al. 2008).

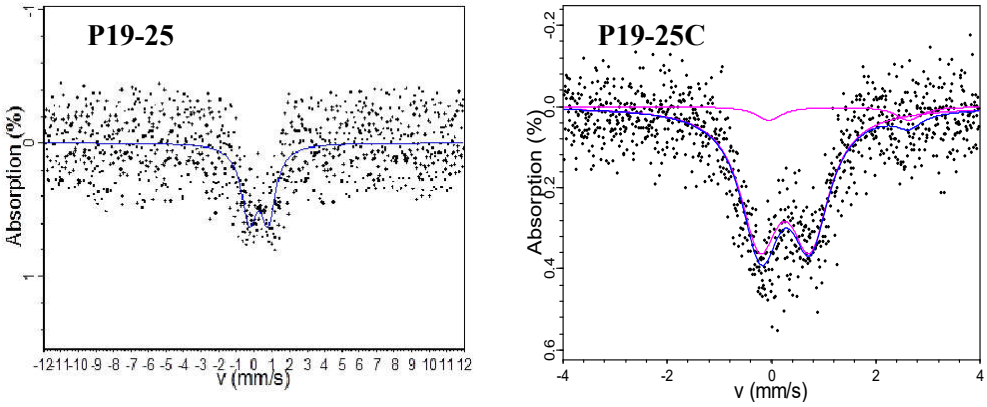

Figure 6.17 Mossbauer spectra of P19-25 and P19-25C glasses

6.1.5 SEM

Figure 6.18 presents BSE images of P48-25 and P48-25C glasses. The first one shows a group of crystals rich mainly in Cr and some Fe with Zn. This corresponds to the XRD results (**Figure** 6.2) where $FeCr_2O_4$ crystals were found in P48-38, but in the particular case of P48-25 the XRD pattern appears X-ray amorphous. This simply means that some spinel is present below the XRD detection threshold. Moreover, the P48-25C sample shows much larger crystals and is also rich mainly in Cr and Mn, Fe, Zn and Na. What is noticeable in **Figure** 6.19 is that Cr is mainly in the crystals, but not in the glass matrix unlike aforementioned elements. Comparing SEM with XRD results regarding P48-25C (**Figure** 6.19, **Figure** 6.3) suggest the presence of $FeCr_2O_4$, however the XRD peaks are not very apparent.

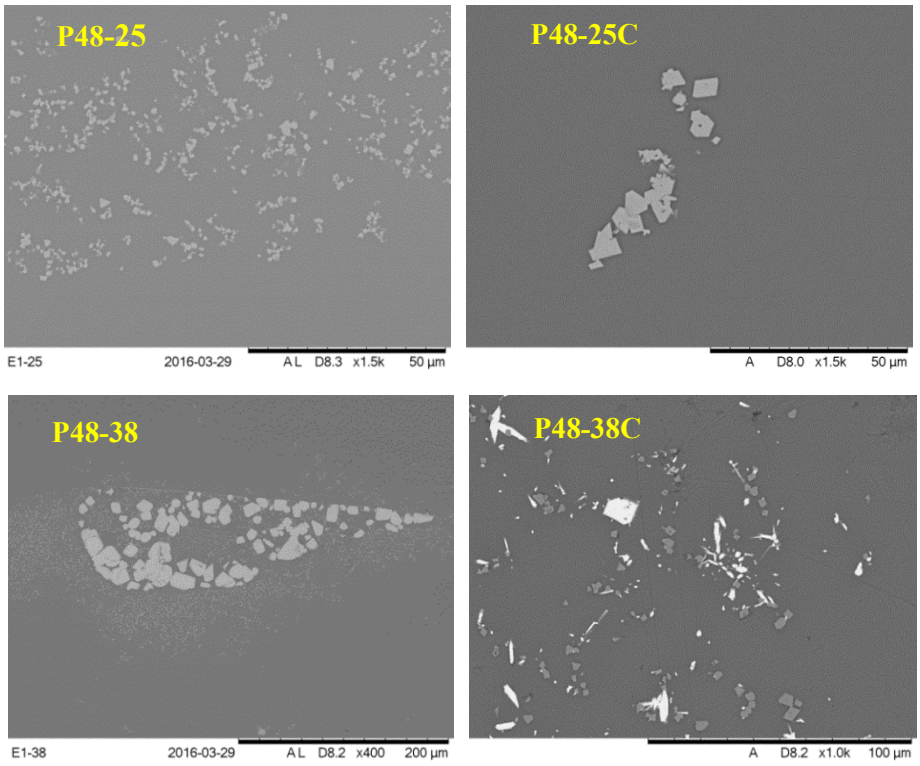

Figure 6.18 BSE images of P48-25, P48-25C and P48-38, P48-38C glasses

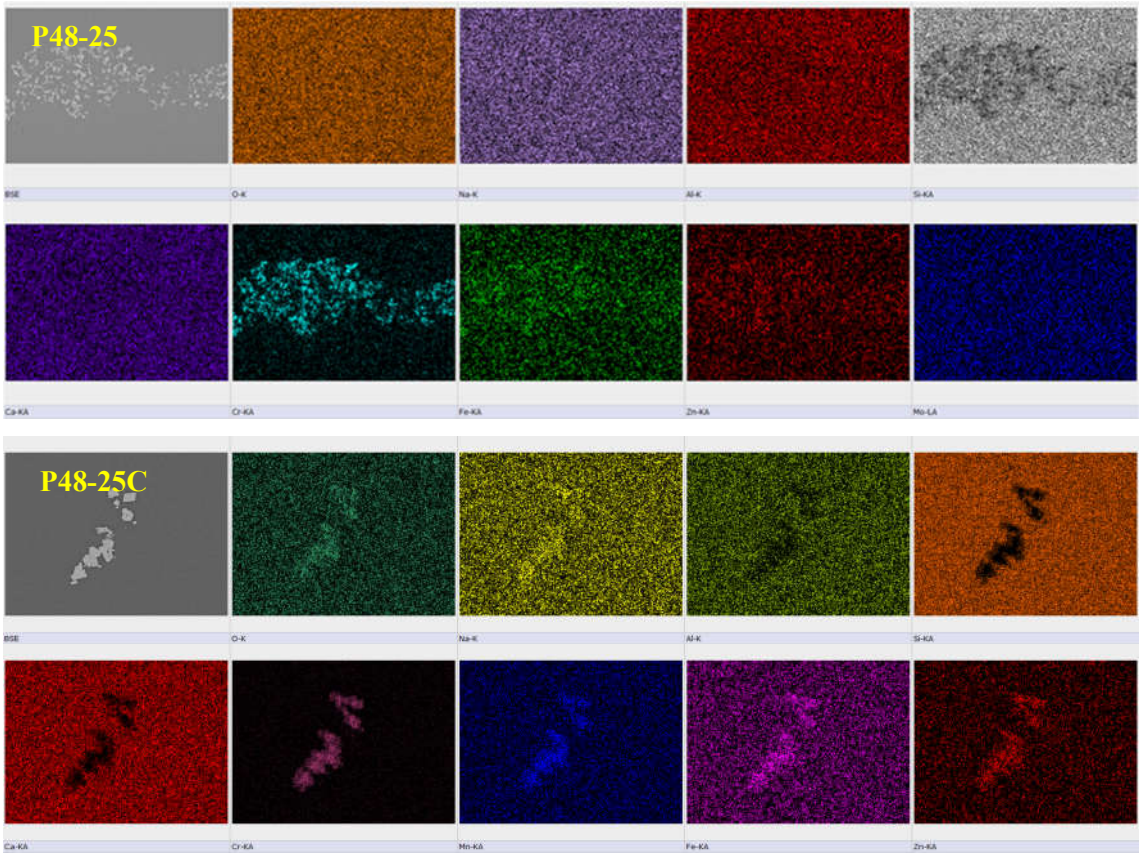

Figure 6.19 X-ray maps of P48-25 and P48-25C glasses

Figure 6.18 also shows BSE images of P48-38 and P48-38C glasses. The first image (P48-38) depicts large bright crystals surrounded by much smaller ones. X-ray maps from **Figure** 6.20 indicate that the bright large crystals are rich in Mo and Ca, which agrees with the XRD findings of $CaMoO_4$ (**Figure** 6.3). Small crystals around $CaMoO_4$ are rich in Cr and Fe, which agrees with the XRD findings, where $FeCr_2O_4$ is again identified. The latter image shows P48-38C which is much richer in crystalline phases. **Figure** 6.20 combined with **Figure** 6.3b (XRD) illustrates the presence of spinel-rich in Cr, Mn and Fe. It seems that Mn was partially incorporated into spinel crystals. The last phase noticed in this picture is rich in Zr which corresponds to the ZrO_2 seen by XRD. Moreover, Zr-rich areas in the picture related to Si are black which indicates that they are Si-depleted regions and this also means that in this case zircon is not formed. The $CaMoO_4$ and $BaMoO_4$ phases identified by XRD (**Figure** 6.3) are not visible on the elemental map of P48-38C.

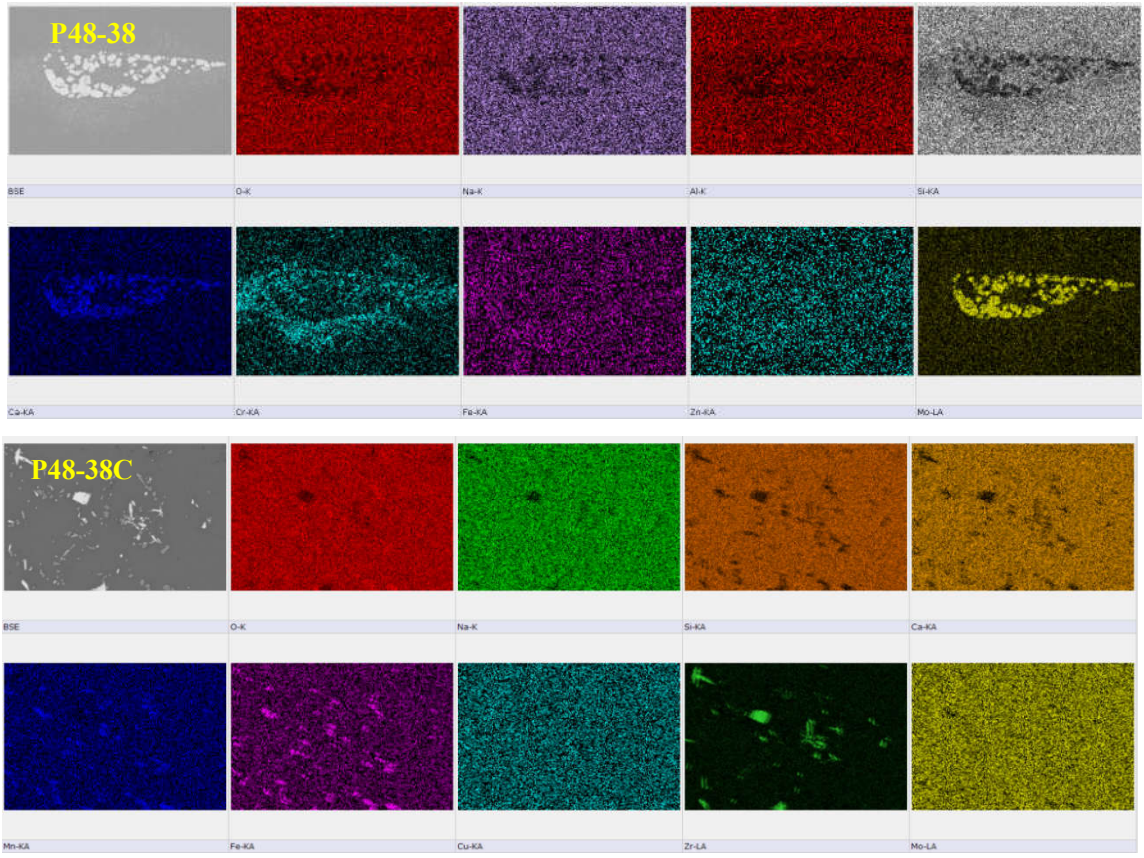

Figure 6.20 X-ray maps of P48-38 and P48-38C type glasses

Figure 6.21 shows images of P19-25 and P19-25C glasses. The former presents light and dark layers at low magnification. Based on **Figure** 6.22 those lighter layers are enriched in Zr, Mo and Al, but those darker layers separating them appear to be richer in Si (hard to see

on the hard copy). This indicates an initial stage of phase separation, which was likely to follow the crystallisation. This result would corespond well with XRD where $CaMoO_4$ was identified. Furthermore, P19-25C shows larger crystals which are rich in Cr, Fe, Mn and Zn. This agrees with the XRD results, where $FeCr_2O_3$ spinels were detected. What is more, some substitutions of Mn and Zn are quite common since spinels can incorporate other elements into their structure as mentioned before (Alton et al. 2002 and Matyáš et al. 2012).

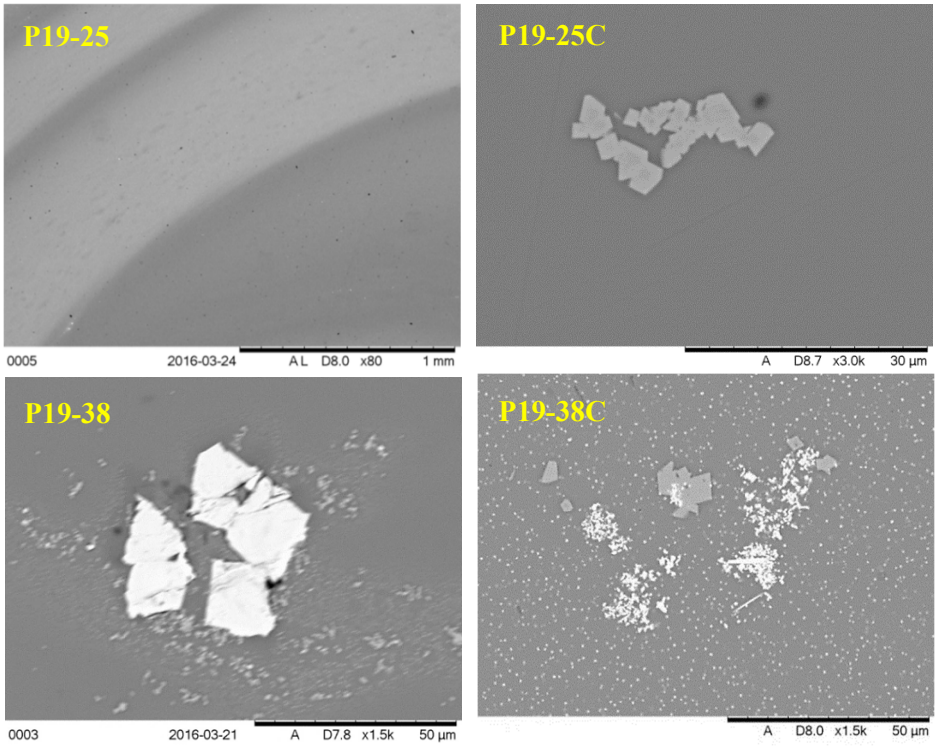

Figure 6.21 BSE images of P19-25, P19-25C and P19-38, P19-38C

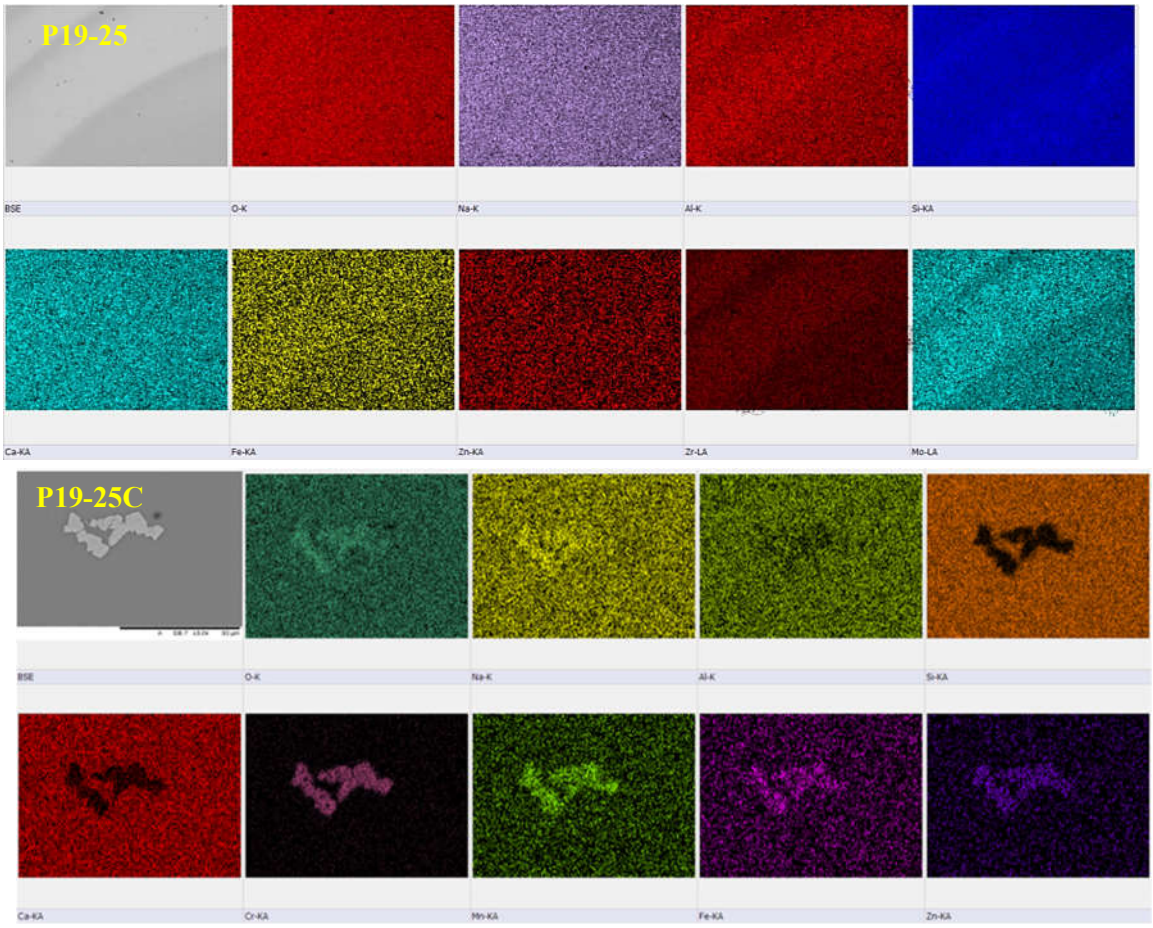

Figure 6.22 X-ray maps of P19-25 and P19-25C

Figure 6.21 also shows BSE images of P19-38 and P19-38C waste glasses. The former one illustrates a large crystal rich in Ca and Mo surrounded by a group of tiny crystals enriched in Cr, Fe and Zn (spinel). Elemental composition of these crystals agrees with previous XRD results, where $CaMoO_4$ and $FeCr_2O_4$ were identified. In the case of P19-38C, the crystallisation process occurred differently to P19-38, because there are obviously spinel crystals containing Cr, Fe and Zn, but there are plenty of tiny white spots visible across the whole sample that are likely to be $CaMoO_4$ (similar morphology observed before e.g. Fig. 5.11), although, Mo signal do not pinpoint them at this magnification. However, an X-ray map taken at higher magnification confirms that these white globular crystals contain Mo and Ca (not shown here). All the crystals identified by SEM agree with the XRD results mentioned before (**Figure** 6.4), where $CaMoO_4$, $FeCr_2O_4$ and ZrO_2 phases were identified. It is also noticeable that areas covered by Zr (**Figure** 6.23) are also enriched in Si, which suggest that some $ZrSiO_4$ might have been formed (not detected by XRD).

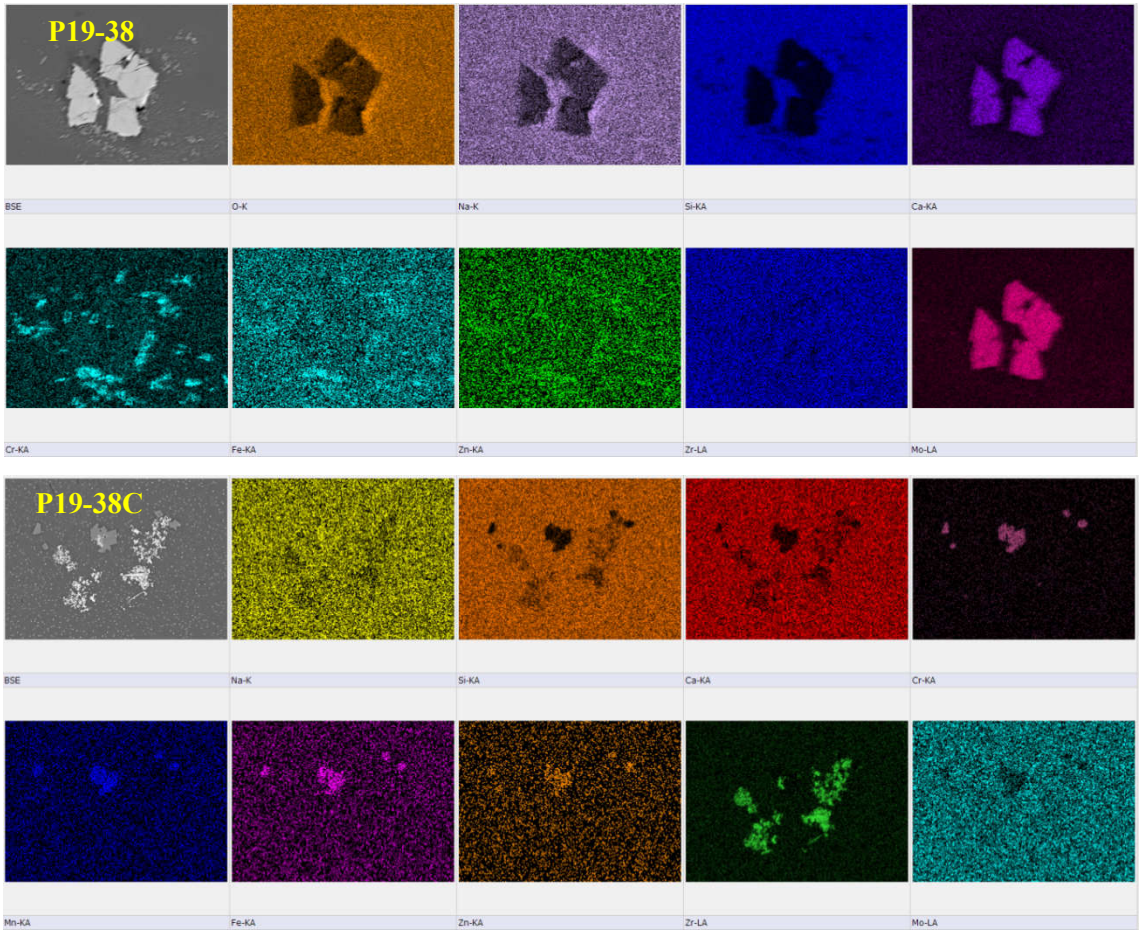

Figure 6.23 X-ray maps of P19-38 and P19-38C

Figure 6.24 shows BSE images of P0-25 and P0-25C glasses. In both cases, some crystals are present. Based on X-ray imaging the former sample contains crystals rich in Cr, Fe and some Zn (**Figure** 6.25). This agrees with XRD data, where $FeCr_2O_4$ phase was found (**Figure** 6.5) the latter glass also contains spinel crystals identified above with some Mn ions incorporated substitutionally. XRD results confirm the spinel as $FeCr_2O_4$ phase.

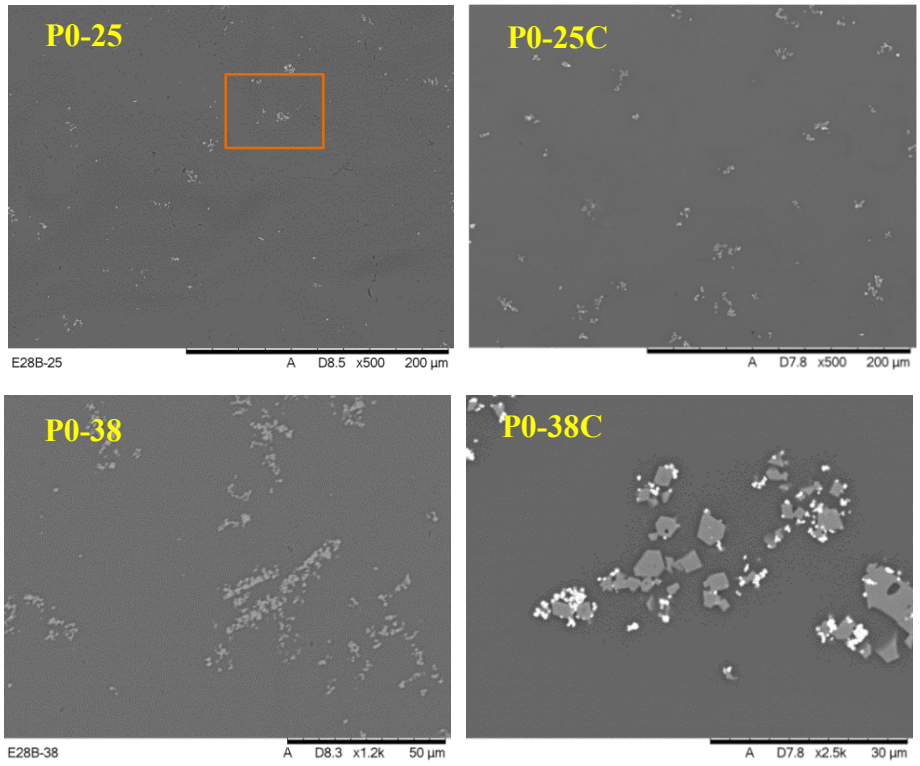

Figure 6.24 BSE images of P0-25, P0-25C and P0-38, P0-38C

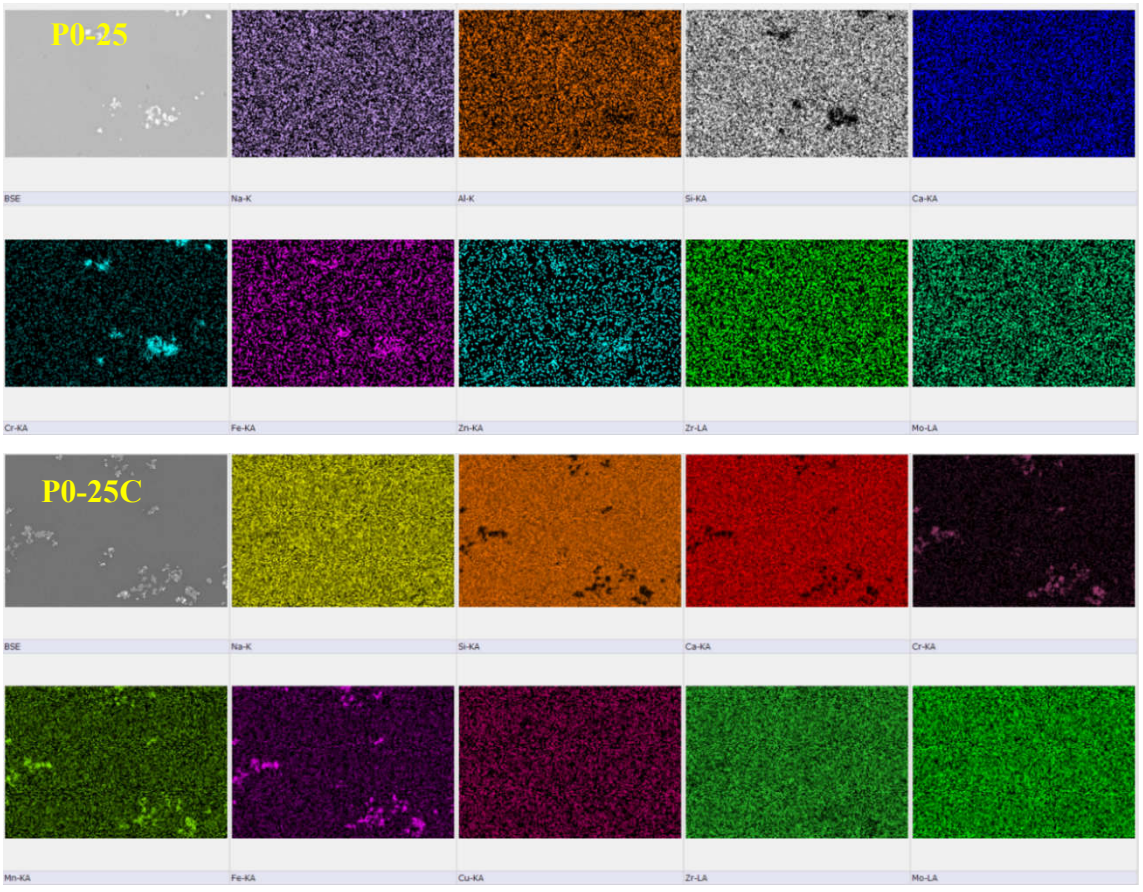

Figure 6.25 X-ray maps of P0-25 and P0-25C

Figure 6.24 shows BSE images of P0-38 and P0-38C glasses. The first one possesses tiny crystals rich in Fe, Cr ($FeCr_2O_4$ spinel) and Ce identified by XRD software as $Ce_{0.62}Zr_{0.38}O_2$. This agrees with the XRD data where the presence of these crystals is confirmed (**Figure** 6.5). The second image representing P0-38C also shows crystals rich in Fe, Cr and Mn ($FeCr_2O_4$ spinel) plus Zr with Ce identified above (**Figure** 6.26). In terms of size, P0-38C has larger crystals than the unmodified counterpart, which are at least 3µm across. Additionally, the brightness of images with Ca and Mo suggest their greater concentration in the modified samples compared to the P0-38 glass.

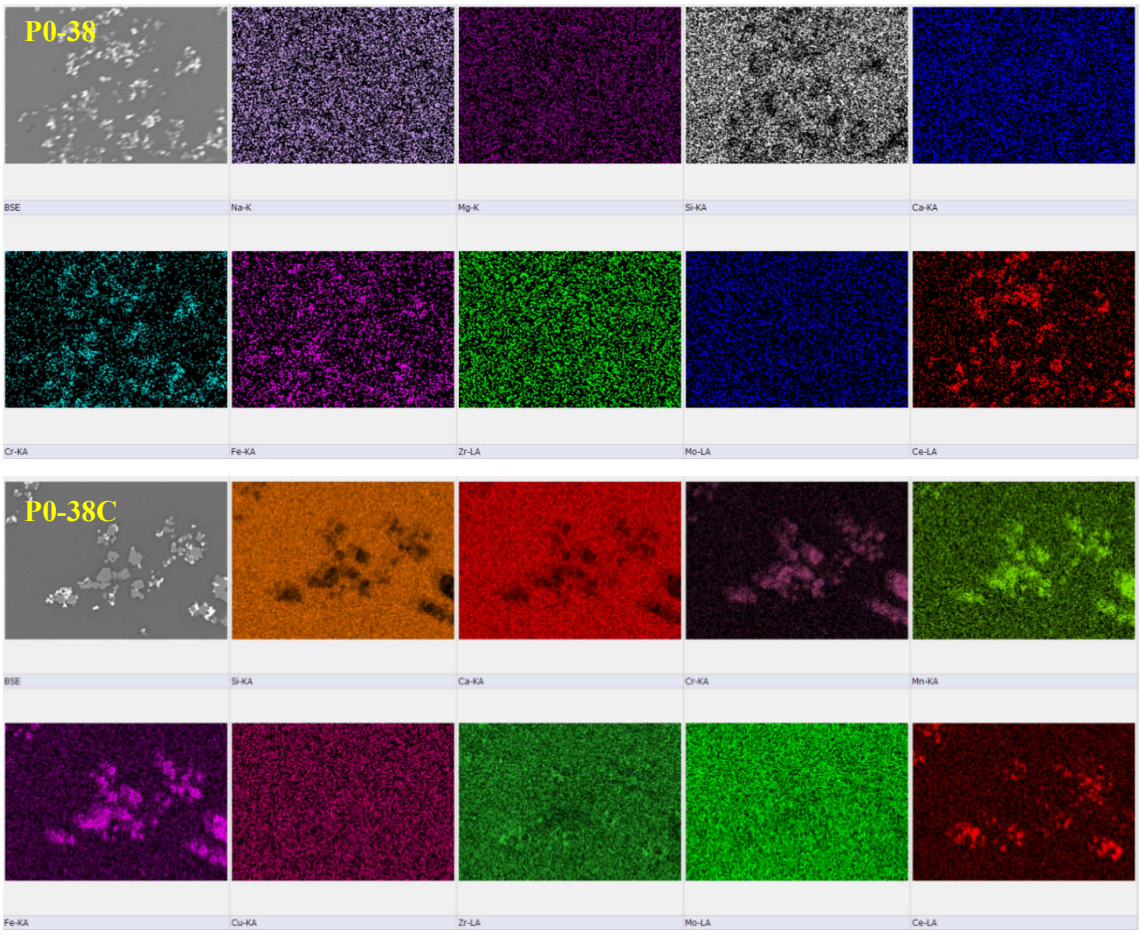

Figure 6.26 X-ray maps of P0-38 and P0-38C

6.1.6 PCT-ICP

Figure 6.27 shows ICP results after 7 and 28 day PCT tests for P48-25 and P48-25C glasses. The most leached elements from examined glasses are B, Li, Mo and Li. On average NL values are greater for glasses after 28 than 7 days which is expected after a longer test time. However, B, Li and Na for P48-25_7 have similar values to the P48-25_28 samples after including standard error. Comparing NL after 7 days between P48-25 and P48-25C glasses it seems that in most cases the mass loss is greater for the P48-25 sample apart from Mo and Ca (extra CaO added). However, the same glasses tested after 28 days demonstrate similar NL values for B, Li, Na and Mo. On the other hand, Al and Ca is leached more for P48-25C, unlike Si. Remaining elements such as Ba, Fe, Nd, Zr, Mg and Zn are released in negligible quantities which makes it difficult to discuss their fate further.

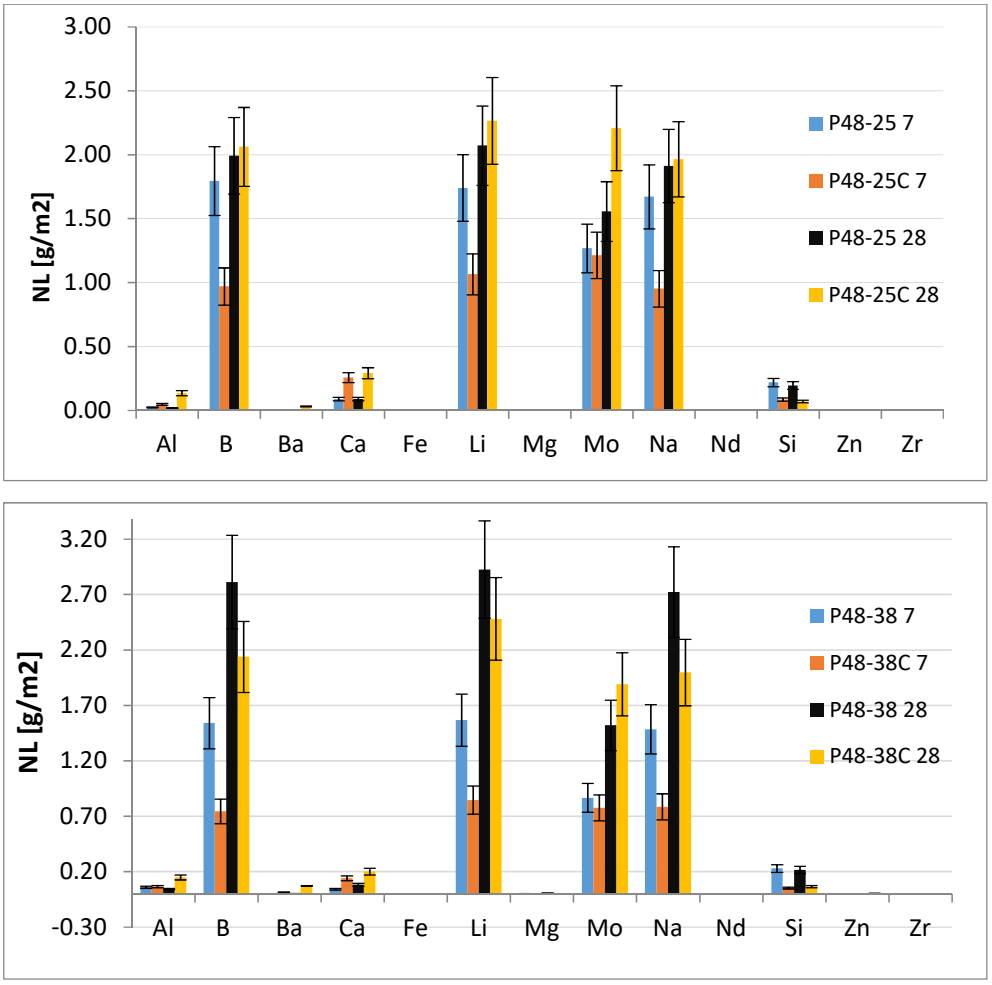

Figure 6.27 NL values of P48-25, P48-25C and P48-38 and P48-38C glasses after 7 and 28 day PCT test

Figure 6.27 also shows ICP results after 7 and 28 day PCT test for P48-38 and P48-38C glasses. The most leached elements are B, Li, Mo and Na. It can be said that in most cases with those elements P48-38 glass released more of those elements into solution than P48-38C after 7 day PCT test (excluding Mo). However, the same glasses tested after 28 day PCT test including standard errors demonstrated similar NL values between P48-38 and P48-38C samples. However, Si was released in smaller quantities (~ 0.2 g/cm^3) after 7 and 28 days for P48-38C. The opposite situation is seen with Al where, after 28 days tests NL values are over three times larger for P48-38C than P48-38 glass, but still do not exceed 0.149 g/m^2. Moreover, NL for Ca is naturally greater for P48-38C glasses due to extra CaO (~ 0.2 g/m^2). Remaining elements such as Zr, Ba, Fe, Nd and Zn are released in too low quantities to be discussed further. Small amounts of the white marks observed on a very few grains of the sample contain Ca and Mo, which relates to the PCT results (**Figure** 6.10), where Mo was released in substantial amounts. It appears that Mo and Ca have been released into solution and then precipitated as powellite on the powdered glass.

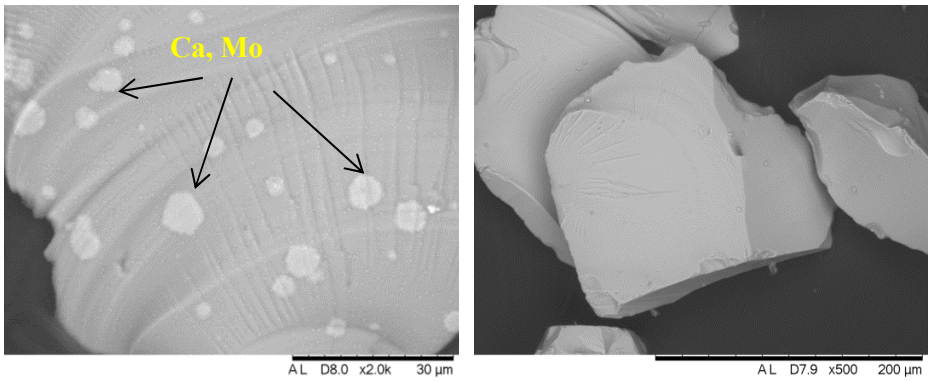

Figure 6.28 BSE image of P48-25 glass after 7 day PCT test with multiple 'parallel' lines are river line from the sample preparation.

Figure 6.29 shows ICP results after 7 and 28 days for P19-25 and P19-25C glasses. Elements, which were leached the most, are B, Li, Na and Mo. After 7 day tests, it is noticeable that the NL values for the aforementioned elements are much larger for unmodified P19-25 glass compared to P19-25C. However, this is not the case for the 28 day test. Considering the error bars (Std. Rel. deviation) it can be observed that NL values are generally alike with a slight tendency for lower NL for modified glass (e.g. B). Si shows much lower releases for modified glass in both tests. However, Ca illustrates the opposite behaviour to Si, where NL values are much higher for P19-25C sample. Elements such as

Al, Ba, Fe, Mg, Nd and Zr have insignificant NL values meaning that further description is not possible.

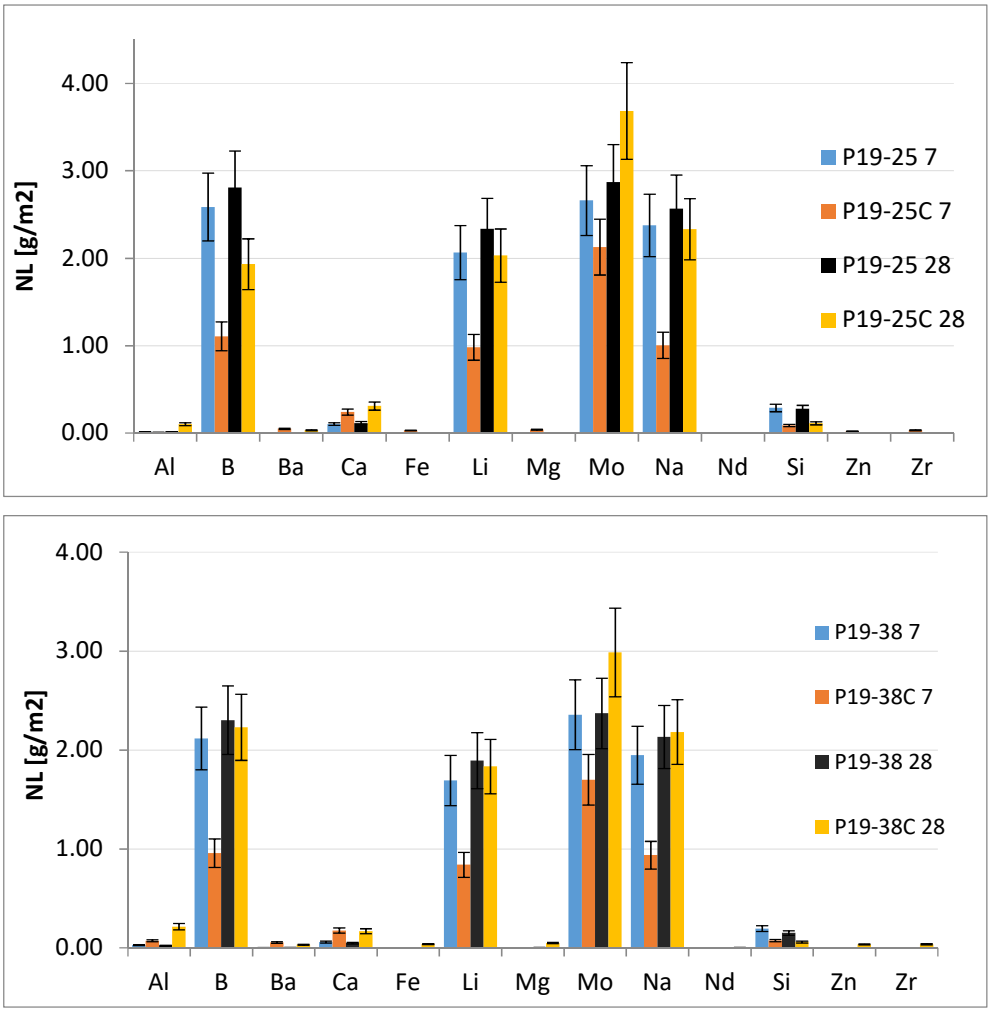

Figure 6.29 NL values of P19-25, P19-25C and P19-38, P19-38C glasses after 7 and 28 days

Figure 6.29 also shows ICP results after 7 and 28 days for P19-38 and P19-38C glasses. What becomes clear is that the elements that leached the most are again B, Li, Mo and Na. NL values for glasses after 7 day test are much higher for P19-38 than for P19-38C glass. The largest NL difference is observed for B and Na, which is approximately twice greater for the P19-38 sample than for P19-38C. On the other hand, 28 day test with incorporated error bars provides very similar results for both above-mentioned glasses. Other elements such as Ca show higher NL values for P19-38C (~ 0.17 g/m^2) than for the unmodified sample (~ 0.04 g/m^2), but Si again released at least 2.5 times fewer ions for P19-38C than for the P19-38 sample (e.g. 0.15 and 0.06 g/m^2 respectively, 28 days). Surprisingly, Al has much higher NL for P19-38C sample (~ 0.02 g/m^2) than P19-38 after 28 days test. Finally,

elements such as Ba, Fe, Mg, Nd, Zn and Zr have very small NL values which make further comment difficult. **Figure** 6.30 shows the grain of P19-38_7 glass with some precipitated round marks rich in Ca and Mo. The SEM investigated PCT samples did not contain a large amount of precipitated powellite marks and it was rather difficult to find them. Nevertheless, dissolved Ca and Mo during drying precipitated as powellite on the glass forming pale marks. This result corresponds well with above PCT results where mainly Mo was released in substantial amounts with some Ca (**Figure** 2.25). Finally, a comparable phenomenon was observed in the sample with P48 simulant.

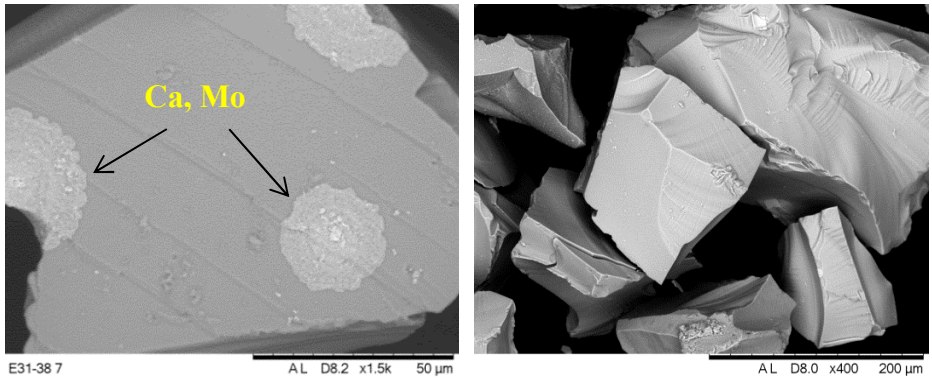

Figure 6.30 BSE image of P19-38 glass after 7 day PCT test

Figure 6.31 illustrates ICP data after 7 and 28 days for P0-25 and P0-25C samples. Elements, which leached the most, are B, Li, Mo and Na. It is clear that NL values after 7 day tests are greater for P0-25 than for P0-25C sample for mentioned ions (e.g. NL for B is circa 1.5 times greater). An exception here is Ca, which behaves in the opposite manner. On the other hand, NL values for those elements after 28 day tests seem to be comparable with a small exception for Mo. Greater NL values for Ca are still characteristic for P0-25C than P0-25 (0.154 versus 0.044 g/m^2). Si demonstrated the opposite leaching behaviour, where NL is greater for unmodified glass (0.147 versus 0.103 g/m^2 for P0-25C, 28 days). Remaining elements such as Al, Ba, Fe, Mg, Nd, Zr and Zn were leached in negligible amounts.

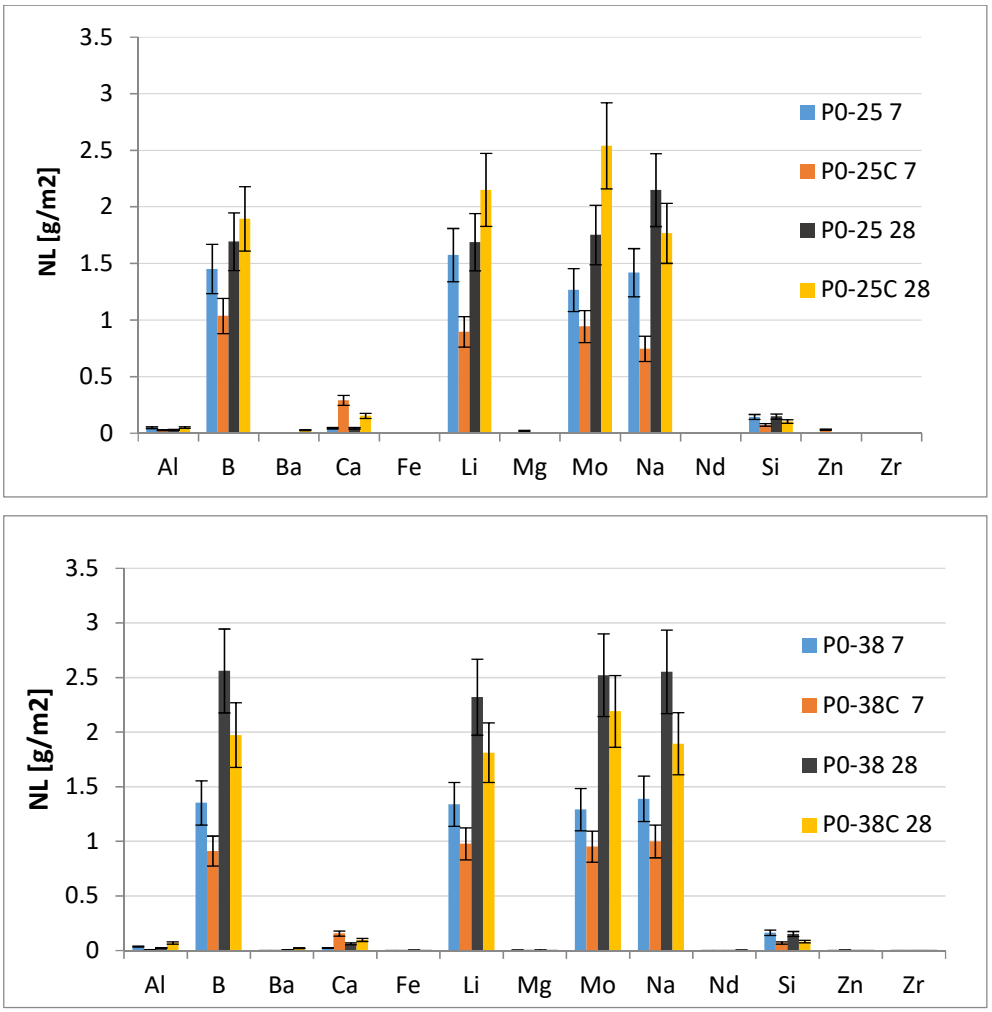

Figure 6.31 NL values of P0 -25, P0-25C and P0 -38, P0 -38C glasses after 7 and 28 days

Figure 6.31 also shows ICP results after 7 and 28 day tests for P0-38 and P0-38C samples. Once again, elements, which were released the most, are B, Li, Mo and Na. The 7 day tests present the same pattern, where modified sample has lower NL values. Moreover, this is also true for Si, where NL is about 2.4 times lower for P0-38C. Due to an extra addition of CaO, NL for Ca is nearly 7 times larger for P0-38C that is 0.155 g/m^2. After 28 day tests, elements with the highest NLs and Si have comparable, but slightly lower leaching tendency to the P0-38C sample. The rest of the elements mentioned before were leached in negligible amounts during all tests. **Figure** 6.32 shows a BSE image of P0-25C glass after 7 day test. This time it was not possible to see white regions containing Ca and Mo on the grains of glass. The reason for this is not clear, perhaps it is associated with low NL value for Mo in P0-25_7 glass.

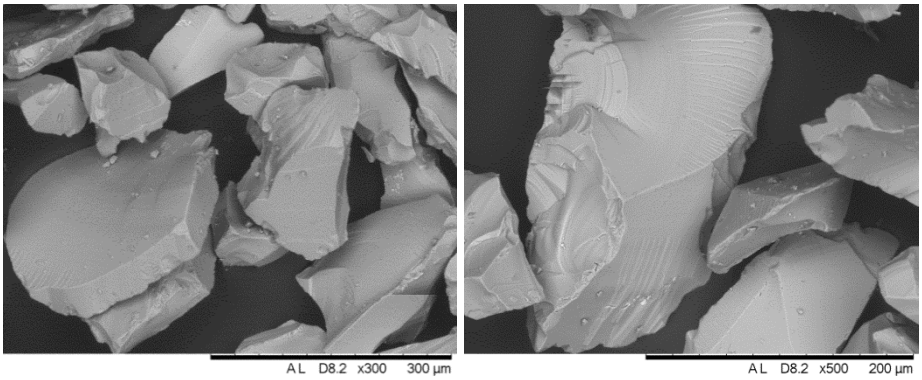

Figure 6.32 BSE image of P0-25C after 7 day PCT test

6.2 Discussion

6.2.1 Effect of P48 waste incorporation into CZ glass

Density

P48, P19 and P0 waste simulants were incorporated into the CZ glass which resulted in an increase of density of produced waste glasses. It is noticeable that modified samples are always denser than their non-modified counterparts. Based on **Figure** 6.1 density of the samples mainly depended on modification of the particular sample rather than the type of waste. For example, the densities of P19-25C and P19-38C are approx. greater by 9.5 % and 9.2% respectively compared to their unmodified counterparts i.e. P19-25 and P19-38. Moreover, that trend was observable as well for P0 type samples, where P0-25C and P0-38C are circa 14 and 10 % denser than their unmodified counterparts. It seems that the addition of Mn, Fe and Ca oxides which have higher densities than unmodified waste glasses are directly responsible for higher density values. As reported by Volf (1984) incorporation of CuO and Mn_2O_3 into silicate and/or borosilicate glass increases its density. As discussed above (p. 98) the structural role of CuO in silicate glasses is a network modifier (increasing NBOs). On the other hand, Mn_2O_3 is considered as intermediate oxide, which means that it may act as a glass former (CN 4) or/and modifier (CN 6) (Ehrt 2013).

T_g, T_p and Kissinger method

Comparing T_g values for P48 and P19 POCO containing glasses between 25 and 38 wt% waste loading, it is noticeable that T_g differences are within measurable error (±5 ^oC). Moreover, the same waste loadings for P48 with P19 type glasses also have T_g values measurable error (Fig. 6.6 - Fig. 6.7). This means that POCO content had a little effect on T_g for measured samples. Although, P0 samples are POCO free the T_g differences between waste loadings (25 and 38 wt%) remain within 8 ^oC (Fig. 6.8) and these values are similar the T_g temperatures of P48 and P19. Considering that aforementioned POCO wastes are MoO_3 rich, this could be in opposition to the research, which says that Mo tetrahedra are associated with modifying cations for example Ca^{2+}, Ba^{2+} to produce molybdate clusters in the glassy network, where the ratio of NBOs originally related to modifiers might be anticipated to decrease and therefore giving a more polymerised network.

The small variation in T_g results suggest that depolymerised domains caused by incorporation of variable waste loading (rich in MoO_3) did not increase in size If concentration of MoO_3 in the waste glasses was the dominating factor affecting T_g values, so samples with the highest POCO content (P48-38 or P48-25) should exhibit the lowest T_g which was not observed. These complex compositions (24 to 26 oxides) contains both oxides which normally increase T_g (e.g. Al_2O_3, ZrO_2, SiO_2) and ones which decrease T_g (e.g. CaO, Mn_2O_3, MoO_3, B_2O_3) giving overall unchanged values of T_g in these waste glasses (Volf 1984, Cassingham et al. 2008, Tan et al. 2015, Shelby 2005). The complex structural interaction in these samples is also expressed by strong overlapping of molybdate and silicate bands in Raman spectra that makes the deconvolution of Q species unfeasible. Therefore, other spectroscopic techniques are required to further examine similar T_g values, for instance ^{29}Si NMR.

In contrast, the T_p differences between those glasses are larger ranging from 5 ºC (P19-25, P19-38 and P0 25 -38) to 63 ºC amid P19-25C and P19-38C. The modified version of P0 type glasses also showed a large difference in T_p values (between waste loading 25 and 38 wt%) of 41 ºC. It is characteristic that the unmodified samples, which underwent much weaker crystallisation exhibit a typical exothermic peak, which is not observed for modified glasses that crystallised heavily and the crystallisation exothermic peak is much less apparent. The addition of Mn, Ca and Cu oxides is known for increasing the fluidity of the glass melt at given temperatures and it is thought that caused much stronger crystallisation in modified samples (Volf 1984, Shah et al. 1996). Caurant et al. (2007) states that fluidity could be an important factor supporting nucleation and crystallisation. In a temperature range where supercooled melt remains suitably fluid for long enough to make it possible for the diffusion of ionic species such as Ba^{2+}, Ca^{2+}, and MoO_4^{2-} to occur over a very short time to create nuclei, which then grow into crystals. It is believed that this delayed crystallisation might have increased the viscosity within the supercooled range and this eventually increased the activation energy of crystallisation (E_a, described below). It appears that higher fluidity of the melt could have helped the crystallisation of other phases to occur in comparison with non-modified glasses, especially P48-38, in which the crystalline peaks are less strong.

An incorporation of waste simulants which are enriched in many nucleating agents such as ZrO_2, MoO_3 or Cr_2O_3 should make the crystallisation easier which means that E_a ought to

be lower. Nevertheless, glass samples with a higher waste loading demonstrate much higher E_a values. According to Reben et al. (2011), nucleation-treated glasses should have lower activation energy for crystallisation. The higher E_a values for partially crystallised glasses can be explained by the formation of the secondary dispersed phases, which in turn increases glass viscosity and make crystallisation more energy demanding. Viscosity data obtained for investigated glasses with 25 wt% waste simulants loading show that viscosity at 850 °C is much lower for modified samples. What is more, XRD data also shows that the modified glasses are always more crystalline than non-modified ones. This could indicate that viscosity of modified samples with 38 wt% waste loading was lower (not measured) at some point, but strong crystallisation might have increased it. Eventually, this could have resulted in increasing the activation energy for crystallisation. This finding is in agreement with past investigations that demonstrate the viscosity increases as a function of time for samples with phase separation at given temperature (Simmons et al. 1974; Takamori & Tomozawa 1979)

Raman spectroscopy

Figure 6.14 shows Raman spectra of P48-25, P48-38 and P48-25C, P48-38C glasses. Incorporation of P48 simulant produced main bands at 320, 389 and 878 to 921 cm^{-1}. These bands are caused by MoO_4^{2-} units associated mainly with Ca and probably Ba, which means that molybdate tetrahedra are charge compensated by these elements, this is confirmed by XRD results (**Figure** 6.3). Based on Brinkman et al. (2013) the peak positions of Ca and Ba molybdates are very similar and cannot be distinguished. In a pure crystalline form, $CaMoO_4$ peaks should be around 879 cm^{-1} nevertheless in the aluminoborosilicate glass it was detected at around 919 cm^{-1} due to a strong ionic interaction of Ca^{2+} (strong field strength - F) with the silicate network. Furthermore, Ca^{2+} and Ba^{2+} ions are expected to bond to at least two NBOs and likely more by sharing NBOs. Caurant et al. (2010) noticed that Raman band in alumina borosilicate glasses in a similar position assigning it to a mutual interaction of Na and Ca ions with molybdate units. On top of that, viscosity values are lower for those modified glasses, which would make it easier for ions (e.g. mainly Ca^{2+} and Ba^{2+}) to move towards depolymerised regions, where MoO_4^{2-} units are located on cooling. Stronger crystallisation also agrees with the XRD results, which shows much stronger peaks, especially for P48-38C glass. In both cases (P48-25 and P48-25C) the shoulder at 878 cm^{-1} is converted into peaks at 38 wt% waste loading, and the intensity of that peak is greater for P48-38C suggesting the more crystalline nature of that sample.

Figure 6.15 shows two families of samples P19-25, P19-38 and P19-25C, P19-38C glasses. The formation of new peaks after P19 waste addition is mainly related to $CaMoO_4$ formation. P19-25 glass has a peak at 913 which converts into a shoulder in P19-38, but 878 peak is growing in the case of P19-38 glass. The transition of the 913 peak to 878 cm^{-1} also indicates the more crystalline nature of P19-38 glass, which formed more $CaMoO_4$. Moreover, it was reported (Chouard et al. 2011) that Mo-O stretching vibrations in glass has peak shifted from 878 cm^{-1} (crystalline) to 920 cm^{-1} (glassy matrix). Caurant et al. (2010) stated that 913 peak suggests that charge compensation mechanism for MoO_4^{2-} units is delivered by Ca and Na ions, but when it moved to 878 cm^{-1} this indicates that charge compensation is provided by Ca^{2+} only and the matrix possess more crystalline nature. On the other hand, the modified glasses show slightly different behaviour. P19-25C has a strong peak at 913 cm^{-1} with a tiny shoulder at 878 cm^{-1}. It is noteworthy that XRD pattern illustrates an amorphous character of that glass. This agrees with a claim that MoO_4^{2-} is both compensated by Ca and Na.

Subsequently, P19-38C sample shows much sharper molybdate peaks with some new peaks as well. The shoulder at 878 converts into a peak and 913 becomes smaller and distorted, but still not a shoulder. Other peaks at 320, 390 792 and 845 cm^{-1} are related to mentioned before $CaMoO_4$. This agrees with XRD earlier results, where that phase was identified (**Figure** 6.4).

P0-25 and P0-38 glass samples show some bands that can be seen at 320 and 922 cm^{-1} (**Figure** 6.16). The latter also has a shoulder at 877 cm^{-1}. As mentioned above these bands are associated with Mo-O stretching vibrations relate to $CaMoO_4$. Comparing P0-25 with P0-25C Raman spectra it can be noticed that the latter possess much larger peaks at 913 cm^{-1}. In the case of modified glasses, peaks at 913 are actually shifted to 921 cm^{-1} due to a slightly different charge compensation mechanism that was described above. P0-38C has also a clear shoulder at 877 cm^{-1} which is associated with $CaMoO_4$. Additionally, bands for P0-38 and P0-38C (mainly) are larger indicating that the molybdate content is greater. Indeed, XRD data shows that greater intensity of powellite peaks suggesting more crystalline samples.

SEM/EDX

Figure 6.18 compares P48-25 and P48-25C glasses. In both cases, there is a group of crystals where the size of individual crystals in these agglomerations is much bigger for P48-25C (~ 5μm), unlike for P48-25 where individual crystals are far below that value. X-ray maps show that both glasses contain mainly Cr and Fe with some incorporation of Zn, however, crystals in P48-25C also contain Mn and Na substitutions and the intensity of the X-ray signal is stronger (brighter images **Figure** 6.19). This agrees with the XRD results where a $FeCr_2O_4$ spinel phase was identified. Moreover, spinels are chemically flexible crystals able to incorporate wide range of other elements to produce solid solutions (Donald 2010). According to Hrma et al (2005), the presence of spinel-forming oxides (Fe, Zn, Ni, Mn and Cr oxides) in a glass may cause precipitation of those crystals on cooling. This agrees with the XRD results where $FeCr_2O_4$ spinel phase was identified with some traces of Mn and Zn. **Figure** 6.18 represents P48-38 and P48-38C glasses. The former one shows a large crystal aggregates mainly rich in Mo and Ca surrounded by a cloud of tiny crystals of spinel enriched mainly in Cr and Fe. Furthermore, based on XRD and SEM results, P48-38C apart from containing $CaMoO_4$ and spinel also contains ZrO_2, SiO_2 (α - quartz), and $BaMoO_4$. It needs

to be highlighted that Zr appears not to react with Si to form zircon which is evidenced by the dark areas in Si map, where the Zr signal is strong. The added CuO is not found to be a part of any crystals particularly spinels, which remains in good agreement with Matyáš et al. 2012.

Figure 6.21 compares BSE images of P19-25 and P19-25C glasses. The former shows bright and dark bands. This illustrates the heterogeneity of that sample at large scale. The brighter layers are enriched in Zr, Mo and Al, but the dark layers are enriched in Si. Conversely, the second sample P19-25C does not show any layers but rather homogeneous glass with some grouped spinels. **Figure** 6.22 confirms that the spinel crystals are enriched in Cr, Fe, Mn and Zn. This disagrees with the XRD results, which shows that P19-25C is a crystal free sample. These results suggest that spinel concentration is below detection level. Furthermore, P19-38 and P19-38C samples (**Figure** 6.21) show heavily crystalline samples. The former contains large crystals (~20 μm across) which relates to $CaMoO_4$ bases on elemental composition. These large crystals are neighboured by a tiny crystallites (<< 5 μm) corresponding to aforementioned spinels containing Cr, Fe and Zn.

The second image possesses very dissimilar morphology mainly due to the size of the crystals. It also contains some spinels, which are additionally enriched by Mn ions, and the size is larger than the previous glass (~ 10 μm across). The new crystalline phase contains Zr identified by XRD as ZrO_2. However, **Figure** 6.23 related to Si X-ray maps indicates that some $ZrSiO_4$ may be formed too. It can be also seen $CaMoO_4$ crystals are scattered across the sample in the form of tiny (<< 1 μm) globular light spots. What is interesting these crystalline spots were not found in the image of P19-38 sample. Based on viscosity measurements (**Figure** 6.2) sample P19-38C is more fluid than P19-38. Therefore, this suggests that more fluid melt of P19-38C had more time to facilitate nucleation and growth of powellite.

P0-25 and P0-25C images are presented in the **Figure** 6.24. Both of them have magnification 500 times with some crystals (<2 μm across). The former sample is enriched in Cr and Fe (some Zn) and the latter sample has crystals containing also Mn ions. All these findings correspond well with XRD data (**Figure** 6.5) where $FeCr_2O_4$ spinel is identified. Moreover, images of Ca and Mo from P0-25C are brighter, than their unmodified counterparts. This also follows XRD section (**Figure** 6.5b) in which $CaMoO_4$ peaks are larger indicating

greater concentration of powellite. Furthermore, 38 wt% P0 waste loading resulted in the formation of another phase that contains Zr and Ce. This phase was found in both glasses (P0-38 and P0-38C) in conjunction with the above mentioned spinels. According to XRD, this phase is $Ce_{0.62}Zr_{0.38}O_2$.

PCT

NL values for the P48-25 and P48-25C samples after 7 and 28 days showed that B, Li, Mo and Na leached the most from these glasses (**Figure** 6.27). It can be said that after 7 days tests B, Li and Na releases are about 1.7 times higher for the P48-25 glass than for P48-25C, but Mo release looks comparable. High values NL of alkaline elements (Na, Li) is related to their role as a network modifier with low field strength. However, B tend to convert from BO_3 triangles to BO_4 tetrahedra on cooling. The modified sample (P48-25C, lower viscosity) should have slightly longer time to enable boron conversion (Caurant et al. 2007). This in turn, should involve more ions such as Na^+ and Li^+ charge compensating BO_4^- units hence making these species less leachable and decreasing their NL values (observed for P48-25C after 7 days). The place of Mo in the glass is different, because it is not incorporated into silicate network only existing as MoO_4^{2-} units (oxyanions) in depolymerised regions (DR), where it is charge compensated mainly by alkaline and alkaline earth elements (Caurant et al. 2007; Caurant et al. 2009). Moreover, Si NL values are circa 2.5 higher for P48-25 glass. In the case of Ca NL displays the opposite trend and it is nearly 2.9 times lower for P48-25 glass, than for P48-25C counterpart with added extra CaO. The literature suggests that moderate additions of CaO and ZnO to borosilicate glass improved the glass chemical durability and meltability (Zhang et al. 2015; Ojovan and Lee 2005). Ca acts mainly not as a modifier, but preferentially charge compensates MoO_4^{2-} to produce a durable powellite phase (Chouard et al. 2011; Caurant et al. 2009). The addition of Ca to borosilicate glass was found to strongly increase the amount of BO_4 units (> 5 mol% CaO) on heat treatment. Also, CaO (> 5 mol%) start forming $Si\text{-}O^-\text{-}Ca^{2+}\text{-}O^-\text{-}Si$ or $Si\text{-}O^-\text{-}Ca^{2+}\text{-}O^-\text{-}B$ units, which is believed to reduce phase separation (Miyoshi et al. 2004). Finally, NL values for all tests for Ba, Fe, Mg, Nd, Zn and Zr appear to be very small. Low NL values of Fe, which is oxidised (Fe^{3+}, Mössbauer data) suggest its glass forming role in the investigated samples. Moreover, Cassingham et al. (2008) reported that Fe_2O_3 incorporation into borosilicate glass drastically improved it durability (up to 10 wt%).

It was reported (Schreiber et al. 1987) that Fe and Mn form a redox couple, where Mn is reduced to 2+ and Fe is mostly oxidised to 3+. However, Mossbauer data for P19-25 and P19-25C, (similar to the samples analysed here) in both cases showed that Fe was completely oxidised. Therefore, it appears that mutual redox interactions in examined multicomponent glasses were possibly more complex, than a redox couple between Mn and Fe. Additionally, negligible leaching of Zr and Al can be related to the fact that those oxides in small amounts exert a positive effect on durability (Volf 1984). Nd is another ion which leaching was close to zero. It was reported by Volf 1984 that incorporation of lanthanoids does not impair glass durability only decreases its viscosity. Its structural role in borosilicate glass is associated with DR (Depolymerised Regions), where Nd^{3+} ions are surrounded by 6 to 8 NBOs located in the same silicate region as MoO_4^{2-} entities, which improves Mo solubility in the glass (Chouard et al. 2011). Finally, Quintas et al. (2011) observed that Nd stable environment in depolymerised regions is little affected by changing modifiers owing to its high field strength.

Figure 6.27 shows also NL values after 7 and 28 days for P48-38 and P48-38C samples. It is noticeable that leaching trends observed above are present here as well. After 7 days, again the same elements B, Li, Mo and Na are leached the most from the glass. What can be observed is that B, Li, Na and Si (much smaller NL) show larger leaching values for unmodified glass P48-38 (excluding Mo). Al mass loss appears to be similar to both glasses, but Ca is greater for P48-38C. However, after 28 days NL values for non-modified and modified compositions again looks comparable to each other after considering measurement errors. Elements such as Ba, Fe, Mg, Nd, Zn and Zr possess NL values close to zero. Comparing NL values after 28 days, it is seen that elements which leached the most (B, Na, Li, Mo) show slightly larger NL values for 38 than 25 wt%. waste loaded samples. This shows that higher waste incorporation (38 wt%) has little detrimental effect on the leachability of the examined elements.

Figure 6.29 shows the highest NL values for B, Li, Na and Mo after 7 and 28 day tests for P19-25 and P19-25C plus P19-38 and P19-38C.The leaching pattern described above is also seen in this case, meaning that NLs after 7 days tests are over two times greater for unmodified samples than for modified ones - P19-25C (B, Li, Na) unlike Mo (similar in both). Though, in general 28 day tests show comparable NLs for both type glasses including error bars.

P0 type samples also show analogous dissolution behaviour to the P48 and P19 samples (**Figure** 6.31). Finally, SEM of P0-25C glass did not show characteristic white features indicative of powellite on the glass grains suggesting lower concentration of powellite from the solution that would reflects the lowest MoO_3 concentration in P0 waste simulant among all examined waste streams.

6.3 Conclusions

Modified samples in this chapter have shown better fluidity and stronger crystallisation by having comparable chemical durability towards unmodified samples. Industrially it is important to be able to incorporate maximum amount of waste without compromising the chemical durability and fluidity of the melt. Lower viscosity provides an opportunity to slightly decrease melting temperature and associated with it volatility of the molten waste glasses. Based on the results and discussion related to all waste simulants incorporation into CZ glasses the following conclusions can be drawn:

- Modified waste glasses (25 and 38 wt% waste loading) are always denser than their unmodified counterparts.

- Viscosities of non-modified samples with 25 wt% waste loading are similar to each other and are always lower, than their modified counterparts (more fluid). It is believed that, all non-modified waste glasses with 38 wt% waste loading were also more viscous than their modified counterparts (not measured).

- In all cases, 38 wt% waste incorporations resulted in stronger crystallisation, than 25 wt% waste loading.

- Incorporation of P48, P19 and P0 waste simulants has a small effect on the T_g and T_p values for unmodified samples and slightly stronger effect on their modified counterparts especially with respect to T_p values.

- Activation energy of crystallisation (E_a) at 38 wt% waste loading is increasing in the following order P0-38(C), P48-38(C) and P19-38(C) for both (un)modified glasses.

- Peaks in Raman spectroscopy are mainly related to $CaMoO_4$ and the major peak of (P48, P19 and P0)-25C and (P48, P19 and P0)-38C is shifted from circa 921 (916 for P19-25) to 912 cm^{-1} suggesting a dual charge compensating role between MoO_4^{2-} tetrahedra and
- at least Ca and Na ions simultaneously, compared to non-modified counterparts, which are likely to be charge compensated by Na^+ only.

- Mössbauer data proves that iron in P19-25 and P19-25C is almost fully oxidised (Fe^{3+}) suggesting its network forming role improving chemical durability.

- SEM/EDX analysis confirms the presence of some crystals identified by XRD: powellite with $FeCr_2O_4$ (spinel) and zirconia. Interestingly, Ca and Ba molybdates are usually not seen at a given magnification (typically white tiny spots). SEM investigation shows that more uniform glasses are obtained with 25 than 38 wt% waste loading.

- PCT test clearly shows larger NL values after 28, than 7 days for 25 and 38 wt% waste loading for all waste simulants. After 7 day tests, modified samples demonstrated almost twice-lower NL values regarding B, Li, Na and Si than, unmodified counterparts. However, 28 day tests show usually comparable NLs for both type samples.

7. Corrosion tests of Inconel 601 & Nicrofer 6025 HT

This chapter investigates the effects of some of the glasses studied on corrosion resistant super alloys: Inconel 601 and Nicrofer 6025HT used for vitrification of nuclear waste by NNL (Harrison et al. 2014). NNL has indicated that Inconel 601 melters were unreliable for melting MoO_3 rich (~ 12 wt %) waste glasses and lasted less than 10 melting cycles, however, Nicrofer 6025 HT melters lasted over 400 melting cycles (NNL 2014). Thus, it was essential to conduct the corrosion tests to establish their performance with tested P type glasses. The CZ and CZ1 glasses studied to establish the source of alumina in the surface voids in Inconel 601.

Figure 7.1 shows an example of a Nicrofer coupon and an Inconel 601 crucible used for corrosion tests with two zones **a** – area above the glass melt, and the **b** - area below the melt surface (submerged), where the original coupon dimensions are 15 x 50 x 1 mm. Initial test using CZ and CZMF-15P glasses used Inconel 601 crucibles for corrosion tests, where only 'below' area was examined.

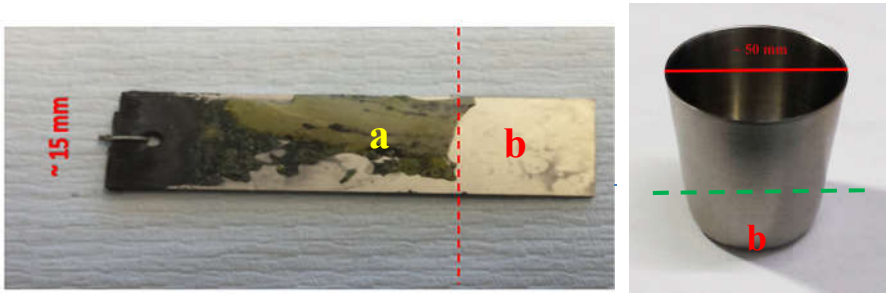

Figure 7.1 Nicrofer 6025 HT coupon and Inconel 601 crucible used for corrosion tests with **a**- above the glass melt and **b**- below the glass melt.

7.1 Inconel 601 tests in CZ glasses

Figure 7.2 shows images of Inconel 601 after corrosion tests conducted for 6 h in CZ and CZ1 (without Al_2O_3) glasses. In both cases, the surface of the Inconel coupon is corroded and full of tiny voids inside the metal. The depth of the voids reaches around 50 µm and it has wider channels (stronger surface corrosion) for CZ1. Those channels are rich in Al and O for both samples (**Figure** 7.3). Thus, the origin of Al and O is not from the glass but from Inconel. Additionally, the glass/Inconel interface is separated by a scale rich in Cr, Mn and a little Zn which is believed to be a spinel-type material. However, that scale is more coherent for CZ than for CZ1 due to a weaker corrosion causing a protective chromia scale on the Inconel/glass interface and dissolving some Cr in the CZ glass (green colour, Volf 1984) (**Figure** 7.2a).

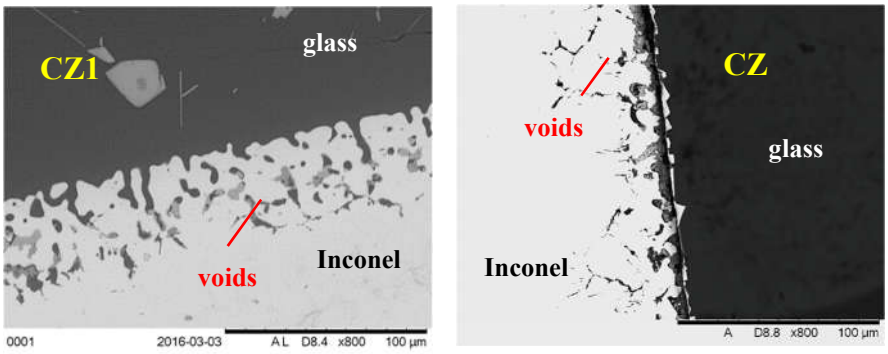

Figure 7.2 Inconel 601/glass interfaces for CZ1 and CZ after corrosion for 6h

Figure 7.2a CZ glass after corrosion test in Inconel 601 crucible

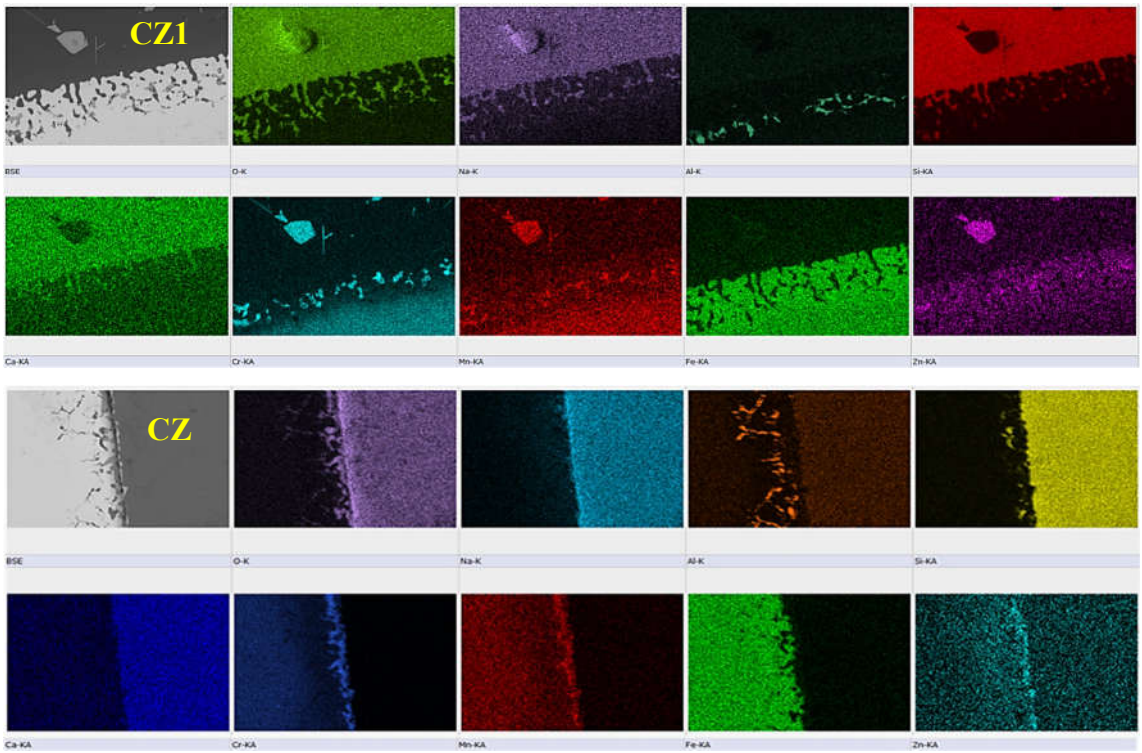

Figure 7.3 X-ray maps of glass/Inconel 601 interfaces after corrosion in CZ1 and CZ for 6 hours.

Figure 7.4 shows images of Inconel 601 corrosion tests with the composition containing 15 wt% of POCO waste (CZMF-15P glass) after 15 minutes, 1 and 6 hours submerged in the melt. In all cases, the chromia rich scale is continuous which provides protection from intensive dissolution of Inconel 601 in the glass melt. What becomes obvious is that the thickness of that chromia scale is much larger after 6 h (~ 6 µm) compared to 1 hour test (~ 2 µm). Formation of voids is observable just after 15 minutes of the glass melting and their depth reaches to around 6 µm whereas the chromia scale grew to around 1.6 µm. Based on **Figure** 7.5 these Cr-rich layers are also enriched in Mn, but Fe is mainly kept outside. These scales also prevent glass penetration into the voids in the Inconel which are enriched in Al and O. Ni that is a part of Inconel alloy that is not as reactive as Cr and does not readily enter the glass regardless of the test time. According to Martino et al. (2004) Cr is easier to corrode in a glass melt than other metals such as Fe, Ni and Co. Finally, some crystals containing Zr and Si are always present near the chromia layer which suggest the formation of $ZrSiO_4$ identified in previous chapters.

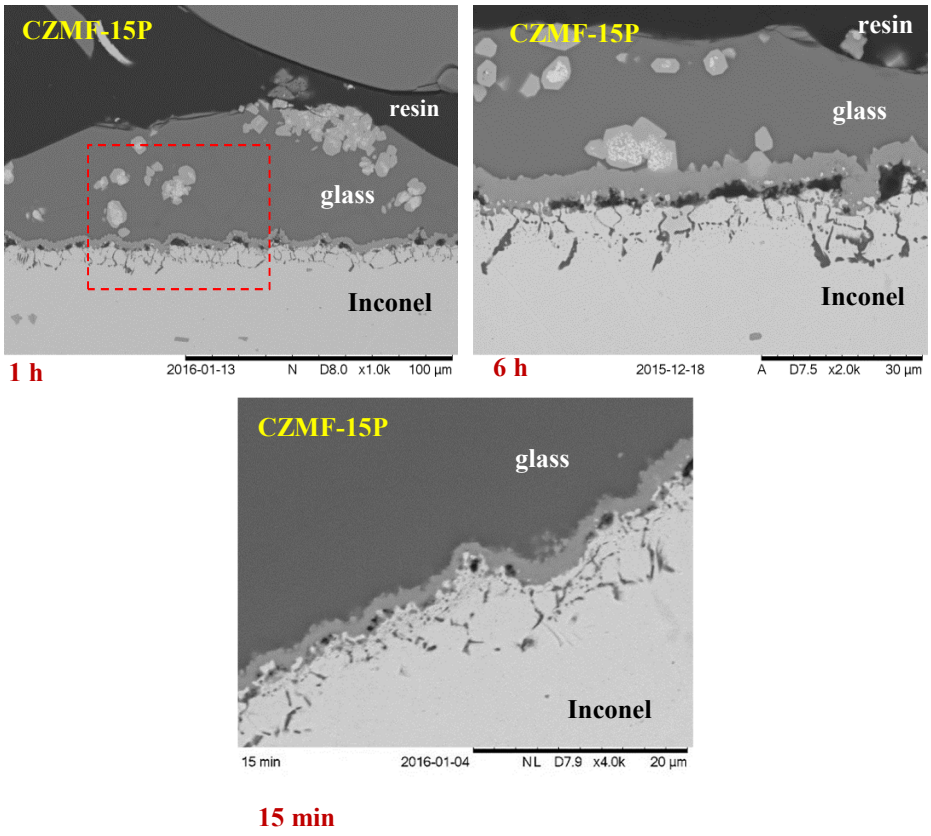

Figure 7.4 Inconel 601/glass interfaces for CZMF-15P after corrosion for 15 min., 1 and 6 h

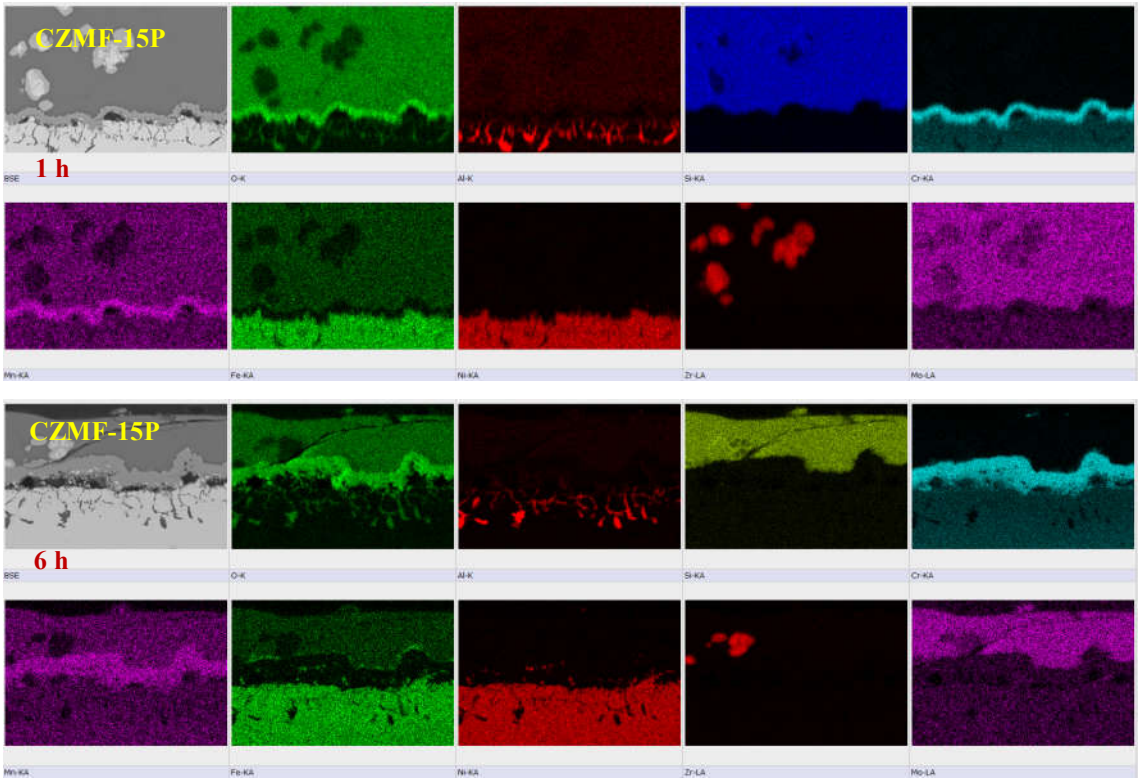

Figure 7.5 X-ray maps of glass/Inconel 601 interface after corrosion in CZMF-15P for 1 and 6 hours.

7.2 Inconel 601 with P19 and P48 waste glasses

P19 type glasses

All corrosion tests in this part have been done for 12 hours to achieve a stronger effect of Inconel 601 dissolution within waste glasses. **Figure** 7.6 shows images of Inconel corrosion with P19-25 and P19-25C glasses above (a) and below (b) the surface of glass melts. It can be seen in **Figure** 7.7 that both samples with sections placed above the melt developed a glassy layer rich in Ca and Mo crystals, which indicates the formation of identified before $CaMoO_4$. Moreover, a characteristic chromia layer is present in both cases with a tendency to be thicker for P19-25C a (~ 6µm) compared to P19-25 a (~3µm) (Fig. 7.6). Additionally, two last images (b) in **Figure** 7.6, shows either Inconel 601 without a glassy layer (damaged by thermal mismatch) or a glassy layer with a characteristic chromia rich scale along the Inconel. This layer is shown by X-ray maps for P19-25C b sample that has some attached glass (**Figure** 7.8).

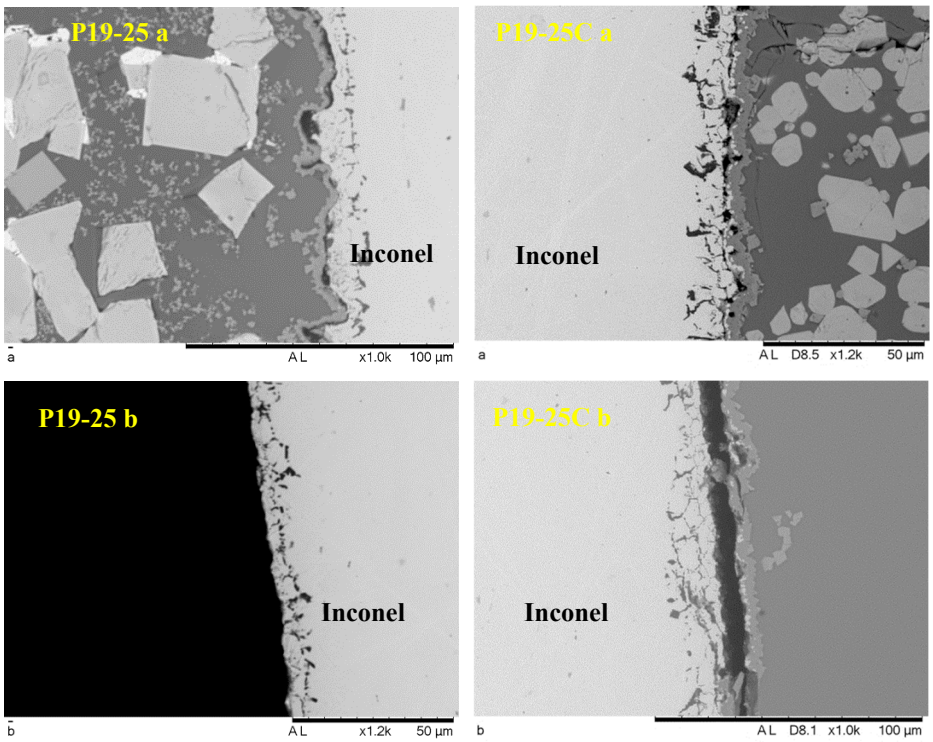

Figure 7.6 Cross sections of glass/Inconel 601 interfaces after corrosion in P19-25 and P19-25C above and below the glass melt surface.

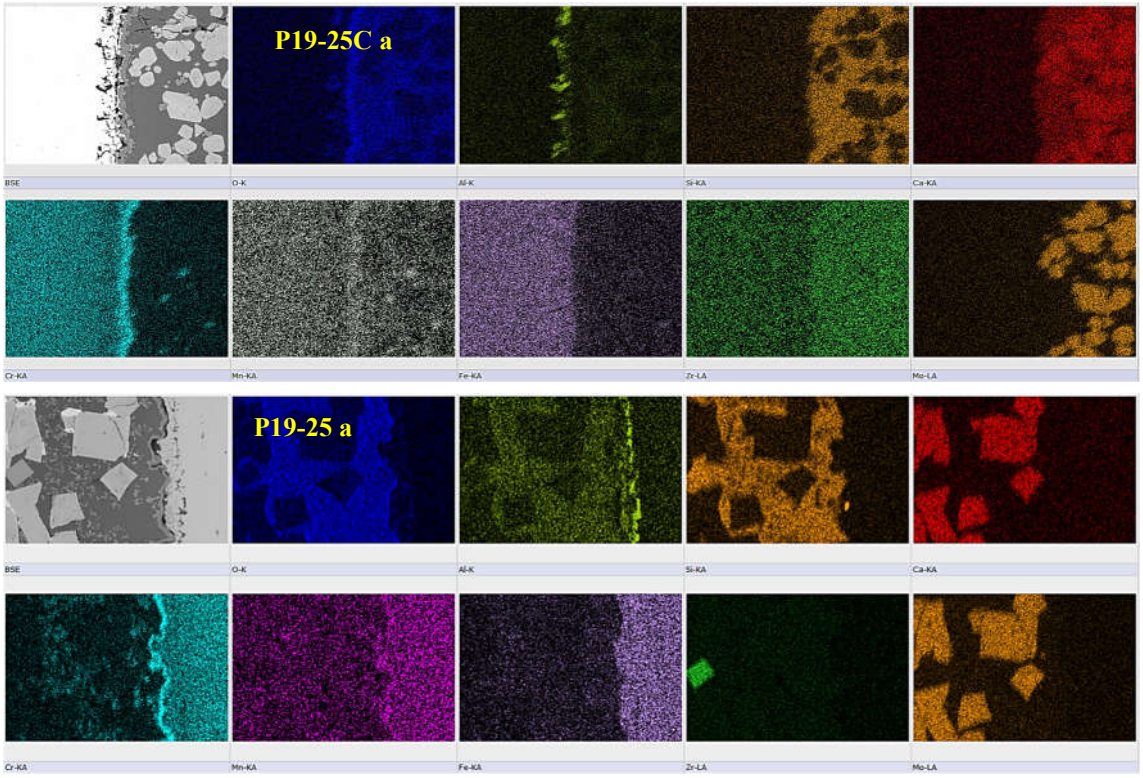

Figure 7.7 X-ray maps of glass/Inconel 601 interface after corrosion in P19-25 and P19-25C above the glass melt

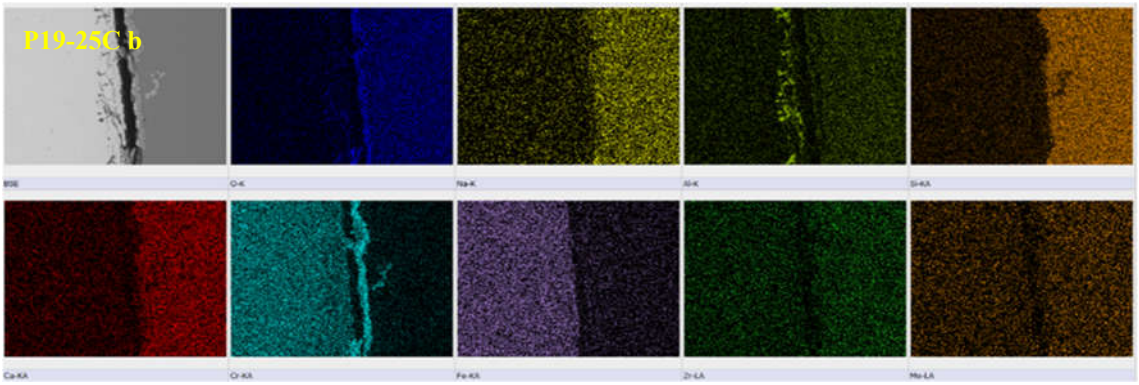

Figure 7.8 X-ray maps of glass/Inconel 601 interface after corrosion in P19-25C b

Figure 7.9 shows the corrosion between Inconel plates and P19-38 and P19-38C glasses. It can be observed that the top images (a) contain a Cr and O containing layer, presumably chromia layer along the Inconel surface and well-developed crystals containing Ca and Mo as shown in the X-ray maps (**Figure**s 8.10, 8.11). Another typical feature is Al and O rich area filling the voids parallel to the surface. It seems that modified P19-38C a glass possesses a slightly thicker chromia scale than the unmodified sample (P19-38 a) in the 'above' zone and that $CaMoO_4$ formation is stronger for the modified counterpart.

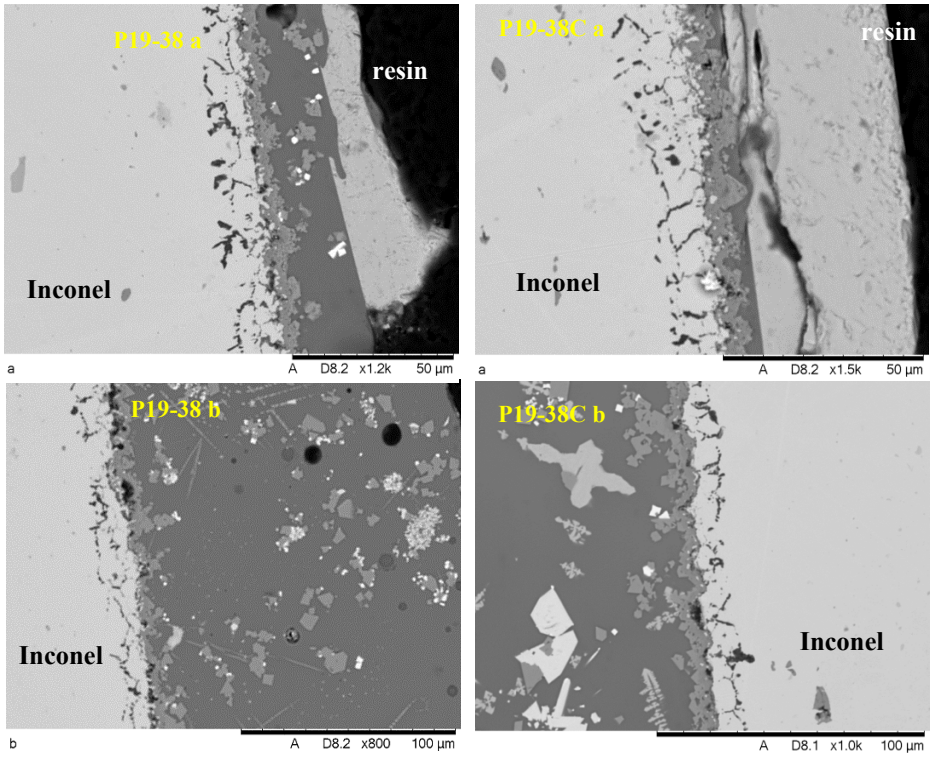

Figure 7.9 Inconel 601 /glass interfaces for P19-38 and P19-38C after corrosion a) & b) areas

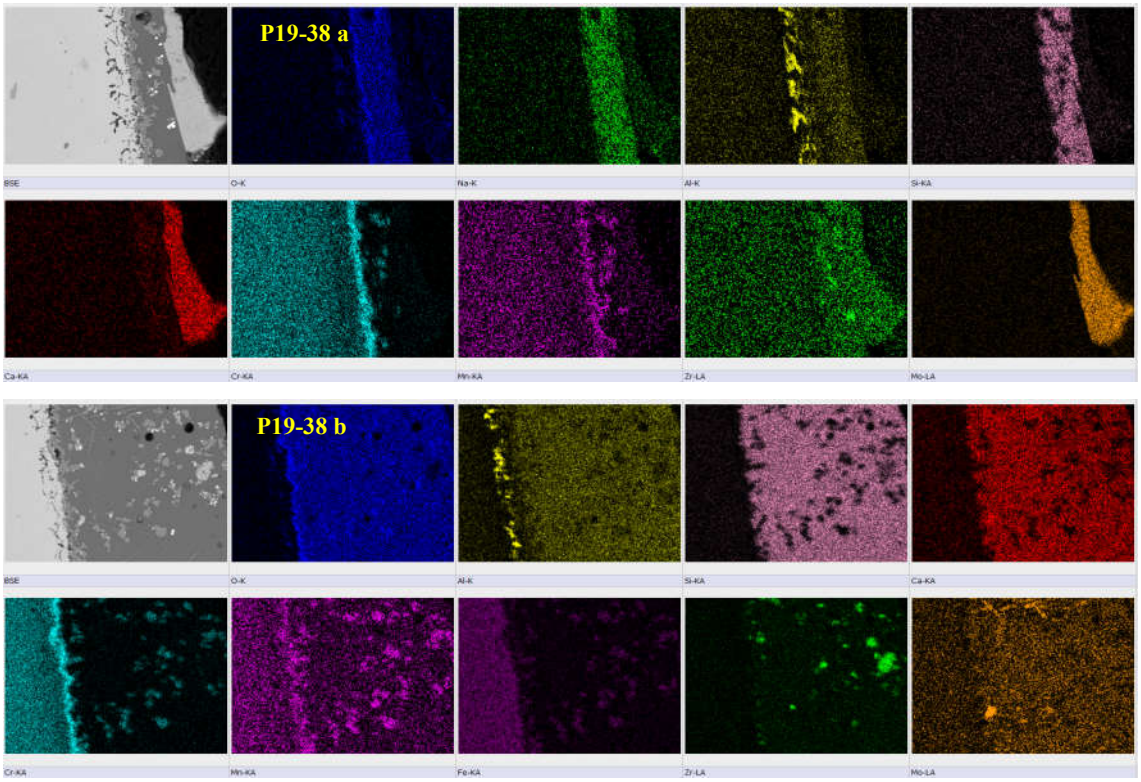

Figure 7.10 X-ray maps of glass/Inconel 601 interface after corrosion in P48-38 a) & b)

Figure 7.9 illustrates corrosion of Inconel 601 submerged inside the melt (P19-38 b and P19-38C b). Interestingly, adjacent glasses are crystal-rich, unlike P19-25 and P19-25C waste glasses, which is presumably related to higher waste loading (38 wt%). **Figure** 7.10 (P19-38 b) proves that these crystals are rich in Cr, Mn and some Fe plus another crystal containing Zr. P19-38C b contains three types of crystals rich in Cr, Mn and Fe, plus Zr and Ca with Mo. It seems that the chromia rich layer is much thicker in the submerged area for modified glasses. It is confirmed again that $CaMoO_4$ crystals form much more above the glass melt, which was also observed for P19 type glasses **Figure 7.11**. Moreover, the effects of strong Mo volatility was also experienced during corrosion tests conducted by NNL, where the parts of the coupons above the glass melts were corroded the most (Harrison et al. 2014a; Harrison et al. 2014b)

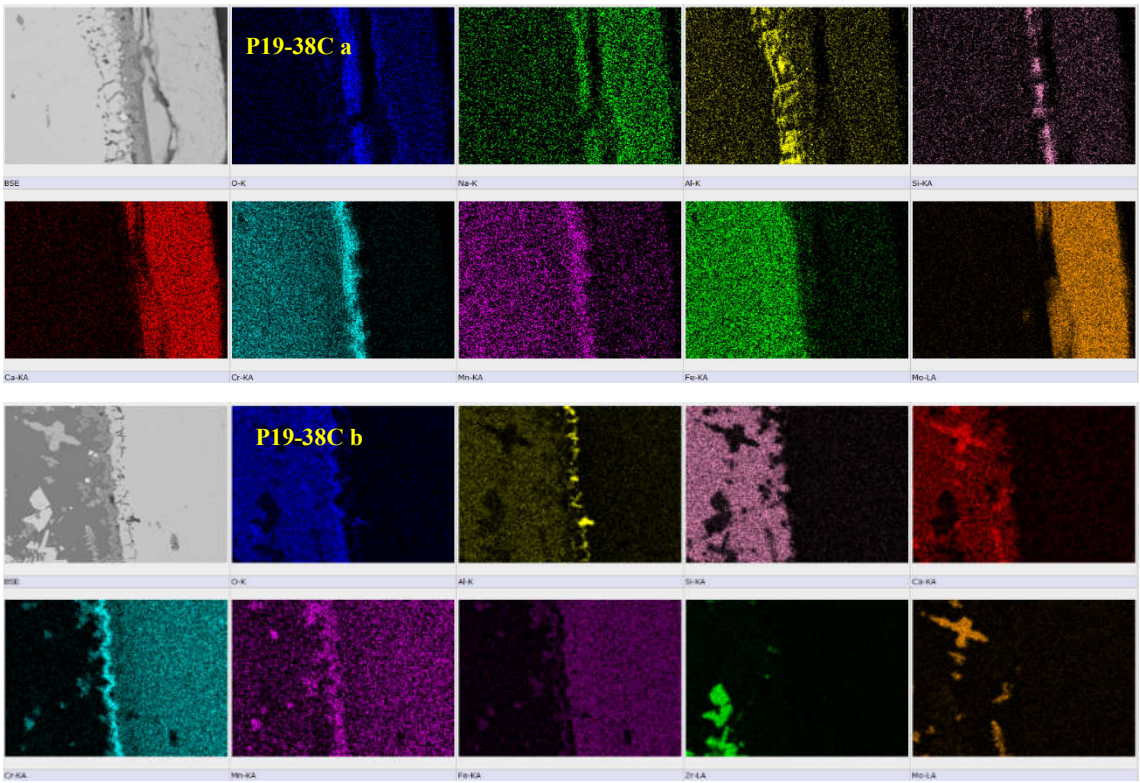

Figure 7.11 X-ray maps of glass/Inconel 601 interface after corrosion P19-38C a) & b)

P48 -38 glass

Figure 7.12 shows images representing corrosion of Inconel 601 plate in the P48-38 and P48-38C glasses. Comparing two samples from 'above' area both samples exhibit the characteristic chromia layer which is thicker and more coherent for P48-38C than for P48-38. To some extent this might be related to lower viscosities of modified glasses and therefore slightly higher corrosion. **Figure** 7.13 shows identify crystals containing Ca with Mo and Zr with Si that probably correspond to powellite and zircon found before in this type of glass by XRD. Those crystals appear to have oxygen depleted zones, but O is a low Z element and it forms soft X-rays which could be reabsorbed by the sample. The two remaining SEM images in the **Figure** 7.12 shows zones submerged in the melt, but without any adjacent glass to Inconel surface. Nevertheless, they show characteristic voids along the coupon's surface rich in Al and O (X-ray maps not provided).

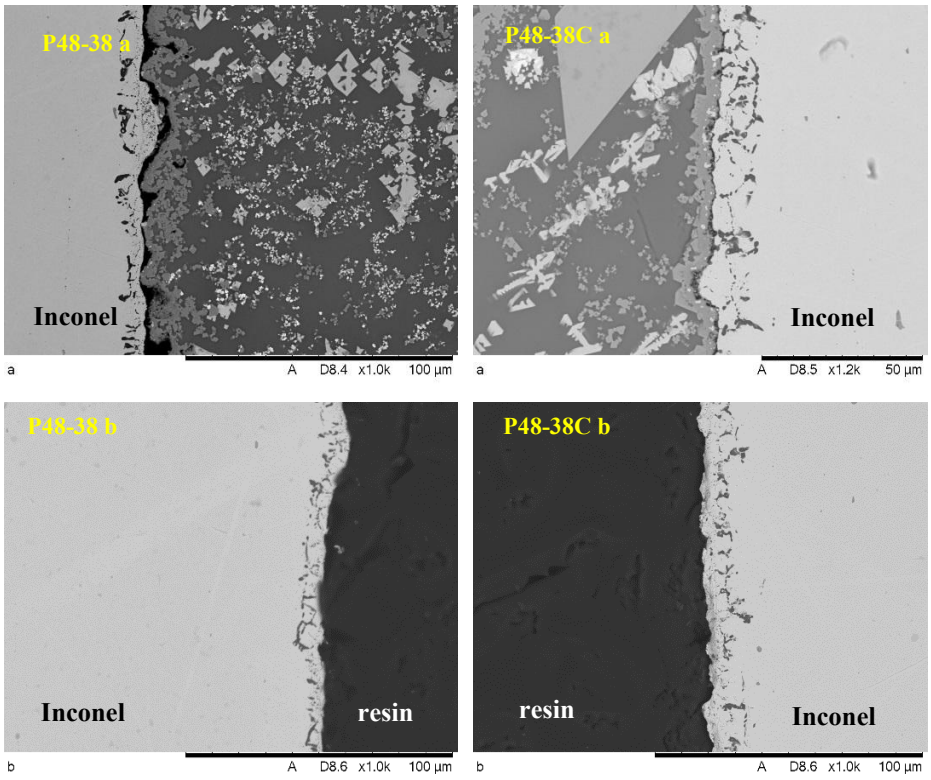

Figure 7.12 Inconel 601 /glass interfaces for P48-38 and P48-38C after corrosion a) & b)

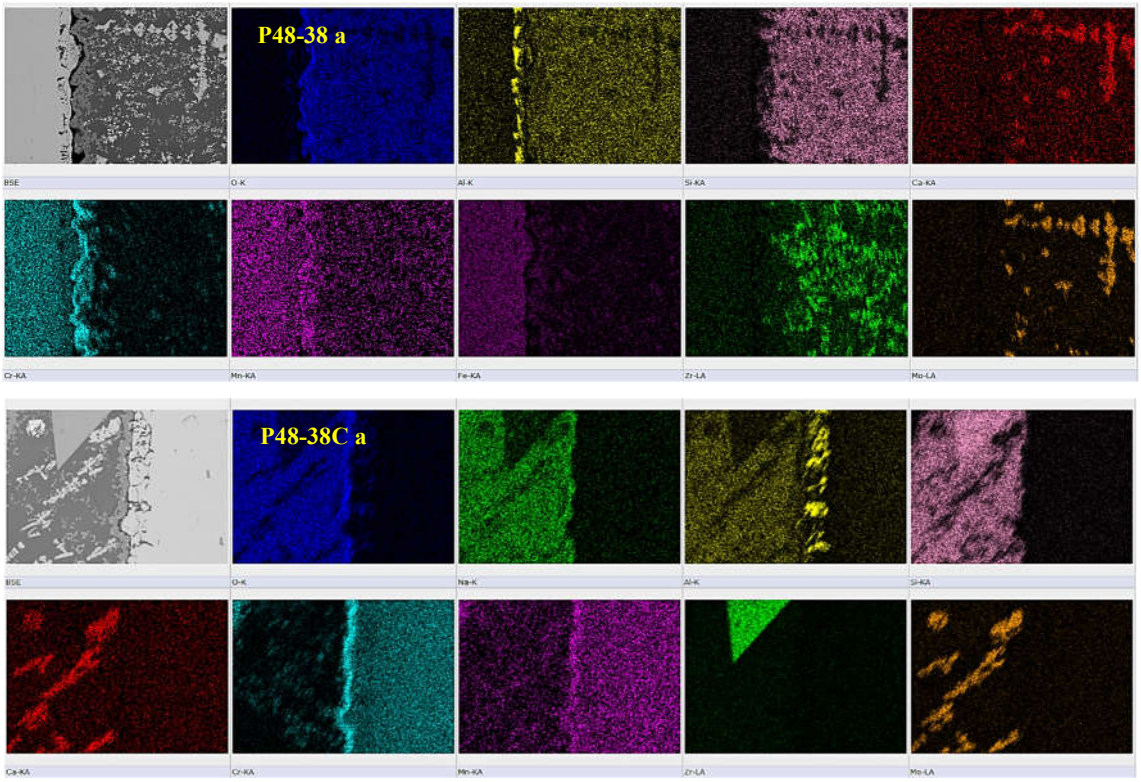

Figure 7.13 X-ray maps of glass/Inconel 601 interfaces after corrosion in P48-38C a) & b)

7.3 Nicrofer 6025 HT and P19 and P48 waste glasses

Figure 7.14 shows the images of the corrosion tests of P19-25 and P19-25C glasses with Nicrofer plates. The top two images represent the 'above' area, which was affected by the volatilised species of the glass melt. Both cases show a weak chromia layer with Al and O rich voids. Crystals rich in Ca with Mo are found in both images with a tendency of powellite crystals to be nearer to the plate edge (~ 10 µm) for the P19-25C than for P19-25 glass (~ 30 µm), implying earlier volatility and formation of powellite in the region for modified sample. Additionally, two square-shaped crystals in P19-25 image contain Zr with Si (**Fig**. 7.15). The two remaining BSE images show the corrosion of the coupon in the 'below' area with typical voids along the edge enriched in alumina. The chromia scale is observed only for P19-25C b with adjacent glass unlike P19-25 b (X-ray maps not included here).

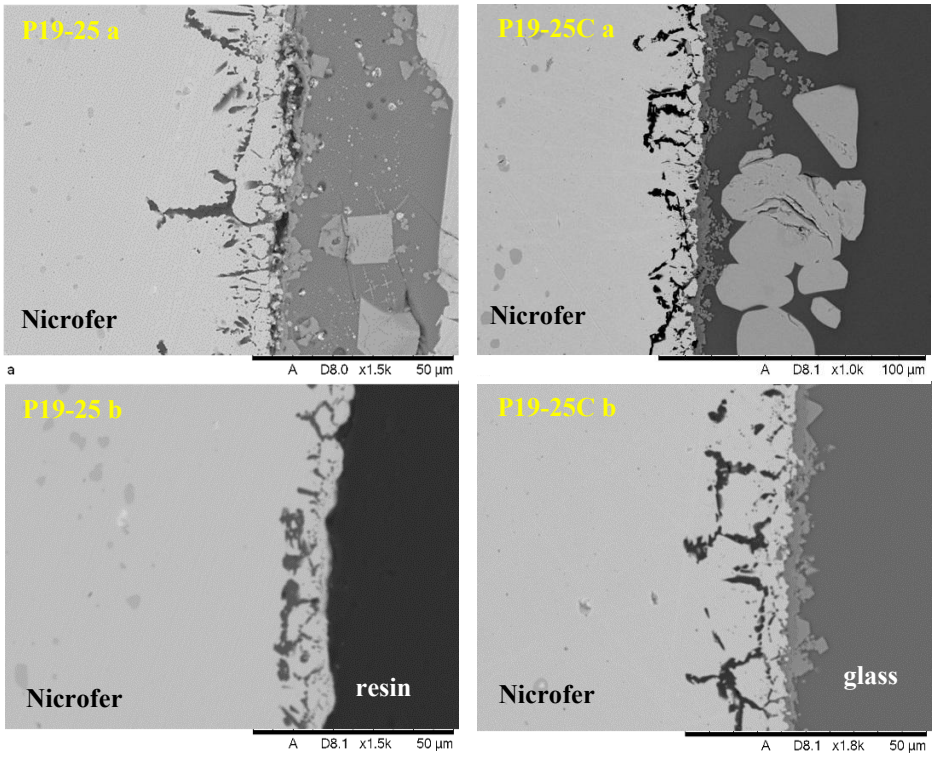

Figure 7.14 Nicrofer 6025 HT/glass interfaces for P19-25 and P19-25C after corrosion a) & b)

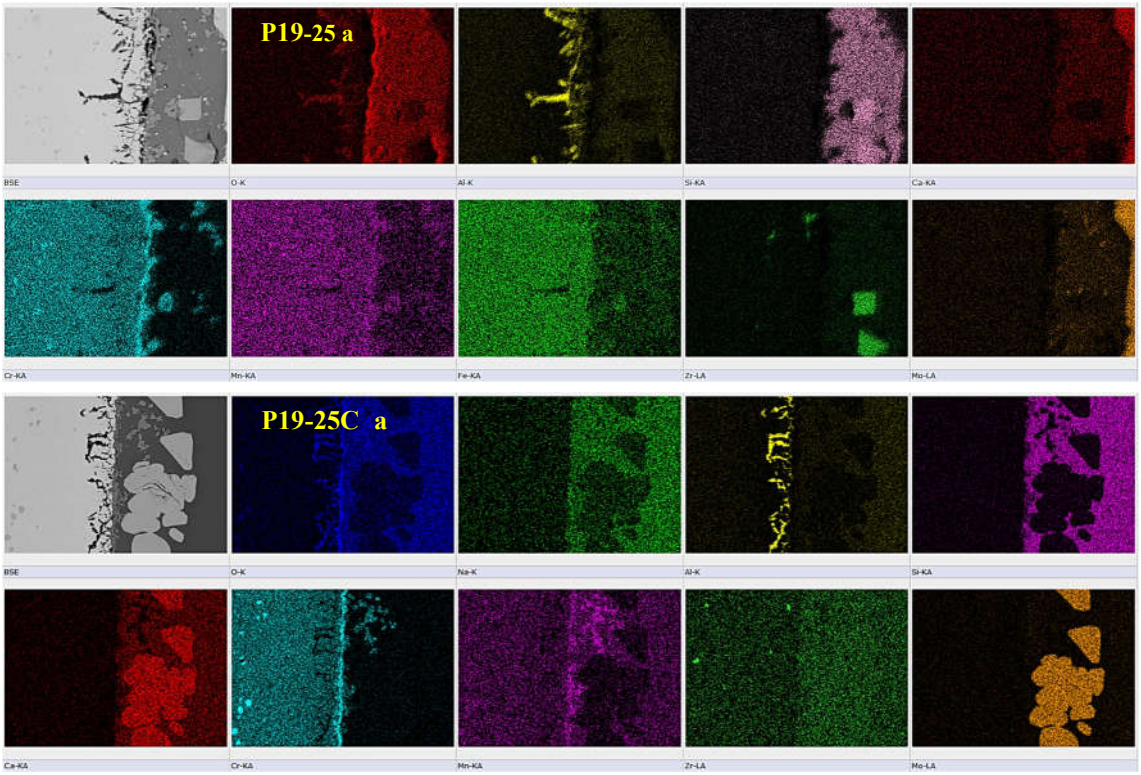

Figure 7.15 X-ray maps of glass/ Nicrofer 6025 HT interfaces after corrosion in P19-25 and P19-25C a)

P19-38 and P19-38C glasses

Figure 7.16 shows BSE images of P19-38 and P19-38C glasses the Nicrofer coupon after 12 h of corrosion test. The 'above' area have typical voids containing alumina and chromia rich scale along the edge. Those features seem to be much larger for P19-38C than for P19-38 glass (equal mag. 1.5k). Moreover, the modified glass also contains a large piece of powellite see **Figure** 7.18. The remaining two images representing the 'below' zone contain typical voids and chromia layers along the Nicrofer edge. Additionally, P19-38C b has some small crystals either rich in Zr or Ca with Mo.

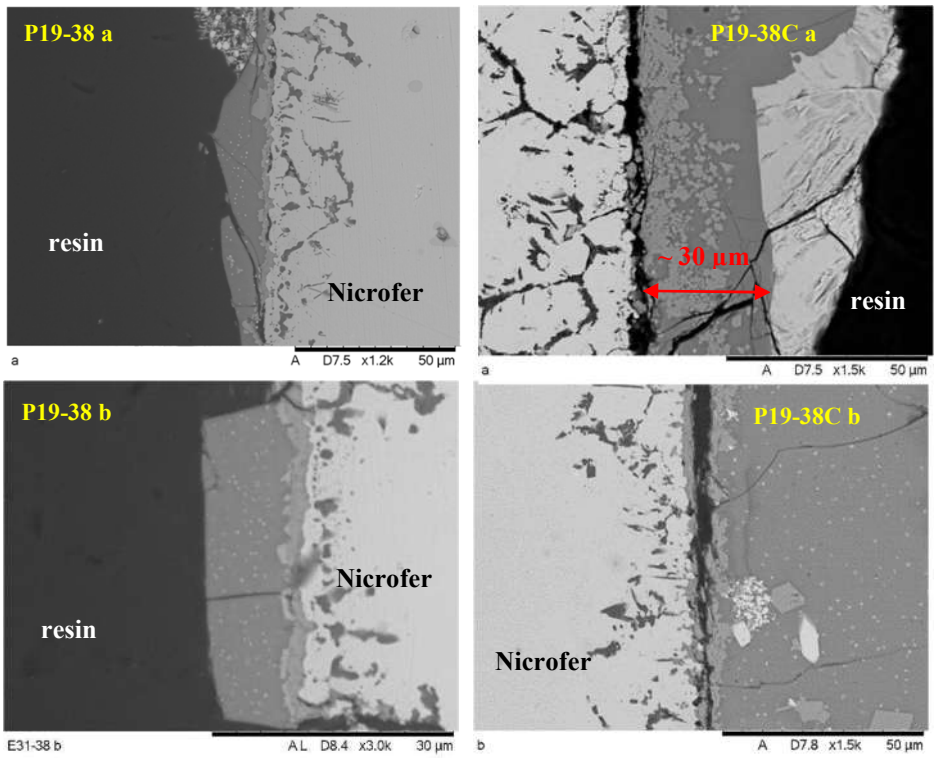

Figure 7.16 Nicrofer 6025 HT/glass interfaces for P19-38 and P19-38C after corrosion a) & b)

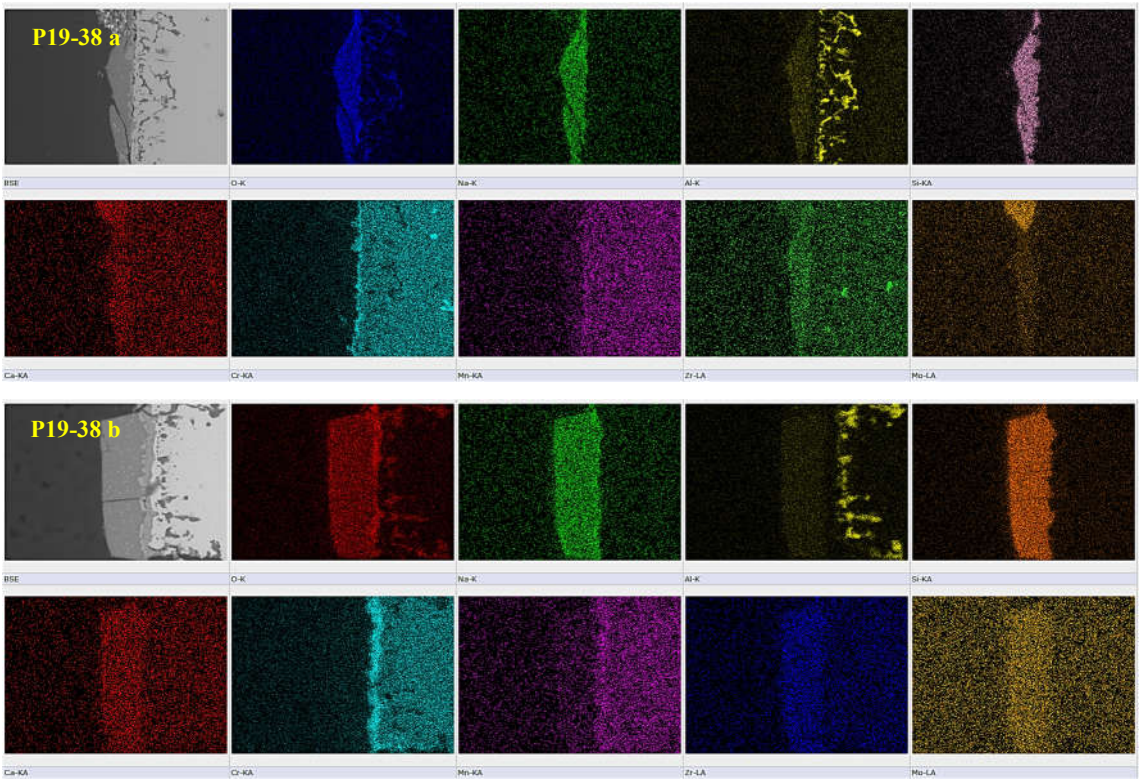

Figure 7.17 X-ray maps of glass/ Nicrofer 6025 HT interfaces after corrosion in P19-38 a) & b)

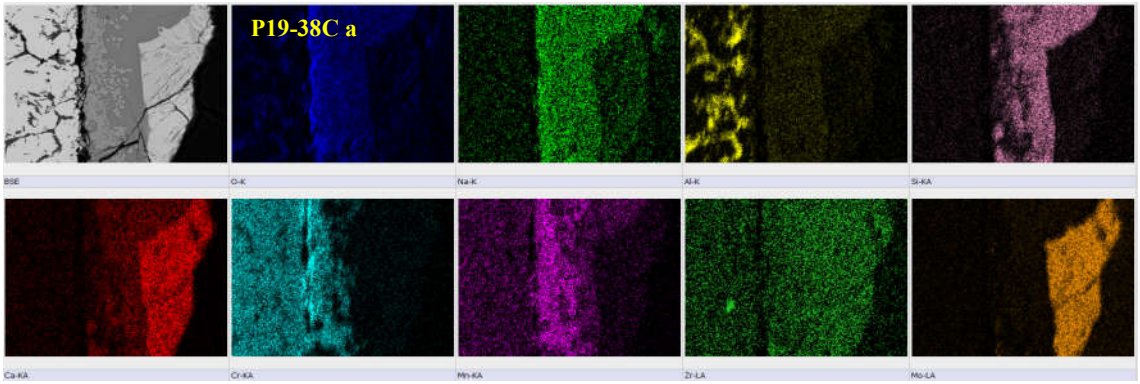

Figure 7. 18 X-ray maps of glass/ Nicrofer 6025 HT interfaces after corrosion in P19-38C a

P48 type glasses

Figure 7.19 shows BSE images of P48-25 and P48-25C glasses with Nicrofer coupons. The top two images have a typical chromia rich layer and alumina rich voids. Moreover, large crystals containing Mo and Ca are present in both glasses that mainly can be seen for P48-25C a. The bottom two images look typical for the submerged area with again alumina voids and chromia scale identified by **Figure** 7.20 and 8.21. The chromia scale looks visually smoother for P48-25 b than for P48-25C b. The irregular Cr rich scale might be related to a lower viscosity of the modified melt, and therefore stronger corrosion and erosion of that scale.

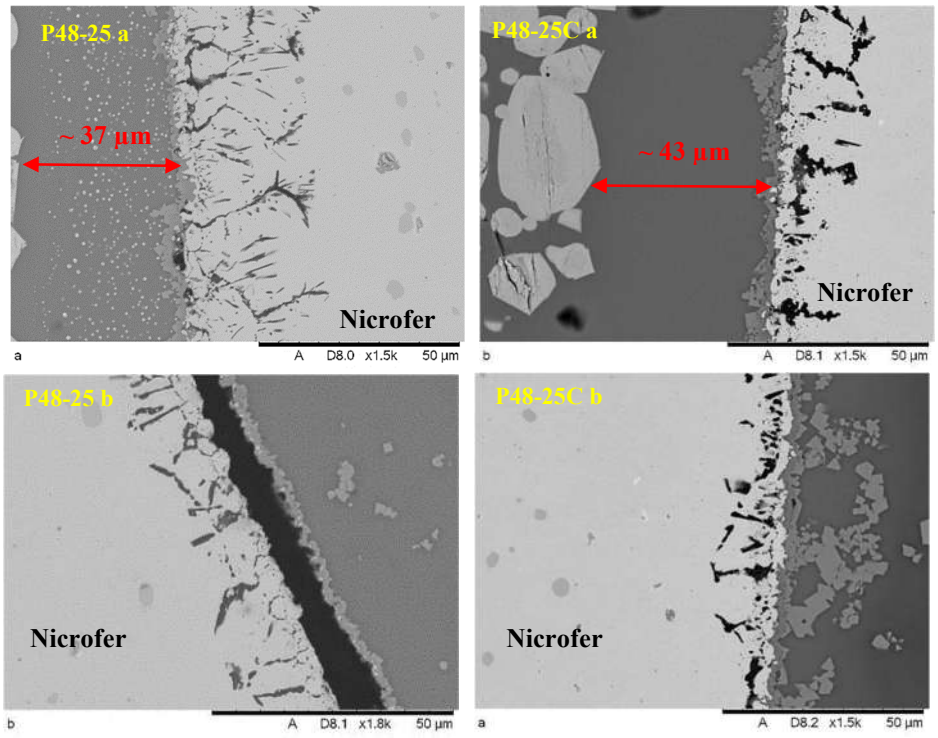

Figure 7.19 Nicrofer 6025 HT/glass interfaces - P48-25 and P48-25C after corrosion a) & b

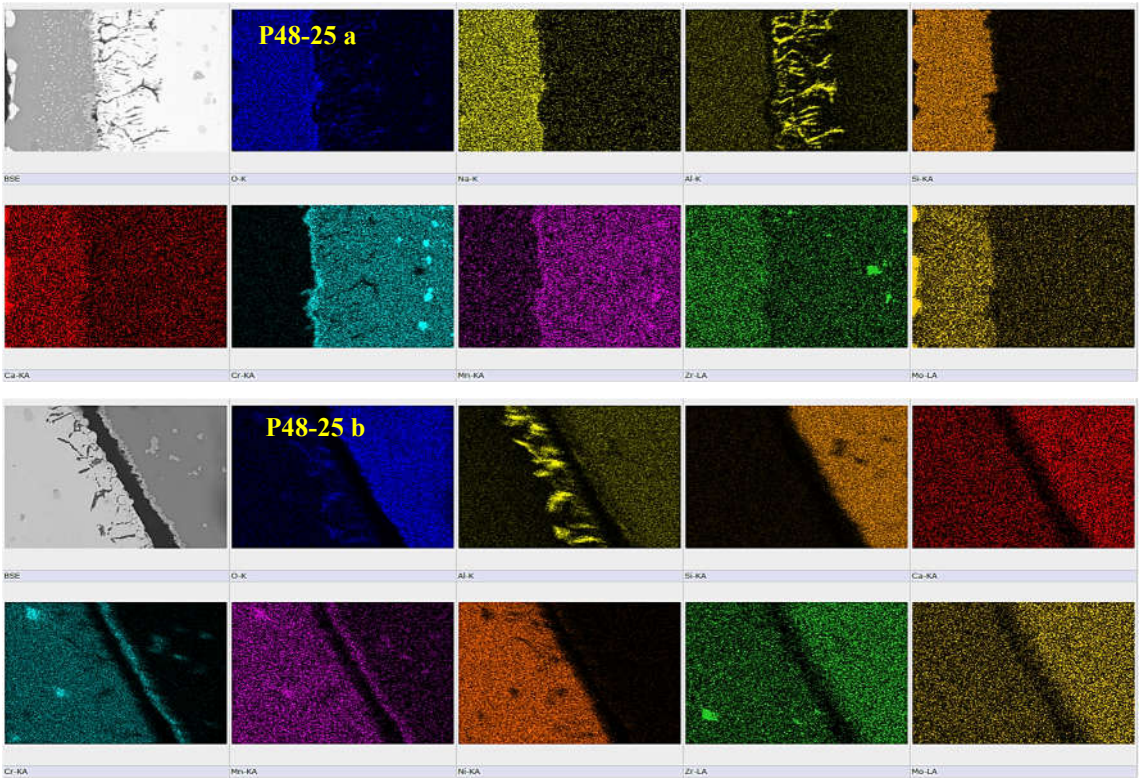

Figure 7.20 X-ray maps of glass/ Nicrofer 6025 HT interfaces after corrosion in P48-25 a) & b)

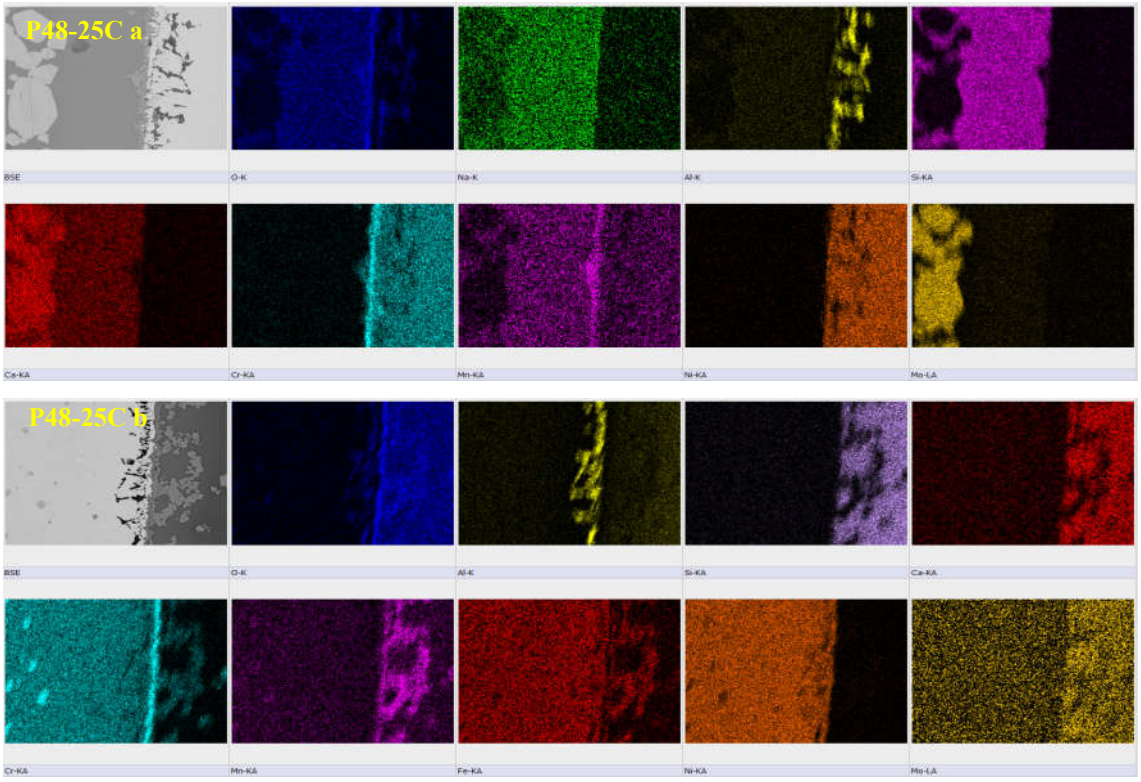

Figure 7.21 X-ray maps of glass/ Nicrofer 6025 HT interfaces after corrosion in P48-25C a) & b)

P48-38 & P48-38C

Figure 7.22 shows BSE images of P48-38 and P48-38C glass interfaces with a corroded Nicrofer coupon. The top two images represent the 'above' zone which was exposed to volatile components of the glass melts that resulted in a glassy layer with crystal phases. Interestingly the chromia scale appears much thinner than before (~ 2-3 µm). The P48-38C sample contains large Ca with Mo-rich crystals formed at the distance of ~ 170 µm from the edge of the coupon (**Figure** 7.23). This also suggests that other elements which formed a glass in that area were more volatile. Comparing the location of powellite crystals from the edge of the coupons between P48-25 a and P48-25C a (~ 43 µm, Fig. 7.19) with P48-38C a (~170 µm, Fig. 7.22) it seems that formation of powellite at 38 wt% waste loading occurred later as if the volatility of Ca and Mo species was reduced by the higher waste content. Conversely, P48-38 shows plenty scattered chromia rich crystals with two square-shaped crystals rich in Zr with Si suggesting $ZrSiO_4$ identified by XRD for this glass. The remaining two BSE images illustrate the Nicrofer corrosion that occurred in the 'below' area. This area shows a typical feature including alumina rich voids near the Nicrofer surface and chromia scale (**Figure** 7.24 showing P48-38C b)

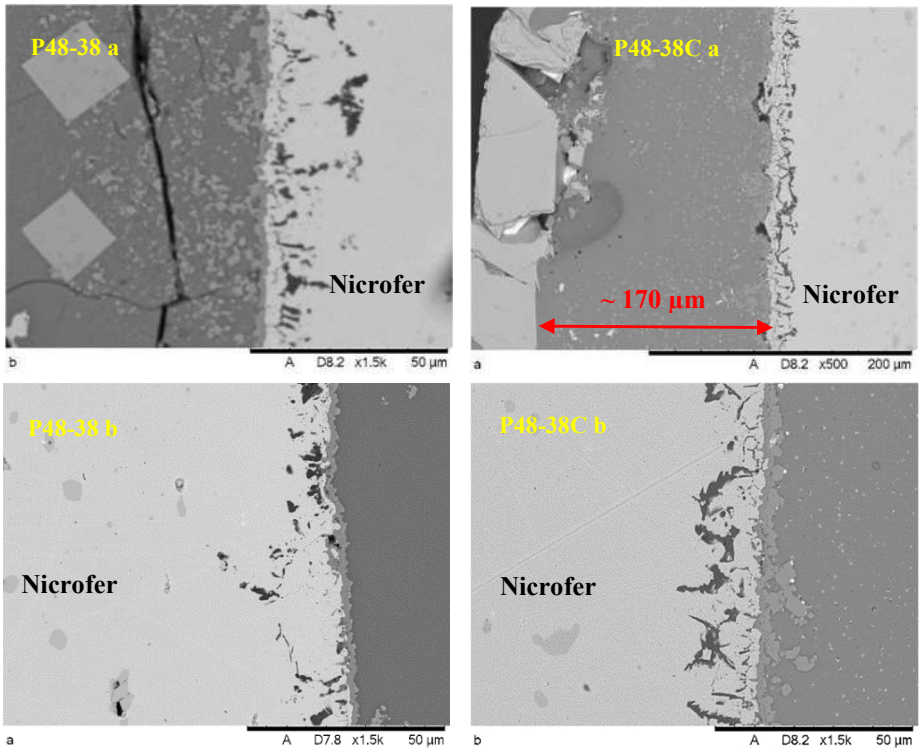

Figure 7.22 Nicrofer 6025 HT/glass interfaces for P48-38 and P48-38C after corrosion a) & b)

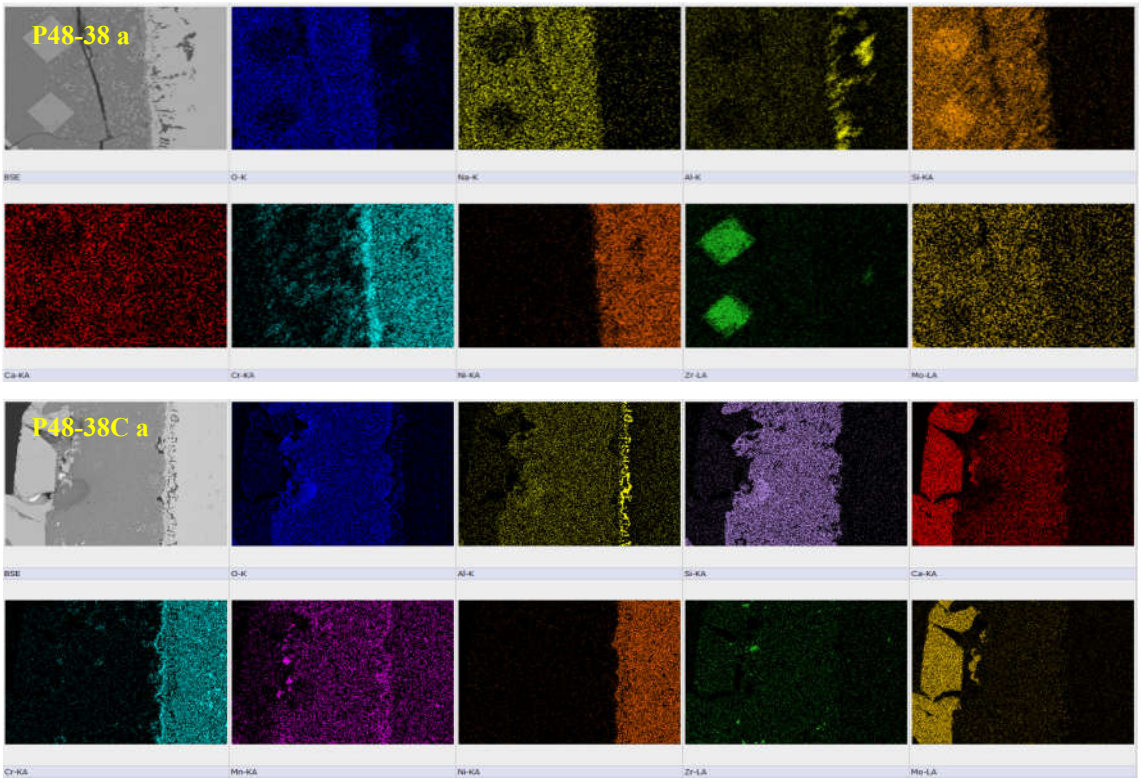

Figure 7. 23 X-ray maps of glass/ Nicrofer 6025 HT interfaces after corrosion in P48-38 a and P48-38C a

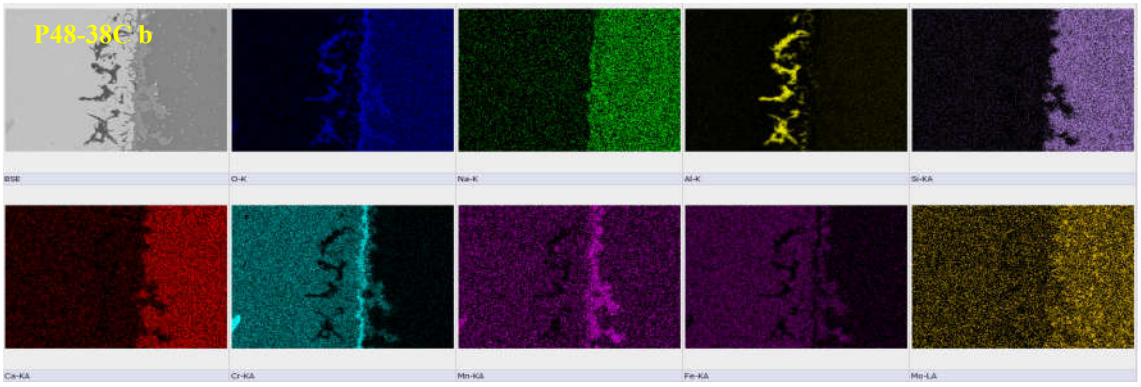

Figure 7.24 X-ray maps of glass/ Nicrofer 6025 HT interfaces after corrosion in P48-38C b

7.4 Discussion

CZ versus CZ1

SEM images show that CZ1 melt was more corrosive than CZ base glass for Inconel 601. The dissolution of the Inconel 601 suggests that it was based on incorporation of Cr into a CZ glass. This resulted in some redox reactions, for example, $Cr^0 \rightarrow Cr^{2+} \rightarrow Cr^{3+}$ which ultimately create reducing conditions in a CZ melt and produced some froth on the surface of the melt. Moreover, Hugon et al. (2009) investigated the corrosion of Inconel 601 and 310s stainless steel in borosilicate glass and observed as well the formation of froth on the melt surface. This is especially true for CZ1 which produced very fragmented chromia protective layer, with some tiny needles rich in Cr and Mn (**Figure** 7.3). These needles seem to have a metallic origin (not included images) just separated from the metallic surface. This agrees with observations, where the metal of the canister was described as a reductant, based on the particular conditions (Pinet et al. 2014; Hugon et al. 2009). Additionally, from electrochemical perspective Cr corrosion in silicate and borosilicate glasses with the formation of chromia scale demonstrates a passive state, meaning that metal is protected by the corrosion's product: Cr_2O_3 scale. However, Di Martino et al. (2004a) noticed that this state is also temperature dependant and 25 ^{0}C higher temperature up to 1050 ^{0}C can lead pure Cr from passive to an active state (quick dissolution). Indeed, Pinet et al. (2014) stated that higher temperatures tend to shift redox equilibria toward the reduced species. Khedim et al. (2008) describes that curves representing the oxygen fugacity correlation of the total Cr solubility for different temperatures and glasses always show three Cr distinct solubility domains, related to specific redox conditions. It was found that Cr solubility under reducing and oxidising conditions (Cr^{6+}) is always high, but only intermediate redox conditions provide a low Cr solubility – protected by chromia scale.

CZ1 glass (no Al_2O_3), aimed to study the origin of alumina inside the voids placed in the subsurface area of the Inconel 601. The alumina presence in the voids is most probably due to oxidation of Al from Inconel 601 itself and it is not related to Al from the glass melt. Hsu et al. (2013) observed that the formation of chromia and alumina are two competing processes, in which the Cr outward intergranular diffusion is drastically reduced by alumina precipitation inside these voids in two similar alloys in borosilicate glass (Inconel 693 and 690). Therefore,

it can be expected that similar alumina precipitation mechanisms reduced the grain boundary attack.

It appears that CZ1 glass was more fluid and therefore more corrosive for the Inconel 601 crucibles. Volf (1984) reported that addition of Al_2O_3 into borosilicate glass increases the viscosity of the borosilicate melt. The glass ingress into Inconel 601 surface is much smaller for the CZ basic glass based on the size of the surface channels. The tiny voids in both cases are filled with alumina. A lack of oxidising agents such as Fe_2O_3 resulted in no formation of continuous protective chromia scale and so this, accelerated the corrosion of Inconel 601, which was mainly delivered by the dissolution of Cr into a glass melt. The green colour of the CZ glass after the corrosion melt (**Figure** 7.2a) suggest the presence of Cr^{3+}/Cr^{2+} species based on the literature (Volf, 1984 and Martino et al. 2004b).

CZMF-15P 1h versus 6h tests

Based on the corrosion tests regarding CZMF-15P sample it seems that the development of protective chromia layer also depends on the testing time. **Figure** 7.4 clearly shows that the thickness of this layer is about three times greater (~ 6 μm) after 6 h compared to 1 h test. This study noticed that initial void formation was the most intensive at the beginning of the test. The alumina voids are already formed just after 15 min of the quick corrosion test in Inconel 601 (up to 6 μm) and so is a thin chromia layer (~ 1.6 - 2 μm). However, the growth of the alumina voids drastically slows down after 7 and 14 days of corrosion tests at 1060 ^{0}C which is about 31 μm in both cases for CZMF-15P sample. On the other hand, the Cr_2O_3 scale formation in that sample slightly differed and it was 12 and 17 μm after 7 and 14 days respectively (Private communication with Xhiane Mao). This is much shorter than could be expected after first 15 min of corrosion tests which already developed clear corrosion effects (**Figure** 7.4) Moreover, Gontier-Moya et al. (1995) reckons that at 1050 ^{0}C the diffusion of Cr which prefers diffusion along the grain boundaries in a Ni-Cr alloy is several orders of magnitude faster, than in alumina. Once again, it could explain that alumina precipitation in grain boundaries reduced the grain boundary corrosion attack and therefore the growth of the alumina voids after 1 and 2 weeks of corrosion test. Finally, Chen et al. (2003) found that diffusion rate of Cr (1050 ^{0}C) along grain boundaries in Ni-16Cr-7Fe alloy is circa 500 times quicker than it is via the grains.

Hugon et al. (2009) reckons that the glass composition plays an important role in the corrosion of Inconel 601 and 310s stainless steel. Moreover, it was found that addition of at least 4.7 wt% Fe_2O_3 to borosilicate glass drastically improved the formation of a coherent chromia scale at the metal/glass interface, which prevented those in-can-melters from excessive corrosion. This means that addition of oxidising agents such as Fe_2O_3 in appropriate amounts might improve the longevity of the melter. In this study, also Mn and less Zn seem to be incorporated into chromia passivation layer, which is believed to partially form a (Mn, Zn, Cr) spinel with unknown stoichiometry. This phenomenon was also observed by abovementioned Xhiane Mao who investigated Inconel 601 corrosion in borosilicate glasses (e.g. CZMF-15P).

Inconel 601

It is clear for P19-25 and P19-25C samples that the area of Inconel 601 above the glass melt is more corroded and the adjacent glass contains more crystals, than the area submerged in the melts. Adjacent glasses to the 'above' area contain lots of crystal grains such as $CaMoO_4$ and $ZrSiO_4$. On the contrary, the 'below' area shows smaller voids near the surface and adjacent glass is more uniform. P19-38 and P19-38C glasses are more crystallised and in the 'above' area containing large pieces of powellite crystals. This time the 'below' area for both samples is crystal rich containing powellite, zircon and chromates (Cr, Mn, Fe). It seems that the chromia scale is slightly more uniform for modified samples (P19-38C) than for P19-38. It can be noticed that P48-38C glass has a more developed chromia layer at the metal/glass interface compared to a non-modified counterpart in the 'above' area (P48-38). The addition of larger amounts of P19 waste (38 wt%) rich in numerous oxides plus extra addition of Ca, Mn and Cu oxides (oxidising agents) as reported by Hugon et al. (2009) had a positive effect on the formation of protective chromia scale, which indicates slightly oxidizing conditions where Cr^{2+} is oxidized into Cr^{3+} and associated with precipitation of protective Cr_2O_3 scale (Khedim et al. 2008 and Martino et al. 2004a). The submerged zone contained smaller corrosion voids, suggesting a less corrosive environment inside the melt. In this case, adjacent glasses were spalled off probably because of the thermal mismatch. It is noticeable that P19 waste glasses with 38 wt% waste loading contain more crystals especially powellite.

Nicrofer 6025HT

The alumina voids in the ‘above‘ area are much larger for P19-25 (~ 40 µm) than for P19-25C glass (~ 20 µm). This implies that an unmodified glass created a more corrosive environment above the melt. The position of powellite crystals for P19-25C closer to the metal/glass interface suggests that as reported by NNL (NNL report, 2014b) corrosive molybdate species were earlier involved in powellite formation. It appears that the lower CaO concentration in the P19-25 glass was unable to mitigate those corrosive molybdate vapours and delivered a greater damage to the coupon surface. Interestingly, the submerged area is much less affected by the melt, because the alumina rich voids penetrated the Nicrofer coupon up to ~ 15 µm for P19-25. However, the depth of voids for P19-25C glass is alike to the ‘above’ area which is ~ 20 µm. This indicates that the modified glass was less corrosive to the Nicrofer so that the void penetration was more limited. Further increase of P19 simulant resulted in a stronger powellite formation (P19-38C a). The chromia layer is fragmented with large alumina voids compared to P19-38 a sample, which has coherent chromia layer and smaller voids. The ‘below’ area in **Figure** 7.16 shows a continuous chromia scale plus some extra crystals (Zr rich and powellite) in the adjacent glass for modified sample. The neighbouring glasses in the melt zone contain tiny spots, which are probably dispersed crystals of powellite.

The two samples from the ‘above’ area (**Figure** 7.19) contain a coherent chromia scale and typical alumina rich voids. Those voids penetrate the Nicrofer 6025HT coupon deeper for the unmodified sample, but the modified one paradoxically has larger voids. The adjacent glass contains plenty of tiny white spots which are probably tiny powellite crystals. However, the P48-25C sample do not contain these tiny crystals, but very large powellite ones at a distance of ~ 42 µm from the chromia scale. The ‘below’ area in both cases possesses a chromia protective scale, which is slightly shattered for the modified sample. This might be related to the lower viscosity of this melt giving higher corrosiveness. This suggests that lower viscosity might be involved in stronger melt convection and therefore stronger erosion phenomena of the chromia scale, which would explain why the scale is not flat at the glass/metal edge (Martino et al. 2004b). **Figure** 7.21 shows a strong signal form Fe and Mn incorporation into chromia scale suggesting the presence of the chromia based spinel. Finally, the alumina rich voids seem to be similar for both glasses.

The 'above' area in the **Figure** 7.22 shows shattered chromia layer with two large square-shaped $ZrSiO_4$ crystals for unmodified sample suggesting reducing conditions, which did not allow Cr to produce a protective Cr_2O_3 layer (low partial pressure of oxygen inside melt) (Pinet et al. 2014 and Khedim et al. 2008). On the other hand, chromia layer for the modified sample is well-developed indicating a more oxidising environment at least in that region. Interestingly, the distance between the chromia layer and the powellite crystal is ~ 170 µm which is much greater than that observed for P48-25C a (~ 43 µm). This suggests that P48-38C glass was less volatile owing to a higher waste loading. The 'below' area for both glasses have a visible chromia scale, which is slightly shattered for modified glass (similar to P48-25C b), which might be related to mentioned earlier chromia scale erosion.

The formation of chromia scale in the case of Inconel 601 and Nicrofer 6025 HT is related to the fact that Cr tend to corrode the most between the main components of these alloys such as Fe, Ni, Co and Cr. The previous studies have always mentioned Cr to be an essential component of corrosion resistant alloys (Bickford et al.1986, Pinet et al. 2004, Martino et al. 2004 a & b and Hsu et al. 2013). The literature says that between the main components of Inconel 601 or Nicrofer 6025HT, Cr is the easiest corroded metal when immersed in the molten glass which relates to the electrochemical properties of these metals. The electrochemical experiments show that the currents density recorded on the passivation plateau are close to 0.4 mA/cm^2 for Cr and this is circa 10 times less compared to values obtained from Co and Ni. This means that corrosion products formed by increasing Cr's potential are more protective than those developed by Co or Ni and this explains why the formation of protective layer is made of Cr_2O_3 instead of those metals (Martino et al. 2004a).

The corrosion tests conducted on Inconel and Nicrofer samples showed at the microscopic level that Inconel corrosion was stronger with waste glasses containing higher levels of MoO_3. It also displays that the modified glass melts were less corrosives based on the depth of the alumina voids for both alloys. It seems that the time for those experiments was not sufficiently long (only up to 12 h) to observe the macroscopic changes to the investigated samples. The tests conducted by NNL provide stronger evidence of necking phenomena that was observed above the melt surface after 100 h (~ 12 wt% MoO_3), where even 50 - 60 % to the Inconel 601 coupon was consumed by corrosion. On the contrary, Nicrofer 6025 HT coupon did not show such as dramatic corrosion. NNL confirms that Nicrofer melter is much more durable

for melting Mo rich waste compared to the Inconel 601 melter, which was strongly corroded after just a few melting cycles (NNL, 2014).

7.5 Conclusions

This study confirms NNL's findings that Nicrofer is more corrosion resistant than Inconel for POCO containing glasses. The corrosiveness of the modified glass melts appears to be lower than unmodified counterparts which further enhances the logic behind that modification. Industrially, it is crucial to change the glass composition in a way to increase the lifespan of the melter without compromising the properties of the waste product. Based on the results and observation from the above chapter the following conclusions can be drawn:

- Al content in the investigated alloys shows that Nicrofer 6025 HT contain around 61 % more Al (2.1 %) and it seems that this affected the size of alumina voids formation, which are wider for Nicrofer samples. Alumina is also formed inside grain boundaries and slows down Cr diffusivity to the surface, which might potentially explain the thinner chromia scale on Nicrofer/glass interface.
- It was observed that the developed chromia scale after 6 h melting was much thicker for Inconel 601 than that one formed after 12h on Nicrofer 6025HT, although waste glass contained more MoO_3 (up to ~ 11wt%). Nevertheless, the size of the alumina voids is larger for Nicrofer than for Inconel sample. The short corrosion examination appears to agree with the results from NNL, where Nicrofer 6025 HT showed much stronger resistance against corrosion with MoO_3 – enriched waste glasses.
- The most intensive corrosion is observable in the first hours of the Inconel 601 corrosion test, where most voids and the Cr_2O_3 layer is largely formed. Even the first 15 minutes test shows the formation of the alumina voids and chromia protective scale.
- Redox and glass compositions play an important role to form a durable protective chromia scale, which could extend the lifespan of the glass melter compare to compositions depleted in oxidisers such as Fe_2O_3, which promote the formation of chromia scale.
- The 'above' area was more corrosive, because of the melt vapours and air, than the glass melts itself based on alumina voids' length.
- It appears that modified glasses were less corrosive for examined metals based on the depth of alumina voids compared to unmodified ones.

8. Conclusions and recommendations for future work

8.1 The solubility of molybdate species

This study evaluates the incorporation behaviour of MoO_3 containing waste into CZ borosilicate glass. That incorporation resulted in $CaMoO_4$ formation, which intensifies for 6 and 8 wt% of MoO_3. It was also found that adding Na_2MoO_4 could lead to powellite formation due to a charge compensating mechanism supported further by addition of Fe_2O_3. The observed crystalline molybdate crystals of $CaMoO_4$ were spherical shape and randomly distributed. Conversely, incorporation of the POCO simulant into CZMF and MZMF glasses produced almost X-ray amorphous glasses at 15 wt% loading. However, higher loadings in these glasses resulted in Ca and Ba molybdates (CZMF) and Ba molybdate, zircon, zirconia and low quartz (MZMF).

Additionally, P-type simulants, with waste loadings at 25 and 38 wt%, were added into glass types unmodified and modified ones; the latter were enriched in extra CaO, CuO and Mn_2O_3. On general, the modified glasses displayed more complex XRD pattern compared to unmodified samples, which could be linked to lower viscosity and therefore longer cooling time. The high MoO_3 content is not only responsible for maximum waste loading in the industry, but it also increases the corrosion between glass melts and melters. Based on the initial study it looks that Inconel 601 was more corroded than Nicrofer 6025 HT, which developed larger alumina voids considered to mitigate the diffusion of Cr to the surface area to form a chromia protective scale. The test conducted by NNL for 100 h displayed that Nicrofer plates did not undergo so dramatic damage as Inconel 601 in waste glasses containing MoO_3 (~ 11 wt%). This corrosion study found that basic CZ and CZ1(No Al) glasses were more corrosive than the examined waste glasses and proved that glass composition plays an important role in determining melter longevity which agrees with the literature (Hugon et al. 2009).

8.2 The effects of the waste incorporation on glass structure and properties

The incorporation of MoO_4^{2-} results in a strong modification of the glass structure and therefore it affects properties of the final waste products. Small additions of MoO_3 to CZ frit produces powellite and it was observed that it mitigated the corrosion of the mullite crucibles compared to basic CZ glass.

Raman spectroscopy showed that molybdenum in the glass exists as MoO_4^{2-} anion; there are two prominent bands at ~ 320-400 cm^{-1} and 890-925 cm^{-1} assigned to bending and stretching vibrations of MoO_4^{2-} respectively. Higher wastes loading of Mo rich waste is reflected by increasing contribution of MoO_4^{2-} bands compared to a basic CZ glass in Raman spectra. The centre of molybdate bands frequently shifts from ~ 921 to ~ 912 cm^{-1} in the case of modified P type samples suggesting different charge compensating mechanisms. It is believed that Ca^{2+} and Na^{+} are involved simultaneously to charge compensate MoO_4^{2-} anion. The incorporation of Na_2MoO_4 into CZ glass displayed that extra addition of Fe_2O_3 (FeO_4^{-}) that change partially the role of Na^{+} from modifier to charge compensator and promotes the formation of $CaMoO_4$ at the expense of Na_2MoO_4.

Overall, higher amount of waste usually slightly decrease T_g and T_p or keep it at similar level for CZMo, CZN, and CZMF or MZMF samples. Incorporation of P-type waste at 25 and 38 wt% had negligible effect on T_g and T_p values. However, modified counterparts showed significant changes for T_p values between 25 and 38 wt% waste loading with a small difference for T_g (~ 10 ^oC).

On general, higher waste loading caused stronger crystallisation. The main phases identified were Ca/Ba molybdates with $ZrSiO_4$, ZrO_2 and α-SiO_2 (MZMF glass). Additionally, P type glasses produced $CaMoO_4$, $FeCr_2O_4$ and ZrO_2. The physical form of molybdates was mostly spherical and randomly distributed sub-micron particles with varying sizes related to the waste loading. The formation of YP due to glass compositions and MoO_3 content was not observed (< 12 wt %) excluding some rare tiny spots. The presence of spinels existed as tiny (~ 2.5 μm) crystals distributed across the samples, sometimes with tendencies to aggregate. Chemical durability of CZMF and MZMF samples show much better durability of the former glasses after 7 and 28 day tests. The PCT test regarding P-type samples showed that NL

values after 28 days were comparable for basic and modified samples. However, 7 day test showed that modified samples had almost half lower NL values.

8.3 Recommendations for future work

The majority of glasses in this project have been melted in a small scale (~ 65 g) in mullite crucibles. It is worth trying to make some compositions in larger platinum crucibles to assess if any clear difference is observable for the final waste products. It is believed that the use of Pt crucible could remove some contamination deriving from the partially dissolved mullite vessels and minimise discrepancies between batched and obtained glass compositions. The P type simulants used for melting were a mixture of nitrides and oxides which after thermal decompositions liberated NO_x, but also resulted in increased volatility. Therefore, to minimise the volatility it is recommended to thermally treat the P-type simulants prior to batching and identify the difference if any exists. The corrosion tests regarding Inconel and Nicrofer plates showed very intensive and corrosive vapours deposited at the area above the glass melts.

The corrosion tests conducted on Inconel and Nicrofer samples exhibited that the latter is more corrosion resistant. Moreover, the NNL test run for a longer time (100 h) clearly prove that Nicrofer samples were much more durable during corrosion tests. It could be recommended that the future tests with new glass compositions using abovementioned alloys should be conducted for a longer time than up to 12 h to observe greater differences between them. Utilised modification of P-type waste glasses evidenced that chemical durability is not compromised and fluidity of the glass melts was much higher which is important for industrial applications to be able to maintain the maximum waste loading at given temperature with an appropriate pouring viscosity. Additionally, other modifications of the waste glasses might be investigated to further enhance the durability, homogeneity and mitigation of YP of the waste product glasses, whereas maintaining the maximum waste loading to keep the number of vitrified canisters to minimum.

References

Abraitis, P.K., 1999. *Dissolution of a Simulated Magnox Waste Glass in Aqueous Solutions at Temperatures Below 100 C*. University of Manchester.

Alton, J., Plaisted, T.J. & Hrma, P., 2002. Kinetics of growth of spinel crystals in a borosilicate glass. *Chemical Engineering Science*, 57(13), pp.2503–2509.

Bart, F., Dussossoy, J.L. & Fillet, C., 2001. Influence of platinum-group metals on nuclear glass properties: Viscosity, thermal stability and alterability. In *Materials Research Society Symposium - Proceedings*. pp. 161–167.

Bickford, D. F., Applewhite-Ramsey, A., Jantzen, C.M., Brown, K.G., 1990. Preliminary General limits at Savannah River. *Journal of the American Ceramic Society*, pp.2896–2902.

Bickford, D.F. & Jantzen, C.M., 1986. Devitrification of defense nuclear waste glasses: Role of melt insolubles. *Journal of Non-Crystalline Solids*, 84(1–3), pp.299–307.

Black R., 2011. Nuclear "cheapest low-carbon option" for UK energy. *BBC Science & Environment*.

Bouchet, L., Rivoallan, A. Mollot, J.F. and Bart F., 2000. Phenomenological study of the reactions between glass frit and simulated fission products calcine.

Brinkman, K., Fox, K., Marra, J., Reppert, J., Crum, J. and Tang, M., 2013. Single phase melt processed powellite (Ba,Ca)MoO4 for the immobilization of Mo-rich nuclear waste. *Journal of Alloys and Compounds*, 551, pp.136–142

Calas, G., Le Grand, M., Galoisy, L. and Ghaleb, D. 2003. Structural role of molybdenum in nuclear glasses: An EXAFS study. *Journal of Nuclear Materials*, 322(1), pp.15–20.

Capobianco, C.J. & Drake, M.J., 1990. Partitioning of ruthenium, rhodium, and palladium between spinel and silicate melt and implications for platinum group element fractionation trends. *Geochimica et Cosmochimica Acta*, 54(3), pp.869–874.

Cassingham, N.J., Bingham, P., Hand, R.J. and Forder, S., 2008. Property modification of a high level nuclear waste borosilicate glass through the addition of Fe2O3. *Glass Technol.: Eur. J. Glass Sci. Technol. A, February 2008, 49 (1), 21–26*, 49(1), pp.21–26

Caurant D., Loiseau P., Majerus O., Aubin V., B.I. and Q.A., 2009. *Glasses, Glass-ceramics and Ceramics for Immobilization of Highly Radioactive Nuclear Wastes*, Nova Science Publishers.

Caurant, D. Majérus, O. Fadel, E. Quintas, A. Gervais, C. Charpentier and T. Neuville, D. 2010. Structural investigations of borosilicate glasses containing MoO3 by MAS NMR and Raman spectroscopies. *Journal of Nuclear Materials*, 396(1), pp.94–101.

Caurant, D. Majérus, O., Fadel, E. Lenoir, M., Gervais, C., Pinet, O. 2007. Effect of molybdenum on the structure and on the crystallization of SiO2-Na2O-CaO-B2O3 glasses. *Journal of the American Ceramic Society*, 90(3), pp.774–783.

Chouard N., Caurant D., Majérus O., Dussossoy J.-L., Ledieu A., Peuget Baddour-Hadjean S., R., Pereira-Ramos J.-P., 2011. Effect of neodymium oxide on the solubility of MoO3 in an aluminoborosilicate glass. *Journal of Non-Crystalline Solids*, 357(14), pp.2752–2762.

Chouard, N., Caurant, D., Majérus, O., Dussossoy, J.L. Klimin, S. Pytalev, D.Baddour-Hadjean, R., Pereira-Ramos, J. P., 2015. Effect of MoO3, Nd2O3, and RuO2 on the crystallization of soda–lime aluminoborosilicate glasses. *Journal of Materials Science*, 50(1), pp.219–241.

Ciecińska, M., Stoch, P., Stoch, A., Nocuń, M., 2015. Thermal properties of 60P2O5–20Fe2O3–20Al2O3 glass for salt waste immobilization. *Journal of Thermal Analysis and Calorimetry*, 121(3), pp.1225–1232.

Cochain, B., Neuville, D. R., Henderson, G. S., McCammon, C. A., Pinet and O. Richet, P., 2012. Effects of the iron content and redox state on the structure of sodium borosilicate glasses: A Raman, Mössbauer and boron k-edge xanes spectroscopy study. *Journal of the American Ceramic Society*, 95(3), pp.962–971.

Cochain, B., Pinet, O. & Richet, P., 2013. Diffusion of sodium ions driven by charge compensation as the rate-limiting step of internal redox reactions. *Journal of Non-Crystalline Solids*, 365(1), pp.23–26.

Connelly, A.J., 2008. Vitrification of historic and future high level nuclear wastes within alkali borosilicate glasses. *PhD Thesis, Sheffield*, (February), p.277.

Connelly, A. J. Hyatt, N. C. Travis, K. P. Hand, R. J. Maddrell, E.R. and Short, R.J. 2011. The structural role of Zr within alkali borosilicate glasses for nuclear waste immobilisation. *Journal of Non-Crystalline Solids*, 357(7), pp.1647–1656.

Cunnane J.C., Bates J. K., Bradley C. R., Buck E. C., Ebert W. L., Feng X., Mazer J. J., and Wronkiewicz D. J. 1994. High Level Waste borosilicate glass a compedium of corrosion characteristics. *U. S. DoE Office of Waste Management*, 2.

Curti, E., Crovisier, J.L., Morvan, G. and Karpoff, A. M., 2006. Long-term corrosion of two nuclear waste reference glasses (MW and SON68): A kinetic and mineral alteration study. *Applied Geochemistry*, 21(7), pp.1152–1168.

De, A.K., Luckscheiter, B., Lutze, W., Malow, G. and Schiewer, E., 1976. Development of glass ceramics for the incorporation of fission products. *Bulletin / American Ceramic Society.*, 55(5), pp.500–503.

Dickson D.P.E. and Berry F.J., 1986. Mossbauer spectroscopy. *Cambridge University Press*.

Donald, I.W., Metcalfe, B.L., Taylor. N.J., 1997. *Review The immobilization of high level radioactive wastes using ceramics and glasses*, Journal of Materials Science Vol.32 pp5851-5887

Donald, I.W., 2010. *Waste immobilization in glass and ceramic based hosts: radioactive, toxic and hazardous wastes*, Oxford: Oxford: Wiley, 2010.

Donald, I.W. & Metcalfe, B.L., 2004. Thermal properties and crystallization kinetics of a sodium aluminophosphate based glass. *Journal of Non-Crystalline Solids*, 348, pp.118–122.

Doremus, R.H., 1994. *Glass science* 2nd ed., New York: John Wiley & Sons Inc.

Dunnet B.F., Steel H. and Crowley D., 2012a. *Vitrification of reprocessing waste and HAST heels using calcium zinc glass. NNL (12)12352*

Dunnett, B. F., Gribble, N., Short, R. Turner E., Steele, C. J., Riley, A D., 2012b. Vitrification of high molybdenum waste. *Glass Technology - European Journal of Glass Science and Technology Part A*, 53(4).

Dyar, M.D., 1985. A review of Moessbauer data on inorganic glasses; the effects of composition on iron valency and coordination. *American Mineralogist*, 70(3–4), p.304 LP-316.

Earnshaw, G.&, 1997. *Chemistry of the elements* 2nd ed. A. (Alan) Earnshaw, ed., Oxford: Butterworth-Heinemann, 1997.

Edmondson, M.J. Maxwell, L.J. Ward, T.R., 2012. A Methodology for Post Operational Clean Out of a Highly Active Facility Including Solids Behaviour – 12386. *WM2012 Conference, February 26 – March 1, 2012, Phoenix, Arizona, USA A*, 0.

Ehrt, D., Jena, F. & Jena, F.D., 2013. Zinc and manganese borate glasses – phase separation, crystallisation, photoluminescence and structure. 54(2), pp.65–75.

Farges, F., Siewert, R., Brown, G. E., Guesdon, A., Morin, G. 2006. Structural environments around molybdenum in silicate glasses and melts. I. Influence of composition and oxygen fugacity on the local structure of molybdenum. *Canadian Mineralogist*, 44(3), pp.731–753.

Frugier, P., Gin, S., Minet, Y., Chave, T., Bonin, B., Godon, N., Lartigue, J. E., Jollivet, P. Ayral, A., De Windt, L. & Santarini, G., 2008. SON68 nuclear glass dissolution kinetics: Current state of knowledge and basis of the new GRAAL model. *Journal of Nuclear Materials*, 380(1–3), pp.8–21.

Galoisy, L. Calas, G. Morin, G. Pugnet, S. & Fillet, C., 1998. Structure of Pd-Te precipitates in a simulated high-level nuclear waste glass. *Journal of Materials Research*, 13(5), pp.1124–1127.

Galoisy, L. Cormier, L., Rossano, S., Ramos, A., Calas, G., Gaskell, P., Le Grand, M., 2000. Cationic ordering in oxide glasses: the example of transition elements. *Mineralogical Magazine*, 64(3), p.409.

Gin, S. Abdelouas, A. Criscenti, L. J. Ebert, W. L. Ferrand, K. Geisler, T. Harrison, M. T. Inagaki, Y. Mitsui, S. Mueller, K. T. Marra, J. C. Pantano, C. G. Pierce, E. M. Ryan, J. V. Schofield, J. M. Steefel, C. I. Vienna, J. D. 2013. An international initiative on long-term behavior of high-level nuclear waste glass. *Materials Today*, 16(6), pp.243–248.

Gin, S. Jollivet, P. Mestre, J. P. Jullien, M. Pozo, C. 2001. French SON 68 nuclear glass alteration mechanisms on contact with clay media. *Applied Geochemistry*, 16(7–8), pp.861–881.

Gin, S., Ribet, I. & Couillard, M., 2001. Role and properties of the gel formed during nuclear glass alteration: Importance of gel formation conditions. *Journal of Nuclear Materials*, 298(1–2), pp.1–10.

Greaves, G. N., Fontaine, A. Lagarde, P.Raoux, D. Gurman, S J., 1981. Local structure of silicate glasses. *Nature*, 293(5834), pp.611–616.

Greaves, G. N. Gurman, S. J. Catlow, C. R.A. Chadwick, A V Houde-Walter, S Henderson, C M B Dobson, B Ral., 1991. A structural basis for ionic diffusion in oxide glasses. *Philosophical Magazine A*, 64(5), pp.1059–1072

Hand, R.J. & Seddon, A.B., 1997. An hypothesis on the nature of Griffith's cracks in alkali silicate and silica glasses. *Physics and chemistry of glasses.*, 38(1), pp.11–14.

Harrison M.T., Gate A.M. and Crowley D., 2014. The effect of yellow phase on Nicrofer 6025HT and Inconel 601 corrosion rates during melting - Issue 2.

Harrison M.T., Gate A.M. and Crowley D., 2014. *The effect of yellow phase on Nicrofer 6025HT and Inconel 601 corroion rates during melting - Issue 1*,

Harrison, M.T., 2014. The Effect of Composition on Short- and Long-term Durability of UK HLW Glass. *Procedia Materials Science*, 7, pp.186–192.

Haynes M.W., 1978. *CRC handbook of chemistry and physics* 2nd ed.: London: Boca Raton, Fla.: CRC.

Henry, N. Deniard, P. Jobic, S. Brec, R. Fillet, C. Bart, F. Grandjean, A. & Pinet, O., 2004. Heat treatments versus microstructure in a molybdenum-rich borosilicate. *Journal of Non-Crystalline Solids*, 333(2), pp.199–205.

Horneber, A., Camara, B. & Lutze, W., 1982. INVESTIGATION ON THE OXIDATION STATE AND THE BEHAVIOUR OF MOLYBDENUM IN SILICATE GLASS. In *Materials Research Society Symposia Proceedings*. pp. 279–288.

Hrma, P., 2002. Crystallization in high-level waste glasses. *Ceram. Trans. 132, 243- 256.*

Hrma, P., 2010. Crystallization during processing of nuclear waste glass. *Journal of Non-Crystalline Solids*, 356(52–54), pp.3019–3025

Hrma, P. Crum, J.V. Bredt, P.R. Greenwood, L.R. Arey, B.W. Smith, H.D., 2005. Vitrification and testing of a Hanford high-level waste sample. Part 2: Phase identification and waste form leachability. *Journal of Nuclear Materials*, 345(1), pp.31–40.

Hsu, J.H. Newkirk, J.W., Kim,. Ray C.W, Brow C.S., Schlesinger R.K., Day M.E. and Delbert E., 2013. Corrosion of Inconel 690 and Inconel 693 in an iron phosphate glass melt. *Corrosion Science*, 75, pp.148–157.

Hugon, I., Gruber, P. & Pinet, O., 2009. Effect of the iron oxide glass content on high temperature metal corrosion for nuclear waste glass melter. , pp.1–11.

Hyatt N.C., Short R.J., Hand J., Lee W.E., Livens F., C.J.M. an. B.R.L., 2004. The Structural Chemistry of Molybdenum in Model High Level. *ISL*.

Ikeda, T., 2014. Infrared absorption and Raman scattering spectra of water under pressure via first principles molecular dynamics. *The Journal of Chemical Physics*, 141(4), p.44501.

Izak, P., Hrma, P., Arey, B.W., Plaisted & Trevor J. 2001. Effect of feed melting, temperature history, and minor component addition on spinel crystallization in high-level waste glass. *Journal of Non-Crystalline Solids*, 289(1–3), pp.17–29.

Lucas J., 1989. Review Fluoride glasses. *J. Mater. Sci., 24 (1989) 1*.

Jantzen C.M., Brown K.G. Pickett J.B., 2000. *Crystaline Phase separation in Phosphate Containing Waste Glasses: Relevance to INEEL HAW*,

Jantzen, C.M., Brown, K.G. and Pickett, J.B., 2001. Impact of Phase Separation on Durability in Phosphate., p.13.

Johnson, J.A. & Johnson, C.E., 2005. Mössbauer spectroscopy as a probe of silicate glasses. *Journal of Physics: Condensed Matter*, 17(8), p.R381.

Khedim, H. et al., 2008. Relationship between chromia solubility and superalloy corrosion in silicate melts - A first attempt. *Materials Science Forum*, 595–598 PA, pp.621–627.

Kim, D.S., Peeler, D.K., Hrma, P., 1995. Effect of crystallisation on the chemical durability of simulated nuclear waste glasses. *Ceram. Trans. 61, 177-185*.

Komarneni, S. & White, W.B., 1981. Hydrothermal Reactions of Clay Minerals and Shales With Caesium Phases From Spent Fuel Elements. *Clays and Clay Minerals*, 29(4), pp.299–308.

KU Leuven, 2016. X-ray diffraction – Bruker D8 Discover. Available at: http://fys.kuleuven.be/iks/nvsf/experimental-facilities/x-ray-diffraction-2013-bruker-d8-discover [Accessed September 27, 2016].

Langowski, M.H., Darab, J.G. and Smith, P.A., 1996. *Volatility Literature of Chlorine, Iodine, Cesium, Strontium, Technetium, and Rhenium; Technetium and Rhenium Volatility Testing*. *U.S. Department of Energy under Contract DE-AC06-76RLO 1830*

L'Annunziata, M., F., 2007. *Radioactivity: introduction and history*, Amsterdam: Elsevier

Larkin, M.J., 1986. Development of highly active waste conditioning at Sellafield. *Nuclear Energy*, 25(6), pp.343–345.

Li H., Hrma P., Vienna J.D., Qian M., Su Y. and Smith D.E., 2003. Effects of Al_2O_3, B_2O_3, Na_2O, and SiO_2 on nepheline formation in borosilicate glasses: Chemical and physical correlations. *Journal of Non-Crystalline Solids*, 331(1–3), pp.202–216.

Lim E.S., Kim B.S., Lee J.H., Kim J.J. 2007. Characterization of the low temperature firing BaO-B2O3-SiO2 glass: The effect of BaO content. *Journal of the European Ceramic Society*, 27(2–3), pp.825–829.

Lutze & Ewing, R.C., 1988. *Radioactive waste forms for the future*, North-Holland.

Suszynska M., Maczka M., Bukowska E. and Berg K.J., 2010. Structure and IRR spectra of copper-exchanged soda-lime silica glass. *Journal of Physics: Conference Series 249 (2010) 012048 IOP*.

Magnin, M., Schuller, S., Mercier, C., Trébosc, J., Caurant, D., Majérus, O. and Angéli, F. and Charpentier, T. , 2011. Modification of molybdenum structural environment in borosilicate glasses with increasing content of boron and calcium oxide by 95Mo MAS NMR. *Journal of the American Ceramic Society*, 94(12), pp.4274–4282.

Mahadevan Pillai V.P., Pradeep T., Bushiri M.J., Jayasree R.S. and Nayar, V., 1997. Vibrational spectroscopic studies of FeClMoO 4 , Na 2 MoO 4 and. *Science*, 53, pp.867–876.

Manaktala H.K., 1992. An assessment of borosilicate glass as a high-level waste form. Nuclear Regulatory Commission Contract NRC-02-88-005

Manara, D., Grandjean, A. & Neuville, D.R., 2009. Advances in understanding the structure of borosilicate glasses: A Raman spectroscopy study. *American Mineralogist*, 94(5–6), pp.777–784.

Marples, J.A.C., 1988. The preparation, properties, and disposal of vitrified high-level waste from nuclear fuel reprocessing. *Glass Technology*, 29(6), pp.230–247.

Matyáš J., Lang J.B., Owen A.T., Kruger A.A., R.C.P., 2012. *HLW Glass Studies: Development of Crystal-Tolerant HLW Glasses*, U.S. Department of Energy under Contract DE-AC05-76RL01830, PNNL-21308

McCubbin, D., Leonard, K.S., McDonald, P., Bonfield, R. and Boust, D. 2006. Distribution of Technetium-99 in sub-tidal sediments of the Irish Sea. *Continental Shelf Research*, 26(4), pp.458–473.

McMillan P.W., 1979. Glass-ceramics. Second ed. London: Academic Press

Mekki A., Holland D., McConville, C.F., 1997. X-ray photoelectron spectroscopy study of copper sodium silicate glass surfaces. *Journal of Non-Crystalline Solids*, 215, pp.271–282.

Mishra, R.K., Sudarsan, V., Kaushik, C. P., Raj, K., Tyagi, A.K. 2007. Effect of BaO addition on the structural aspects and thermophysical properties of sodium borosilicate glasses. *Journal of Non-Crystalline Solids*, 353(16–17), pp.1612–1617.

Miyoshi H., Chen D., Masui H., Yazawa T. and T. Akai 2004. Effect of calcium additive on structural changes under heat treatment in sodium borosilicate glasses. *Journal of Non-Crystalline Solids*, 345–346, pp.99–103.

Morgan, S., 2005. *Characterisation and Interaction of Simulated High Level, Radioactive Waste (HLW) with Borosilicate Glass*. University of Sheffield.

Moya, E. G., Moya, F., Sami, A., Juvé, D., Tréheux, D. and Grattepain, C., 1995. Diffusion of chromium in alumina single crystals. *Philosophical Magazine A*, 72(4), pp.861–870.

Musić, S., Popović, S. & Gotic, M., 1989. Influence of iron ions on the structural properties of Zn-borosilicate glasses. *Journal of Radioanalytical and Nuclear Chemistry Articles*, 130(2), pp.299–310.

Navrotsky, A. & Kleppa, O.J., 1968. Thermodynamics of formation of simple spinels. *Journal of Inorganic and Nuclear Chemistry*, 30(2), pp.479–498.

NDA, 2011. *Vitrified High Level Waste from POCO. SITE CUSTODIAN WASTE TYPE 2F38/C. NDA: Sellafield Limited*

NNL, 2014. Privet communication with Nick Gribble and James Stevens from VTR and WVP, Sellafield.

Ojovan and Lee, 2014. *An introduction to nuclear waste immobilisation* Second ed. W. E. Lee, ed., Amsterdam: Elsevier

Ojovan and Lee, 2005. *An introduction to nuclear waste immobilisation* W. E. Lee, ed., Oxford: Oxford: Elsevier, 2005.

Ojovan, M.I., L.W.E., 2007. *New developments in glassy nuclear wasteforms* W. E. Lee, W. E. Lee, & B. Lee, eds., Hauppauge, N.Y.: Hauppauge, N.Y.: Nova Science Publishers, 2007.

Ojovan, M. & Batyukhnova, O., 2007. Glasses for Nuclear Waste Immobilization. *WM '07 Conference*.

Ojovan, M.I., Hand, R.J., Ojovan, N.V and Lee, W.E., 2005. Corrosion of alkali-borosilicate waste glass K-26 in non-saturated conditions. *Journal of Nuclear Materials*, 340(1), pp.12–24.

Ojovan, M.I., Pankov, A. & Lee, W.E., 2006. The ion exchange phase in corrosion of nuclear waste glasses. *Journal of Nuclear Materials*, 358(1), pp.57–68.

Ozeki, T., Murata, K., Kihara, H. and Hikime, S.O., 1987. Studies on the interaction of molybdate ion and magnesium ion observed in the Raman spectra of the mixture solutions. *Bull. Chem. Soc. Jpn. 1987: 3585-3589.*

Pacaud, F., Fillet, C. & Jacquet-Francillon, N., 1991. Effect of platinoids on French LWR reference glass properties. In *MRS Proceedings*. p. 161.

Palmer, R.A., 1995. History of radioactive waste - how did we get here? *Ceram. Trans. 61, 99-104*.

Paul, A., 1990. *Chemistry of glasses* 2nd ed., London: Chapman and Hall, 1990.

Pegg, I.L. et al., 2010. *Mitigation of Yellow Phase Formation at the Rokkasho HLW Vitrification Facility - 10107*,

Perry D.L., 2011. *Handbook of Inorganic Compounds, Second Edition* 2nd ed., New York: CRC Press, Taylor and Francis group.

Pinet, O., Hugon, I. & Mure, S., 2014. Redox Control of Nuclear Glass. *Procedia Materials Science*, 7, pp.124–130.

Polyakova I.G., 2000. Alkali borosilicate systems: Phase diagrams and properties of glasses. *Physics and Chemistry of Glasses*, 41(5), pp.247–258.

Pope, S.J.A. & West, Y.D., 1995. Use of the FT Raman spectrum of Na2MoO4 to study sample heating by the laser. *Spectrochimica Acta Part A: Molecular Spectroscopy*, 51(12), pp.2011–2017.

Quang, R. Do et al., 2003. Vitrification of HLW Produced by Uranium/Molybdenum Fuel Reprocessing in COGEMA's Cold Crucible Melter. *9th ASME International Conference on Radioactive Waste Management and Environmental Remediation: Volumes 1, 2, and 3*, 3, pp.1585–1591.

Quayle, B.E., 2003. *Suitability of Nicrofer 6025HT as a replacement material for Inconel 601 in the construction on WVP melter vessel. RAT (03) 3591*,

Quintas A., Caurant, D., Majérus, O. & Lenoir, M., 2011. Structural study of a rare earth-rich aluminoborosilicate glass containing various alkali and alkaline-earth modifier cations. *XXIst International Congress on Glass*, Jul 2007(Strasbourg, France), pp.1–4.

Quintas, A., Caurant, D., Majérus, O., Charpentier, T., Bart, F. & Dussossoy, J.L. 2008. Effect of the nature of alkali and alkaline-earth oxides on the structure and crystallization of an aluminoborosilicate glass developed to immobilize highly concentrated nuclear waste solutions. Atalante May 19-22, 2008

Raman, S.V., Phase Equilibria, Viscosity, Durability, and Raman Spectra in the System for Idaho Nuclear Waste Forms. *Ceramic Transactions*, pp.185–198.

Rose, P.B., 2007. *The Crystallisation and Aqueous Durability of Borosilicate Nuclear Waste Glasses*. University of Sheffield.

Rose, P.B. et al., 2011. Crystallisation of a simulated borosilicate high-level waste glass produced on a full-scale vitrification line. *Journal of Non-Crystalline Solids*, 357(15), pp.2989–3001.

Saraiva G.D., Paraguassu W. , Maczka M., . Freire P. T. C, Lima J. A.Jr.. Paschoal C.W.A, M.F.J. and S.F.A.G.S. et al., 2008. Temperature-dependent Raman scattering studies of Na2MoO4. *Journal of Raman Spectroscopy*, 38(April), pp.1538–1553.

Schiewer, E. Rabe, H., Weisenburger, S., 1982. MATERIALS BALANCE - SCIENTIFIC FUNDAMENTALS FOR THE QUALITY ASSURANCE OF VITRIFIED WASTE. *Materials Research Society Symposia Proceedings*, pp.289–297.

Schreiber, H.D. et al., 1987. Mutual interactions of redox couples via electron exchange in silicate melts - Models for geochemical melt systems. *Center for Glass Chemistry , Virginia Military Institute, Lexington*, 92(2), pp.9233–9245.

Schuller, S. et al., 2008. Phase separation and crystallization of borosilicate glass enriched in MoO3, P2O5, ZrO2, CaO. *Journal of Non-Crystalline Solids*, 354(2–9), pp.296–300.

Scott, P. A., Goles, R. W., and Peters, R.D., 1985. *Technology of Off-Gas Ceramic Melters*,

Shah, J.G., Patki, V.A. & Raj, K., 1996. Dta , Powder Xrd and Sem Study of Manganese-Containing Borate Glasses. , 15, pp.417–421.

Shanggeng, L., Yaozhong, J. & Delu, L., 1990. Devitrification behaviour of GC-12/9B HLW-glass. *Waste Management*, 10(1), pp.23–27.

Shelby, J.E., 2005. *Introduction to Glass Science and Technology* 2nd Editio., Cambridge: The Royal Society of Chemistry.

Short, R., 2004. *Incorporation of Molybdenum in Nuclear Waste Glasses*. University of Sheffield: ISL

Short, R.J., Hand, R.J., Hyatt, N.C. and Möbus, G., 2005. Environment and oxidation state of molybdenum in simulated high level nuclear waste glass compositions. *Journal of Nuclear Materials*, 340(2–3), pp.179–186

Short R., Turner E., Dunnet B. and Riley A., 2008. Devitrified and phase separated material found in simulated high level nuclear waste glasses containing Ca and Zn additions. *Materials Research Society*, 1107.

Short, R.J. and S.C., 2014. Privet communication with Rick Short and Carl Steele from VTR and WVP, Sellafield, 2014.

Short, R., 2014. Phase Separation and Crystallisation in UK HLW Vitrified Products. *Procedia Materials Science*, 7, pp.93–100. Available at: http://linkinghub.elsevier.com/retrieve/pii/S2211812814010566.

Sickafus, K.E., 2000. Radiation Tolerance of Complex Oxides. *Science*, 289(5480), pp.748–751.

Simmons, J.H., Mills, S.A. & Napolitano, A., 1974. Viscous Flow in Glass During Phase Separation. *Journal of the American Ceramic Society*, 57(3), pp.109–117.

Spilman, D.B., Hench, L.L. & Clark, D.E., 1986. Devitrification and subsequent effects on the leach behavior of a simulated borosilicate nuclear waste glass. *Nuclear and Chemical Waste Management*, 6(2), pp.107–119.

Sproull, J.F., 1994. High level radioactive waste glass production and product description. *Scientific basis for nuclear waste management XVII : symposium held November 29-December 3, 1993, Boston, Massachusetts, U.S.A. /*, 333, pp.15–25.

Stefanovsky, S., Shiryaev, A., Choi, A. & Marra, J., 2013. Valence and Coordination of Iron and Manganese in Simulated SB6 Nuclear Waste Glasses. In *TMS2013 Supplemental Proceedings*. John

Sułowska, J., Wacławska, I. & Olejniczak, Z., 2013. Vibrational Spectroscopy Structural studies of copper-containing multicomponent glasses from the SiO 2 – P 2 O 5 – K 2 O – CaO – MgO system. *Vibrational Spectroscopy*, 65, pp.44–49.

Sundaram, S.K. & Perez Jr., J.M., 2000. *PNNL-13347: Noble Metals and Spinel Settling in High Level Waste Glass Melters*, U.S. Department of Energy

Szumera, M., 2015. Molybdenum modified phosphate glasses studied by 31P MAS NMR and Raman spectroscopy. *Spectrochimica Acta - Part A: Molecular and Biomolecular Spectroscopy*, 137, pp.111–115.

Takamori, T. & Tomozawa, M., 1979. Viscosity and Microstructure of Phase? Separated Borosilicate Glasses. *Journal of the American Ceramic Society*, 62(7–8), pp.373–377.

Tan S., 2015. The incorporation and solubility of sulphate, chloride and molybdate anions in borosilicate and aluminosilicate glasses. University of Sheffield: PhD thesis

Tan, S., Ojovan, M.I., Hyatt, N.C., Hand, R.J., 2015. MoO3 incorporation in magnesium aluminosilicate glasses. *Journal of Nuclear Materials*, 458, pp.335–342.

Taurines, T. & Boizot, B., 2011. Synthesis of powellite-rich glasses for high level waste immobilization. *Journal of Non-Crystalline Solids*, 357(14), pp.2723–2725.

Taurines, T. & Boizot, B., 2012. Microstructure of powellite-rich glass-ceramics: A model system for high level waste immobilization. *Journal of the American Ceramic Society*, 95(3), pp.1105–1111.

Taurines, T., Neff, D. & Boizot, B., 2013. Powellite-rich glass-ceramics: A spectroscopic study by EPR and Raman spectroscopy. *Journal of the American Ceramic Society*, 96(9), pp.3001–3007.

Thien, B.M.J., Godon, N., Ballestero, A., Gin, S., Ayral, A. 2012. The dual effect of Mg on the long-term alteration rate of AVM nuclear waste glasses. *Journal of Nuclear Materials*, 427(1–3), pp.297–310.

Tomozawa, M., 1994. *Fundamentals of inorganic glasses*, Journal of the American Ceramic Society, Vol.62 (7-8), pp.373-377

Tulyaganov, D.U., Reddy, A.A., Kharton, V.V., Ferreira, J.M., 2013. Aluminosilicate-based sealants for SOFCs and other electrochemical applications - A brief review. *Journal of Power Sources*, 242(November), pp.486–502.

Turvey and Hone, 2000. Storage of Liquid High-Level Radioactive Waste at Sellafield.

Varshneya, A.K., 1994. *Fundamentals of inorganic glasses*, Boston: Academic Press, Inc., an imprint of Elsevier, 1994.

Vogel, W., 1994. *Glass chemistry* Second edi., Berlin : Springer-Verlag, 1994.

Volf, M.B., 1984. *Chemical approach to glass*, New York: Elsevier Science.

World Nuclear Association, 2017. Nuclear Power in the United Kingdom. Available at: http://www.world-nuclear.org/information-library/country-profiles/countries-t-z/united-kingdom.aspx.

World Nuclear Association, Nuclear Power in the World Today. *Jan 2016*. Available at: http://www.world-nuclear.org/info/current-and-future-generation/nuclear-power-in-the-world-today/.

World Nuclear News, 2015. Russia connects BN-800 fast reactor to grid. Available at: http://www.world-nuclear-news.org/NN-Russia-connects-BN800-fast-reactor-to-grid-11121501.html.

Yadav, A.K. & Singh, P., 2015. A Review on Structure of Glasses by Raman Spectroscopy. *RSC Adv.*, 5, pp.67583–67609.

Young, H.D., 2014. *University physics with modern physics technology update [electronic resource]* Thirteenth. R. A. Freedman & A. L. Ford, eds., Pearson Education, International ed of 13th revised ed.

Zhang, H., Corkhill, C.L., Heath, P.G., Hand, R.J., Stennett, M.C., Hyatt, N.C. 2015. Effect of Zn- and Ca-oxides on the structure and chemical durability of simulant alkali borosilicate glasses for immobilisation of UK high level wastes. *Journal of Nuclear Materials*, 462, pp.321–328.

Zhao, P., Kroeker, S. & Stebbins, J.F., 2000. Non-bridging oxygen sites in barium borosilicate glasses: results from 11B and 17O NMR. *Journal of Non-Crystalline Solids*, 276(1–3), pp.122–131.

Appendix 1

Waste glasses -XRF (mol %)												
Oxide	P48-25	P48-38	P19-25	P19-38	**P0-25**	**P0-38**	P48-25C	P48 -38C	P19-25C	P19-38C	**P0-25C**	**P0-38C**
Al_2O_3	3.50	3.92	3.85	4.63	4.09	4.89	3.03	3.39	3.40	3.96	3.67	4.20
BaO	0.61	1.00	0.31	0.59	0.21	0.31	0.54	0.90	0.28	0.51	0.19	0.27
CeO_2	0.27	0.62	0.41	0.56	0.33	0.90	0.24	0.55	0.36	0.48	0.29	0.77
Cr_2O_3	0.12	0.30	0.21	0.46	0.21	0.32	0.10	0.26	0.19	0.39	0.18	0.27
Cs_2O	0.25	0.40	0.04	0.42	0.22	0.47	0.21	0.36	0.03	0.36	0.19	0.41
Fe_2O_3	0.77	1.43	1.01	1.67	1.31	2.16	0.66	1.12	0.92	1.42	1.17	1.84
Gd_2O_3	0.32	0.16	0.14	0.51	0.31	0.58	0.28	0.14	0.12	0.43	0.27	0.50
La_2O_3	0.08	0.08	0.06	0.05	0.13	0.17	0.07	0.07	0.05	0.04	0.12	0.15
Li_2O*	5.37	6.03	5.42	6.00	6.33	7.31	4.77	5.38	4.73	5.13	5.54	6.25
MgO	1.97	3.44	3.38	4.77	3.03	5.15	1.73	3.05	3.01	4.06	2.67	4.45
MoO_3	3.37	5.39	2.19	3.57	1.01	1.62	2.94	4.77	1.96	3.05	0.92	1.39
Nd_2O_3	0.08	0.28	0.36	0.89	0.48	0.69	0.07	0.25	0.32	0.75	0.42	0.60
NiO	0.17	0.30	0.32	0.48	0.41	0.50	0.15	0.27	0.29	0.41	0.36	0.43
Pr_2O_3	0.09	0.08	0.08	0.16	0.09	0.22	0.08	0.07	0.07	0.14	0.08	0.19
Sm_2O_3	0.00	0.15	0.05	0.03	0.07	0.12	0.00	0.13	0.04	0.03	0.06	0.10
SrO	0.28	0.39	0.27	0.40	0.31	0.51	0.25	0.34	0.24	0.34	0.28	0.44
TeO_2	0.00	0.00	0.00	0.00	0.00	0.00	0.00	0.00	0.00	0.00	0.00	0.00
Y_2O_3	0.05	0.11	0.04	0.10	0.07	0.14	0.05	0.10	0.03	0.09	0.06	0.12
ZrO_2	1.96	3.33	1.75	2.92	1.35	2.19	1.74	2.93	1.55	2.48	1.20	1.90
SiO_2	46.20	41.51	45.39	39.82	45.93	41.10	40.41	35.70	39.38	35.20	40.11	35.47
B_2O_3	17.14	14.95	17.03	15.22	16.32	14.91	15.02	13.07	15.13	12.95	14.42	12.88
Na_2O	8.31	7.27	7.98	8.12	7.85	6.78	7.02	6.25	7.09	6.91	6.93	5.86
CaO	5.61	5.68	6.17	5.42	6.33	5.36	13.22	13.69	13.24	13.63	13.41	13.80
ZnO	3.49	3.18	3.55	3.20	3.63	3.59	3.14	2.86	3.15	2.72	3.21	3.10
CuO							2.89	2.93	2.97	3.02	2.84	3.06
Mn_2O_3							1.40	1.40	1.45	1.49	1.39	1.54
Total	**100.00**	**100.00**	**100.00**	**100.00**	**100.00**	**100.00**	**100.00**	**100.00**	**100.00**	**100.00**	**100.00**	**100.00**

***Li_2O calculated by difference**

Appendix 2

Waste glasses – XRF (mol %)						
Oxide	CZMF-15P	CZMF-20P	CZMF-25P	**MZMF-15P**	**MZMF-20P**	**MZMF-25P**
SiO_2	45.66	44.34	41.62	45.92	44.50	42.80
B_2O_3	16.79	15.86	15.01	16.57	15.78	15.04
Na_2O	7.72	7.23	7.29	7.76	7.59	7.31
Li_2O^*	3.59	3.39	3.18	3.58	3.38	3.16
ZrO_2	5.81	5.31	5.67	6.14	5.55	5.43
SiO_2	3.32	3.46	3.43	3.63	3.50	3.27
CaO	2.64	2.38	2.85	2.32	2.27	2.14
Mn_2O_3	3.39	3.68	3.61	3.05	3.48	3.74
ZnO	3.65	3.97	4.20	3.67	3.76	4.13
MoO_3	4.45	6.07	7.92	4.36	5.95	7.64
ZrO_2	2.17	2.99	3.58	2.11	2.94	3.79
BaO	0.72	1.11	1.32	0.70	1.06	1.23
Cs_2O	0.00	0.03	0.07	0.04	0.04	0.08
SrO	0.08	0.16	0.25	0.14	0.17	0.23
P_2O_5	0.00	0.00	0.00	0.00	0.03	0.00
Total	**100.00**	**100.00**	**100.00**	**100.00**	**100.00**	**100.00**

***Li_2O calculated by difference**